2D nanopores: fabrication, energy harvesting and field-effect sensing

Thèse N° 9516

Présentée le 21 juin 2019

à la Faculté des sciences et techniques de l'ingénieur
Laboratoire de biologie à l'échelle nanométrique
Programme doctoral en biotechnologie et génie biologique

pour l'obtention du grade de Docteur ès Sciences

par

Michael GRAF

Acceptée sur proposition du jury

Prof. Ph. Renaud, président du jury
Prof. A. Radenovic, directrice de thèse
Prof. M. Mayer, rapporteur
Prof. M. Drndic, rapporteuse
Prof. C. Guiducci, rapporteuse

2019

ÉCOLE POLYTECHNIQUE
FÉDÉRALE DE LAUSANNE

Abstract

Solid-state nanopores are man-made, nano-sized openings in membranes separating two chambers containing an electrolyte solution. When applying an electric field across the membrane, the nanopore provides the only path for mobile ions to pass from one side of the membrane to the other. This current of ions is highly dependent on the pore size, membrane thickness, and surface charge. Small modulations in the system can lead to a large current modulation. We take advantage of this by translocating biomolecules through the nanopore. Typically, molecules such as DNA have an intrinsic charge in solution and will be attracted by the electric field generated around the nanopore. If the size of the pore allows it, they will thread into the pore and translocate to the opposite chamber. When this happens, we record characteristic current modulations associated with the geometry of the analyte. The amount of signal we measure, as well as the spatial resolution, is dependent on the membrane thickness. Generally, the thinner the membrane, the more ion current is generated and therefore the larger is the recorded signal. Therefore, the isolation of mono-atomic crystals of carbon, also known as graphene, at the beginning of the 21st century sparked much interest in using 2D materials for nanopore sensors. The thickness of these materials is approaching the distance between two bases in a DNA molecule, which raised the hopes of sequencing DNA when it passes through the orifice. However, lack of control of the translocation dynamics, as well as technical challenges related to the fabrication of 2D membranes, limited their practical use.

In this thesis I will show that 2D nanopores can be fabricated reliably and provide a very flexible platform, not only allowing the analysis of single-molecules through different sensing modalities, but also the harvesting of energy:

Fabrication. First I will introduce the reader to 2D nanopores made in molybdenum disulfide (MoS_2). MoS_2 is a semiconducting material that sparked much interest in scaling down transistors and has shown better properties in nanopore-experiments than graphene. In the last few years, I gained a lot of insights into 2D-nanopore fabrication. Therefore, I will first detail how MoS_2-nanopore devices can be fabricated reliably and I will discuss potential pitfalls that researchers might encounter when manufacturing these devices. Furthermore, I will show what to expect after a successful fabrication process and how these devices can be characterized. I hope to motivate more researchers to study this fascinating material. This chapter will also serve as a foundation for the rest of the thesis where I use this system for a novel biosensor and to generate energy.

Blue Energy. We realized that nanopores in atomically thin MoS_2 not only provide a system with low resistance to ionic current but also exhibit excellent ion-selectivity. Therefore, we developed an energy-harvesting system based on the osmotic pressure generated when concentration gradients are applied across the membrane. Energy harvested through concentration gradients is called Blue Energy and would provide a sun-and-wind independent energy source at estuaries around the world. Converting this osmotic energy through reverse-electrodialysis relies on ion-selective membranes. Typically, to achieve good ion permeability ratios, alkaline conditions are used to boost the surface charge in solution. First, I will detail the results obtained with this alkaline system. Second, by exploiting the photo-excitability of MoS_2 membranes, I will show that we can raise the ion selectivity of the membrane by a factor of 5 while staying at a neutral pH. I carefully investigate different spurious effects such as heat which could explain this behavior and conclude that the observed effect is due to a change in the surface charge caused by light-induced charge generation. Furthermore, I will show that the behavior of small nanopores is dominated by surface conductance and thus displays a reduced apparent osmotic potential. I will introduce a formalism based on the Dukhin number to quantify these effects in the case of a concentration gradient system.

Nanopore-FET. Although ionic sensing with nanopores allows the precise measurements of single molecules, the spatial resolution in ionic sensing is limited by the access resistance. The access resistance is a physical effect originating from the transition of ions from a bulk volume to the confinement of nanopore. This limitation can potentially be overcome by an alternative sensing scheme independent from the ionic current. I will show how to extend the typical ionic sensing modality of nanopores with a supplementary sensing scheme taking advantage of the semiconducting properties of MoS_2. In this work, I attempted to fabricate a freestanding nanoribbon of monolayer MoS_2 in which a nanopore is drilled. The nanoribbons are then contacted through metal leads, which allow measuring the current through the material itself (transverse current). The ionic current and the transverse current are recorded simultaneously and show correlated current modulations when DNA molecules translocate through the nanopore. The precise sensing mechanism of these devices is currently not well understood but is believed to originate from the charged molecules themselves or from local potential changes near the nanopore. I will discuss the challenges in fabricating such devices which will hopefully provide insights for anyone interested in the fabrication of MoS_2-based sensors. Furthermore, I will discuss the observed signals and propose possible explanations for the observed current traces.

Keywords: solid-state nanopore, nanopore, 2D-material, molybdenum disulfide, MoS_2, transition metal dichalcogenide, fabrication, PMMA, PDMS, transfer, single-molecule detection, blue energy osmotic power generation, reverse electrodialysis, transmission electron microscopy, laser, field-effect transistor, transverse sensing, nanofabrication, DNA translocation, biosensor

Zusammenfassung

Synthetische Nanoporen sind künstliche nanometer-grosse Öffnungen in Membranen, die zwei Kammern einer Salzlösung verbinden. Wenn ein elektrisches Feld über die Membran angelegt wird, bietet die Nanopore die einzige Verbindung durch die mobile Ionen von einer Seite zur anderen gelangen. Dieser Ionenstrom hängt stark von dem Durchmesser der Pore, der Membrandicke und der Oberflächenladung ab. Kleine Veränderungen in diesem System können zu einer starken Veränderung des Stromes führen. Biomoleküle die durch die Nanopore gezogen werden, können ebenfalls diesen Ionenstrom verändern. Typischerweise haben Moleküle, wie zum Beispiel DNA, eine inhärente elektrische Ladung und werden dadurch von dem elektrischen Feld angezogen, das um die Nanopore herum erzeugt wird. Wenn die Größe der Pore es erlaubt, werden die Moleküle in die Pore eingefädelt und in die gegenüberliegende Kammer verschoben. In diesem Fall messen wir charakteristische Stromveränderungen, die mit der Geometrie des Moleküls zusammenhängen. Die Grösse des aufgezeichneten Signals, sowie die räumliche Auflösung hängt von der Membrandicke ab. Je dünner die Membran ist, desto mehr Strom wird fliesst und desto größer ist das aufgezeichnete Signal. Daher haben monoatomare Kohlenstoffkristalle, auch Graphen genannt, zu Beginn des 21. Jahrhunderts ein großes Interesse zur Verwendung von 2D-Materialien in Nanoporensensoren geweckt. Die Dicke dieser 2D-Materialien gleicht ungefähr dem Abstand zwischen zwei Basen in einem DNA-Molekül, wodurch die Hoffnung erstand, dass Sequenzierung von DNA die durch diese Pore gezogen wird, möglich ist. Die mangelnde Kontrolle über die Dynamik, mit welcher sich das DNA Molekül bewegt, sowie technische Herausforderungen bei der Herstellung von 2D-Membranen haben jedoch bisher praktische Anwendungen eingeschränkt.

In dieser Doktorarbeit werde ich zeigen, dass 2D-Nanoporen zuverlässig hergestellt werden können und dass sie eine sehr flexible Plattform bieten, die nicht nur die Analyse von einzelnen Molekülen durch alternative Sensormodalitäten ermöglichen, sondern auch für die Energiegewinnung verwendet werden können:

Osmotische Energie. Wir zeigen, dass Nanoporen im atomar dünnen Molybdändisulfid (MoS_2) ein System mit niedrigem Widerstand bilden. Zusätzlich weisen solche Poren ausgezeichnete Ionenselektivität auf. Dadurch haben wir ein Energiegewinnungssystem entwickelt, das auf dem osmotischen Druck basiert, der erzeugt wird, wenn ein Konzentrationsgradient über die Membran erzeugt wird. Energie, die durch Konzentrationsgradienten gewonnen wird, wird als blaue Energie bezeichnet und könnte, installiert an den weltweiten Flussmündungen,

eine alternative Energiequelle zu Sonnen- und Windkraft darstellen. Die Umwandlung dieser osmotischen Energie durch Umkehrelektrodialyse beruht auf ionenselektiven Membranen. Um gute Ionenpermeabilitätsverhältnisse zu erreichen, werden normalerweise alkalische Bedingungen verwendet, um die Oberflächenladung der Membran zu verstärken. Zuerst werde ich unsere Ergebnisse, die wir mit diesem alkalischen System erhalten haben, beschreiben. Zweitens möchte ich durch Ausnutzung des photoelektrischen Effekts von MoS_2 Membranen zeigen, dass wir die Ionenselektivität der Membran bei neutralem pH-Wert um einen Faktor fünf erhöhen können. Ich habe verschiedene Störeffekte untersucht, die dieses Verhalten erklären könnten, und schlussfolgere, dass der beobachtete Effekt auf eine Veränderung der Oberflächenladung zurückzuführen ist. Licht, das auf die Oberfläche des Materials trifft, kann negative Ladungen im Material erzeugen die die Oberflächenladung verstärken. Des weiteren werde ich zeigen, dass das Verhalten kleiner Nanoporen von der Oberflächenleitfähigkeit dominiert wird und somit ein vermindertes osmotisches Potential aufweist. Ich werde einen Formalismus einführen, der auf der Dukhin-Zahl basiert, um diese Effekte im Falle eines Konzentrationsgradienten zu quantifizieren.

Feldeffekt Sensor. Obwohl die Ionenmessung mit Nanoporen die Eigenschaften einzelner Moleküle aufdeckt, ist die räumliche Auflösung bei der Ionenmessung durch den Zugangswiderstand begrenzt. Der Zugangswiderstand ist ein physikalischer Effekt, der aus der Aufstauung von Ionen aus einem grossen Raum in den extrem kleinen Einschlussbereich der Nanopore resultiert. Diese Einschränkung kann möglicherweise durch ein alternatives, vom Ionenstrom unabhängiges Messungsschema überwunden werden. Ich werde zeigen, wie man die typischen Messungen des Ionenstroms mit einem zusätzlichen Sensor erweitern kann, der auf den halbleitenden Eigenschaften von MoS_2 basiert. In dieser Doktorarbeit habe ich versucht, ein freistehendes Nanoband aus MoS_2 herzustellen, in dem eine Nanopore gebohrt wird. Diese Nanobänder werden dann mit metallischen Verbindungen versehen, wodurch ein Strom durch das Band selber (Querstrom) geleitet wird. Der Ionenstrom und der Querstrom werden gleichzeitig gemessen und zeigen korrelierte Strommodulationen auf, wenn sich DNA-Moleküle durch die Nanopore bewegen. Den genauen Mechanismus dieser alternativen Messung verstehen wir bis jetzt noch nicht sehr gut, aber wir nehmen an, dass er von lokalen Potentialänderungen in der Nähe der Nanopore oder von dem direkten Einfluss der Ladung des Moleküls stammt. Ich werde die Herausforderungen bei der Herstellung solcher Sensoren diskutieren und hoffe dadurch einen Einblick zu bieten für jeden der an der Herstellung solcher auf MoS_2 basierten Sensoren interessiert ist. Außerdem werde ich die gemessenen Signale diskutieren und mögliche Erklärungen für die beobachteten Stromverläufe vorschlagen.

Stichwörter: Synthetische Nanopore, Nanopore, 2D-Material, Molybdändisulfid, MoS_2, Übergangsmetalldichalcogenid, PMMA, PDMS, Transfer, Einzelmoleküldetektion, Erzeugung von osmotischer Energie, Umkehrelektrodialyse, Transmissionselektronenmikroskopie, Laser, Feldeffekttransistor, Querstrom, Nanofabrikation, Biosensor

Acknowledgements

I would like to start with thanking my high-school teachers at *Kantonsschule Olten* for awakening my scientific interest. Thank you for being such inspiring teachers! I hope one day I will be able to inspire young people the same way you inspired me. Many people have made my PhD thesis an unforgettable experience over the years. I will now try to mention everyone that has in one way or another taught me science, discussed results or had beers with me. To be fair I will start with my host lab during my Master thesis, where I learned all the basics of working in a wet-lab. Thanks to Jeffrey Tang, Tchern Lenn and Alan Lowe for all the effort you put into teaching the inexperienced me. Later, when I started my thesis at EPFL Lorenz Steinbock invested a lot of time in teaching me the art of glass making. Thanks, Lorenz for all the insights! After a while, I decided to turn my back on glass nanocapillaries and joined the Chinese superteam working on 2D nanopores: Jiandong Feng and Ke Liu! Ke basically taught me all there is to know about nanofabrication in our cleanroom. Furthermore, they involved me early on in papers that they were writing. Thank you so much for this! Jiandong was equally important to me: His deep knowledge of the scientific literature made him a walking library saving me from tedious literature searches. Apart from that, his super sharp intellect and deep understanding of many different aspects of science have always pushed me forward. The work he did during his thesis has raised the bar to new levels. I am very grateful that you let me work with you on all these crazy projects! Thank you for all your help and inspiration! Apart from teaching me all the lab-work necessary to get started on my project, Ke was also a very reliable beer partner. Thank you for the countless liters of beer over the years! We were able to solve most problems over these alcohol infused discussions. As an old Chinese proverb correctly says: *No beer, no data!* This brings me to another unforgettable person: Po-Ling Chang. Apart from scientific collaborations and beer related wisdom, he treated the lab regularly to home-made Chinese food. Thank you so much for the great time and a for being such a great friend.

I would also like to thank Hendrik Deschout for a great time as my table neighbor, the beers, parties and great discussions. Also, thanks to Lely Feletti for being an amazing person with a great family to hang out! Now, I would like to thank the current nanopore superteam: Martina Lihter and Mukeschchand Thakur. Martina has become my close collaborator and friend. I want to thank you for your endless support, be it scientific or otherwise. I hope I will be able to give back some of this help in the future. Muki, the latest addition to our nanopore team, has immediately found a place in my heart due to his kind and lighthearted personality. Thank you for a great time!

Thanks to Jochem Deen for great feedback and discussion. I really appreciate all the work you have invested in making my unreadable Python codes accessible to everyone. Great job! Thanks to our lab-knight Michal Macha for all the dark jokes and great fun in the office! Thanks to Sebastian Davis for great rugby matches, mind-blowing Monty Python reenactments, and attempts of explaining cricket to me. Special thanks also to very talented musician Andrey Chernev for unforgettable concerts and solving difficult nanofabrication problems! Thanks to Vytautas Navikas for amazing visuals and all the bullying. Thanks to Sanjin Marion for your drive to improve the status quo in the lab. Thanks, Evgenii Glushkov for amazing laughs and epic house parties! Also, I would like to thank our visitors Jens Gundlach and Andrew Laszlo for great discussions, beer-time, and amazing biopore science. Thanks, Jens for always eating my tomatoes at lunch! Thanks to Martine Truan for making everything administrative going super smoothly!

Thanks to all the summer students and interns that have made contributions in various ways: Andrei Kiselev, Alexander Timin, and Filip Ilievski! You guys are amazing!

Thanks to all the members of our neighbor lab LANES who taught me a lot in solid-state physics and allowed me to use their equipment. Thanks to Andras Kis for opening his lab for me. Special thanks to Dmitrii Unuchek, Dumitru Dumcenco, and Dmitry Ovchinnikov for a great discussions!

Thanks to the whole center for micronanotechnology (CMI) staff for your amazing support! Special thanks to Zdenek Benes for amazing electron-related support. Further, I would like to thank the whole team of the interdisciplinary centre for electron microscopy (CIME) for the great support on electron microscopes. Thanks, Duncan Alexander for teaching me everything about the TEM!

Many thanks to the members of my thesis committee for evaluating my work and the wonderful discussions we had: Marija Drndic, Michael Mayer, Philippe Renaud, and Carlotta Guiducci. Special thanks to Carlotta for mentoring me during my PhD and giving me the opportunity to teach young students as a teaching assistant.

My biggest gratitude, however, goes to my thesis director Aleksandra Radenovic. She made all the amazing experiences in my life reality. She hooked me up with a lab in Berkeley to do my Master thesis, then took me in as a PhD student when I came back. Thanks for the countless opportunities to travel around the world and present our work. You have always believed in me, even when I didn't. The trust you put in me allowed me to work independently, which helped developing super important skills for the future. I am eternally thankful for all the opportunities you selflessly provide to your students. Thank you!

To end, I would like to thank my family. First, my parents Marcel and Kathrin for giving me an amazing childhood and therefore the framework needed to master life successfully. Danke vel mol! Also, I would like to thank my sister Isabelle for being patient because I did not see her as often as I would have wished to. Muchas gracias chica! Lastly, I would like to thank my wife Bruna for enduring this difficult time with me. Your love has kept me alive over these years.

Lausanne, 10 April 2019 Michael Graf

Contents

Abstract (English/Deutsch) **i**

Acknowledgements **v**

List of figures **xiii**

List of tables **xvii**

1 Introduction **1**

1.1 Brief Overview of the Nanopore Field 1
1.2 Applications of Biological Nanopores 6
1.2.1 DNA sequencing 6
1.2.2 Precision ruler 7
1.3 Applications of Solid-State Nanopores 7
1.3.1 Single-molecule sensor 7
1.3.2 A biological model 8
1.3.3 Water filtration 9
1.3.4 Power generation 9
1.3.5 DNA sequencing with solid-state nanopores 10
1.4 The Physics of the Nanopore 12
1.4.1 General principles 12
1.4.2 The ionic current 13
1.4.3 Conductance of MoS_2 pores 14
1.5 Translocation Physics 15
1.5.1 Polymer physics 16
1.5.2 Capturing the DNA with a nanopore 18
1.5.3 Voltage dependence 20
1.5.4 Salt concentration dependence 21
1.5.5 Viscosity effects 24
1.6 Beyond Ionic Sensing 24
1.6.1 Optical detection 25
1.6.2 Tunneling current 25
1.6.3 FET-like sensing 26
1.7 Molybdenum Disulfide 27

1.7.1 Sources 28
1.7.2 Characterization 30
1.8 Structure and content of this thesis 32

2 MoS_2 Nanopore Fabrication 35
2.1 Overview of the Procedure 36
2.2 Comparison to other Methods 37
2.2.1 Limitations of the approach 39
2.3 Substrate Fabrication 39
2.3.1 Types of noise 40
2.3.2 Reducing noise 40
2.3.3 Electrical discharge 41
2.3.4 Coating 41
2.3.5 Leakage 42
2.3.6 MoS_2 sources 43
2.4 Transfer onto the SiN_x membrane 44
2.4.1 Transfer with PMMA 45
2.4.2 Transfer with PDMS 46
2.5 Transfer Quality 47
2.5.1 TEM 48
2.6 Nanopore Drilling and Characterization 49
2.6.1 Nanopore creation by TEM drilling 49
2.6.2 Nanopore creation by ECR 50
2.6.3 Current measurements 50
2.7 Experimental Set-Up 54
2.7.1 Amplifiers set-up 54
2.7.2 Analog-to-digital conversion set-up 54
2.7.3 Flow-cell 55
2.7.4 Device handling 55
2.7.5 Pore wetting 56
2.7.6 Electrodes 56
2.8 Data Acquisition 57
2.9 Data Analysis 58
2.9.1 Current voltage relationships 58
2.9.2 Translocation data analysis 58
2.9.3 A selection of available software 58
2.10 Anticipated Results 59
2.10.1 Chip fabrication 59
2.10.2 DNA translocations 60
2.10.3 Osmotic power generation 62

3 Blue Energy **63**
3.1 Summary . . . 63
3.2 Introduction . . . 64
3.3 Results . . . 65
3.4 Methods . . . 70
3.4.1 Nanopore fabrication . . . 70
3.4.2 Nanofluidic measurements . . . 71
3.4.3 Characterization of single-layer MoS_2 transistors . . . 71
3.4.4 Data analysis . . . 72
3.4.5 Computational simulations . . . 73
3.5 Supplementary Figures and Tables . . . 75

4 Light-Enhanced Blue Energy **83**
4.1 Summary . . . 83
4.2 Introduction . . . 84
4.3 Results . . . 85
4.3.1 Experiment . . . 85
4.3.2 Laser induced surface charge changes . . . 86
4.3.3 Osmotic power generation . . . 88
4.3.4 Estimation of the surface charge . . . 88
4.3.5 Photoluminescence . . . 89
4.4 Discussion . . . 91
4.4.1 Heat . . . 91
4.4.2 Evidence for increased surface-charge density . . . 92
4.4.3 Surface vs. bulk conductances . . . 92
4.4.4 Consequence of the light boosting . . . 94
4.4.5 Outlook . . . 95
4.5 Methods . . . 96
4.5.1 Nanopore fabrication . . . 96
4.5.2 Optical measurements . . . 97
4.5.3 Data analysis . . . 98
4.5.4 COMSOL numerical modeling – heat . . . 98
4.5.5 COMSOL numerical modeling – nanopore . . . 99
4.6 Supplementary Data . . . 100
4.6.1 Heat discussion . . . 100
4.6.2 Derivation of the modified GHK equation . . . 103
4.6.3 Surface conduction domination . . . 103
4.6.4 Surface charge measurements . . . 104
4.6.5 Supplementary figures and tables . . . 105

5 Transverse Detection of DNA in a MoS_2 Nanopore **113**
5.1 Summary . . . 113
5.2 Introduction . . . 113
5.2.1 Tunneling electrodes and field-effect sensing . . . 114
5.3 Device Fabrication . . . 115
5.3.1 Design principles . . . 115
5.3.2 Summary of the fabrication steps . . . 116
5.3.3 Alignment of subsequent EBL steps . . . 118
5.4 Results . . . 122
5.4.1 Conductance measurements . . . 122
5.4.2 Ionic gating . . . 122
5.4.3 DNA translocations . . . 123
5.4.4 Decoupling the grounds . . . 124
5.4.5 Second dataset . . . 126
5.5 Discussion . . . 129
5.5.1 Yield . . . 129
5.5.2 Sensing principle . . . 129
5.5.3 Signal comparison . . . 134
5.5.4 Signal improvement through the transverse channel . . . 134
5.5.5 Noise . . . 137
5.5.6 Stability . . . 137
5.5.7 Metal contacts . . . 138
5.5.8 Gating . . . 138
5.5.9 TEM induced damage . . . 139
5.6 Challenges . . . 140
5.6.1 Fabrication challenges . . . 140
5.7 Conclusion and Outlook . . . 143
5.8 Supplementary Figures and Tables . . . 144

6 Outlook and Conclusion **149**
6.1 Fabrication . . . 149
6.2 Blue Energy . . . 151
6.3 Transverse Detection . . . 154

A Appendix **159**
A.1 Materials . . . 159
A.1.1 Reagents . . . 159
A.1.2 Equipment . . . 161
A.2 Protocol . . . 165
A.2.1 Fabrication of silicon nitride chips. . . . 165
A.2.2 Fabrication of a test wafer for leakage analysis . . . 169
A.2.3 Transfer . . . 170
A.2.4 Nanopore formation . . . 174

A.2.5 Precision painting 177
A.2.6 DNA translocations 177
A.3 FET Process Flow 178

Curriculum Vitae **209**

List of Figures

1.1 Schematic drawing from Wallace H. Coulter's patent 2
1.2 Publication evolution 3
1.3 Method to create small nanopores 5
1.4 MoS_2 as a reverse electrodialysis membrane 11
1.5 Principle of the nanopore sensor 12
1.6 FEM simulation 15
1.7 Event rate 19
1.8 Contribution of the access resistance 21
1.9 Dwell time 22
1.10 Current enhancement and DNA docking 23
1.11 Monolayers of MoS_2 and graphene 28
1.12 Vertical growth of WSe_2 29
1.13 Growth of MoS_2 crystals on sapphire 30
1.14 TEM imaging of MoS_2 32

2.1 Overview of the fabrication process 37
2.2 Types of noise, PSD 41
2.3 Gold plating the test chips 42
2.4 Leakage tests 44
2.5 Troubleshooting MoS_2 transfer 45
2.6 PDMS-assisted selective transfer of MoS_2 47
2.7 Beam damage 48
2.8 TEM images of suspended MoS_2 49
2.9 Diameter and thickness of the aperture 53
2.10 Flow-cell design 56
2.11 Anticipated results: substrate fabrication 60
2.12 Anticipated results: DNA translocations 61
2.13 Anticipated results: osmotic power generation 62

3.1 Operation schematic of osmotic energy harvesting with MoS_2 nanopores 65
3.2 Electrical conductance and chemical reactivity of the MoS_2 nanopore 66
3.3 Osmotic power generation 69
3.4 Demonstration of a self-powered nanosystem 70

S3.1 The subtraction of electrode contribution and stability of nanopore generator . 76
S3.2 pH and pore size-dependent osmotic power generation 77
S3.3 Ion selectivity: ideal cation selectivity 78
S3.4 Molecular dynamics simulated power generation 79
S3.5 Continuum based Poisson-Nernst-Planck model 80
S3.6 Molecular dynamics modeled conductance as a function of thickness 80
S3.7 Simulated power generation vs. thickness 81
S3.8 Characterization of a single-layer MoS_2 transistor with nanopores and SMU . . 82

4.1 Experimental overview 86
4.2 Experimental set-up 87
4.3 Effect of laser light on the osmotic energy conversion 89
4.4 Effect of laser light on the osmotic power 90
4.5 Photoluminescence measurements 91
4.6 Surface conduction contribution 94
4.7 Modified GHK model 95
S4.1 Laser spot size 105
S4.2 Simulated effect of the surface charge 106
S4.3 Surface charge measurements 107
S4.4 Photo-oxidation 108
S4.5 Permeability ratio simulations 108
S4.6 FEM simulation of the heat produced by the laser 109
S4.7 Heat calculation 110
S4.8 Analytical heat estimation 111

5.1 Device design summary 117
5.2 Fabrication 118
5.3 Three-step EBL alignment 120
5.4 Alignment precision 121
5.5 Conductance measurements 124
5.6 Experimental data of 80 nt ssDNA translocation 125
5.7 Electrical set-up 127
5.8 TEM image of the device 128
5.9 Translocation data for differently charged analytes 128
5.10 Translocation dynamics 133
5.11 Example of cross-talk 135
5.12 Scatter plots of the translocations 135
5.13 Correlation between the channels 136
5.14 Signal-to-noise ratio 136
5.15 Noise performance 137
5.16 Photogating of a MoS_2-nanopore FET 139
5.17 Influence of TEM irradiation on MoS_2 conductance 140
5.18 Delamination of metal contacts 141

5.19 HSQ as an electrical insulation material 142
5.20 PMMA reflow during ALD 143
5.21 Oxygen RIE 143
S5.1 Bad electrode insulation 145
S5.2 Supplementary conductance measurements 145
S5.3 Supplementary ionic gating 146
S5.4 Ribbon cracking after fabrication 146
S5.5 A selection of contaminated SiN_x apertures 147

6.1 Early process-flow 150
6.2 Impression of the blue energy set-up 152
6.3 Blue energy design proposal 154
6.4 Impression of the FET set-up 156

A1.1 Fabrication 165
A1.2 Insufficient etching of the aperture 168

List of Tables

1.1 Properties of ssDNA 17

2.1 Current-amplifiers available 54
2.2 Available nanopore-software 59

S3.1 Membrane thickness vs. power generation 75

S4.1 Laser powers 105
S4.2 Electrode potentials 106
S4.3 Overview of results 106

A1.1 Complete process flow for the FET device 179

1 Introduction

This chapter serves as an introduction to nanopores and the relevant physics. Before discussing possible applications of solid-state and biological nanopores, I will put the nanopore field into a historical context. After, I will discuss in detail the physics needed to understand this thesis. Last, I will discuss alternative sensing methods, such as field-effect and tunneling-current. The last paragraph (section 1.8 (page 32)) of the introduction will then shortly summarize the structure of this thesis.

The following historical overview might interest people starting in the nanopore field, but can be skipped by more experienced readers.

1.1 Brief Overview of the Nanopore Field

The nanopore field was born in the late 40s when Wallace H. Coulter proposed a novel way of counting red blood cells to speed up clinical measurements. He developed a device containing a thin membrane that separates two chambers filled with a saline solution. The only connection between the two reservoirs was a small hole. He placed an electrode in each chamber and measured the current of ions through this hole. When he applied a hydraulic pressure to drive the red blood cells, they would temporarily block the hole and induce a decrease in the ionic current measured by the electrodes. Coulter patented his counting method in 1953.[1] Nowadays it is commonly referred to as *resistive pulse sensing*. A schematic drawing extracted from his patent explaining the working principle is shown in Figure 1.1.

His first prototypes were fairly crude: The membrane separating the chambers was a cellophane wrapper of a cigarette box.[2] The hole to connect the chambers was done by punching a hot needle through the cellophane wrapper. The Coulter counter has become a commercial success and has been widely used in hospitals since the 60s to quickly characterize blood cell concentration. The American company *Beckman Coulter* acquired *Coulter Corporation*, founded by Wallace H. Coulter, in 1998.[3] The smallest aperture sizes in the Coulter counter are fairly large ($\approx 100\,\mu m$) to allow erythrocytes ($\approx 8\,\mu m$) to pass. In the 70s Ralph W. DeBlois found

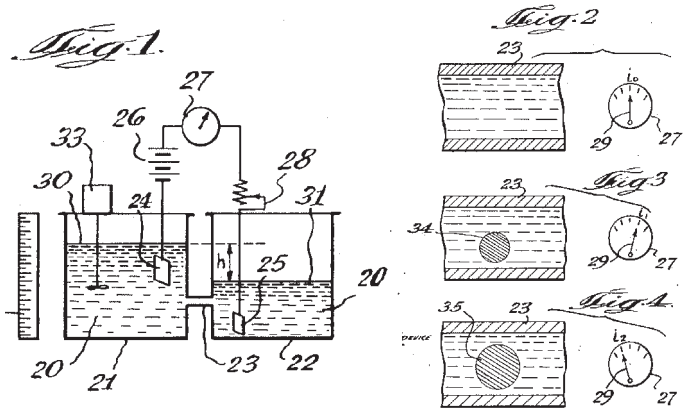

Figure 1.1 – Schematic drawing from Wallace H. Coulter's patent. a, A hydraulic pressure is created by a difference in volume in the two chambers (30/31). The electrodes (24/25) are used to measure the ionic current through the orifice (23). A mixing element (33) provides a homogeneous solution. **b**, When cells migrate through the orifice the ionic current is reduced proportionally to the size of the cell (34/35). The figure was taken from Coulter's patent.[1]

a way to decrease the aperture size to the submicron-scale using track-etched membranes. With this apparatus, it was now possible to count smaller objects such as viruses.[4] The real revolution in resistive pulse sensing arrived in the 90s nearly 4 decades after Coulter's invention. Researchers found ways to reduce the orifice size from millimeters and micrometers to nanometers.

During the 80s, David Deamer scribbled a concept into his notebook that served as the main driving force of the nanopore field: deoxyribonucleic acid (DNA) sequencing. In his early ideas, he describes a small channel through which DNA is electrophoretically driven. Due to different sizes of each base in the DNA strand, the current change should be unique, allowing the direct reading of a DNA strand.[5] In 1996, John Kasianowicz, Eric Brandini, Daniel Branton and David Deamer showed the first translocations of DNA through a biological nanopore. This naturally occurring α-hemolysin pore is formed by monomers spontaneously forming a heptameric channel of 2.6 nm diameter.[6]

In parallel to the development of small orifices, the field of ion-channel electrophysiology that emerged in the 1970s has played a major role in the nanopore field. The patch-clamp method allowed researchers to measure the ionic current through isolated biological channels. A large interest in these measurements led to the development of patch-clamp amplifiers, which are still widely used in the nanopore field. Furthermore, biological channel proteins have gained more and more interest in the field of biosensing. These protein channels can self-assemble and insert spontaneously into lipid bilayers. These lipid bilayers can be created over a large orifice in an insulating material such as polytetrafluoroethylene (PTFE). These protein pores have been widely used to analyze molecules. In recent years protein pores have made tremendous advances, being able to sequence DNA as the molecule is threaded through the pore using an enzyme.[7,8] Furthermore, biological nanopores provide means of measuring

the motion of single motor proteins at unprecedented spatial and temporal resolution.[9] Recently *Oxford Nanopore Technologies*, an England based company, has developed and commercialized a USB-key sized DNA sequencer based on biological nanopores. Many papers have been published using this novel sequencer, but of special significance is the sequencing and assembly of a human genome in 2018[10] or the de-novo assembly of a bacterial genome.[11] The main advantage of the nanopore sequencing method is the long read-lengths, allowing de novo assemblies of long repetitive structures.[10] The small size of the device makes it especially promising for on-site sequencing in challenging environments.[12] As a proof of concept, the company has sent one of their devices to the international space station to investigate whether sequencing could be reliably done in microgravity.[13] To illustrate the enormous traction nanopores have gained in the last few years, Figure 1.2 shows the number of publications per year using the search term *nanopore*.

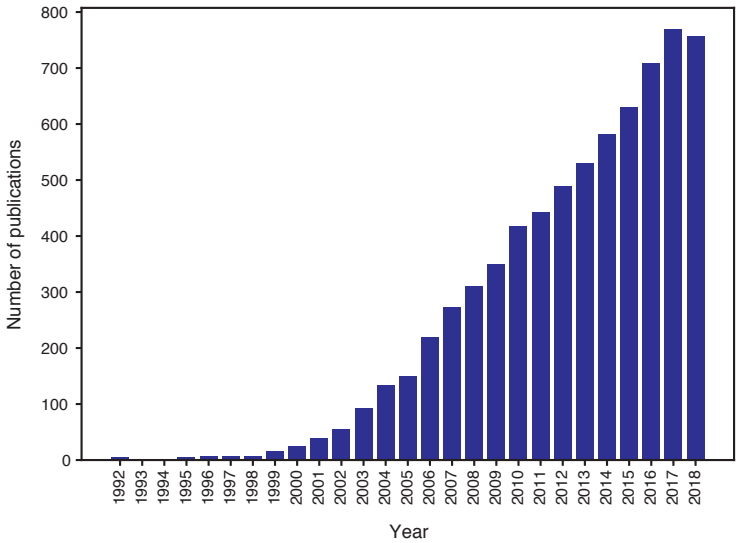

Figure 1.2 – Publication evolution. Number of publications per year using the search term *nanopore*. Data obtained from WebOfScience*.

Biological nanopores have outrun solid-state nanopores in recent years due to their intrinsic reproducibility in terms of geometry. Furthermore, no fabrication steps are needed since biological nanopores are self-assembled and insert spontaneously into a lipid bilayer, which makes them easy to use and accessible to a larger amount of laboratories. However, biological nanopores have a fixed geometry, which limits their application to analytes of a certain size. On the other hand, protein engineering can be used to change local charges or geometry. Furthermore, the stability of biological nanopores as well as their embedding lipid-bilayer is very dependent upon external factors such as temperature, pH, voltage and salt concentration. Solid-state nanopores, therefore, provide an excellent alternative to overcome some of the shortcomings of biological nanopores. In particular, solid-state nanopores can be integrated into devices and show very good stability in non-physiological conditions.

*https://www.webofknowledge.com/

The first true solid-state nanopores were fabricated in 2001 by the group of Jene A. Golovchenko by ion-beam sculpting of silicon nitride (SiN_x) membranes. This new method allowed the creation of nanopores down to 5 nm diameter, allowing the detection of DNA.[14] In a follow-up study, the group showed that the translocation time of DNA is highly dependent on the length of the polymer, effectively allowing sizing of DNA molecules. Furthermore, they observed multilevel current blockade signals, where the second level has twice the amplitude of the first.[15] This effect has been observed ever since in solid-state nanopores and is caused by folding of the DNA molecule.[15,16] Effectively, folding of a double-stranded DNA (dsDNA) introduces four strands of DNA simultaneously into the nanopore, doubling the volume of excluded ions. In 2003, the group of Cees Dekker showed a method of nanopore fabrication with nanometer control. The membranes in this work were not based on SiN_x, but on silicon dioxide (SiO_2). Large, 20 nm holes in were shrunk under an electron beam irradiation in a transmission electron microscope (TEM).[17] One particularity that both fabrication methods of that era had in common was the shrinking of larger holes. On a side-note, pore-shrinking is also possible on SiN_x membranes (Figure 1.3). Similarly to the first nanopore paper of Golovchenko's group Dekker's group observed DNA folding and dwell time dependences on the polymer length in SiO_2 nanopores.[17] In the next few years, the SiN_x membrane became the standard material of choice due to well-established fabrication procedures in micro- and nanotechnology facilities. The fabrication methods evolved as well. First, with the increasing popularity and availability of high-quality transmission electron microscopy (TEM)s instead of shrinking large pores, small nanopores are drilled directly into the membrane.[18] Alternatively, the group of Vincent Tabard-Cossa has developed a method to fabricate small nanopores by applying a large electric field across the membrane.[19] In this method SiN_x membranes are subjected to high electric fields until the membrane breaks. Doing this in a controlled way allows the creation of nanopores of any given size. This method has been adopted by many research groups and is commonly known as controlled dielectric breakdown (CDB). This invention opened the field of solid-state nanopores to many researchers without access to expensive TEM and helped to boost the scientific progress in the field. Very recently, another method combining CDB with laser irradiation has proven to be very effective in creating thin nanopores in SiN_x membranes.[20–22]

In 2010 three research groups published the use of graphene as a separating membrane for nanopore experiments.[23–25] The theoretical thickness of single-layer graphene is only about 0.335 nm,[26] which approaches the distance between bases in the DNA (0.34 nm). The hope was that a graphene membrane can provide the resolution needed to identify the nucleotides when DNA passes through the pore. Unfortunately, bad wetting properties of graphene nanopores as well as strong sticking of DNA to graphene have severely limited the number of published research papers.[27]

The next ultra-thin material used as a separating membrane was molybdenum disulfide (MoS_2) in 2014.[28] These membranes were easier to wet than graphene and provided a good platform to investigate molecule translocations. For instance, by using a gradient of potassium chloride (KCl) and room temperature ionic liquid (RTIL) single-nucleotides were slowed enough to be

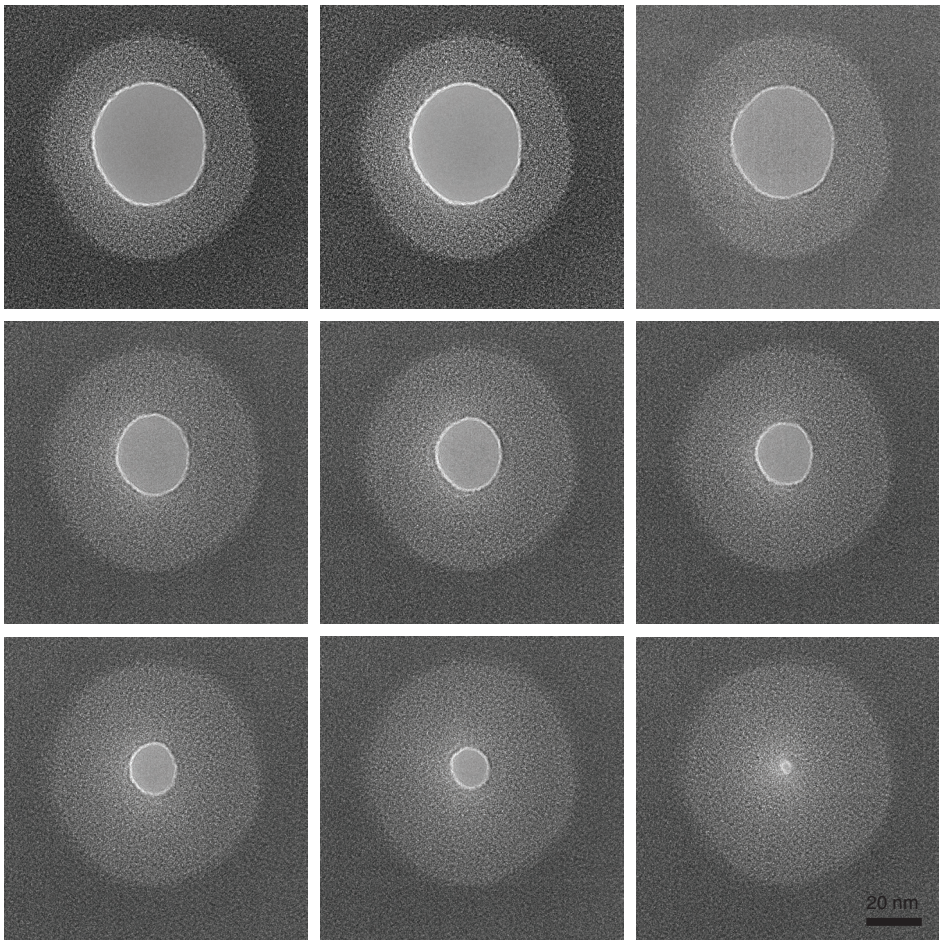

Figure 1.3 – Method to create small nanopores. A large hole can be made in SiN_x through e-beam lithography (EBL) and reactive ion etching (RIE). Then a TEM can be used to shrink this large hole while imaging the sample. This gives good control over the final pore size. As a plus, the pore thickness is reduced (as seen from the contrast difference). Images acquired on a FEI Talos, interdisciplinary centre for electron microscopy (CIME).

differentiated through their ionic signature.[29] This work proved, for the first time, that MoS_2 nanopores have the sensitivity to differentiate between the four nucleotides. However, the translocation physics of a nucleotide is dramatically different from that of a polynucleotide where hundreds of nucleotides are connected through a sugar-phosphate backbone to form a long polymer. Similarly to CDB used to create nanopores in SiN_x membranes, in 2015 we published a method to create nanopores in MoS_2 membranes at subnanometer precision by applying a moderate voltage across the membrane.[30] Other ultrathin materials, such as hexagonal boron-nitride (h-BN),[31] tungsten disulfide (WS_2)[32] and the metal carbide $Ti_3C_2T_x$,[33] have been tested as membranes for DNA translocation.

In the following two sections I discuss very briefly the major applications of nanopores. I will mostly concentrate on the application of solid-state nanopores, mentioning only two major accomplishments of biological nanopores.

1.2 Applications of Biological Nanopores

Biological nanopores are currently dominating the real-world applications of nanopores due to the successful commercialization of a DNA-sequencer.

1.2.1 DNA sequencing

Most progress in the nanopore field was driven by its potential to sequence DNA. Although the idea was proposed in the 90s, it took almost 20 years to achieve the first demonstration of sequencing using a biological nanopore. A major part of the problem was the control of the translocation speed. Ideally, the DNA molecule should translocate with a constant speed that is slow enough to allow the probing of the individual bases as they pass through the constriction. The second crucial requirement was the shape and charges of the protein channel used to translocate the DNA: The shape should contain a short and narrow constriction (sensing region), which ideally spans only a few bases. The charges inside the pore determine whether DNA is able to properly enter the pore and translocate.

In 2010, the group of Jens Gundlach introduced the protein pore mycobacterium smegmatis porin A (MspA).[34] The constriction of MspA is about 1.2 nm in diameter and only 0.5 nm long, which could potentially resolve single-nucleotides. Furthermore, in order to get single-stranded DNA (ssDNA) to translocate through the pore some of the negatively charged amino-acids were replaced by neutral asparagines. Using DNA hairpins they stalled the translocation of ssDNA at predefined locations (dsDNA is not able to pass the 1.2 nm constriction) and examined the current observed. They observed a large current difference for different homopolymers. Furthermore, single-nucleotide substitutions in the homopolymers located just before the hairpin (nucleotide in the sensing region of the pore) showed different current traces for each nucleotide. This work showed that DNA sequencing is in principle possible. However, the approach using hairpins to define which part of the molecule is read is impractical and would require tremendous effort in sample preparation. In 2012, they expanded the MspA system with phi29 DNA polymerase (DNAP) to precisely control the translocation rate.[7] In this approach DNA is mixed with DNAP, which binds the DNA molecules and synthesizes the complementary strand. The large enzyme attached to the DNA strand causes it to stall at the nanopore and the stepwise motion of the polymerase threads the molecule through the constriction in a regular and controlled manner. The ionic current through these MspA pores is defined by 4 nucleotides. By synthesizing a known sequence containing all 256 possible quadromers Andrew Laszlo and coworkers managed to properly calibrate the system and successfully decode long nanopore reads.[8]

In parallel to the academic progress towards nanopore sequencing, the England-based company *Oxford Nanopore Technologies* successfully developed and commercialized a handheld DNA sequencer based on the amyloid secretion channel CsgG from *Escherichia coli*.[35]

1.2.2 Precision ruler

A similar system to the above-described DNA sequencing approach can be used to investigate molecular motors at unprecedented temporal and spatial resolution.[9] By analyzing ionic current modulations while a protein such as a helicase (HEL308) is translocating along the DNA, it is possible to infer the dynamics of the protein action. The exact location of the protein on the DNA can be determined at a resolution of 40 pm, which allowed, for the first time, to probe sub-steps within the hydrolysis cycle of the protein.[9]

1.3 Applications of Solid-State Nanopores

1.3.1 Single-molecule sensor

The most obvious application of solid-state nanopores is the detection of single-molecule translocation. It is well established that the translocation of molecules induces a current change. The question is whether we can extract any useful information from the current change other than just knowing that a molecule has passed through the pore.

DNA length

Sizing of DNA is probably the most obvious application of nanopores. The dwell time, the time the molecule spends in the nanopore, should, in principle, scale with the length of the DNA molecule. Precise sizing of DNA molecules could replace gel-electrophoresis commonly used in determining DNA length. An obvious advantage of the nanopore compared to gel-electrophoresis lies in the amount of material required for the analysis: in theory, if a nanopore sensor is properly calibrated, a single DNA molecule is sufficient to extract its length. However, the realization of a practical DNA sizing apparatus using nanopores has been slowed down by non-linear translocation dynamics (described in more detail in section 1.4).

Protein identification

Using nanopores to quantify and characterize folded proteins in solution is of great interest, since it would allow to probe the protein in its native state. However, in solid-state nanopores protein translocations are still quite challenging to resolve, since many proteins have a very small size and therefore translocate extremely rapidly. As a consequence, many of the translocation events are missed since the dwell time is shorter than the smallest resolvable time of the amplifier.[36] The development of high-bandwidth and low-noise amplifiers increased the limit of detection and allowed smaller proteins to be detected more reliably.[37] For freely translocating proteins, the amplitudes of the current drops observed correlate with the volume of the protein.[37,38] A more elaborate system has been developed by Yusko et al.[39] In this work, solid-state nanopores were coated with a lipid bilayer to anchor the proteins through a flexible tether-protein. Compared to free translocations, the speed of the tethered proteins now

depends on the viscosity of the lipid bilayer. This slowed translocations allowed probing the current while the proteins rotate in the nanopores. Sophisticated models allow the extraction of five parameters from the current signal of a single-protein: approximate shape, volume, dipole moment, rotational diffusion coefficient and charge.

Protein sequencing

DNA sequencing has proven to be extremely useful in medical applications. However, there is a large discrepancy between the genetic sequence (genotype) and its outcome on the organism (phenotype). Even though huge efforts are made to better relate the genotype to phenotype, understanding the transcriptome is utterly complex. An easier representation of the phenotype of a cell is its protein content (proteome). Identifying the proteome is extremely important since it is the result of a dynamic response of the transcription machinery. In medicine, this would allow easier screening of drug candidates on a cellular level to determine possible effects on the body, without having to wait for a whole organism phenotype change. Currently, mass-spectrometry is typically used to sequence proteins.[40] Many problems such as detection limit and dynamic range (concentration range) impede the mass-spectrometer from becoming a true whole-cell protein analysis tool. Needless to say, the nanopore field has become increasingly interested in this problem, since the nanopore detector could provide a single-protein detection limit. In order to read the amino-acid sequence during protein translocation, the tertiary structure needs to be disrupted. This is usually done in strong denaturants. Here, solid-state nanopores have a clear advantage over the biological counterpart, since they are much more stable in extreme buffer conditions. Sodium dodecyl sulfate (SDS) can not only help to unfold the proteins, but also *coats* the protein with a uniform electrical charge,[41] important for electrophoretic translocation. Subnanometer pores in SiN_x seem to be able to extract some information related to the amino acid sequence,[42] encouraging future development of a solid-state nanopore protein sequencer. An interesting approach to biopolymer sequencing was developed by Bush et al.[43] By combining a nanopore with a mass spectrometer, conventional electrospray injection using a background gas could be avoided. A nanopore acts as a nanospray injecting nozzle with a small enough opening diameter to inject single-ions directly from the liquid inside the tip into the analysis-chamber of the mass-spectrometer.

1.3.2 A biological model

Cells are filled with pores and channels. The main function is the transport of ions and molecules between organelles. The nuclear pore complex (NPC), for instance, is covering the nuclear envelope and is responsible for all the traffic between the cytoplasm and the nucleoplasm. This large protein complex is not only an extremely efficient transporter but also a great gatekeeper. The complexity of biological pores and channels often impedes our ability to understand the underlying processes. Solid-state nanopores can help to simplify these systems. FG-nups (nucleoporins with chains of phenylalanine-glycine repeats) are believed

to be responsible for the selectivity of NPC. To better understand the behavior of these FG-nups, Kowalczyk et al.[44] have linked different types of FG-nups to a silicon nitride nanopore. Observing the transport of different molecules through these biomimetic nanopores allows to draw conclusions about the role of the different nucleoporins in the selectivity of the NPC.[44]

1.3.3 Water filtration

I have mainly covered the analysis of biomolecules so far. However, nanopores can do much more than detecting analytes. One of the largest problems facing society is access to fresh water. A third of the population is already living in countries with limited water access. In the future, this number will increase substantially.[45] Desalination of seawater comes with a great energy expense. Especially older technologies like evaporation of seawater and condensation of fresh water consume a substantial amount of thermal energy. Reverse osmosis is an alternative to evaporation and provides an energy-efficient way of desalinating seawater. At heart of the reverse osmosis technology lies a semi-permeable membrane. Ideally, these membranes are selective to ions, i.e. they let water move freely, whereas retaining ions or other larger molecules. Desalination is then achieved by feeding seawater at a high pressure to the membrane. Due to the ion selectivity, ions will be retained, whereas freshwater penetrates the membrane. In the end, one side will be desalinated water while the opposite side will be more concentrated. The type of membrane defines the efficiency of the process. Obviously, the larger the permeation to water, less energy is needed to push the seawater through the membrane. A candidate for novel membrane materials is carbon nanotubes. Surprisingly, the water transport in these tubes was shown to be three orders of magnitude larger than expected from hydrodynamic models.[46] Another way of improving the permeability of water of a reverse osmosis membrane is to reduce its thickness. Considering a porous membrane of area A and thickness l, the water flux would be proportional to $\frac{A}{l}$. The first obvious candidate to be tested for desalination was graphene, the 2D-material superstar. Very high water transport and very efficient ion retention were observed.[47] Other than graphene MoS_2 has been investigated for desalination. Molecular dynamics (MD) simulations suggest that the water flux through a MoS_2 pore is superior to graphene due to the hydrophilic nature of the Mo atom.[48] To my knowledge, no experimental work has carefully investigated the desalination properties of porous single-layer MoS_2 membrane. If 2D-membranes were to become a viable option for desalination a few major problems need to be solved. First, large-scale, defect-free synthesis is needed. Second, a method for generating pores of a uniform and well-controlled size is imperative. Last, but not least the mechanical stability of these membranes needs to be improved to withstand the high pressures of the reverse osmosis systems.

1.3.4 Power generation

In a similar spirit as the reverse osmosis for desalination, thin membranes can be used to generate electricity. This is done by applying a chemical potential difference (concentration difference) across the membrane. All energy harvesting methods based on ion concentration

differences are summarized under the term *Blue Energy*. In practice, this energy source can be used anywhere where river water (low salinity) is flowing into an ocean (high salinity). To estimate how much energy is actually available from this chemical potential difference we can look at the free energy of mixing of salt and freshwater:[49]

$$\Delta_{\text{mix}}G = 2RT[c_m \ln(c_m) - \chi c_s \ln(c_s) - (1-\chi)c_r \ln(c_r)] \tag{1.1}$$

, where R is the universal gas constant, T the temperature, c_i the concentrations of mixed ($i = m$), river ($i = r$) and seawater ($i = s$). χ is the volumetric fraction of seawater. Using typical values for the concentration of seawater (0.6 M) and river water (0.024 M) we can calculate a maximum value of $\Delta G \approx 2500\,\text{J}\,\text{l}^{-1}$. This value is per liter river water, which is the limiting factor in a real-world application. Depending on how much freshwater a power plant could process, values of up to 1 GW are theoretically possible (at a freshwater rate of $400\,\text{m}^3\,\text{s}^{-1}$).[49] This energy is independent of wind and sun and runs 24 hours, 7 days a week.

There are currently two different methods of extracting this energy. First, water permeable membranes can be used to generate a water flow from the more dilute side to the more concentrated side. This increases the pressure in the compartment of the higher concentrated side. This pressure can then be used to power a turbine. This approach is called pressure-retarded osmosis (PRO).

However, if the separating membrane is ion permeable an osmotic pressure is generated and the ions will flow from the more concentrated to the less concentrated side to equilibrate the chemical potential difference. If the membrane is selective for only one ion type (anion or cation), a net current is induced that can be converted to an electron current at electrodes placed on each side of the membrane. In practice, a stack of cation and anion selective membranes are used to increase the produced current. This technology is called reverse electrodialysis (RED). Similarly as explained above, the thickness of the membrane defines the achievable ionic currents. Figure 1.4 summarizes the principle of RED using the example of a nanopore in a MoS_2 membrane.

Two chapters in this thesis are dedicated to energy harvesting using RED and MoS_2 membranes. First, in chapter 3 (page 63), I will present that MoS_2 membranes are several orders of magnitude more efficient in energy conversion than conventional membranes. Then in chapter 4 (page 83) I will show that we can further boost the energy conversion with light to create a solar-blue energy hybrid device, which could be used to boost the efficiency of the energy conversion during the daytime.

1.3.5 DNA sequencing with solid-state nanopores

The holy grail of solid-state nanopore research is to use the technology to sequence DNA. Why are solid-state nanopores still far away from this goal whereas biological nanopores have already solved the problem? In this section, I will try to summarize a few arguments why

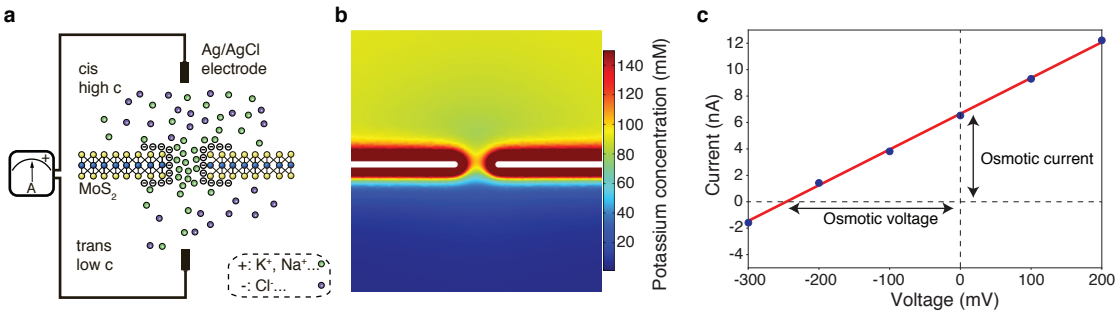

Figure 1.4 – MoS_2 as a reverse electrodialysis membrane. **a**, Schematic of the experimental set-up. A salt concentration gradient provides chemical energy which is converted to electrical energy by a net current of ions through the cation-selective nanopore. **b**, Finite element model simulation of the potassium (K^+) distribution at the charged wall of a 6 nm nanopore, indicating the cation selectivity. **c**, Current-voltage relationship of a KCl concentration ratio of 1000 using a 6 nm pore. The current measured at zero applied voltage is defined as the osmotic current, whereas the voltage at which the current is zero is defined as the osmotic voltage. *This Figure was published in Nature Protocols, 2019, Graf et al.*[50]

solid-state pores have not reached the goal of sequencing DNA yet.

Speed control. Biological nanopores have achieved sequencing due to step-wise and controlled threading of the DNA through the nanopore with the help of an enzyme.[8] In absence of any motion control the translocation of DNA is not smooth: first, the speed increases during DNA translocation.[51] Second, Brownian motion jiggles the DNA molecule back-and-forth during the translocation process, washing out any possible signals associated to the sequence.[52]

Reproducibility. It is impossible to fabricate two solid-state nanopores that are atomically identical. This makes it very hard to reproduce experimental results exactly. Furthermore, the calibration of current levels of a solid-state nanopore for DNA sequencing would be difficult, since every device might have slightly different values.

Noise. Conventional solid-state nanopore substrates (silicon) are much noisier than lipid bilayers in biological nanopores. This avoids high bandwidth measurements.

To summarize, in order to use solid-state nanopores as a sequencing tool, the translocation velocity needs to be reduced and smoothed. Alternatively, low-noise substrates might allow measurements at higher bandwidths and would, therefore, tolerate faster translocation velocities.

After having introduced the major applications of nanopores, I will dedicate the next session to the physics of the nanopore. In this section, I describe the general principles and physical mechanisms that are important to understanding this thesis.

1.4 The Physics of the Nanopore

1.4.1 General principles

The principle of a nanopore-sensor is fairly simple as already mentioned in section 1.1. An insulating material serves as a separating membrane between two reservoirs of an electrolyte solution. When a small hole is fabricated in the insulating membrane, a connection between the two chambers is establish. Applying a voltage across the membrane induces an electric field that is concentrated at the nanopore, driving ions from one side of the chamber to the other. A current amplifier can quantify the ion flow across the membrane. The direction of the applied field and the polarity of the ions in the electrolyte define the direction of flow. A certain pore size and membrane thickness produces a certain ionic current (Figure 1.5a). Charged molecules placed into one side of the chamber (called *cis*-side) will diffuse close to the nanopore and will be electrophoretically threaded through the pore. During the passage, the molecule temporarily blocks the ion flow through the nanopore, inducing a current drop signal recorded by the amplifier (Figure 1.5b). Once the molecule terminates the translocation it diffuses away from the nanopore into the second chamber (called *trans*-side) (Figure 1.5c).

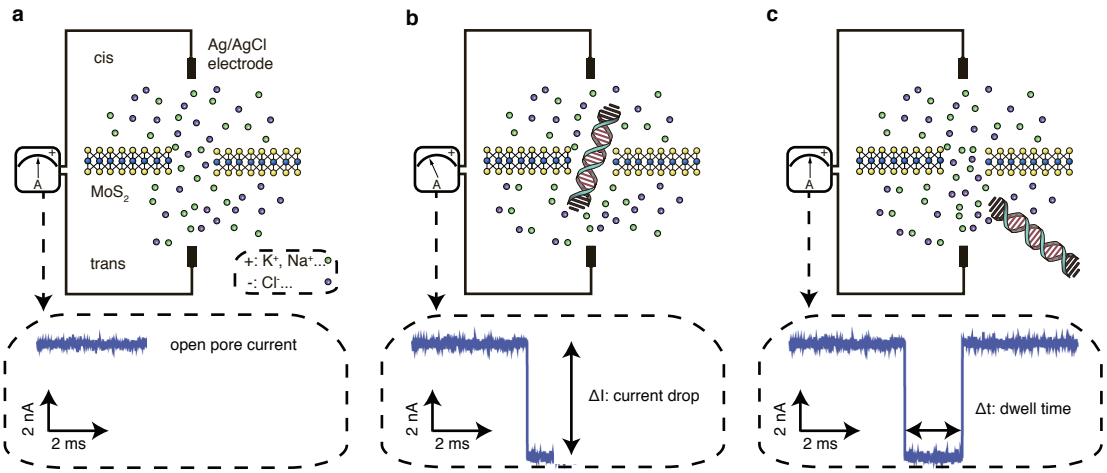

Figure 1.5 – Principle of the nanopore sensor. **a**, A pore in an insulating material induces an ion current measured by a current-amplifier. **b**, A translocating molecule such as DNA temporarily blocks this current producing a current drop signature on the amplifier readout. **c**, Once the translocation is over the current recovers to baseline level. *This Figure was published in Nature Protocols, 2019, Graf et al.*[50]

Electrodes

Typically, in systems where the electrolyte contains chloride (Cl^-), the electrodes, used to apply the voltage and measure the current, are based on a silver wire. To ensure a Faradaic charge transfer process and eliminate capacitive effects on the silver wire, the metal is chlorinated beforehand to produce silver/silver-chloride (Ag/AgCl) electrodes. This chlorination can be done using either a hydrogen peroxide (H_2O_2) or KCl solution. Even in a small and thin layer,

the chlorinated surface is usually large enough to support the small currents measured in a nanopore experiment (<20 nA), i.e. the chlorinated layer does not get consumed during the duration of the experiment. Furthermore, the AgCl salt has a very low solubility, therefore, it does not go into solution and stays at the electrode interface. In terms of electrochemistry, the reactions at the electrodes can be written as: $AgCl + e^- \rightleftharpoons Ag + Cl^-$. This means that the side with the negative bias will release a Cl^- ion into the solution for each electron, whereas the opposite electrode will inject an electron into the circuit by incorporating a Cl^- ion to form AgCl. If the two electrodes are immersed in solutions with different chloride concentrations, then an electrochemical electrode potential is generated. This is also known as the reversal potential or Nernst potential and can be written as: $E = E_0 - \frac{RT}{nF} \ln \frac{[\text{Red}]}{[\text{Ox}]}$, where R is the universal gas constant, T the temperature in Kelvin, F the Faraday constant, [Red] the concentration of reduced species (Cl^-) and [Ox] the concentration of oxidized species (AgCl). The standard potential E_0 is about 222 mV for a Ag/AgCl electrode. The subtraction of this potential is important when measuring the osmotic potential generated by an ion-selective membrane (see subsection 3.4.2 (page 71)).

1.4.2 The ionic current

The conductance through a nanopore system depends mainly on the length of the pore (thickness of the membrane) and the opening size. Obviously, the larger the nanopore the higher the current and the higher the conductance, whereas the thickness of the membrane is inversely proportional to the current, i.e. thicker membranes reduce the ionic current. In most cases, the ionic current through a nanopore can be modeled by the combination of the purely geometrical consideration with the access resistances. The channel resistance of a cylindrical pore can be written by $G_{\text{channel}} = \sigma \frac{\pi d^2}{4l}$, where σ is the bulk conductivity (10.5 S m^{-1} for 1 M KCl), d is the pore diameter and l is the pore length (or membrane thickness). The access resistances are semi-spherical cupola shaped regions of resistance that are formed on each side of the nanopore due to the convergence from the bulk to a narrow constriction.[53] According to Hall, this access resistance can be derived by assuming a planar disc at the pore entrance and gives the following expression: $R_{\text{access}} = \frac{1}{2d\sigma}$.[53] The total resistance of the nanopore system is therefore: $R_{\text{total}} = R_{\text{channel}} + 2R_{\text{access}}$. Combining everything yields the following equation for the total conductance through a nanopore:[54]

$$G = \sigma \left[\frac{4l}{\pi d^2} + \frac{1}{d} \right]^{-1} \tag{1.2}$$

From Equation 1.2 we can see that thin membranes such as MoS_2 (l is small) are dominated by the access resistance part ($\frac{1}{d}$) of the equation, effectively simplifying the equation to $G_{\text{ultrathin}} = \sigma d$. This means that these thin membranes are highly dominated by the access resistance and their spatial resolution does not correspond to the membrane thickness, but

rather to the sum of the membrane thickness and the two access resistances. In terms of DNA sequencing, this increases the smallest theoretical sensing length to several bases. The access resistance can be visualized using finite element model (FEM) simulations. An example is shown in Figure 1.6a, where a significant potential drop starts to develop some distance from the nanopore. Furthermore, it has been measured experimentally using a atomic force microscope (AFM) and related techniques.[55,56]

Equation 1.2 predicts the ionic current surprisingly well for highly concentrated salt solutions. However, at lower concentrations, the surface charge of the nanopore can play a significant role. In thicker pores, a significant electroosmotic flow (EOF) will contribute to the ionic current. I will not detail the consequences of the EOF since all membranes considered in this thesis are ultrathin and this effect can be ignored. Nevertheless, another surface-related effect plays a large role in thin membranes: surface conductance. This phenomenon typically does not depend uniquely on the pore rim charges (as EOF does) but on the surface charges on the membrane in the vicinity of the nanopore. Lee et al. have developed an extension of Equation 1.2 to incorporate surface conduction effects:[57]

$$G = \kappa_b \left[\frac{4l}{\pi d^2} + \frac{1}{1 + 4\frac{l_{Du}}{d}} + \frac{2}{\alpha d + \beta l_{Du}} \right]^{-1} \tag{1.3}$$

In this equation κ_b is the bulk conductivity of the electrolyte, l_{Du} is the Dukhin length and α, β are geometrical factors (usually defined as $\alpha = \beta = 2$). The Dukhin length l_{Du} is defined as the ratio of surface conductance over bulk conductance, i.e. $l_{Du} = \frac{\kappa_s}{\kappa_b}$. It denotes the relative importance of the surface conduction compared to the bulk conduction. Another useful dimensionless entity is the Dukhin number: $Du = \frac{4l_{Du}}{d}$. The normalization with the pore size allows it to quantify the contributions of the electrical current inside the nanopore. For example, a Dukhin number of 2 would imply that the current origination from surface contributions is twice as large than bulk. The concept of surface conduction can be visualized by simulating the electrical potential with a FEM software. Comparing the distribution of the potential in absence (Figure 1.6a) and presence (Figure 1.6b) of a surface charge illustrates the important contribution of the surface conduction. The surface conduction effect has severe consequences on the osmotic potential (discussed in more detail in subsection 4.6.3 (page 103)).

1.4.3 Conductance of MoS_2 pores

Equation 1.2 describes the conductance of large nanopores in MoS_2 quite well, but overestimates the conductance of small pores (<4 nm).[58] The main issue with Equation 1.2 is the assumption that the conductivity κ_b is equal in the bulk and inside the nanopore. In very small pores, the extreme confinement inside the pore approaches the size of the ions, which leads to different electrophoretic mobilities and possibly hydration layers. The conductivity

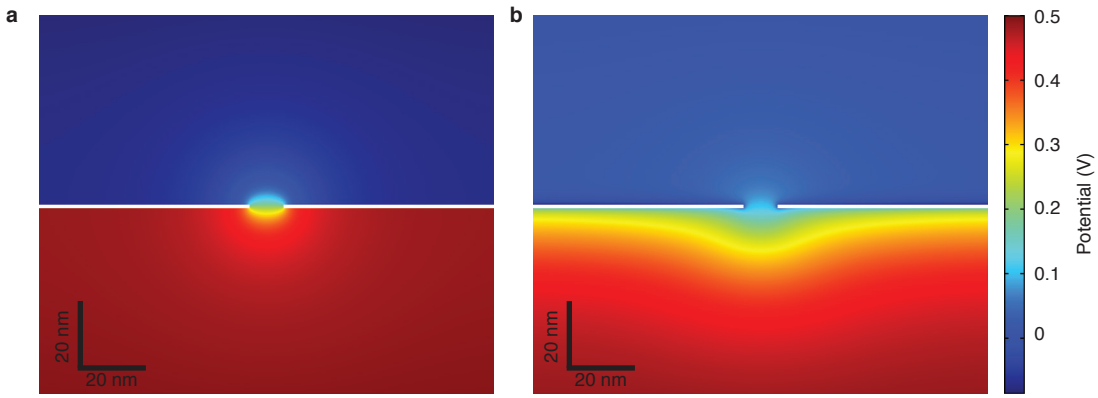

Figure 1.6 – FEM simulation. Potential distribution in a 10 nm pore placed in the center of a 1nm thick membrane when a potential of 500 mV is applied. The salt concentration was set to 10 mM. The color-table is spectral and indicates 0 V in blue and the applied 500 mV in red. **a**, No surface charge is considered on the separating membrane. **b**, The separating material has a surface charge of –100 mC m^{-2}. Figure made using COMSOL Multiphysics.

inside a very tiny pore is likely to be smaller than in the bulk. Pérez et al.[58] have investigated the conductivity in the pore through MD simulations and have found that a 1 nm large pore has only about 20 % conductivity compared to the bulk. The authors derived a formula to more precisely predict the conductance of small nanopores:

$$G = \sigma_{\text{bulk}} \left(\frac{1}{2} \sum_i \exp\left(\frac{-4\phi^i}{\pi d^2} \right) \frac{d}{\delta^i + \epsilon^i d} \right) \left(\frac{4l + \pi d}{\pi d^2} \right)^{-1} \tag{1.4}$$

, where i describe the ion species, d the effective diameter and $l = 0.96$ nm the thickness. For the KCl ion pair the values are: $\delta^{K^+} = 0.38$ nm, $\delta^{Cl^-} = 0.41$ nm, $\epsilon^{K^+} = 1.03$ and $\epsilon^{Cl^-} = 0.97$. Furthermore, MD simulations have shown that the effective diameter is about 0.3 nm less than the physical size of the pore (such as obtained by a TEM image).[58] Estimating the correct conductance for small nanopores in MoS_2 is especially important when the expression is used to estimate the pore size from conductance measurements (as typically done during electrochemical reaction (ECR) pore creation, subsection 2.6.2 (page 50)).

After having established the basic physics of a static nanopore setting, I would like to introduce the physics and dynamics of analytes.

1.5 Translocation Physics

In this section, I will discuss how a translocating molecule modulates the ionic current. Naively, one might think that the insertion of a charged molecule invokes a purely physical blockage which reduces the number of ions that can pass. The reality is slightly more complicated and depending on the type of nanopore, the surface charges, and the salt concentration the effect on the ionic current can vary largely. In some cases, even a current enhancement can be observed instead of a current decrease. The most studied analyte for nanopore translocations

is DNA. It will, therefore, serve as the model polymer in the next sections. However, the contexts described can be applied to other charged polymers as well.

1.5.1 Polymer physics

DNA is a polymer. The word polymer means *many parts* and refers to the fact that DNA is made up of small building blocks (monomers). Each of these monomers has a 5-carbon sugar (deoxyribose), a phosphate group and a nitrogenous base. There are four different versions of the nitrogenous base: adenine, guanine, cytosine, and thymine. Together with the phosphate group and the sugar, they make up the four nucleotides. In a chain of nucleotides, the sugars are joint together through the phosphate by means of phosphodiester bond to form a nucleic acid. In ssDNA this is the point where the story ends. dsDNA, on the other hand, is made from two ssDNA strands through base-pairing (hydrogen bonds) between the nucleobases. This forms a double-helix (two antiparallel strands). This tertiary structure makes the polymer much stiffer and therefore has great consequences on the translocation dynamics in nanopore experiments. In the remainder of this section, I will explain the relevant concepts of polymer physics in order to understand how DNA interacts with the nanopore system.

In polymer physics, the occupation of space is of special interest. Imagine the DNA molecule from chromosome 1, our largest chromosome. It contains about 250 million base pairs (bp). If that whole piece of DNA would be put on a table linearly, it would take up 7.5 cm. Obviously, we do not have this kind of space in the nuclei of our cells (6 µm, 10'000 time smaller). In the case of DNA, the polymer is not only compacted through its intrinsic flexibility but also through compacting-proteins that condense DNA in a controlled way. Different models are used for different polymers because the chemical bonds vary and allow for more or fewer degrees of freedom. I will concentrate on the models used to describe the major properties of ssDNA and dsDNA.

Worm-like chain model

The most widely used model to estimate the properties of ssDNA and dsDNA is the worm-like-chain model (WLC). This model is more appropriate for stiff polymers, where the flexibility is mainly coming from the bending of the contour and not from the rotation of the bonds. The WLC is based on the freely rotating chain model, which assumes independent, free torsion angles with fixed bond length l and bond angle θ. One consequence of the WLC model is the persistence length of the polymer:[59]

$$l_p = l\frac{2}{\theta^2} \tag{1.5}$$

, where l is the length of the bond and θ is the bond angle. The persistence length is an important quantity since it describes at which length the polymer behaves rather like a flexible rod (l_p»l) and at which lengths the polymer shape is dominated by random three-dimensional

Physical Property	Ionic Concentration [M] 0.001	0.01	0.1	0.5	1	Measurement Method	Ref
l_p [nm]	4.9-8.4	2.6-4.4	0.8-1.3	-	-	Diffusion, (FRAP)	69
$\langle R \rangle$ [nm], 40 nt	7	6.9	6.6	6.2	5.8	FRET	62
l_p [nm]	3	-	2.5	2	1.6	FCS	65
l_p [nm]	-	6	3.5	2.2	1.5	FRET	64
l_p [nm]	-	3.25	1.75	2	1.5	SAXS	70
R_g [nm], 100 nt	-	7	6	5.8	5	SAXS	70

Table 1.1 – Estimation of properties of ssDNA. All values are approximative.

structure (l_p«l). For charged molecules, such as DNA, the persistence length depends on the electrolyte environment due to charge screening.[60] In terms of nanopore experiments, the stiffness (estimated from the persistence length) of the molecule gives us information on the probability of a polymer to translocate in a linear, coiled or folded fashion. The rigidity also plays a role in trapping polymers at the pore mouth[61] (see subsection 1.5.4).

Another important quantity with regards to nanopore experiments is the radius of gyration. It describes the overall size of a polymer of any configuration (linear, ring-shaped, branched). For linear polymers the radius of gyration can be described by their mean-square end-to-end distance:[59]

$$\langle R_g^2 \rangle = \frac{\langle R^2 \rangle}{6} \tag{1.6}$$

Experimentally, the persistence length of DNA can be determined through Förster resonance energy transfer (FRET)[62,63] by tagging both ends of the polymer with a donor and acceptor dye. Alternatively, fluorescence recovery after photobleaching (FRAP), fluorescence correlation spectroscopy (FCS) and small-angle x-ray scattering (SAXS) measurements have been used as well.[64,65] Furthermore, the persistence length of DNA can also be measured on a single-molecule level through magnetic tweezers and AFM.[66] While a persistence length of 54 nm for the stiffer dsDNA molecule has been widely accepted in the literature,[66,67] the value for the very flexible ssDNA has posed more difficulties. Since understanding the properties of ssDNA is crucial especially in light of possible sequencing with nanopores, I tried to summarize some of the reported properties of ssDNA in different conditions (Table 1.1). The table shows that values for the persistence length differ highly between different experimental conditions. Especially, a strong dependence on the ionic strength is observed. The stiffness of ssDNA is even believed to be dependent on the sequence.[68]

After having introduced the two main players: DNA and nanopores, I would like to describe the physical processes involved in bringing the DNA to the nanopore.

1.5.2 Capturing the DNA with a nanopore

First, the DNA undergoes diffusion until it reaches the vicinity of the nanopore, where the electric field is concentrated. Once the DNA reaches the point where the field is a large enough it gets electrophoretically driven through the pore. The electric field profile created by a potential V a distance r away from the pore can be described by the length l and the diameter d by:[71]

$$V(r) = \frac{d^2}{8lr}\Delta V \tag{1.7}$$

The drift velocity of the DNA is therefore $v(r) = \mu\nabla V(r)$, with μ being the electrophoretic mobility of DNA. The limit distance at which the DNA motion switches from a diffusive to a drift regime can be defined as expressed as:

$$r^* = \frac{d^2\mu}{8lD}\Delta V \tag{1.8}$$

, where D is the DNA diffusion coefficient. For a typical small nanopore (2 nm) in a MoS_2 membrane ($l \approx 1$ nm), this distance would be $r^*_{\text{dsDNA, 1 kbp}} = 4.68\,\mu\text{m}\,\text{V}^{-1}$ and $r^*_{\text{ssDNA, 100 nt}} = 0.225\,\mu\text{m}\,\text{V}^{-1}$ for a 1 kilobase pairs (kbp) long dsDNA and 100 nucleotides (nt) of ssDNA respectively. The following values of μ and D were extracted from the literature:[72,73] $\mu_{\text{dsDNA}} = 3.75 \times 10^{-4}\,\text{cm}^2\,\text{V}^{-1}\,\text{s}^{-1}$, $\mu_{\text{ssDNA}} = 1.83 \times 10^{-4}\,\text{cm}^2\,\text{V}^{-1}\,\text{s}^{-1}$, $D_{\text{dsDNA, 1 kbp}} = 40 \times 10^{-9}\,\text{cm}^2\,\text{s}^{-1}$, $D_{\text{ssDNA, 100 nt}} = 4 \times 10^{-7}\,\text{cm}^2\,\text{s}^{-1}$. r^* is inversely proportional to the membrane thickness, highlighting that ultra-thin membranes such as MoS_2 have larger capture radii than conventional SiN_x membranes.

Assuming that the translocation rate is purely dependent on the diffusion of molecules to the capture area of the pore (r^*), then we can calculate the statistical arrival rate of diffusing molecules using Smoluchovski's seminal work from 1916.[74] He was studying the kinetics of coagulation in solution and therefore needed to calculate the probability of a molecule being absorbed on a sphere of radius R. In short, the problem consists of an infinitely large volume containing molecules at a constant bulk concentration c. Upon diffusion of a molecule to a sphere it gets absorbed and the effective concentration of molecules on the sphere becomes $u = 0$. This is equivalent to the problem in nanopore capturing. Once a molecule diffuses into the capture radius, the electric field drives it through the nanopore resetting the concentration of molecules inside on the capture radius to 0. The diffusion equation Smoluchovski wrote to solve this problem, $\frac{\delta(r,u)}{\delta t} = D\frac{\delta^2(r,u)}{\delta t^2}$, combined with the conditions that the concentration outside the sphere is c at all times and that the concentration on the sphere is 0 for $t > 0$ allows to calculate the amount of molecules arriving at the spherical border during a time dt: $J\,dt = 4\pi DRc[1 + \frac{R}{\sqrt{\pi Dt}}]\,dt$. At equilibrium ($t \gg 0$), the second part of this equation can be ignored. Dividing the equation by two and replacing the sphere with our capture radius r^* we can write the diffusion-driven translocation rate as: $R_{\text{diff}} = 2\pi Dr^*c$.[36] Combining with

Equation 1.8 we get an expression that is independent of the diffusion constant:

$$R_{\text{diff}} = \frac{\pi d^2 \mu}{4l} \cdot c \cdot \Delta V \tag{1.9}$$

We immediately see that the translocation rate increases quadratically with pore size and decreases with the membrane thickness. The electrophoretic mobility μ of DNA is roughly constant for strands longer than about 500 bp, rendering the translocation rate roughly independent of the DNA length.

Furthermore, Equation 1.9 implies that the capture radius and therefore the capture rate is linearly dependent on the applied voltage. However, in small nanopores, the observed event rates are depending exponentially on the applied voltage.[71] In small MoS_2 nanopores we observe the same phenomenon (Figure 1.7). This effect is associated with an energy barrier created by the confinement of the DNA into an extremely small space, as well as charge interactions. Both MoS_2 and SiN_x membranes are negatively charged provoking electrostatic repulsion energy that needs to be overcome by the applied electric field. In larger nanopores (>10 nm) a linear relationship is observed since the energy barrier of threading the DNA into the pore is negligible.[75]

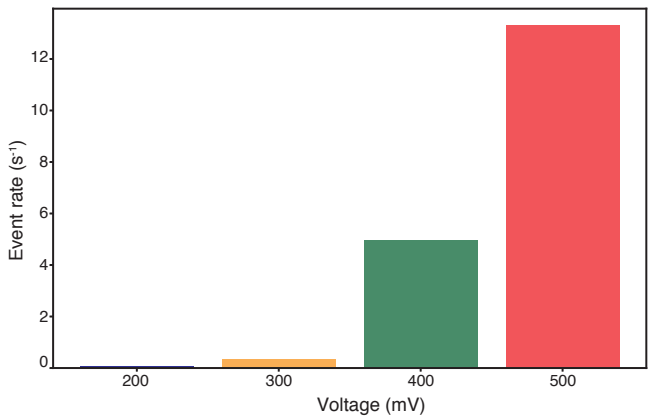

Figure 1.7 – Event rate. Number of translocations of 2 kbp dsDNA through a 2 nm MoS_2 pore. *This Figure was published in Nature Protocols, 2019, Graf et al.*[50]

If the translocation rate is dominated by the energy barrier, then the rate can be expressed as[71] $R_{\text{barrier}} = \omega e^{\frac{q\Delta V - U}{k_b T}}$, where q is the charge of one end of the DNA, U the barrier height, k_b the Boltzmann constant, T the temperature and ω the rate of threading attempts. This equation explains the exponential increase in the translocation rate of small nanopores. Strong increases in capture rate are observed when a salt concentration gradient across the membrane is applied.[71] In order to get an increase in translocation rate, the lower salt concentration should be applied on the *cis* side (with the DNA). This effect is due to an increasing electric field at the nanopore mouth due to a local imbalance of ions: Considering the symmetric case, for each K^+ ion passing through the pore a Cl^- ion passes in the opposite direction. Now, if

the concentration on the *cis* side is much lower, a chemical potential is generated and ions from the more concentrated chamber move to the more dilute side. In this case, the electric field drag ions of one charge polarity in the direction of the chemical gradient and the ions with the opposite charge polarity against the chemical gradient. This effectively introduces an ion selectivity at the pore and creates a charge imbalance and therefore an electric field. In the case of a typical DNA translocation experiment. The ground electrode is placed in the *cis* chamber and a positive potential is applied in the *trans* chamber. A lower salt concentration in the *cis* chamber and an electric field pointing from *trans* to *cis* means that Cl^- ions are electrophoretically moved against their chemical gradient, whereas K^+ ions move in the same direction as the electric field. This creates a charge-imbalance at the pore mouth with the *cis*-side having an excess of K^+ ions and therefore an increased voltage drop on the *cis* side. The capture radius from Equation 1.8 therefore changes to become: $r^* = r^*_{\text{symmetric}} \frac{c_{\text{trans}}}{c_{\text{cis}}}$. A ten-fold gradient, e.g. 100 mM / 1 M increases the capture radius ten-folds!

1.5.3 Voltage dependence

As previously described the capture rate is dependent on the voltage linearly (larger pores) or exponentially (smaller pores). But how do other characteristics such as current drop ΔI and dwell time t_d scale with the applied voltage? Naively, the current drop ΔI should scale linearly with the voltage if we assume that the nanopore is a resistor (with higher resistance during the translocation): $\Delta I = V \cdot (\frac{1}{R_{\text{open}}} - \frac{1}{R_{\text{blocked}}})$.

Current blockade

The change in current blockade is best expressed in conductance changes $\Delta G = \frac{\Delta I}{V}$, since it removes the purely Ohmic contribution. Careful measurements by Kowalczyk et al. have shown increasing values of ΔG in large (>10 nm) SiN_x nanopores.[76] The most realistic explanation to enlarged ΔG with voltage comes from the contribution of the counterions: the current through the nanopore during a translocation event is not solely defined by the volume the molecule occupies, but also through mobile counterions sliding along the DNA molecule. At lower voltages, the counterions do not conduct. Only at higher voltages (<150 mV) this layer becomes mobile and contributes to the overall current measured through the nanopore.[76] Another important factor is how much of the DNA is probing the access resistance: At higher voltages, the DNA-blob is more tightly condensed into the access resistance region due to stronger electrophoretic force. This larger amount of DNA inside this region increases the current drop contribution of the access resistance (Figure 1.8). A similar effect can be expected from ssDNA since the molecule is much more flexible and therefore allows to occupy a much larger volume of the access resistance.[76] However for ssDNA homopolymers, ΔG values are decreasing with voltage (in SiN_x), suggesting a stretching mechanism.[77] The blocked current in a 8 nm graphene nanopores was shown to be linearly dependent on the voltage,[25] i.e. ΔG was constant. In MoS_2 nanopores I have observed a linear increase of ΔI with voltage as well

(see Figure 2.12 (page 61)f). However, in ultra-thin nanopores such as graphene or MoS_2, the voltage range that can be probed is usually restricted (<500 mV) due to poor stability (subsection 2.2.1 (page 39)).

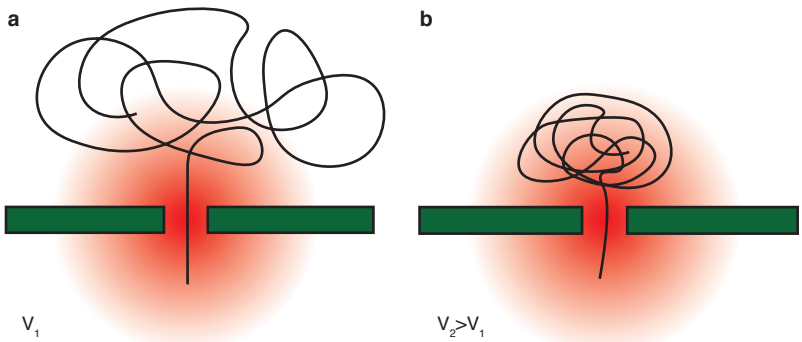

Figure 1.8 – Contribution of the access resistance. a, The amount of DNA inside the access resistance region (illustrated by red gradient) defines the contribution to the current blockage. **b**, Higher voltage electrophoretically compresses the DNA, effectively increasing the amount of DNA inside the access resistance region. Figure inspired by Kowalczyk et al.[76]

Dwell time

In a small, 3.5 nm pore in SiN_x an exponential decrease of the dwell time with voltage was observed.[78] This suggests that DNA-pore interactions dominate the translocation process. Furthermore, in low salt conditions, the DNA interaction can be decoupled from the actual translocation. The DNA interaction was responsible for the exponential decay of the dwell time with higher voltage, whereas the translocation time was linearly decreasing with voltage.[79] In a 8 nm graphene nanopore, the dwell times were reported to be linearly dependent on the applied voltage in the probed voltage range (0 mV to 400 mV).[25] During translocations of 2 kbp dsDNA in a small MoS_2 nanopore I observed a wide distribution of dwell times, indicating an interaction with the nanopore (Figure 1.9). There seems to be a linear trend with increasing voltage, but looking at the distributions, the lower voltages have multiple subpopulations (Figure 1.9, probability density function (PDF)). This might be due to unsuccessful translocations that manifest as access resistance blockages.

So far I have discussed the consequence of the pore-geometry and the applied voltage on the translocation behavior. In addition to these effects, the electrolyte solution itself is another important player in the translocation-game.

1.5.4 Salt concentration dependence

Current reversal

Smeets et al. have investigated in detail how signals from dsDNA translocation are influenced by salt concentration.[76,80] Surprisingly, they found a reversal of the ion current for KCl con-

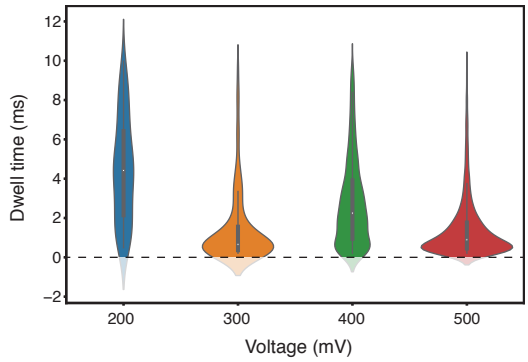

Figure 1.9 – Dwell time. Dwell time of 2 kbp dsDNA a 2 nm MoS_2 pore. The boxplots are surrounded by a PDF of the underlying dataset. There seem to be subpopulations in the dataset of 200 mV, 300 mV and 400 mV condition. At lower voltages, probably not all found events are translocations, but rather probing of the pore mouth, i.e. access resistance probing. The data presented here is from the dataset reported in Figure 2.12 (page 61).

centrations below 370 mM. This effect can be explained by taking into account the mobile counterions that are formed at the charged pore wall and around the highly negatively charged DNA. Passing the DNA through the nanopore actually increases the number of mobile ions in the pore and therefore increases the ionic current measured at the electrodes.

If a translocating DNA molecule is increasing the ionic current at low salt-concentrations, what happens if the molecule is in front of the nanopore, probing the access resistance? This process is called docking and describes the stochastic threading of the DNA molecule into the nanopore. Depending on the stiffness of the molecule and the applied voltage, shorter or longer docking times occur. Combining long docking times with low salt-concentrations allow us to decouple and observe this process from the ionic current signal. In the next paragraph, I will briefly introduce this process.

DNA docking

Experimentally, Kowalczyk et al. have shown that at a low salt concentration (100 mM KCl) current increases during translocation at low voltages (<200 mM) and high voltage (>600 mM).[79] However, at applied voltages in between these values, the translocation signal is a current decrease followed by a current increase. Both, the amplitudes of the current enhancement and the current drop increase with voltage. Furthermore, the length of the current increase depends exponentially on the voltage, whereas the current decrease depends linearly. This suggests that the two processes are largely independent. The most likely explanation is that the current drop is associated with the threading process, where a large coil of DNA is probing the access resistance of the nanopore, as supported by the independent findings of Vlassarev et al.[81] The current increase is then associated with the actual DNA translocation. At very low voltages, the amplitude of the current increase is not large enough to capture, whereas, at very high voltages, the capture time is too fast to record. Importantly, this study shows that

the access resistance is an important contributor to the ionic current traces. Furthermore, nanopore signals at high-salt conditions could be made of undistinguishable docking and translocation parts. Depending on the applied voltage the docking part can be longer than the actual translocation! Figure 1.10 visualizes the process of the current enhancement.

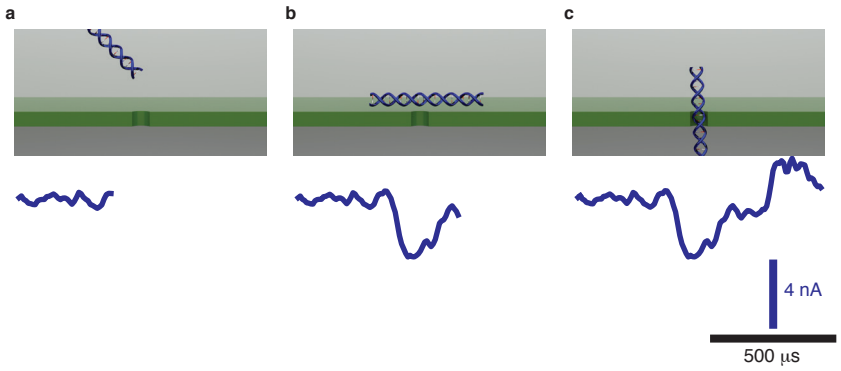

Figure 1.10 – Current enhancement and DNA docking. Top: Ionic current trace. Bottom: Illustration of the translocation dynamics at low salt-concentrations. **a**, The open pore current describes the current through the pore when no part of the analyte influences any resistance of the system. **b**, The first current decrease is associated with the DNA probing the access resistance of the nanopore (docking process). **c**, Once the DNA is threaded it translocates and bring an excess of mobile counterions into the pore, effectively increasing the ionic current. The current trace used to illustrate the process was recorded at low salt-condition in a 20 nm thick SiN_x pore.

High salt effects

Not only low salt conditions can induce counterintuitive current behaviors, also high salt can induce current increases. However, the mechanism is quite different compared to the low salt case. The effect has been observed in gradient condition, where the *cis*-side concentration was fixed to 1 M and the *trans* side concentration increased. The current change due to dsDNA translocation changed from a decrease ($c_{cis} < 2$ M) to an increase ($c_{cis} > 2$ M).[82] The effect was attributed to a competition between the blocked part of the nanopore (responsible for current decreases) and the outer part (between pore rim and DNA). The outer part has a more ions pumped into the pore due to stronger EOF when DNA (negative surface charge) enters the nanopore.[82]

Symmetric high-salt conditions show interesting behaviors as well. For instance, replacing the usually used 1 M KCl with 1 M lithium chloride (LiCl) increases the translocation time of DNA.[83] Increasing the concentration of LiCl to 4 M can slow down DNA translocation 10 times. This effect was assigned to stronger transient binding of Li^+ counterions, which reduces the DNA charge.[83]

1.5.5 Viscosity effects

We have discussed the effects of different types of salt and their concentration. But what happens, if the classical solvent, water, is replaced by something else? In this paragraph, I will discuss the effects of the solvent-viscosity on DNA translocations. The most obvious approach would be to increase the viscosity of water by adding a viscous water-soluble substance such as glycerol. Fologea et al.[84] have investigated the effect of glycerol on the DNA translocation time. The experimental results suggest that the translocation time is linearly related to the viscosity of the solution, e.g. a solution of 1.5 M KCl containing 50 % glycerol shows 5 times longer translocation times than pure water with 1.5 M KCl. However, even though the salt concentration does not change, the observed ionic currents decrease rapidly due to lower electrophoretic mobilities of the ions. Therefore any increase in translocation time comes at the cost of a lower signal.

Another approach is to replace the aqueous solvent with another conductive solution. An interesting candidate is the family of room temperature ionic liquid (RTIL). As the name suggests, these are salts that are liquid at room temperature. To assess their usefulness for translocations through solid-state nanopores, Feng et al.[29] has developed a system where one side (the *cis* side) consist of the RTIL $BmimPF_6$, whereas the other side (*trans*) was 2 M KCl in water. The gradient system improved the conductivity (and therefore the signal) of the system. If an exclusively RTIL would have been used, the ionic current would be too low to yield any useful information. Very long translocation times were observed when the molecules passed from the high-viscosity *cis* side to the low-viscosity *trans* side. Further, with this system objects as small as single-nucleotides could not only be detected but differentiated.[29]

I have now established the most important rules governing the ionic current as well as its modulation due to translocation of the analyte. In the next section, I will discuss alternative read-out methods of the ionic current signal, as well as sensing modalities that do not rely on the ionic current.

1.6 Beyond Ionic Sensing

So far we concentrated the discussion on ionic current sensing. However, ionic sensing in combination with other sensing modalities has been explored in the literature. In this part, I will introduce alternative sensing methods explored and lay the foundations for the field-effect nanopore work described in this thesis. A major advantage of the nanopore system is the fact that the nanopore can deliver single-molecules to a location of interest due to an applied electric field. In the studies I am describing below, the nanopore and the electric field concentrated in its vicinity are used to bring molecules to the location of interest. A nanopore-independent sensing modality is then used to detect the molecules. One advantage of such an approach is the possibility of simple parallelization: An ion-current-independent measurement would allow densely packed sensors with nanopores to work in parallel using a single reservoir. Ion current measurements, in contrast, would always require electrical and

fluidic isolation between individual nanopores in order to avoid averaging the signal over all nanopores present. Furthermore, integrating an electrical sensor into the membrane itself could overcome the resolution problem due to the access resistance of the nanopore (sensing of multiple nucleotides at a time).

1.6.1 Optical detection

One way of reading the ionic current of many nanopores at the same time, without electrically insulating each nanopore, relies on an optical measurement method. Basically, there are two different optical approaches: detect the translocation of fluorescently tagged analytes[85] or visualize the ion flow through the nanopore optically. I will concentrate on the optical visualization of the ion flow, since it is part of the sensor system and does not require any modifications of the analyte. The method to visualize ion currents has its origin from the patch-clamp community.[86] The idea is that Ca^{2+} sensitive dyes are added to the experimental buffer. In combination with total internal reflection fluorescence (TIRF) microscopy, the number of photons emitted by the dyes is proportional to the ion current. This allowed the simultaneous measurement of 9 closely spaced nanopores in a SiN_x membrane.[87]

1.6.2 Tunneling current

Electrodes that sense the conductance changes induced by passing nucleotides were first theoretically investigated by Zwolak et al.[88] Later, Lagerqvist et al. have shown theoretically that transverse electrical current could differentiate between nucleotides of ssDNA translocating through a nanopore.[89] They imagined electrodes embedded in the nanopore wall that would be used to pass current through the translocating bases. These currents should be large enough to identify each base. Experimentally, single-nucleotides, as well as nucleosides, can be identified by measuring the tunneling current through nanogap electrodes.[90,91] Combining the tunneling current readout with a nanopore would allow reading the individual bases when the DNA translocates through the nanopore. Experimental attempts to fabricate such devices showed that in order to achieve true tunneling detection, the distance between the electrodes needs to be smaller than 2.5 nm.[92–94] This remains extremely challenging to achieve experimentally. The signal obtained from tunneling through the molecules can be greatly improved by bonding probe molecules with hydrogen bond donors and acceptors to the electrodes.[95] Watson-Crick hydrogen bonds then ensure a reproducible contact with the electrode.[96] Furthermore, this so-called recognition-tunneling approach improves the dwell time of the molecules at the electrode, increasing the measurement time. Using the recognition-tunneling approach, it was possible to identify single-nucleotides inside an oligonucleotide.[97]

1.6.3 FET-like sensing

Apart from attempts in combining tunneling electrodes with nanopores, a second class of devices using field-effect transistor (FET)-like approach was developed. At the same time as graphene nanopores emerged in 2010 theorists have started to predict that the transverse signal through a graphene nanoribbon with a nanopore should be able to discriminate between different nucleotides.[98–100] In 2013, Traversi et al. have shown the first experimental realization of a graphene nanoribbon device.[101] Simultaneous events on the graphene transverse current and the ionic current were observed. The graphene signal was associated with a local potential change induced by a translocating circular dsDNA. In 2015, Puster et al. have shown that ionic translocation events in graphene nanopores can induce strong capacitive signals measured on the transverse current. Using a simple circuit model, the authors found that depending on the resistance between the electrode and the solution differently shaped transverse signals can manifest.[102] These signals are believed to be purely capacitive, for example, a simple grounded piece of metal in the vicinity of the nanopore would generate the same signals as a graphene nanoribbon. The signals observed and the conclusions drawn between the two research groups were quite different. This illustrates the issue of reproducibility in fabricating these devices. Only in 2018, another experimental paper investigated the graphene nanoribbon current.[103] In this work, Heerema et al. used scanning transmission electron microscopy (STEM) to sculpt nanoribbons over an opening in a SiN_x membrane, effectively making the ribbons freestanding. They developed a novel differential current amplifier to completely avoid capacitive cross-talks (assuming that capacitive signals are equal on the two leads). Unfortunately, only four correlated events were presented in the paper, making it difficult to compare the obtained data with previous experiments. In accordance with similar work the reproducibility and the yield of the fabrication method was extremely low (1 out of 180 devices).

Other than graphene nanoribbons, Xie and coworkers have shown that silicon nanowires in close proximity to a nanopore in a SiN_x membrane can be used to sense the local electrical potential. Interestingly, combining the signal of several FET-nanopore pairs on the same membrane lead to a nearly perfect reconstruction of the ionic signal (which is the sum of all the currents through the nanopores).[104]

Devices based on silicon nanowires and graphene nanoribbons have so far been the only FET-like nanopore sensors experimentally tested. The problem of using graphene in FET-like devices is its lack of an intrinsic bandgap. Engineering a bandgap increases fabrication difficulty and decreases the electronic mobility. With the emergence of single-layer MoS_2 transistors and nanopores in single-layer MoS_2 membrane, theorists have played with the idea of using a MoS_2 ribbon to detect DNA translocations. Using density functional theory (DFT) simulations Farimani et al. have investigated the density of states when DNA was placed into a MoS_2 nanopore and have found significant changes around the Fermi level energy for different bases.[105] In an experimentally more applicable analysis, Sarathy et al. have investigated the electronic conductance in constricted MoS_2 ribbons with a nanopore.[106] The first realization

of this work is that the conductance of the nanoribbon depends highly on the location of the nanopore, i.e. the conductance increased when the nanopore was placed away from the center of the ribbon. This is due to preferential electron flow through the wider part of the ribbon if the nanopore is placed away from the center. Furthermore, due to the negative backbone of the DNA molecule and its helical structure, the authors found a periodic conductance modulation during the translocation process. However, due to the dominating charge of the backbone, no difference in gating between bases was found.[106] Qiu and Sarathy et al. have used a combination of MD simulations and electronic transport calculations to show that the transverse current through a MoS_2 membrane is able to identify methylation sites on the DNA.[107]

In chapter 5 (page 113), I am presenting an experimental implementation of a FET-nanopore-based on MoS_2 and how such devices can be used to detect analytes. I will further discuss different sensing mechanisms and comment on the strong discrepancy between experimental results and the theoretical calculations mentioned above.

1.7 Molybdenum Disulfide

Up to this point in this thesis, we have mentioned MoS_2 many times, but in order to appreciate the material and put it into context (especially with its more famous cousin graphene), I dedicate this section to MoS_2 and 2D-materials in a broader sense. I will shortly go through the history of 2D-materials, then shift the focus on growth and characterization.

In their 2005 paper, Novoselov et al. have presented a novel way of isolating individual crystal planes from a variety of layered materials.[108] This groundbreaking work has provoked the emergence of the field of 2D-materials. The way the authors have produced these materials is very simple and poses the question why this has not been discovered earlier: by simply rubbing the bulk crystal on a surface, individual layers that form the bulk structure are detached. Some of these flakes are single layers. What made this discovery possible in the first place was not so much the exfoliation technique, but the fact that these monolayer flakes are visible on some surfaces with an optical microscope. The authors used a SiO_2 covered silicon substrate, but other materials such as SiN_x work as well. The contrast comes from the interference of the monolayer with the optical path of reflected light. Calculations allow designing substrates that maximize the contrast.[109–111] The most notable materials that were successfully exfoliated in this early work were boron-nitride (BN), MoS_2 and graphite. Exfoliated monolayer graphite, also called graphene, became the most prominent of all due to its surprising and fascinating physical properties. Graphene single-handedly created a whole new field of 2D-materials science. Only 5 years after publishing their seminal work the authors were awarded the Nobel Price in Physics.[112] Graphene has a hexagonal lattice of carbon atoms (see Figure 1.11a). It has no bandgap and is, therefore, a conductor. MoS_2 belongs to the family of transition metal dichalcogenide (TMD)s and its monolayer crystal is a three-atom-thick material (see Figure 1.11b) with a direct bandgap of 1.8 eV, making it a semiconductor. This intrinsic

bandgap of monolayer MoS_2 allowed the fabrication of the first ultrathin FET.[113]

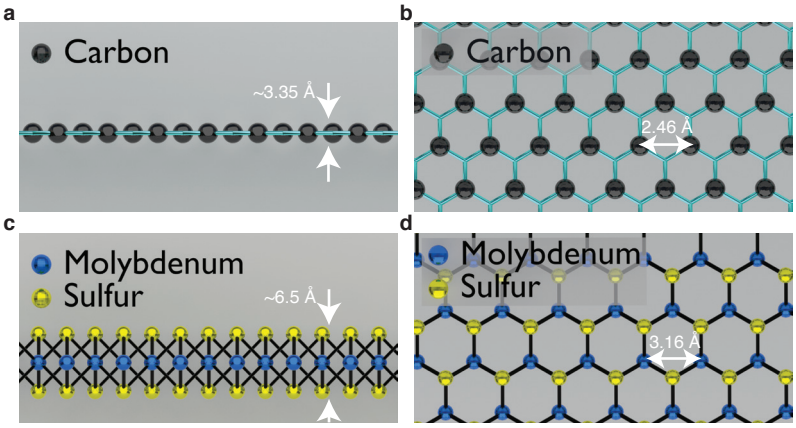

Figure 1.11 – Monolayers of MoS_2 and graphene. The interlayer distance is typically used to describe the thickness of the material. **a**, Sideview of a single layer graphene (≈ 3.35 Å[114]), **b**, Top-view of graphene. The lattice parameter is ≈ 2.46 Å.[115] **c**, Sideview of single layer MoS_2 (≈ 6.5 Å[113]). **d**, Top-view of monolayer MoS_2. The lattice parameter is ≈ 3.16 Å[116]

1.7.1 Sources

Monolayer MoS_2 flakes can be obtained by the exfoliation method described above or it can be directly grown as a monolayer single crystal using chemical vapor deposition (CVD). Exfoliation methods produce high-quality monolayers (little defects), but the method is not scalable.[117] In contrast, direct growth of 2D-MoS_2 gives good morphological control and provides the scalability needed for device fabrication. However, grown material has shown to be of slightly poorer quality than the exfoliated material.[117] Nevertheless, continuous improvement in the quality of grown materials has sparked a lot of research interest in growth methods in recent years. CVD has been successfully used to grow large-scale, high-quality and uniform graphene layers. This success is mainly due to the self-limiting behavior of carbon atoms on surfaces like Ni and Cu. However, this does not apply to transition metal dichalcogenides (TMDs), making it extremely challenging to precisely control the growth parameters such as the ratio of lateral to vertical growth rate.[118] Tilted scanning electron microscopy (SEM) images of tungsten diselenide (WSe_2) illustrate this process nicely, showing vertical growth in the center of laterally grown crystals (Figure 1.12). The growth approaches used to synthesize MoS_2 can be roughly categorized into two approaches: thermal vapor sulfurization (TVS) and thermal vapor deposition (TVD).

TVS

CVD growth using the TVS method relies on sulfurization of the target substrate. In short, the substrate is coated with a precursor material such as Mo or MoO_3. These materials are deposited on the target using evaporation or sputtering processes. The coated substrate is

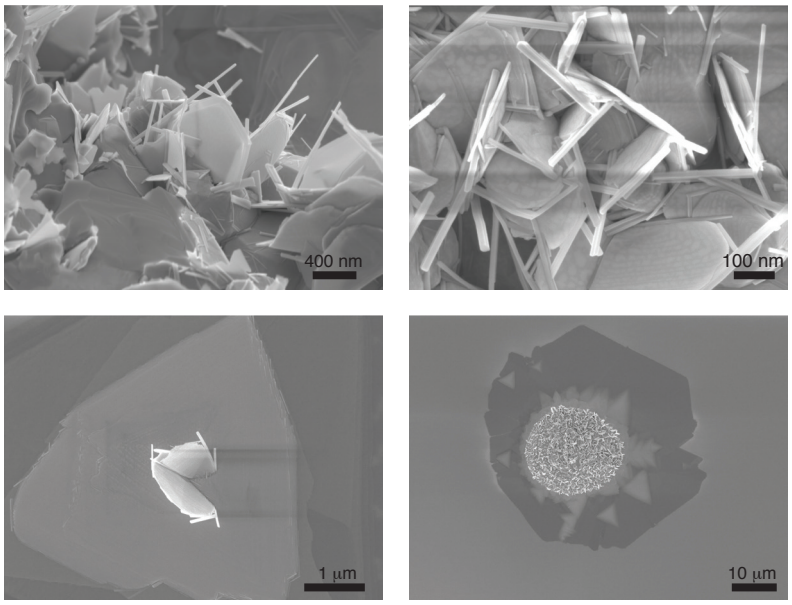

Figure 1.12 – Vertical growth of WSe_2. All images were taken with a Zeiss Merlin SEM at the center for micronanotechnology (CMI), EPFL. Samples were grown by Michal Macha, LBEN, EPFL.

then placed in a furnace with a carrier gas-flow (N or Ar) to induce the sulfurization. The sulfur powder can be placed upstream of the heating zone. It will then evaporate and is transported via the carrier-gas to the coated substrate (in the middle of the heating zone). Alternatively, H_2S gas can replace the sulfur powder and provide the sulfurizing agent. The temperature in the heating zone is then raised up to 900 °C to induce the sulfurization. The layer thickness and the crystal sizes are highly dependent on the sulfurization temperature. It is possible to grow continuous films of MoS_2 using this approach, but they are highly polycrystalline, which is problematic in electronic applications. In general, TVS produced MoS_2 has a higher electrical resistance than mechanically exfoliated MoS_2.[118]

TVD

In CVD growth using the TVD approach the two precursors are separated from the substrate. The molybdenum precursor is placed away from the substrate into the heating zone instead of coating the substrate with the precursor. In summary, the process relies on the evaporation and sublimation of the two precursors into the carrier gas, transport to the substrate and the diffusion of the reaction species onto the substrate. Such a set-up leaves many more free parameters such as the distance of the precursors to the substrate and the carrier gas flow. If tuned correctly, the quality of the crystals is higher than in the TVS approach and are comparable or even superior to mechanically exfoliated MoS_2.[118] For both growth approaches, the most popular substrate is sapphire. Due to its crystallinity and nearly matching lattice constant MoS_2 grows epitaxially on top of the substrate. As a result, the crystals of MoS_2 grow as unilateral triangles with angles of 30° between each other (see Figure 1.13). This facilitates

the merging of the individual triangles into a larger continuous film.

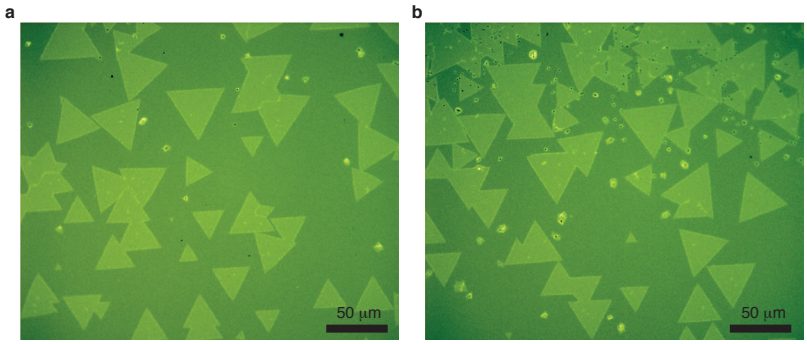

Figure 1.13 – Growth of MoS_2 crystals on sapphire. Optical micrographs of single-layer MoS_2 crystals grown on a sapphire substrate. The epitaxial growth is characterized by regular triangles, rotated 30° from each other.

1.7.2 Characterization

The grown material needs to be characterized first. For simple nanopore applications, we are particularly interested in the number of defects and whether the growth is monolayer or contains multiple layers. For applications such as the FET-nanopore, we are also interested in the size of the monocrystalline part, the grain boundaries, and the electrical properties.

Optical contrast

An optical reflection microscope is able to visualize MoS_2 crystals on a multitude of different substrates. Even on the transparent sapphire substrate, the monolayer crystals are visible (see Figure 1.13). The contrast in a reflection set-up is made from light reflected from the different layers of the substrate (MoS_2, SiN_x and SiO_2). Different layers can reflect the light at different phases, which can lead to constructive and destructive interference. This means that the thicknesses of the underlying layers define the contrast and some combination of material can lead to much stronger optical contrast than others. The ideal layer thicknesses can be calculated analytically.[110,111] However, for MoS_2-nanopore applications thick underlying dielectric materials (such as 300 nm SiO_2) might introduce other, unwanted, consequences (see subsection 2.3.3 (page 41)).

Photoluminescence

photoluminescence (PL) describes all the light emission from any matter due to the absorption of photons. It is provoked by photoexcitation, i.e. an incident photon excites an electron to a higher energy level. The decay from this higher energy level back to the ground state can then emit a photon (luminescence). Bulk MoS_2 has basically no photoluminescence signal due to its indirect bandgap. When thinned down to a monolayer a transition from indirect to a direct

bandgap occurs and a strong photoluminescence signal is observed.[119] In direct-bandgap materials this is due to the recombination of electrons and holes, which are produced by the incident laser light through a polarization process. In MoS_2 the PL signal can identify the number of layers since the signal becomes stronger with decreasing thickness.[119] Other than the thickness, the underlying substrate plays also an important role on PL intensity[120,121] due to interferences (as shown in subsection 4.3.5 (page 89)). Furthermore, the PL intensity is enhanced through defects in the layer.[122]

Raman

Raman spectroscopy is a subpart of the PL spectrum covering shorter wavelengths. It probes vibrational modes of crystals and is very sensitive to the number of layers. With decreasing thickness the Raman peak is redshifted, allowing the precise determination of the number of layers.[123] Raman spectroscopy can reveal much more than just the number of layers. It can give information about the strain, local temperature, doping level, and adsorbates on the material.[124]

Transmission electron microscopy

I have used TEM quite extensively to characterize my work. I have dedicated a small part in subsection 2.5.1 (page 48) to TEM characterization of MoS_2 samples. The TEM is a very powerful tool to investigate the integrity of MoS_2 samples. For example, using fast Fourier transform (FFT) filtering it is possible to differentiate between the Mo atom and the two S atoms in a TEM image (see Figure 1.14).

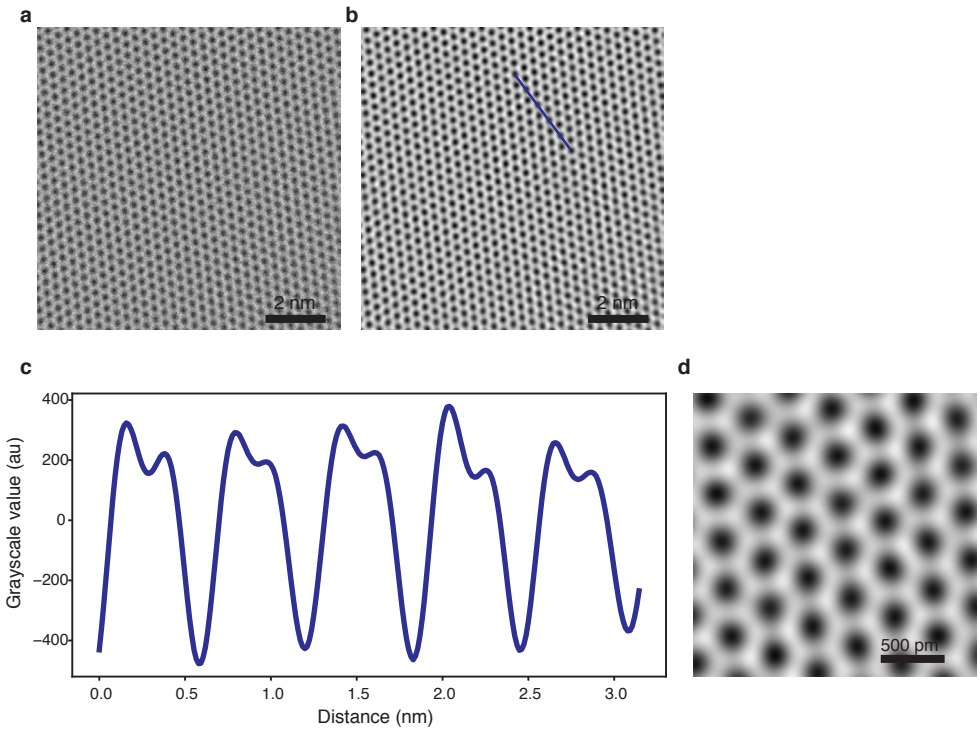

Figure 1.14 – TEM imaging of MoS_2. **a**, Raw HR-TEM image of the lattice of MoS_2. **b**, FFT-filtered image. The blue line denotes the location of the line plot in **c**. **c**, Line-plot of the grayscale values along the lattice. The difference between the Mo atom and the two S atoms can be clearly seen. **d**, Zoom of the FFT-filtered image showing the contrast difference between Mo and 2S. All images were taken on a FEI Talos in the CIME

1.8 Structure and content of this thesis

This thesis is divided into four parts:

1. Fabrication: In chapter 2 (page 35), I describe the fabrication of a MoS_2 as well as its characterisation. Furthermore, DNA detection data is shown as an example application.

2. Blue energy: In chapter 3 (page 63), I introduce the concept of energy generation using MoS_2 nanopores. In chapter 4 (page 83), I extend the ideas presented in chapter 3 and show how light can be used to improve the performance of the energy conversion.

3. Transverse sensing of DNA: In chapter 5 (page 113), I describe the main project of my PhD thesis. I show proof-of-principle data obtained through measuring the sheet current across a MoS_2 membrane.

4. Outlook and conclusions: In chapter 6 (page 149), I will shortly discuss the impact of the research presented in this thesis. Furthermore, I will address possible future steps and discuss where the research might lead to.

Additionally, the appendix contains a complete list of materials and equipment needed for making MoS_2 nanopores (section A.1 (page 159)) and step-by-step instructions of the whole fabrication process (section A.2 (page 165)). Last but not least the process-flow for fabricating the MoS_2-FET-nanopore (chapter 5 (page 113)) is detailed in section A.3 (page 178).

2 MoS_2 Nanopore Fabrication

First, I will detail the fabrication of MoS_2 nanopores that can be used as single-molecule sensors based on ionic current sensing or in reverse electrodialysis applications to generate power. There are step-numbers in this chapter, which refer to the detailed protocol attached to the appendix (section A.2 (page 165)). A list of materials needed to follow this protocol can be found in section A.1 (page 159). This text is the preprint version of

Michael Graf[1], Martina Lihter[1], Mukeshchand Thakur[1], Vasileia Georgiou[2,3], Juraj Topolancik[2,4], B. Robert Ilic[4], Ke Liu[1], Jiandong Feng[5], Yann Astier[2] and Aleksandra Radenovic[1]. **Fabrication and Practical Applications of Molybdenum Disulfide Nanopores**. Nature Protocols 14.4 (2019), pp. 1130.

If not otherwise noted, all figures and the data shown within are my own work. M.G., M.L., and M.T. contributed equally. K.L. and J.F. performed initial work on device fabrication, MoS_2 transfer and pore characterization. M.G., J.T., V.G., and B.R.I developed substrate fabrication process, V.G. fabricated the substrates. Y.A. supervised the substrate fabrication process. J.F., K.L., and A.R. developed the ECR pore drilling method. M.G. built the transfer microscope setup, M.G. and M.L. developed PMMA transfer method and optimized MoS_2 cleaning procedure, M.T. developed PDMS transfer method, M.L. and M.G. performed TEM characterization, M.L. and K.L. optimized the TEM pore drilling method. M.G. developed the translocation data acquisition and analysis software. M.G., M.L., and M.T. fabricated the devices. M.G. performed the translocation experiments presented. M.G., M.L., M.T., J.T., and A.R. wrote the manuscript.

[1]Laboratory of Nanoscale Biology, Institute of Bioengineering, School of Engineering, EPFL, Lausanne, Switzerland
[2]Roche Sequencing Solutions, Pleasanton CA, USA
[3]Institute for Research in Electronics and Applied Physics and Maryland Nanocenter, University of Maryland, MD, USA
[4]Center for Nanoscale Science and Technology, National Institute of Standards and Technology, Gaithersburg MD, USA
[5]Department of Chemistry, Zhejiang University, Hangzhou, China

2.1 Overview of the Procedure

The procedure is divided into three parts: substrate preparation (Step 1-Step 30), molybdenum disulfide (MoS_2) transfer (Step 37), and nanopore creation (Step 38). A graphical overview of all the involved steps is illustrated in Figure 2.1. In order to make a large number of devices at once, as many steps as possible should be performed on a wafer-scale. For technical reasons, the fabrication of the substrates is done on a wafer, while the material transfer and nanopore fabrication are processed at a chip-scale. Developing wafer-scale MoS_2 growth and transfer methods will allow more efficient device fabrication in the future. The objective is to fabricate substrates used to suspend the monocrystalline material. The starting point is a 4" silicon wafer, where both sides contain a thin layer of silicon dioxide (SiO_2) and silicon nitride (SiN_x). E-beam lithography (EBL) is then used to write nanometer-sized circles on the front-side resist (Step 1-Step 18). Each of these will later serve as one thin aperture on the chip. A reactive ion etching step then transfers this pattern to the wafer by etching away the SiO_2 and SiN_x layers (Step 11). On the backside of the wafer, we use photolithography to create openings that serve for potassium hydroxide (KOH) wet-etching of the silicon (Step 27-Step 30). In this step, it is important that the backside square is perfectly aligned with the previously written aperture. By exposing the backside to KOH the silicon gets etched leaving a suspended SiN_x membrane with a nanometer-sized aperture. Leakage analysis (Step 31-Step 36) is done on representative wafers from the batch fabrication. This is to analyze the level of defects (e.g. pin-hole defects) on the wafers and avoid current leakage during the nanopore experiments. After dicing the wafer, the MoS_2 is transferred to the substrate. In order to be able to transfer MoS_2 one needs to obtain exfoliated or chemical vapor deposition (CVD) grown material, best on a sapphire substrate, but other substrates such as SiO_2 or SiN_x might also work. Commensurability of the sapphire lattice with the single-crystal domain of MoS_2 ensures large grain sizes and relatively low number of defects compared to the growth on other substrates. The material is now transferred and aligned from the sapphire substrate to the aperture in the SiN_x membrane. There are several possible strategies to transfer the monocrystalline MoS_2 which are discussed in subsection 2.3.6 below. Briefly, a polymer such as poly(methyl methacrylate) (PMMA) (Step 37 Option A) or polydimethylsiloxane (PDMS) (Step 37 Option B) is used to lift a part of the MoS_2 material from the growth substrate. The different methods have their own advantages and limitations which will be discussed in detail. Once the material is transferred, a nanopore of a suitable size is created. Two options are available, depending on the accessible equipment: one option is transmission electron microscopy (TEM) drilling (Step 38 Option A), where we carefully focus the electron beam to an extremely small spot size. The material is very unstable under electron beam irradiation. Therefore we will provide the best strategies for getting the desired results by inducing the least amount of damage to the material. Furthermore, we show how to assess the quality and cleanliness of the material. The second option to create nanopore is an electrochemical reaction process[30] (Step 38 Option B), which offers a fine control on the pore size by simple means of a voltage source and a current amplifier. Precision painting (Step 39-Step 43) is performed to reduce the capacitance of the chip and reduce leakage current. The silicone paint is applied around the SiN_x membrane and can

be performed after TEM imaging and drilling (Step 38 Option A) or before electrochemical reaction (ECR) drilling (Step 38 Option B). Also, we will provide strategies for a proper flow-cell design, how to reduce noise in the system and how to properly wet the nanopore.

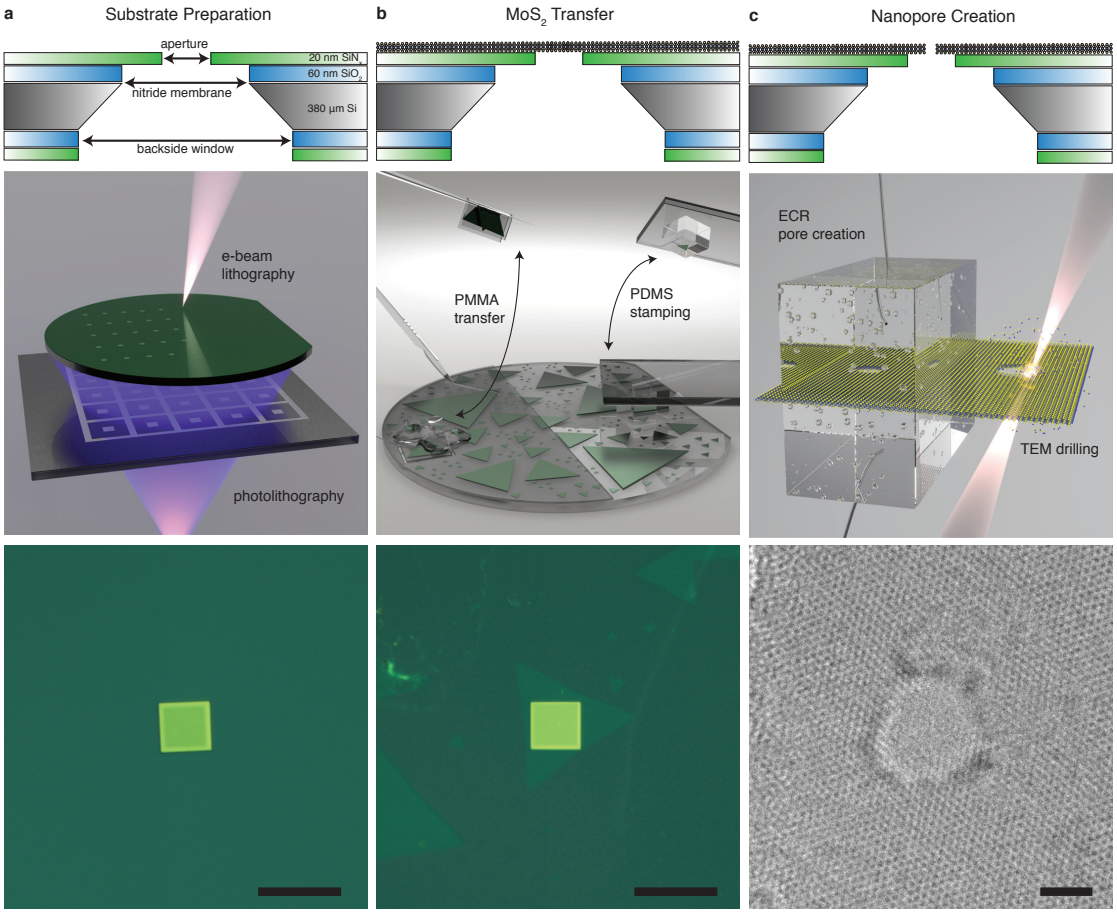

Figure 2.1 – Overview of the fabrication process. **a**, Substrate preparation (Step 1-Step 30). Top: a schematic of the finished device. Middle: illustration of the involved methods. EBL is used to pattern the aperture, whereas photolithography is used to create the backside opening for KOH etching. Bottom: an optical micrograph of the resulting freestanding silicon nitride membrane. The scale bar is 20 µm. **b**, Transfer of MoS_2 (Step 37). Top: a schematic of the device when MoS_2 has been transferred. Middle: an illustration of the two options of transferring the material. PMMA or PDMS-assisted lift-off and alignment on the target substrate. Bottom: an optical micrograph of a single crystal MoS_2 (triangle) transferred to the silicon nitride membrane. The scale bar is 20 µm. **c**, Drilling of a nanopore (Step 38). Top: a schematic of the finished device. Middle: illustration of the two nanopore creation methods, TEM drilling and ECR pore creation, available to users. Bottom: a TEM image of a drilled nanopore. The scale bar is 2 nm. *This Figure was published in Nature Protocols, 2019, Graf et al.*[50]

2.2 Comparison to other Methods

There are many advantages of the fabrication procedure described in this protocol over previously published procedures. First, the substrates are fabricated at the wafer scale using EBL and reactive ion etching (RIE) etching to achieve the aperture. In similar work, the aperture

has been fabricated using focused ion beam (FIB),[24] which typically requires chip-per-chip alignment, limiting the throughput and producing additional costs. Furthermore, using electrochemical reaction (ECR), we describe an alternative way of producing the nanopores which greatly reduces the costs and increases the throughput. It will be straightforward to expand this technique to the wafer scale by using individually addressable microfluidic channels and customized software.

In terms of material, MoS_2 provides some advantages over the better-known graphene monolayers. First of all, deoxyribonucleic acid (DNA) is less sticky to the surface of MoS_2, whereas in graphene significant stickiness is observed.[105] Other transition metal dichalcogenide (TMD)s or alternative ultra-thin 2D-materials might provide equal or better properties than MoS_2. So far only tungsten disulfide (WS_2)[32] and hexagonal boron-nitride (h-BN)[31] have been investigated as alternative membrane materials. We have tried tungsten diselenide (WSe_2) as well, but no advantage was found. Therefore, more explorative work is needed to evaluate the large number of possible candidate materials available.[125]

In terms of the 2D-material transfer, most of the existing transfer methods rely on polymers which are spin-coated on exfoliated or CVD-grown MoS_2 and then detached from the substrate using an etching solution such as KOH or NaOH.[126–128] This might induce defects in the MoS_2 which is highly problematic for nanopore devices application. These methods are also limited by residual contamination by the etchants, demanding additional cleaning steps. Moreover, many methods usually involve the large-scale transfer of materials,[129–132] which lacks the precision in aligning the micron-sized 2D-monocrystals over the specific membrane area). Since the suspended area is quite small, large area transfer also results in a waste of material especially if one has a limited supply. Both transfer methods (PMMA- and PDMS-assisted, respectively) described in this protocol are inspired by already published works and are further adapted. The PMMA-assisted transfer is based on the wedging transfer method[133] which employs water-assisted lift-off. The published method enables a microscale precision by manual alignment under the microscope and repositioning of the same layer many times. In our approach, we cut the PMMA pieces down to $0.25\,mm^2$ and it is possible to manipulate them by a microcapillary on a water droplet. Deterministic transfer of 2D-materials by using PDMS has been demonstrated.[132] However, while this is a method suitable for exfoliated material, it represents a challenge in the case of CVD-grown monolayer since it cannot be easily detached from the growth substrate. We address this issue by using PDMS stamps in combination with water assisted lift-off. The PDMS transfer methods are attractive since they require fewer steps of post-transfer cleaning, however, the flake repositioning is not possible in this case in contrast to PMMA-assisted approach. Both methods are etchant-free, which reduces the number of steps and retains the quality after the transfer. In summary, the transfer can be done highly precisely, fast, economic and can be extended to other 2D-materials.

In terms of performance, devices made in MoS_2 were predicted to achieve single-base resolution due to their small thickness. MoS_2 is thicker than graphene, but is believed to capture the ionic current better, since the ions are actually larger than the thickness of graphene

membranes.[105] Furthermore, interesting electrical properties, in particular, the intrinsic band-gap, allow the creation of more sophisticated devices and pave the way for exploring alternative sensing mechanisms.[134]

2.2.1 Limitations of the approach

The main drawback of solid-state 2D-MoS_2 nanopores and 2D-materials, in general, is their stability. Compared to nanopores made in thin SiN_x, MoS_2 nanopores are more prone to widening and damage, especially in solution. Also, the noise level is higher mainly due to mechanical vibrations and charge fluctuations of the suspended material. An eventual chemical modification could solve this issue. With the PMMA and PDMS transfer methods described here, there is still a risk of having unwanted polymer residues as contamination on a suspended 2D-material which can affect the pore creation and translocation signals. Nanopore fabrication by using an electron beam is time-consuming and expensive and not reproducible for very small pores. ECR overcomes this limitation but on the other hand, it is possible to create multiple pores.[135] So far, only the substrate fabrication is done on the wafer scale all the other steps are done chip by chip. Wafer-scale growth and transfer of 2D-material together with individually addressed microfluidic channels and ECR could lead toward nanopore parallelization that will enable high throughput of translocation data, as well as the upscaling of nanopore power generation. However, in terms of DNA sequencing, there are still fundamental limitations related to translocation speed that need to be resolved.[136–138]

2.3 Substrate Fabrication

(Step 1-Step 30). The substrates used to suspend MoS_2 are typically silicon-based because of the microfabrication technology developed for the electronics industry. The main element of the chip is a thin membrane (in our case 20 nm) which has the role of supporting the 2D-material. It is made of low-stress SiN_x, good dielectric material with high mechanical strength. In order to insulate the membrane from the underlying silicon substrate, a 70 nm SiO_2 layer is deposited between the silicon and the SiN_x (Step 2-Step 3). Additionally, this configuration also reduces the total capacitance of the chip.[139,140] Silicon can be sculpted by the very well-established anisotropic etching with KOH or tetramethylammonium hydroxide (TMAH) (Step 20-Step 30). The etch rate is strongly dependent on the surface orientation yielding a much faster etch rate in the (100) direction than in (111). This results in a pyramidal pit in silicon. The SiN_x etching rate is orders of magnitude slower than the rate of silicon which ensures that SiN_x membranes stay intact until the Si/SiO_2 layers get completely removed. Moreover, the thicknesses of the SiN_x (20 nm) and SiO_2 (70 nm) layers define the contrast of the monolayer when observed through an optical reflection microscope due to constructive/destructive interferences,[110] which is important for characterization and alignment. However, silicon is a semiconducting material with resistivity depending on the doping level. A large surface of the silicon is exposed to the ionic solution through the etched pyramidal channel. This

high capacitance system typically has an order of magnitude higher noise than biological nanopores.[141]

2.3.1 Types of noise

The detection of molecule translocations, especially DNA sequencing, relies on a good signal-to-noise ratio. In order to improve the performance of the device, one should minimize the background noise mainly coming from the nanopore chip and the interface with the electronics. The overall noise can be presented as power spectral density (PSD) as a function of frequency and generally contains several components as shown in Figure 2.2: flicker (pink) noise, thermal (white) noise, dielectric (blue) noise and capacitive (purple) noise. Flicker (pink) noise, or 1/f noise, dominates the low-frequency part of the spectrum and influences the stability of the measurements. The source of this type of noise in solid-state nanopores is not well understood, but it mainly originates from the movement of ions at the pore-electrolyte interface and their convective flow in the bulk.[142] It depends on the pore size, salt concentration,[143] pH[142,144] and surface related effects such as charge fluctuations,[144] hydrophobic-hydrophilic interactions, and nanobubble formation.[145] An additional increase of 1/f noise in 2D-nanopores can come from mechanical vibrations of 2D-material.[145,146] Thermal (white) noise is frequency independent and originates from thermal fluctuations of charge carriers inside the nanopore. Dielectric (blue) and capacitive (purple) noise dominate at 1 kHz to 10 kHz and >10 kHz, respectively, and are closely related to dielectric loss (heat dissipation) and the coupling of amplifier's noise with the capacitances[147–149] in the system. Since the DNA translocation events in solid-state nanopores generally have dwell times on the order of microseconds, their readout will be profoundly affected by this high-frequency noise. For that reason, reducing the capacitance is very important. The capacitance, C, of each layer in the chip can be described by $C = \epsilon_0 \cdot \epsilon_r \frac{A}{L}$, where ϵ_0 is permittivity of vacuum, ϵ_r relative permittivity of the particular dielectric layer, A the surface exposed to the solution, L the thickness of the particular layer.

2.3.2 Reducing noise

Reducing the noise can be done by carefully choosing the substrate and membrane material such as a glass substrate[149] or low-doped silicon.[149] Since different layers on top of each other act as capacitors in series, the total capacitance will be dominated by the layer with the lowest capacitance. The noise can be reduced by adding a thicker layer of dielectric material in the chip structure, such as SiO_2[139,140] or glass,[149] by increasing the SiN_x membrane thickness (L) and decreasing the surface area of the membrane and the aperture. A thicker supporting membrane of small dimension provides better robustness and reduces the capacitance. The aperture should also be as small as possible to restrict the part of the 2D-material that is exposed to the solution, leading to better mechanical stability and thus lowering the 1/f noise.[150] However, increasing the thickness while reducing the aperture could lead to a channel-like configuration, where the total ionic resistance is not governed by the 2D-nanopore but by the

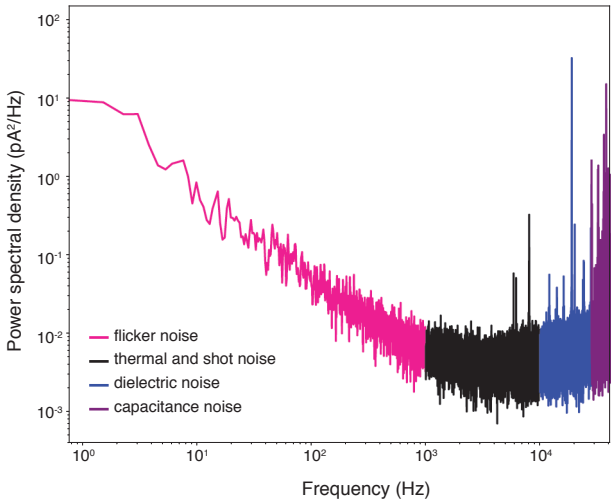

Figure 2.2 – Types of noise, PSD. The PSD of a current trace obtained at 200 mV in a MoS_2 nanopore is plotted as a function of frequency. The different noise components (color-coded) indicate approximately which frequency range is dominated by which noise source. *This Figure was published in Nature Protocols, 2019, Graf et al.*[50]

SiN_x aperture instead. We explain this in more detail in subsection 2.6.3.

2.3.3 Electrical discharge

Although reducing the noise of the system sounds promising, it can cause other serious technical problems such as 2D-material damage due to electrical discharges.[151] Especially during wetting of the device, charges can build up in the flow-cell, which then lead to discharges when an electrical path is created by the electrolyte solution. The amplitude of this discharge is highly dependent on the capacitance of the device. A high capacitance device ($\approx$ 1 nF) can create an electrical field up to 0.1 V nm^{-1} whereas a low capacitance device (< 80 pF) can create an electrical field of 1 V nm^{-1}.[151] This emphasizes the potential problem occurring when using atomically thin membranes suspended on low capacitance substrates such as glass.

2.3.4 Coating

Coating the chips using silicone elastomer (Step 39-Step 43) has been proven so far to be a safe option to reduce the noise substantially. Painting the surface exposed to the liquid outside the SiN_x membrane improves dielectric properties[141] of the substrate and reduces the capacitance. The coating needs to be resistant to the solution used in experiments. The type of coating we describe in this protocol is not compatible with organic solvents and room temperature ionic liquids (RTILs).[152]

2.3.5 Leakage

Defects in the low-stress SiN_x/SiO_2 thin-film bilayers such as charge traps and pin-holes provide additional paths for current flow, thereby affecting the current leakage through the membrane into the substrate. Such defects are introduced during film growth and sample handling during membrane fabrication, nanopore formation, and MoS_2 transfer. Current leakage can significantly impact ionic current measurements during DNA translocation through MoS_2 nanopores. While some leakage seems to be necessary for charge dissipation to ensure structural stability of the membranes (well-insulated membranes with 200 nm thick SiO_2 underlayer proved to be highly unstable), excessive leakage is not desirable because it increases the background signal and reduces the signal-to-noise ratio. To assess fabrication-induced damage and to quantify variation of current leakage across a 4" substrate, we defined an array of membranes in an arrangement as shown in Figure A1.1 (page 165). Nanopores and EBL alignment markers were not patterned on these substrates. Additional defects can be introduced while defining these features in fully-built devices. Since it is difficult to measure the current leakage in hundreds of devices in a fluidic cell, we covered the test wafer on both sides with 50 nm thick layers of Au deposited at an angle of 45° by biased target deposition (BTD). We utilized the BTD technique, which is traditionally used in the fabrication of tunnel junctions to ensure a good sidewall coverage in the KOH etched vias and to prevent interface mixing and formation of defects in SiN_x/SiO_2 layers. Individual $5 \times 5\,mm^2$ chips supporting single membranes were carefully isolated by cleaving without damaging the metalized surfaces, effectively creating 180 large-area metal-insulator-metal (MIM) junctions. The substrate side of a 4" wafer with an array of etched vias and trenches covered with Au and separated single-membrane devices are shown in Figure 2.3a-b.

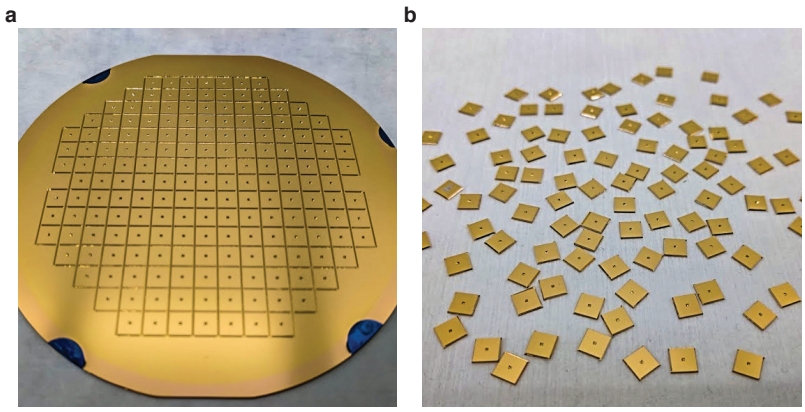

Figure 2.3 – Gold plating the test chips. a, The backside of a test wafer with an array of membranes. **b**, isolated chips with single membranes. Photo credits: Juraj Topolancik. *This Figure was published in Nature Protocols, 2019, Graf et al.*[50]

We measured current leakage in the MIM junctions at voltages ranging from –10 V to 10 V using a parameter analyzer. Typical I-V curves of the measured devices are presented in Figure 2.4a. The curve is non-linear and highly asymmetric, which is unusual for symmetric MIM junction and is more characteristic of a metal-semiconductor junction. This suggests

that current leakage through the Si substrate is likely a significant contributor to charge transport. Figure 2.4b shows the measured I-V curves of 90 MIM junctions showing leakage current variations at a small bias from −1 V to 1 V. The plot indicates that there is an order of magnitude variation in leakage current across the wafer which can be attributed to the non-uniform distribution of defects. It is important to note, that this approach is useful to assess the general quality of the SiN_x layer but overestimates the leakage since current paths on the whole chip surface are taken into account. In addition, the metal coating provides a low-resistance contact to the silicon nitride membrane facilitating the electron transfer. In a nanopore experiment, only the vicinity of the membrane will be in contact with the electrolyte. Furthermore, the charge-transfer of ions to the silicon nitride surface is much more limited than in the case of a metal contact and is typically associated with trap-assisted tunneling of electrons.[19] To further investigate the integrity of our devices in the experimental environment, we performed I-V curves in 1 M potassium chloride (KCl). We found a much lower leakage conductance of only about 323 pS (Figure 2.4c). Compared to typical conductances of small nanopores (> 10 nS) this leakage current is not a significant contribution. It is important to note that the leakage current is highly dependent on the surface area of the SiN_x membrane, growing when the membrane size is increased. Therefore, it is crucial to design the membrane as small as possible.

2.3.6 MoS_2 sources

The easiest way of obtaining single-layer MoS_2 crystals is to exfoliate them mechanically from a bulk MoS_2 crystal using the scotch-tape method.[108,153] In this process, the tape is used to peel off a thin flake from the crystal. By repeating this process many times on the cleaved flake, one can obtain layers of different thicknesses, including monolayers, which then can be transferred to the future device surface by pressing the tape down and peeling it off. However, the yield in obtaining monolayers in this way is low, and one needs to spend a lot of time identifying single-layer flakes under a microscope. This method has several limitations: as exfoliation is a random process, the probability to obtain a single layer directly on the location of the membrane is low, requiring another transfer process.

A better way of obtaining large quantities of single-layer crystals is the direct crystalline thin-film growth on different dielectric or semiconductor surfaces such as sapphire, SiO_2 and SiN_x by CVD method.[154,155] In this method, the 2D-material is grown in a reacting chamber at a well-controlled temperature and pressure condition from molybdenum and sulfur precursors. A more specific type of CVD method is metal-organic CVD (MOCVD)[155] in which the metalorganic precursors are typically introduced into the reacting chamber as ultrapure gases. The material used for nanopore devices needs to have good quality, to produce a uniform monolayer with low defect density resulting in high mechanical and chemical stability. Minimizing grain boundaries during the growth increases the probability of having a uniform layer above the aperture. Furthermore, the monocrystalline region needs to be large enough to be easily aligned with the substrate.

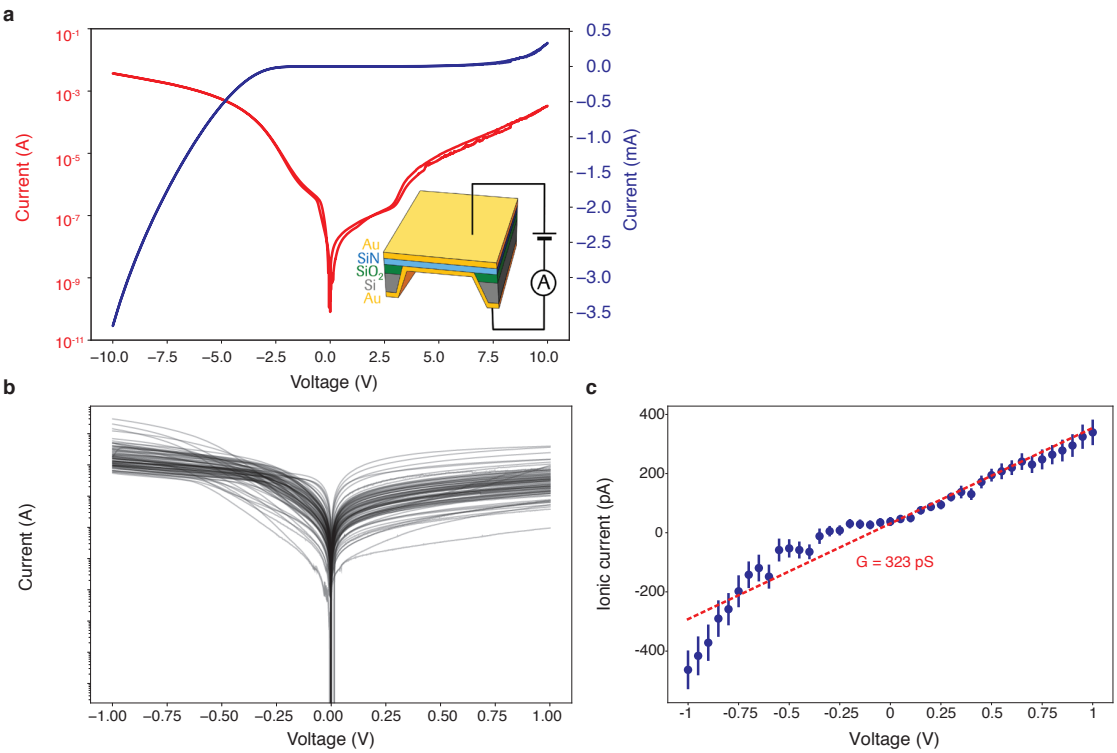

Figure 2.4 – Leakage tests. a, I-V curve of MIM junctions from the test wafer plotted on a logarithmic scale to emphasize the rapid current changes around 0 V. The right axis (blue) shows the same data on a linear scale to emphasize the observed asymmetry. Inset: a schematic of the leakage current measurement. **b**, I-V curves of 90 MIM junctions. **c**, I-V curve in 1 M KCl of a SiN_x membrane without an aperture. The I-V was generated by fitting the current trace of each voltage change to a single exponential decay function (capacitive decay due to membrane charging), the error bars represent the uncertainty of this fit. **a** and **b**: data obtained by Juraj Topolancik. *This Figure was published in Nature Protocols, 2019, Graf et al.*[50]

2.4 Transfer onto the SiN_x membrane

Although a direct growth of MoS_2 over apertures in SiN_x membranes has been shown before,[156] it is quite challenging to achieve a uniform monolayer grown over a suspended area. The transfer of the material from the growth substrate to the SiN_x aperture is an alternative and reliable way of obtaining 2D-monocrystal over the aperture. However, besides the quality of the MoS_2, one of the most critical steps in nanopore fabrication in 2D-materials is the transfer. If the suspended MoS_2 region is damaged or detached (Figure 2.5a), misaligned with respect to the aperture (Figure 2.5b) or too contaminated (Figure 2.5c and d), the devices are generally unusable. Appropriate transfer methods, including the cleaning procedure, will ensure a good transfer of the MoS_2 material from one substrate to the other without compromising quality. Here we describe two methods based on already published papers, both of which depend on water penetration between the MoS_2 layer and the underlying substrate, usually sapphire. Due to different surface energies of these materials ($MoS_2$is hydrophobic, while sapphire is hydrophilic) the MoS_2 detaches from its growth substrate.[129,130,133]

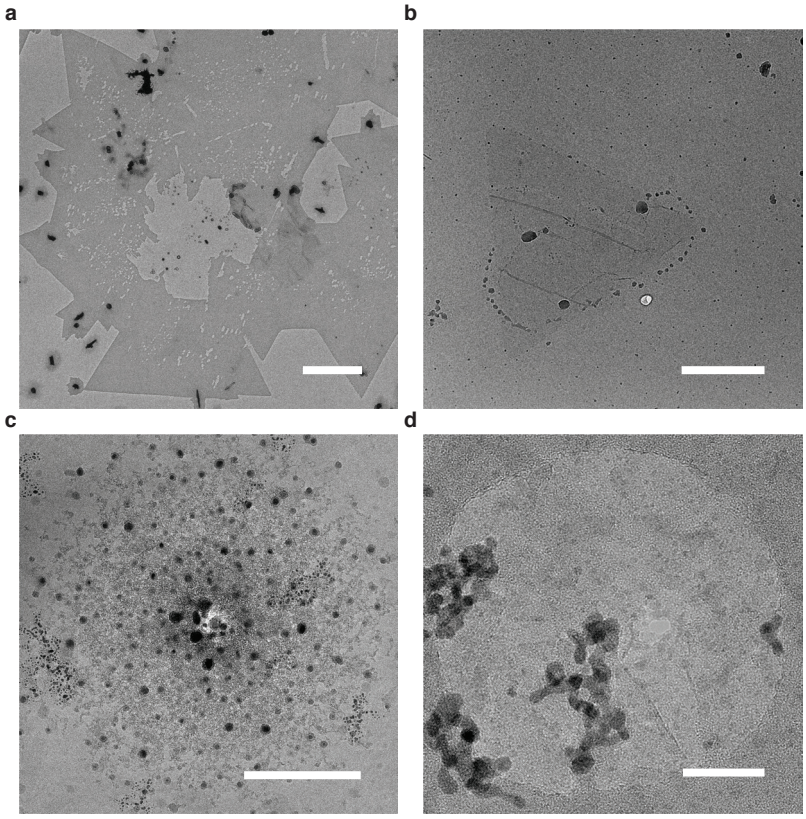

Figure 2.5 – Troubleshooting MoS_2 transfer. TEM images (Talos, 80 kV) **a**, detachment of a transferred MoS_2 from the SiN_x aperture area after experiments in solution. The scale bar is 5 µm. **b**, MoS_2 mono crystal misaligned in respect to the aperture. The scale bar is 1 µm. **c**, contaminated SiN_x aperture. The scale bar is 200 nm. **b**, PMMA contamination of a freestanding MoS_2 monolayer. The scale bar is 20 nm. TEM images by Martina Lihter. *This Figure was published in Nature Protocols, 2019, Graf et al.*[50]

2.4.1 Transfer with PMMA

(Step 37 Option A). PMMA is deposited as a few hundreds of nanometers thick films by spin-coating onto the substrate carrying the MoS_2. To perform multiple transfers using a single growth substrate, the spin-coated PMMA layer is cut into small patches (such as 0.25 mm^2) using a sharp razor blade. An individual patch is lifted-off by placing a water droplet near the edge and slightly poking the flake by a needle which enhances the water penetration between the layer and the substrate. Once the PMMA starts floating on the water droplet, it can be picked up with a glass microcapillary. At this point, the PMMA-MoS_2 layer folds around the microcapillary tip and is transferred to another water droplet on the SiN_x chip. The layer evenly unfolds once it touches the water. The position of the layer is then be precisely adjusted under a 50x long-working-distance objective on a reflection microscope. The layer is manipulated with a glass-microcapillary attached to the x-y-z stage while the chip is fixed by vacuum to a small heating platform. Heating up to 40-50 °C enables faster water evaporation. If the MoS_2 is misaligned, it can be re-aligned by adding a water droplet, which detaches the layer from the surface and allows to repeat the alignment. If the SiN_x surface is very

hydrophobic, the contact angle of the water droplet will be large, and the PMMA layer floating at the surface will be curved with respect to the chip surface. This can make it difficult to adjust the exact position of the monocrystals especially if they are relatively small. Instead of water, a non-polar organic solvent can be used as a transfer medium to circumvent this minor issue. It is important to note that exposing the SiN_x surface to oxygen plasma or piranha solution will make the surface hydrophilic and therefore facilitate better alignment using water as a transfer medium. However, in our experience, hydrophilic surfaces have poor adhesion to MoS_2, which can result in the layer detachment in solutions (Figure 2.5a). Any pre-treatment to render the SiN_x hydrophilic should, therefore, be avoided. After the PMMA-assisted transfer, one should start the cleaning procedure (Step 37A xiii-xv) as soon as possible to remove all the polymer successfully. The cleanliness of the 2D-material is crucial for nanopore devices for many reasons: 1st the polymer residues locally increase the thickness and make it difficult to drill through the material no matter which technique is used (Figure 2.5d). 2nd enlarged thickness near the pore region decreases the conductance decreasing the apparent pore size and conductance blockage caused by DNA translocations (see Equation 2.1). 3rd Flexible polymer chains can disturb the flow of ions and DNA molecules, creating an unstable current baseline, and sometimes even gradual clogging of the hole. The cleaning protocol depends on the polymer used for the transfer procedure. The procedure can be divided into two parts: 1st, the majority of the polymer gets removed with several iterations of dissolving and diluting in hot acetone followed by rinsing in hot isopropyl alcohol (IPA) and deionized (DI) water. 2nd is an annealing process at temperatures higher than 300 °C in an inert atmosphere where any residual PMMA chains are thermally degraded.

2.4.2 Transfer with PDMS

(Step 37 Option B). Transfer of MoS_2 using PDMS has been reported earlier[127,131,133,157] on diverse substrates. The technique relies on the hydrophobic-hydrophilic property of the MoS_2 and substrate respectively. In our experiments, we use a small PDMS-stamp (< 1 mm^2) anchored to a glass slide (Figure 2.6a-c) to lift-off mono-crystalline MoS_2 grown on a sapphire substrate using the capillary-force exerted by water. The PDMS stamps are hydrophobic, thin, flexible and optically transparent, they can be operated easily using a simple micro-manipulator (Figure 2.6d) to lift-off and perform the transfer of MoS_2 onto the SiN_x membrane with good precision. Briefly, the PDMS stamp (hydrophobic) is brought in physical contact with the MoS_2 (hydrophobic) surface which is grown on a sapphire substrate (hydrophilic). Following this, a water-droplet is placed around the edge of the PDMS/ MoS_2 /sapphire surface and using a micromanipulator the PDMS stamp is slowly lifted off (Z-direction). Due to the capillary action, the water penetrates between the sapphire and MoS_2 transferring MoS_2 directly onto the PDMS surface where it adheres by hydrophobic interaction. The PDMS stamp being optically transparent allows precise alignment of the MoS_2 to the SiN_x membrane. The transfer is terminated by simply stamping the MoS_2 to the SiN_x membrane. The technique can be used to transfer multi-layer MoS_2 and can be extended to other hydrophobic TMDs grown on a hydrophilic substrate. No further cleaning steps are required in this technique.

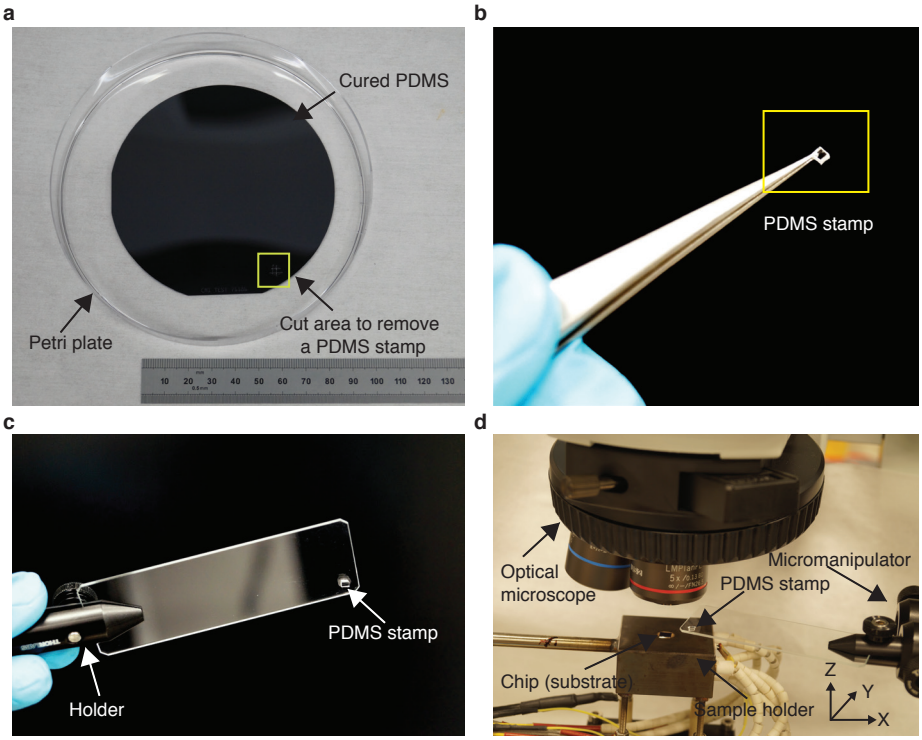

Figure 2.6 – PDMS-assisted selective transfer of MoS_2. **a**, PDMS is baked on a clean silicon wafer inside a petri dish. The highlighted area points to the place where a small stamp is removed using a scalpel (Step 37B i-iv). **b**, Highlighting a single PDMS stamp cut in **a** (Step 37B v). **c**, PDMS stamp mounted on a clean glass slide with a micromanipulator holder (Step 37B vi). The holder is fixed on a micromanipulator stage for MoS_2 transfer. **d**, MoS_2 transfer experiment set-up with a micromanipulator stage equipped with XYZ axes control with a holder for glass slide with PDMS stamp. The sample holder stage comprises a substrate placement area equipped with a vacuum suction for stabilizing the substrate in addition to XYZ axes and yaw motions. The whole process of transfer is monitored using an optical microscope with a 5x and 50x objectives. Figure made by Mukeshand Thakur. *This Figure was published in Nature Protocols, 2019, Graf et al.*[50]

2.5 Transfer Quality

Optical microscopy and photoluminescence can be used to quickly confirm if the 2D-material was successfully grown, transferred and aligned onto the desired surface. Transmission electron microscopy (TEM) has become a standard tool not only for detailed inspection and nanopore imaging but also for drilling nanopores. Ionic current measurements are routinely used for pore characterization in ionic solution and have the advantage of providing direct information on the pore size at any time during the experiment. In combination with the ECR process[30] for creating nanopores, it is possible to avoid the use of TEM altogether thereby enabling a low-cost and simple nanopore fabrication.

2.5.1 TEM

High-resolution TEM (HR-TEM) is a technique with subnanometer resolution and gives the best insight into the quality and cleanliness of 2D-material at the atomic level. The imaging of 2D-crystals is extremely challenging since the electron beam can induce damage in the structure of the crystal. In the case of MoS_2 the main mechanism can be described as a "knock-on" damage where the atom is ejected from the crystal due to inelastic scattering of the incident electrons.[158] Since the lighter atoms need less energy to be displaced, the S atoms will be more easily ejected (the knock-on threshold voltages for Mo and S are 560 kV and 80 kV, respectively).[159,160] In order to prevent material damage, the imaging needs to be performed at a low acceleration voltage and in a high vacuum environment to avoid any excess of moisture and gaseous molecules. We perform imaging with 80 kV acceleration voltage while keeping the electron current density below 0.05 pA nm^{-2}. However, even at this condition sulfur vacancy defects can still be introduced and can lead to layer-cracking over time (Figure 2.7). Figure 2.8a shows a suspended MoS_2 double layer over the aperture in SiN_x. Polymer residues can be seen as amorphous patches and chains which can interact with the beam causing hydrocarbon deposition. As mentioned earlier, the regions exposed to the electron beam should have as little contamination as possible since residues can migrate and contaminate the clean parts. Selected area diffraction can give information about the crystal structure of the material and verify if the transfer was successful. Figure 2.8b shows a diffraction pattern characteristic for 2H-phase MoS_2 . Due to specific growth conditions sometimes there could be more than one crystalline layer stacked on top of each other. In HR-TEM imaging mode, the layers rotated at a certain angle with respect to each other will give specific Moiré patterns. Figure 2.8c shows the aperture area with the regions where the layers with different orientations are overlapping. In this case, the diffraction pattern consists of many signals coming from individual layers rotated respectively to each other (Figure 2.8d). The information about the crystal structure can also be obtained from the fast Fourier transform (FFT) of the image. Since commercial TEM holders are usually made for 3 mm diameter TEM grids, it may be necessary to design a custom-made holder that fits the nanopore chip.

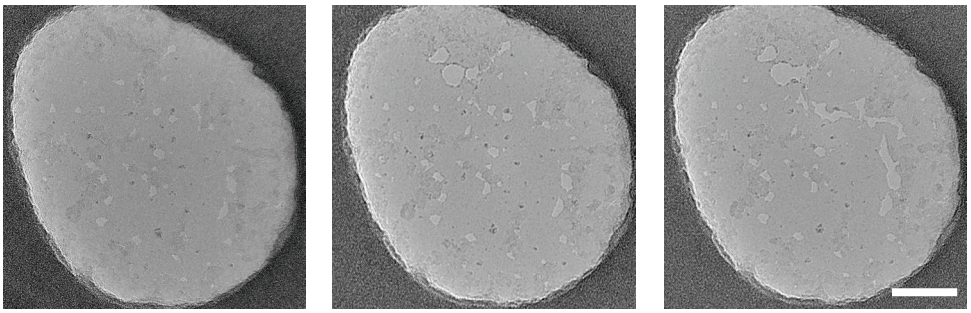

Figure 2.7 – Beam damage. Successive damage of a MoS_2 monolayer by an electron beam. The scale bar is 20 nm. Figure by Martina Lihter. *This Figure was published in Nature Protocols, 2019, Graf et al.*[50]

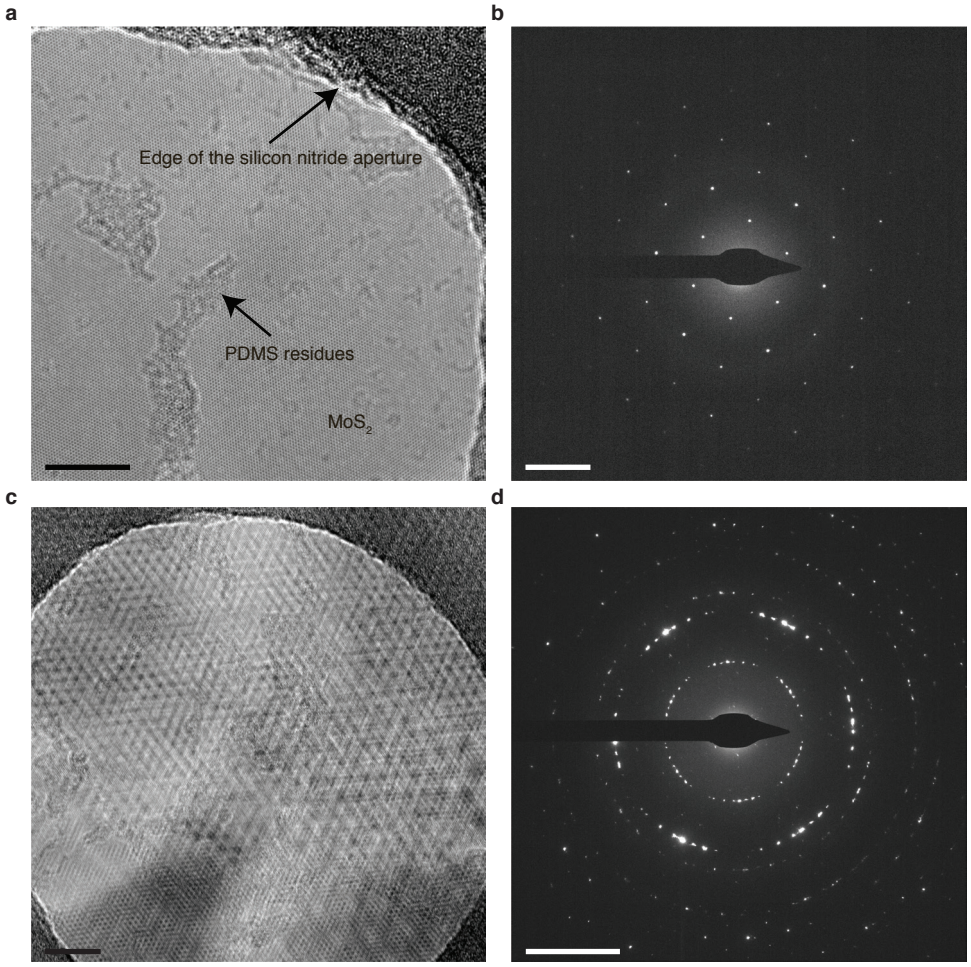

Figure 2.8 – TEM images of suspended MoS_2. a, A two layer MoS_2 crystal suspended over a hole. The two layers are perfectly aligned and therefore increase the imaging contrast. The scale bar is 20 nm. **b**, The diffraction image of **a** showing the perfect alignment of the layer. The scale bar is 5 nm^{-1}. **c**, Multi-layer MoS_2 where the individual are misaligned. In high-resolution TEM this leads to aesthetically pleasing interference patterns (Moiré patterns). The scale bar is 20 nm. **d**, The diffraction image of **c** allowing to identify the number of layers and their orientation towards each other. The scale bar is 5 nm^{-1}. All images were taken with a FEI Talos TEM at the interdisciplinary centre for electron microscopy (CIME) at EPFL. *This Figure was published in Nature Protocols, 2019, Graf et al.*[50]

2.6 Nanopore Drilling and Characterization

2.6.1 Nanopore creation by TEM drilling (Step 38 Option A)

The drilling can be performed in the same mode (HR-TEM bright field 80 kV) as the imaging. The beam should be set to the smallest spot-size enabling better precision during pore creation. First, the area of interest is placed in the center of the field of view. The beam is then quickly contracted to the smallest spot in the center of that area. If the layer is clean, within a second one will notice the local damage of the layer. During the pore growth process, the beam spot can be continuously increased up to the desired pore size to monitor the process more

easily. Once the pore is grown to the desired size, the beam should be blanked immediately to stop further damaging the layer. After spreading the beam, it is safe to unblank the beam and image the nanopore. In this approach, the critical step for making small pores is fast beam contraction. During the contraction time, the current density is drastically increases, which sometimes causes the layer to be damaged before reaching the smallest possible beam size. From our experience, creating nanopores smaller than 2 nm with the TEM is not very controllable, and extreme care has to be taken since it is very easy to destroy the sample. Furthermore, the TEM technique is expensive, time-consuming (only one sample can be inspected at the time) and requires a skillful operator.

2.6.2 Nanopore creation by ECR (Step 38 Option B)

Nanopores can also be created in ionic solution by applying a high potential difference across the membrane, thereby triggering an electrochemical reaction on the surface of the material. There are two variations of this technique: applying a series of short high-voltage pulses[161] or a stepwise increase of voltage until a certain threshold value is reached.[30] We use the second approach, which enables us to create pores below 2 nm with high precision. We start with a low voltage around 200 mV which we slowly increase in steps by 100 mV. The leakage current is usually constant for a certain voltage value. Once the critical voltage is reached, the current starts increasing more prominently indicating pore growth (an example can be found in subsection 2.10.2). One can monitor the growth process by observing the current level and terminate the process when the pore has reached the conductance corresponding to the desired size. The threshold value highly depends on the number of active sites in the material, i.e. defects, the thickness of the material and cleanliness. From our experience the threshold voltage can vary between 800 mV and 2.5 V. The advantages of this method are many:

1. The pore creation can be done in-situ avoiding contamination from the TEM.
2. The drilling can technically be done with the same nanopore set-up, which makes it a low-cost, simple and accessible technique comparing to TEM.
3. A big advantage comes from the fact that this process is scalable, enabling parallel nanopore fabrication.

2.6.3 Current measurements

Due to their simplicity, ionic current measurements represent the primary characterization method in the nanopore field, providing quick information on the nanopore size. By varying the measurement conditions such as pH, one can get insights into more specific material properties such as the membrane capacitance or the surface charge density. Comparing to TEM imaging this is an easier and cheaper way of nanopore size characterization, but unfortunately, it does not provide any information about the cleanliness and the number of pores.

We have learned about the ionic conductance, G, of nanopores in subsection 1.4.2 (page 13) (the conductance model itself was presented in Equation 1.2).

Experimentally, the value of G can be measured by recording the ionic current baseline at a specific voltage. Due to asymmetric charge distributions, pore geometries or improper wetting, the current-voltage dependence is not always linear, so it is more accurate to record the current at different values of voltages. The value G can then be easily extracted from the slope of the linear I-V dependence. While recording the ionic current, it is important to acquire enough data since the current is exponentially dropping or increasing, respectively, within the first few seconds after the voltage switch. This happens because the voltage changes cause charging (or discharging) of the capacitors in the system. The real baseline current value can thus be fitted exponentially from this decay region, or linearly from the points after the decay where the current is stabilized. Due to their fine structure 2D-material pores are very susceptible to electrochemical reactions and voltages applied, so in order to reduce the risk of pore enlargement, it is better to stay below ±400 mV, or even less depending on the conditions and the quality of the material. Exposure to laser light,[32] high level of oxygen in solution or the presence of reactive species can enhance the degradation of 2D-material. If the material has a large number of defects, it will be also more prone to electrochemical reactions.[30]

Molecule translocations and pore-size estimation. While passing through the pore a molecule is blocking the flow of ions which causes a conductance drop ΔG:

$$\Delta G = \frac{G(d) - G(d_{\text{eff}})}{G(d)} \tag{2.1}$$

where $G(d)$ is an open pore conductance and $G(d_{\text{eff}})$ the conductance of a partially blocked pore. The effective pore diameter, d_{eff}, denotes the diameter that corresponds to a pore with the same conductance as the blocked pore. It can be expressed by: $d_{\text{eff}} = \sqrt{d^2 - d_{mol}^2}$, where d and d_{mol} are the diameters of the pore and the translocating molecule, respectively. Due to the access resistance, a detected current signal does not necessarily need to be caused by translocation through the channel. A drop in conductance can be provoked when a molecule temporarily resides inside the pore sensing region, partially enters or just probes the access resistance.[162,163] The dwell-time and the current drop of a translocation event highly depends on the applied voltage. Consequently, recording current traces at different voltages should indicate if a certain current trace is a translocation. If the pore size is known, it is advantageous to calculate the expected conductance drop based on the diameter of the molecule and compare it with the experimental values. Since the blockage contains information on how big the pore diameter is with respect to the diameter of the translocating molecule, one can use DNA as a molecular ruler to extract the pore diameter from the conductance drop of DNA.[31,54,150] This is particularly useful when the pore is created in situ by controlled dielectric breakdown (CDB) or ECR.[19,30] In general, it is better to use double-stranded DNA (dsDNA) because it is more rigid than single-stranded DNA (ssDNA)[54] and consequently tends to fold less. For the size estimation of relatively small pores (smaller than ≈6 nm) one should avoid using very long DNA (>10 kilobase pairs (kbp)) since it can easily fold and clog the pore.

The influence of small aperture on total G

The conductance equation (Equation 1.2) is valid only if the resistance of the system is dominated by the 2D-pore. In other words, the resistance of the aperture must be negligible compared to the resistance of the nanopore, otherwise, the total conductance will be reduced (Figure 2.9a). Due to this, a certain conductance value can be misinterpreted as a MoS_2 pore even if the actual layer got broken. This reduced conductance also reflects on the DNA blockage percentage which becomes lower than expected for 2D-material (Figure 2.9b).

Influence of multiple pores

In the case that one has multiple pores far away from each other, the DNA blockage would be higher than predicted due to the contribution of access resistance.[30] However, by increasing the number of pores and by reducing the distance between them, the total conductance should scale sub-linearly, meaning that the conductance per pore strongly decreases with the number of pores.[164]

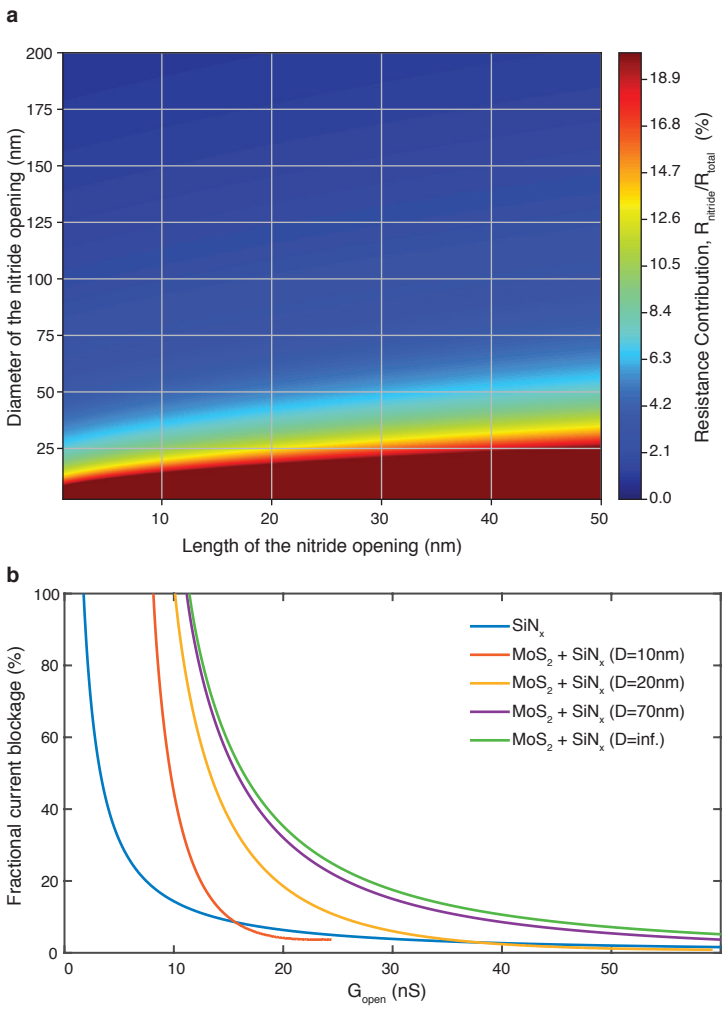

Figure 2.9 – Diameter and thickness of the aperture. **a**, The contribution of the aperture R_{nitride} to the total resistance of the system R_{total} ($= R_{\text{MoS}_2} + R_{\text{nitride}}$) is estimated by comparing its resistance to the resistance of a 2.5 nm hole in monolayer MoS_2 suspended on the aperture. The color-coded values are percentages of this aperture resistance and are cut-off at 20 % (red color) for visibility. **b**, The expected fractional current blockage due to DNA translocation is plot as a function of the conductance of the device and different substrate geometries. The blue curve represents the expected fractional current blockage of a pore in a SiN_x membrane without suspended MoS_2. The green curve represents a MoS_2 membrane that is not suspended ($D = \infty$) to illustrate the theoretically best configuration. The other curves show a pore suspended on an aperture of variable size (10 nm, 20 nm and 70 nm), which illustrates the influence of the size of the aperture. The thickness of SiN_x was set to 20 nm whereas the effective thickness of MoS_2 was set to 1.6 nm. This can be helpful to estimate the influence of the aperture on observed translocation traces. *Figure credits:* ***b****, Martina Lihter. This Figure was published in Nature Protocols, 2019, Graf et al.*[50]

Amplifier	Bandwidth	I_{limits}	DAQ	V_{limits}	Company
Axopatch 200B	100 kHz	200 nA	No*, BNC	1 V	Molecular Devices, San Jose, CA, USA
Chimera VC100	1 MHz	20 nA	Yes, USB3	1 V	Chimera Instruments, New York, NY, USA
FEMTO DLPCA-200	500 kHz	200 mA	No, BNC	10 V	FEMTO Messtechnik, Berlin, Germany
eONE	100 kHz	20 nA	Yes, USB2	380 mV	Elements, Cesena (FC), Italy
EPC 10 USB	60 kHz to 100 kHz	2 µA	Yes, USB2	2 V	HEKA Elektronik, Lambrecht/Pfalz, Germany

Table 2.1 – A selection of current-amplifiers used in nanopore experiments. * Analog-to-digital-converter unit available separately.

2.7 Experimental Set-Up

2.7.1 Amplifiers set-up

A low noise current amplifier is used to measure the current generated at the Ag/AgCl electrodes. Historically, the patch-clamp amplifier Axopatch 200B (Molecular Devices, San Jose, California, United States) has been widely used in nanopore experiments due to its excellent noise performance and simplicity of use. The maximal achievable bandwidth is set to 100 kHz, which is enough for most purposes, but might not be sufficient for small molecule translocations, such as proteins, where typical dwell times are in the order of a few microseconds.[36] Furthermore, the Axopatch 200B can apply a maximum voltage of 1 V, which might not be sufficient for all applications such as ECR or dielectric breakdown.[19] Amplifiers with larger bandwidths up to 1 MHz especially created for nanopore experiments such as the Chimera Instruments VC100 (New York, NY, USA) are available but suffer from drawbacks such as small current ranges (e.g. ±20 nA). Furthermore, in order to take advantage of the larger bandwidth, the devices need to be very low-noise, i.e. glass nanocapillaries or membranes fabricated on glass substrates.[149] To alleviate the need to apply higher voltages and potentially measure higher currents than possible with an Axopatch 200B or a Chimera VC100, we use the variable gain low-noise amplifier Femto DLPCA-200 (FEMTO Messtechnik, Berlin, Germany). This flexible instrument allows measuring anything from the pA to mA range. A selection of available current amplifiers useful for nanopore experiments can be found in Table 2.1.

2.7.2 Analog-to-digital conversion set-up

The Chimera amplifier has an analog-to-digital converter integrated and connects to the PC through a high-speed USB3 connection. Both, the Axopatch 200B and the FEMTO DLPCA-

200 require a separate analog to digital converter. We are using a PXI-4461 card (National Instruments, Austin TX, USA) with two channels. The outputs allow application of up to 10 V whereas the two input-channels can sample at a maximum of 200 kHz and provide a 24 bit resolution. The two channels allow simultaneous and synchronized recording of two amplifiers at the same time. Combining this acquisition card with the FEMTO amplifier allows us to apply voltages higher than 1 V to create nanopores through the ECR method.

2.7.3 Flow-cell

The function of the flow-cell is to safely secure the nanopore chip and to properly seal the chip to the chamber in order to avoid unwanted current leakage. All materials used need to be electrically insulating. Disposable flow-cells using PDMS can be prepared by designing appropriate molds (machined or photolithography). Here we describe a two-part flow-cell based on computer-numerical-control (CNC) machined PMMA. The advantage of using PMMA over other materials is its transparency after polishing. Transparency is crucial in order to detect bubbles during the filling process. A rendering of a disassembled version of the proposed flow-cell set-up can be found in Figure 2.10a. The flow-cell is comprised of two PMMA blocks that can be screwed together. The nanopore chip is sandwiched by two rubber O-rings placed in the appropriate grooves in the PMMA blocks. To avoid breakage of the fragile silicon chip, a groove with dimensions matching the chip in one of the PMMA blocks can be added. This groove will fit the O-ring and the chip so that the surface is leveled with the rest of the PMMA block. In such a configuration breakage of the device by screwing the parts together can be completely avoided (Figure 2.10b). The horizontal inlet is used to apply the liquid to the nanopore. Typically, we use 1 ml insulin syringes with needles slightly shorter than the inlet length to avoid contact and breakage of the chip. The second, vertical channel acts as an outlet during liquid injection and washing. Furthermore, it allows inserting the Ag/AgCl electrodes. In order to prevent evaporation of the buffer solution, the channels can be sealed by glass slides or PDMS plugs. Since these flow-cells are reusable, a good cleaning strategy is needed in order to completely remove analyte residues. For this purpose, we use an ultrasonic bath in diluted soap (RBS 25 solution), followed by several DI-water washes and rinsing in ethanol.

2.7.4 Device handling

To mitigate the problem of breaking MoS_2 due to electrical discharges (mentioned in subsection 2.3.3), a few simple preventive measures should be introduced: 1st wear antistatic gloves and a grounded wrist strap at all times when handling the flow-cells. 2nd perform all work on a grounded anti-static table-mat. Additionally, any charge build-up can be neutralized using an Ag/AgCl connection between the two sides of the membrane during wetting and handling of the flow-cell.

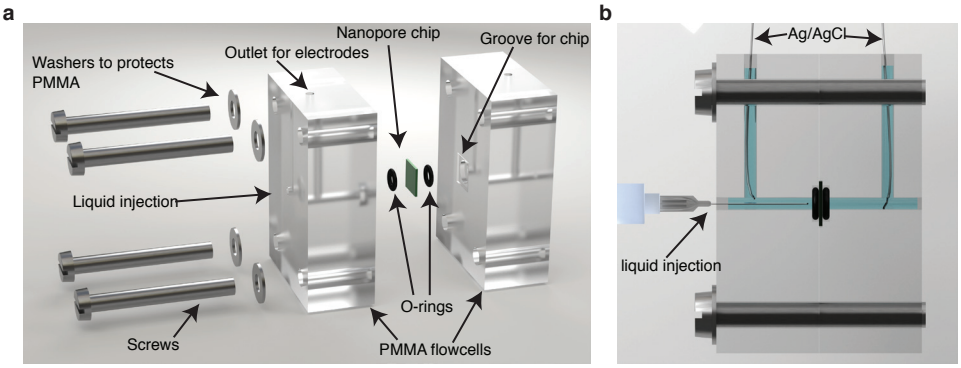

Figure 2.10 – Flow-cell design. a, Parts of the flow-cell assembly. **b**, Side-view of the assembled system. A syringe is used to inject the liquid to the horizontal channels. The vertical channels act as an outlet for the liquid and a place for the Ag/AgCl electrodes. *This Figure was published in Nature Protocols, 2019, Graf et al.*[50]

2.7.5 Pore wetting

Ethanol and DI-water at a 1:1 (vol:vol) ratio is used to wet the pore (Step 38B i-iv) due to its lower surface tension. In our experience, the ultrathin membrane wets very rapidly (a few minutes) rendering lengthy soaking unnecessary. Usually, salt solutions buffered with tris(hydroxymethyl)aminomethane (Tris) and ethylenediaminetetraacetic acid (EDTA) adjusted to pH 7.4 are injected after the wetting step. EDTA is added for the purpose of DNA translocations since this chelating agent binds divalent cations and prevents DNA from coagulating. Degassing the buffers is very important since nanobubbles can form at the nanopore and block the ionic current.

2.7.6 Electrodes

In nanopore measurements, conventional reference Ag/AgCl/KCl electrodes are used. Besides having a stable electrode potential they are also nonpolarizable, which means there is no need to overcome an overpotential in order for the current to flow. In other words, in this way, the potential difference across the membrane is equal to the potential difference that is applied. If the experiments are performed in chloride-based solutions and the measured currents are low (nA), electrodes can be made simply by chlorinating a silver wire and inserting them directly into the sample solution. The chlorination is usually done by leaving the silver wire in a bleach solution or electrochemically by applying a positive potential to the silver wire inserted into a KCl solution. In this way, one gets a greyish AgCl coating which should be thick enough to ensure stable current measurements. Since AgCl is photosensitive[165] electrodes need to be freshly prepared before each experiment and stored in the dark.

2.8 Data Acquisition

Solid-state nanopore data is typically acquired at bandwidths of about 10 kHz due to the fairly high noise in silicon-based nanopore devices. Reducing the noise level of the nanopore chip using glass substrates made it possible to push the bandwidth to 10 MHz.[149] Typically, the data is acquired through an analog-to-digital converter running at an appropriate sampling frequency. The data can then be saved as received by the card or specialized software is used to save only the frames that contain the signal of interest while discarding the rest. In simple terms, the software analyzes the currently received signal frame and detects by a simple thresholding method whether a translocation event occurred or not. In the case of a detected translocation event, the software saves the current frame. If no event is detected the frame is discarded. This strategy allows to keep the file-sizes to reasonable values (this is especially important at high bandwidths) and facilitates the subsequent analysis.

A carefully designed acquisition software with automation features should help the experimenter to save time and improve reproducibility. We will discuss a few key elements that can help to improve productivity:

Automatic voltage sweep. The user should be able to select the voltage range and the time spent at each point (dwell time). In order to avoid unilateral charging of the membrane, the sweeps should be done in alternating polarity, i.e. 0 mV, 100 mV, –100 mV, 200 mV and –200 mV...

Digital low-pass. Depending on the acquisition bandwidth used, the signal needs to be digitally filtered in order to lower the noise and make translocation events visible.

Signal detection. At low voltages the translocation rate might be very small, making it crucial to record only when translocations occur. This can be achieved by implementing a live translocation detection. For example, a simple threshold can be defined as: $y(t) < \mu_y - S * \sigma_y$ current signal, μ_y the signal mean and σ_y, the standard deviation of the signal. S is a parameter chosen by the user to set the sensitivity of the detection. Once the condition is satisfied, the current sequence can be saved.

Automatic Zap. This function applies a negative voltage of chosen amplitude and duration. This is useful to unclog the nanopore.

Feedback Loop. Automatic voltage reset (0 V) when the device reaches a predefined conductance value. This is especially useful for the ECR method where the controlled growth of the nanopore should be stopped at a certain conductance.

Typically, LabView (National Instruments, Austin TX, USA) provides an easy to use environment for developing the acquisition software. Depending on the devices used, other programming languages such as Python can be powerful tools as well.

2.9 Data Analysis

In this part, we provide a broad overview of the data-analysis work-flow.

2.9.1 Current voltage relationships

Ideally, the recorded file should contain current and voltage data. The data is then segmented into piecewise constant voltage values. Due to the high capacitance of the nanopore device, a short decay of the current is observed when the voltage switches. The current in each segment should then be fitted to an exponential decay function: $y(t) = Y_0 \cdot e^{-\frac{t}{\tau}} + Y$, where Y is the current at infinite time, corresponding to the current of interest in the I-V characteristic; $Y_0 + Y$ is the initial current of the decay and τ the decay rate. Extracting Y and plotting it for all voltages V will lead to the I-V curve. The slope of this curve corresponds to the conductance S ($= \frac{1}{R}$). This conductance value can then be used to estimate the pore size (see subsection 2.6.3).

2.9.2 Translocation data analysis

The first step in analyzing translocation data is to find the location in the trace, where the event occurs. One way to detect these abrupt current changes is to create a mean and variance trace which, combined, provide a thresholding condition for detecting the current drops. These detection algorithms can be implemented using appropriate digital filters and are widely used in existing nanopore software (see Table 2.2). After the coordinates of the events are found, the internal structure of the translocation might be of interest. Algorithms such as the CUSUM[166] are useful to extract sub-event levels. Typically, scatter plots and histograms of the current drop versus the dwell time are built in order to reveal subpopulations linked to the structure of the molecules during the translocation.

2.9.3 A selection of available software

Many research groups have developed their own software to handle nanopore data and often made it publicly available. The general requirement for such a software is first to extract translocation events from the noisy signal. Once the locations of the translocation events have been found, the software fits the amplitude and dwell time of the event. Not all programs can handle multi-level events. The amplitude and dwell time are fitted using different methods. In some cases, the effects due to distortions caused by the filter are considered, but most programs do not. From all the software listed in Table 2.2, MOSAIC is probably the most comprehensive, but likely the one with the steepest learning curve.

Name	Functions	Language	Ref	Lab
OpenNano-Pore	Event extraction, multi-level fitting, statistic	Matlab	[166]	LBEN, EPFL, Switzerland[1]
PythIon	Trace viewer, event extraction	Python	-	Wanunu Lab, Northeastern, Boston, Massachusetts, USA[2]
MOSAIC	Multistate nanopore data, highly extensible	Python	[167]	NIST, Gaithersburg, Maryland, USA[3]
Transalyzer	Event detection, statistics	Matlab	[168]	Dekker Lab, TU Delft, The Netherlands[4]
Nanopore Analysis	Event detection, statistics	Matlab	[169]	Long Lab, East China University of Science and Technology, Shanghai, China[5]
Chimera Software	Acquisition software for Chimera amplifier, event filter, automatic I-V creation	Python	-	LBEN, EPFL, Switzerland[6]

Table 2.2 – A Selection of available nanopore data analysis software. [1]https://lben.epfl.ch/page-79460-en.html. [2]https://github.com/rhenley/Pyth-Ion. [3]https://pages.nist.gov/mosaic/. [4]https://github.com/voyn/transalyzer/. [5]http://ytlong.ecust.edu.cn/_t300/main.htm. [6]https://github.com/Microtubulus/ChimeraSoftware.

2.10 Anticipated Results

2.10.1 Chip fabrication

There are two key components in assessing the success of the substrate fabrication. First, the size of the resulting membrane (Step 1-Step 30) can be assessed using an optical microscope (in reflection configuration). Typically, membranes are slightly larger than theoretically predicted due to imprecision in the alignment of the pattern to the crystal axis of the silicon substrate. Figure 2.1a (bottom) shows an example of an optical micrograph of a fabricated SiN_x membrane. Second, the success of creating the aperture using EBL and RIE (Step 15-Step 19) can be assessed by TEM. Figure 2.11a shows a TEM image of a successful aperture in SiN_x membrane. The size and shape of the aperture can be compared to the designed patterns. These holes tend to be roughly 20 % larger than designed, which is probably due to backscattering of electrons during the EBL. Another common problem is that these holes are only partially open, it is thus imperative that the fabricated substrates are checked in a TEM. Alternatively, if no TEM is available, the fabricated chip can be placed in a flow-cell and the conductance can be measured to estimate the aperture size using Equation 1.2.

After MoS_2 transfer (Step 37), the most reliable method of checking the cleanliness and success of the transfer is TEM. Figure 2.11b shows an intact and clean monolayer of MoS_2 suspended over the aperture in the SiN_x membrane. Condensing the electron beam on that same sample allows the creation of MoS_2 nanopore (Figure 2.11c). The time during which the condensed beam irradiates the spot defines the pore size. Figure 2.11d shows a collection of different

pore-sizes ranging from 1 nm to 4 nm in diameter that are achievable using TEM irradiation. Of course, creating a bigger pore size is always possible by shifting the beam or the sample to irradiate the intact parts of the monolayer membrane.

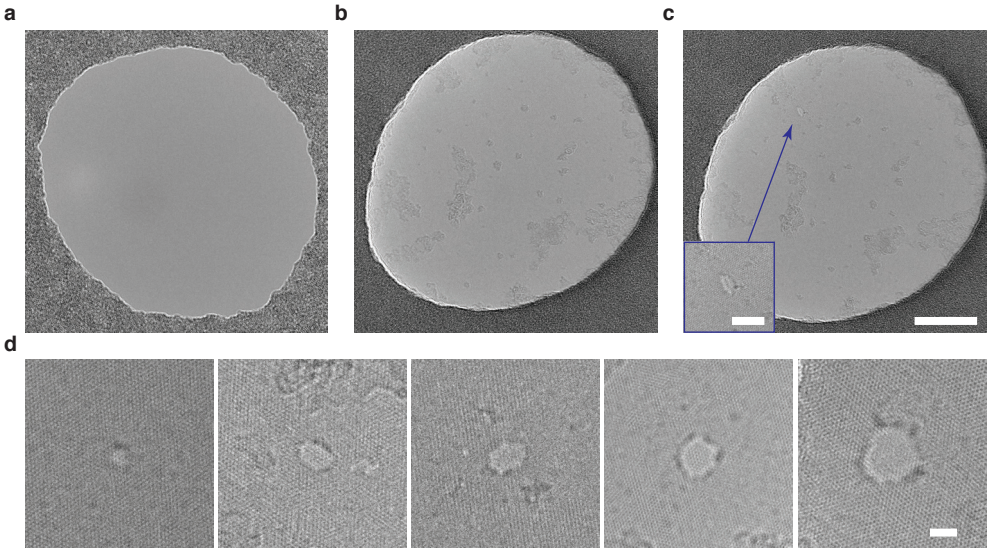

Figure 2.11 – Anticipated results: substrate fabrication. TEM images (FEI Talos, 80 kV) **a**, A clean successfully etched SiN_x aperture. **b**, clean MoS_2 monolayer suspended over the SiN_x aperture. **c**, The same area as in **b** after drilling the nanopore (inset) by electron beam. The scale bar is 20 nm. **d**, Nanopores of different sizes created by electron beam. The scale bar is 2 nm. Figure by Martina Lihter. *This Figure was published in Nature Protocols, 2019, Graf et al.*[50]

2.10.2 DNA translocations

Figure 2.12 shows example data obtained with a MoS_2 nanopore using the PDMS transfer method and ECR to generate the nanopore. A voltage of 900 mV was sufficient to induce a steady current increase (Figure 2.12a, at 40 s). The voltage is then reset to zero. An I-V response was then recorded between –200 mV and 200 mV and yielded a conductance of 10.6 nS (Figure 2.12b). The pore size can thus be estimated to be about 2 nm using equation Equation 1.2. The *cis*-side buffer is then exchanged with buffer containing 2 kbp dsDNA at a concentration of 10 ng µl^{-1}. This DNA was translocated at transmembrane voltages of 200 mV, 300 mV, 400 mV and 500 mV. An extract of the current trace at 500 mV can be found in Figure 2.12c. A scatter plot of the current drop and dwell time is shown in Figure 2.12d. Representative translocation events for each voltage are shown in Figure 2.12e. Typically, the current drop depends linearly on the voltage applied (Figure 2.12f), i.e., the conductance change induced by the dsDNA is roughly constant as a function of the applied voltage range.[77] Figure 1.7 showed the event rate extracted from this dataset.

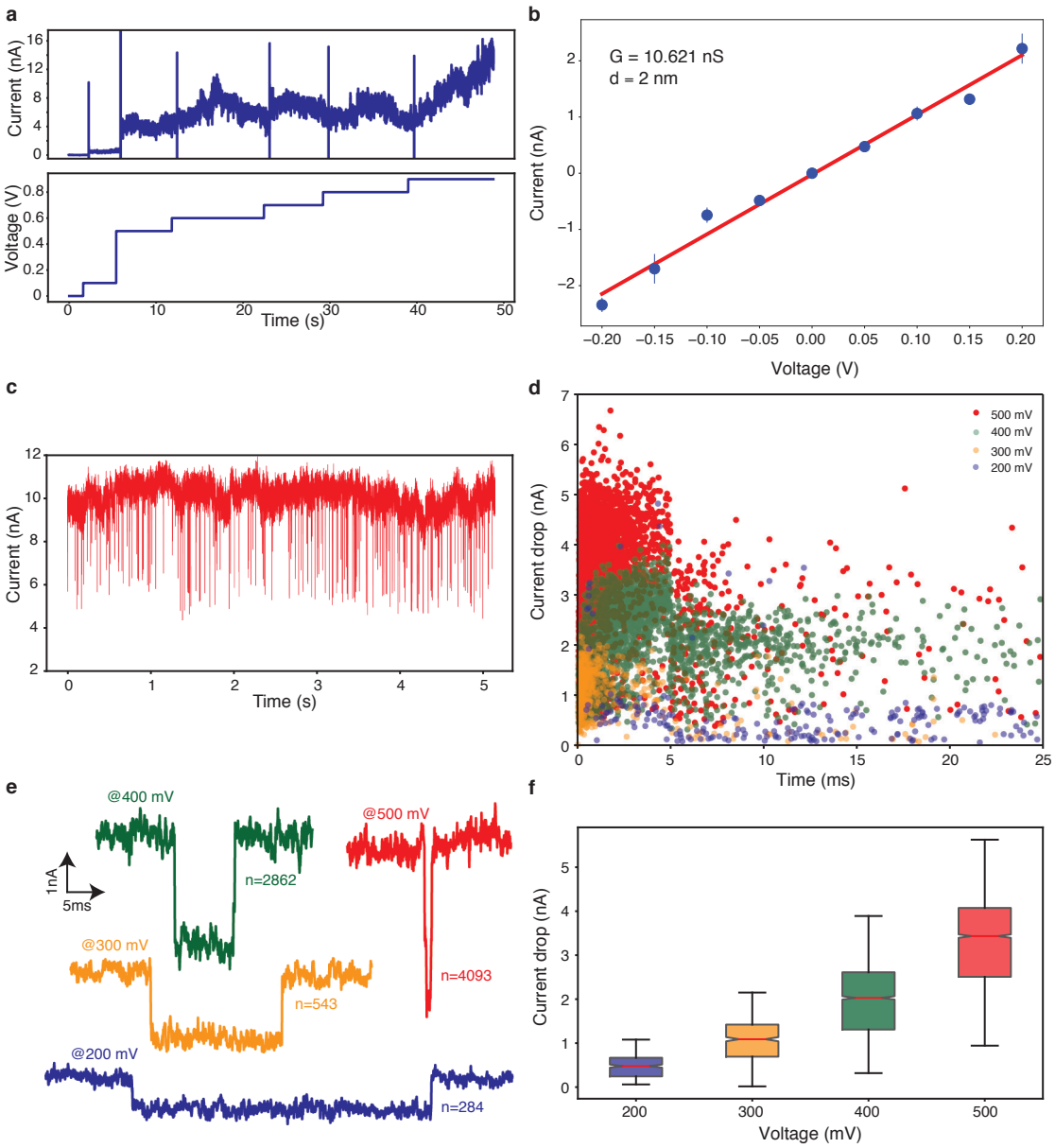

Figure 2.12 – Anticipated results: DNA translocations. **a**, The ECR trace used to create a nanopore. The sudden increase of the current at 900 mV is associated with a pore generation. **b**, The I-V curve used to estimate the pore size. **c**, A typical translocation trace in a 2 nm large pore recorded at a voltage of 500 mV. **d**, Scatter plot of current drop versus dwell time for different translocation voltages (color-coded). **e**, Example of a representative event for each voltage. The number of recorded translocations for each condition is reported next to trace. **f**, Boxplot of the current drops reported in **d**. The current drop increases linearly with the applied voltage. The red line indicates the median values, the upper and lower ends of the box denote the upper and lower quartile, whereas the whiskers encompass the rest of the data points. This is typically used to confirm that the observed events are translocations. *This Figure was published in Nature Protocols, 2019, Graf et al.*[50]

2.10.3 Osmotic power generation

Osmotic Power Generation. The application of MoS_2 nanopores for power generation relies on a salt concentration gradient. Substrate fabrication and the flow-cell set-up are identical to biomolecule detection experiments. After verifying the nanopore size at symmetrical 1 M / 1 M KCl condition, the current was set to zero (no osmotic pressure present). The *trans*-side was washed, and the buffer was replaced by 1 mM KCl to create a 1:1000 concentration ratio. The first thing to notice is that the previously zeroed current is now non-zero value. A net current from the more concentrated to the less concentrated side was thus established. I-V-curves taken in this condition show a prominent current offset. The electrode potential was then subtracted from the obtained value to retrieve the component due to osmotic pressure. Figure 2.11 shows the observed osmotic current (a) and voltage (b) values of a 5 nm MoS_2 nanopore. Typically, there is a saturation of the achievable osmotic power at a 1:100 concentration gradient, i.e. increasing the concentration gradient further does not significantly change the osmotic power generated.

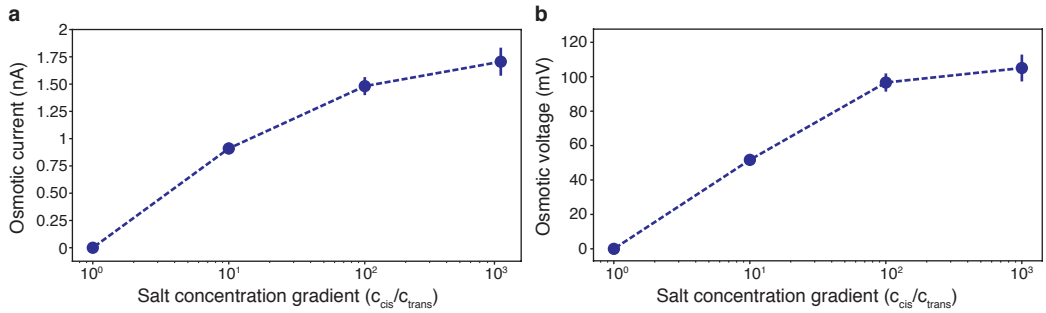

Figure 2.13 – Anticipated results: osmotic power generation. All data points are extracted from a linear fit to the I-V. A linear model that takes into account the measurement error (current) and the uncertainty on the applied voltage was used to extract standard deviation values of the slope and the offset.[170] The error bars are then calculated by propagating these standard deviation values by using a classical uncertainty propagation method as explained in detail in.[171] **a**, Osmotic current as a function of the salt concentration gradient (osmotic pressure). The osmotic current is defined as the net current at zero voltage generated by the **b**, The osmotic voltage as a function of the osmotic pressure. The osmotic voltage is defined as the voltage needed to counteract the osmotic current, i.e. the voltage at which the current is zero. *This Figure was published in Nature Protocols, 2019, Graf et al.*[50]

3 Blue Energy

This chapter is the preprint of:

Jiandong Feng[1], Michael Graf[1], Ke Liu[1], Dmitry Ovchinnikov[2], Dumitru Dumcenco[2], Mohammad Heiranian[3], Vishal Nandigana[3], Narayana R. Aluru[3], Andras Kis[2] and Aleksandra Radenovic[1]. **Single-layer MoS_2 nanopores as nanopower generators.** Nature 536, 197–200 (2016)

J.F. and A.R. conceived the idea, designed all experiments, and wrote the manuscript. J.F. and M.G. performed measurements and data analysis. J.F. and K.L. fabricated the nanopore device. D.O. fabricated the MoS_2 transistor and D.D. performed chemical-vapour-deposition MoS_2 growth under A.K.'s supervision. J.F. and D.O. demonstrated the self-powering of the nanosystem. M.H., V.N., and N.R.A. built the computational nanofluidics model and interpreted the simulation results. All authors provided constructive comments on the manuscript.

3.1 Summary

Power generation from the osmotic pressure difference between freshwater and seawater is an attractive, renewable and clean energy harvesting method.[172–174] An electrokinetic phenomenon known as streaming potential occurs when the electrolyte is driven through narrow pores either by a pressure gradient,[175] or an osmotic potential from a salt concentration gradient.[176] For this task, 2D material membranes are expected to be the most efficient since water transport through a membrane scales inversely with the membrane thickness.[176–178] Here, we demonstrate the use of single-layer molybdenum disulfide (molybdenum disulfide (MoS_2)) nanopores as osmotic nanogenerators. A large, osmotically induced current is observed from salt gradient with an estimated power density of up to $1 \times 10^6\,\mathrm{W\,m^{-2}}$ which

[1]Laboratory of Nanoscale Biology, Institute of Bioengineering, School of Engineering, EPFL, 1015 Lausanne, Switzerland
[2]Laboratory of Nanoscale Electronics and Structures, Institute of Electrical Engineering and Institute of Materials Science and Engineering, School of Engineering, EPFL, 1015 Lausanne, Switzerland
[3]Department of Mechanical Science and Engineering, Beckman Institute for Advanced Science and Technology, University of Illinois at Urbana-Champaign, Urbana, Illinois 61801, USA

can be attributed mainly to the atomically thin membrane of MoS_2. In addition, low power requirements for nanoelectronic and optoelectric devices can be provided by a neighboring nanogenerator that harvests energy from the local environment,[179–182] for example, piezoelectric zinc oxide nanowire arrays[179] and single-layer MoS_2.[183] Here, we use our MoS_2 nanopore generator to power a MoS_2 transistor, thus demonstrating a self-powered nanosystem.

3.2 Introduction

Compared to graphene, MoS_2 nanopores have already demonstrated better water transport behavior[28,105] due to enriched hydrophilic surface sites (molybdenum) after transmission electron microscopy (TEM) irradiation[184] or electrochemical oxidation.[30] The osmotic power is generated by separating two reservoirs containing potassium chloride (KCl) solutions with different concentrations with a freestanding MoS_2 membrane into which a single nanopore has been introduced.[28] A chemical potential gradient arises at the interface of these two liquids at a nanopore in a 0.65 nm thick single-layer MoS_2 membrane and drives ions spontaneously across the nanopore, forming an osmotic ion flux towards an equilibrium state, as shown in Figure 3.1a. The presence of surface charges on the pore screens the passing ions by their charge polarity and thus results in a net measurable osmotic current, known as reverse electrodialysis.[172] This cation selectivity can be better understood by analyzing the concentration of each ion type (potassium (K^+) and chloride (Cl^-)) as a function of the radial distance from the center of the pore, as shown in the simulation results from molecular dynamics (MD) (Figure 3.1b). MoS_2 nanopores were fabricated either by TEM[28] (Figure 3.1c) or by the recently demonstrated electrochemical reaction (electrochemical reaction (ECR)) technique.[30] With a typical nanopore diameter in the 2 nm to 25 nm range, a stable osmotic current can be expected due to the long time required for the system to reach its equilibrium state. The osmotic current and voltage across the pore were measured by using a pair of Ag/AgCl electrodes to characterize the current-voltage (I-V) response of the nanopore.

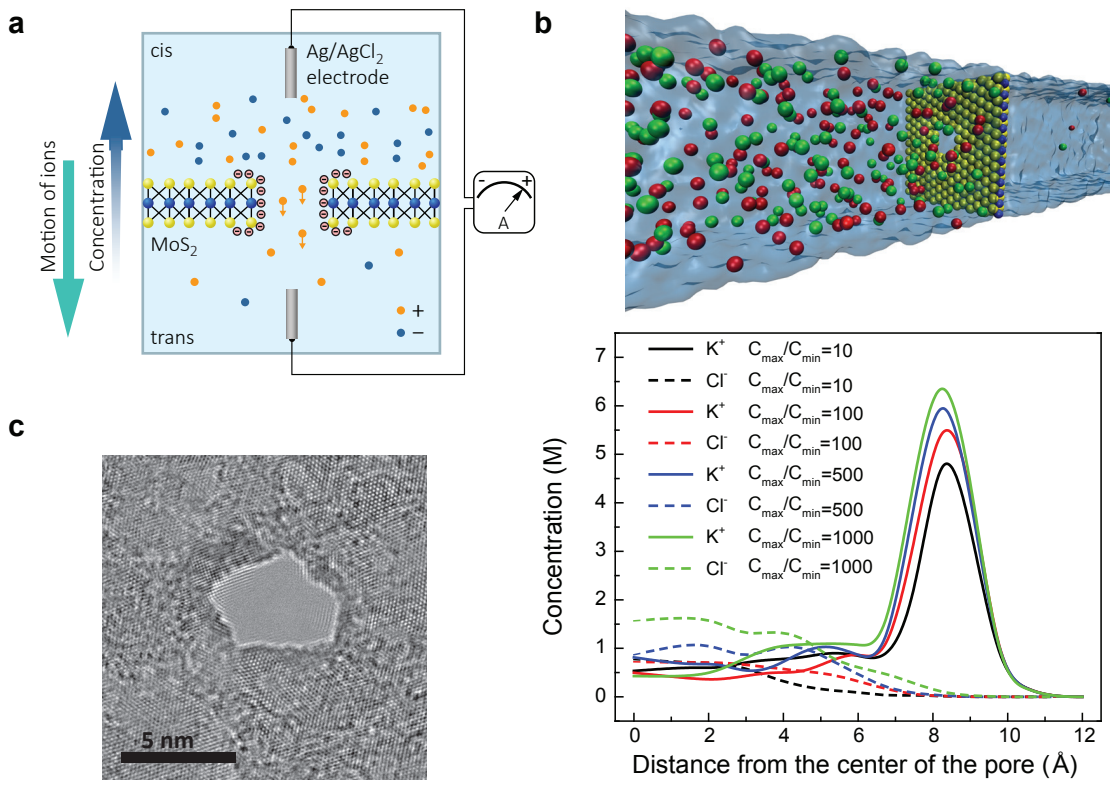

Figure 3.1 – Operation schematic of osmotic energy harvesting with MoS_2 nanopores. **a**, Solutions with different concentrations are separated by a 0.65 nm thick MoS_2 nanopore membrane. An ion flux driven by chemical potential (voltage, concentration, liquid-liquid junction, pH) through the pore is screened by the negatively charged pore, forming a diffusion current composed of mostly positively charged ions. **b**, Top panel: schematic of a typical simulation box used in MD simulations. Bottom panel: MD simulated K^+ and Cl^- concentrations as a function of the radial distance from the center of the pore. The region near the charged wall of the pore is representative of the ionic double layer. C_{max}, maximum concentration. C_{min}, minimum concentration. **c**, Example of a TEM-drilled 5 nm MoS_2 nanopore. *This Figure was published in Nature, 2016, Feng et al.*[171]

3.3 Results

To gain a better insight into the performance of the MoS_2 nanopore power generator, we first characterized the ionic transport properties of MoS_2 nanopores under various ionic concentration and pH conditions, which can provide information on the surface charge of the MoS_2 nanopore. Figure 3.2a shows I-V characteristics of MoS_2 nanopores with various diameters. Large pore conductance originates from the ultrathin membrane. The conductance also depends on salt concentration (Figure 3.2b) and shows saturation at low salt concentrations which is a signature of the presence of surface charge on the nanopore.[185,186] The predicted pore conductance (G) taking into account surface charge ($\sum$) contribution is given by:[57]

$$G = \kappa_b \left[\frac{4l}{\pi d^2} + \frac{1}{1 + 4\frac{l_{Du}}{d}} + \frac{2}{\alpha d + \beta l_{Du}} \right]^{-1} \tag{3.1}$$

where κ_b is the bulk conductivity; L is the pore length, d is the pore diameter; l_{Du} is the Dukhin length which can be approximated by $l_{Du} \approx \frac{|\Sigma|/e}{2c_s}$; e is the elementary charge and c_s is the salt concentration; α is a geometrical prefactor that depends on the model used ($\alpha = 2$);[57] β can also be approximated to be 2 to obtain the best fitting agreement.[57] From the fitting results shown in Figure 3.2b, a surface charge value of –0.024 C m^{-2}, –0.053 C m^{-2} and –0.088 C m^{-2} is found for three size pores of 2 nm, 6 nm and 25 nm at pH 5, respectively. This result is comparable to the recently reported charge of graphene nanopores (–0.039 C m^{-2}[187] and nanotubes (–0.025 C m^{-2} to –0.125 C m^{-2})[176] at pH 5. The surface charge density can be further modulated by adjusting pH to change the pore surface chemistry (Figure 3.2c). The conductance increases with the increase of pH, suggesting the accumulation of more negative surface charges in MoS_2 nanopore. The simulated conductance from equation (Equation 3.1) at 10 mM is linearly proportional to the surface charge values, thus pH changes could significantly improve the surface charge up to the range of –0.3 C m^{-2} to –0.8 C m^{-2}. The chemical reactivity of MoS_2 to pH is also supported by previously reported zeta potential measurements on MoS_2.[188] However, similar to other nanofluidic systems,[176,187] we also notice that the surface charge density varies from pore to pore, which means that different pores can have disparate values of equilibrium constant due to the various combinations of Mo and S atoms[105] at the edge of the pore, as illuminated by MD simulations.[178]

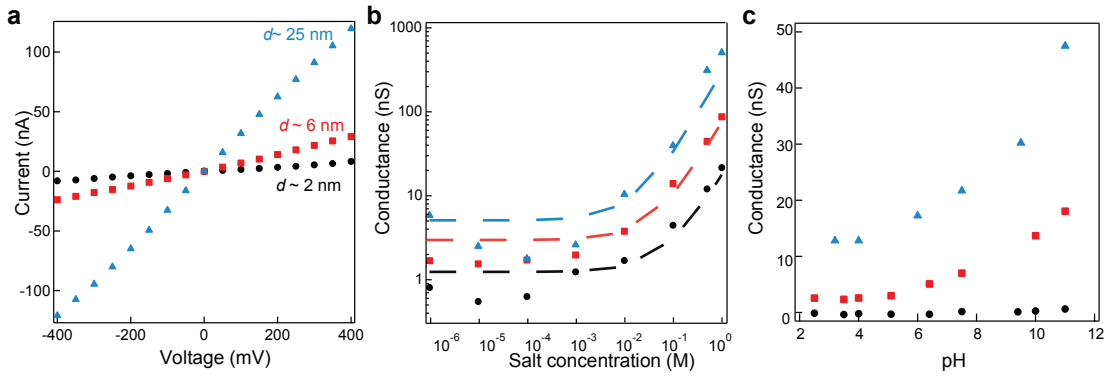

Figure 3.2 – Electrical conductance and chemical reactivity of the MoS_2 nanopore. **a**, Current-voltage response of MoS_2 nanopores with different pore sizes (2 nm in black, 6 nm in red and 25 nm in blue) in 1 M KCl at pH 5. **b**, Conductance as a function of salt concentration at pH 5. By fitting to the equation Equation 3.1, the extracted surface charge values are –0.024 C m^{-2}, –0.053 C m^{-2} and –0.088 C m^{-2} for a 2 nm, 5 nm and 25 nm pore, respectively. **c**, Conductance as a function of pH for 10 mM KCl for a 2 nm, 6 nm and 25 nm pore, respectively. *This Figure was published in Nature, 2016, Feng et al.*[171]

Next, we introduced the chemical potential gradient system by using the KCl concentration gradient system. The concentration gradient ratio is defined as $\frac{c_{\text{cis}}}{c_{\text{trans}}}$, where c_{cis} is KCl concentration in the *cis* chamber and c_{trans} in the *trans* chamber, ranging from 1 mM to 1 M. The highly negatively charged surface selectively passes the ions by their polarity (in this case K^+ ions), resulting in a net positive current. By measuring the I-V response of the pore in the concentration gradient system, Figure 3.3a, we can measure the short-circuit (I_{sc}) current corresponding to zero external bias while the osmotic potential can be obtained from

the open-circuit voltage (V_{oc}). The pure osmotic potential V_{os} and current I_{os} can be then obtained by subtracting the contribution from electrode-solution interface at different concentrations which follows the Nernst equation[176,189] (Figure S3.1). The osmotic potential is proportional to the concentration gradient ratio (Figure 3.3b) and shares a similar trend with the osmotic current (Figure 3.3c). The measured osmotic energy conversion is also pH dependent, as shown in Figure S3.2a,b. The increase of pH leads to higher generated voltage and current, suggesting the importance of surface charge on the ion-selective process. The extracted osmotic potential is the diffusion potential and it arises from the differences in the diffusive fluxes of positive and negative ions, due to the ion-selective property of the pore where cations diffuse more rapidly than anions (Figure 3.1). The diffusion potential, V_{diff} can be described as:[189]

$$\mathrm{V_{diff}} = \mathrm{S(\Sigma)_{is}} \frac{\mathrm{RT}}{\mathrm{F}} \ln \left[\frac{\mathrm{a_{KCl}^{cis}}}{\mathrm{a_{KCl}^{trans}}} \right] \tag{3.2}$$

where $S(\Sigma)_{is}$ is the ion selectivity[190] for the MoS_2 nanopore (equal 1 for the ideal cation selective case and 0 for the non-selective case), defined as $S(\Sigma)_{is} = t_+ - t_-$, where t_+ and t_- are the transference numbers for positively and negatively charged ions respectively. F, R, T are the Faraday constant, the universal gas constant, and the temperature, while a_{KCl}^{cis} and a_{KCl}^{trans} are the activities of K^+ ions in the *cis* and *trans* solutions. By fitting the experimental data presented in Figure 3.3b to equation Equation 3.2, the ion selectivity coefficient is found to be 0.4, suggesting efficient cation selectivity. This is because the size of our nanopores lies in the range where the electrical double layer overlap can occur inside the pore[186] since the Debye length λ_D = 10 nm for 1 mM KCl. As shown in Figure S3.3d, with the concentration gradient of 10 mM / 1 mM in a 5 nm pore, the ion selectivity approaches nearly 1, presenting the conditions for the ideal cation selectivity.[190] To further test the cation-selective behavior of the pore, we also investigated the relationship between power generation and the pore size. As shown in Figure 3.3d, small pores display better voltage behavior, indicating the better performance on ion selectivity. The ion selectivity $S(\Sigma)_{is}$ decreases from 0.62 to 0.23 as the pore size increases. The surface potential distribution for different pore sizes (2 nm, 5 nm and 25 nm) is calculated to compare the selectivity difference (Figure S3.3a, b and c). It has been proven that the net diffusion current only stems from the charge separation and concentration distribution within the electrical double layer[191] and therefore, the total current can be expected to increase more rapidly within the double layer overlap range compared to larger pore sizes (Figure 3.3d). The slight decrease might be attributed to reduced local concentration gradient in the larger pore and also to probable overestimation of the redox potential subtraction. The current can be calculated using either a continuum based Poisson-Nernst-Planck (PNP) model or MD simulations. The measured dependence of the osmotic potential and osmotic current as a function of the concentration ratios (Figure 3.3b, c) is well captured by both computational models (MD prediction in Figure S3.4 and continuum analysis in Figure S3.5). In addition to possible depletion of local concentration gradient in large pores, the non-monotonic response to pore size (Figure 3.3d, Figure S3.2c, d) is also predicted by continuum-based PNP

model (Figure S3.5b), as a result of the decrease of ion selectivity. In order to gain further insight into the thickness scaling, we first verified the pore conductance relation proposed in equation Equation 3.1 using MD (Figure S3.6). Interestingly, the ion mobility is also found to scale inversely with membrane thickness (Figure S3.7a, b), which may conform to the previous observations.[192] We then performed MD simulations of multilayer membranes of MoS_2 to investigate the power generated by those membranes. We observe a strong decay of the generated power as the number of layers is increased (Figure S3.7c, d), indicating the ultimate osmotic power generation in 2-dimensional membranes. The consistency between experiments and theoretical model highlights two important contributions playing key roles for achieving efficient power generation from a single-layer MoS_2 nanopore: atomic-scale pore thickness and the surface charge.

Assuming a single-layer MoS_2 membrane with homogeneous pore size of 10 nm and porosity of 30 %, by exploiting parallelization, the estimated power density would reach $10^6\,\mathrm{W\,m^{-2}}$ with KCl salt gradient. These values exceed by 2 to 3 orders of magnitudes results obtained with boron nitride nanotubes[176] and are million times higher than reverse electrodialysis with classical exchange membranes,[172] as detailed in Table S3.1.

Apart from KCl salt concentration gradients, the nanopore power generator concept can also be applied to liquid-liquid junction systems with a chemical potential gradient, since the diffusion voltage originates from the Gibbs mixing energy of the two liquids. This will allow exploring high-performance nanopore-based generators based on a large number of available liquid combinations.[191] For example, we showed a large power generation based chemical potential gradient from two types of liquids.

Considerable energy could be generated by exploiting parallelization with multiple small pores or even a continuous porous structure with a large area of single-layer MoS_2 membrane,[156] which can be scaled up for mass-production using the recently reported ECR pore fabrication technique[30] or oxygen plasma-based defect creation.[47] On the other hand, the use of individual nanopores as a micro/nano power source has also been expected since a long time.[189] Here, we demonstrate that an individual osmotic generator can also serve as a nanopower source for a self-powered nanosystem due to its high efficiency and power density. For the nanoelectronic device, we choose the recently demonstrated high-performance single-layer MoS_2 transistor (Figure 3.4) due to its excellent operation in low power range.[113] We characterize the single-layer MoS_2 transistor in the configuration schematically shown in Figure 3.4b, where we use two nanopores to apply voltages to the drain and gate terminals of the transistor. As shown in Figure 3.4c, varying the top gate voltage in the relatively narrow window of $\pm 0.78\,\mathrm{V}$, we could modulate the channel conductivity by a factor of 50 to 80. Furthermore, we fix the gate voltage and vary the drain-source voltage V_s, as shown on Figure 3.4c (inset) and obtain a linear I_s-V_s curve demonstrating efficient injection of electrons into the transistor channel. Further calibration with a standard power source can be found in Figure S3.8. This system is an ideal self-powered nanosystem in which all the devices are based on single-layer MoS_2.

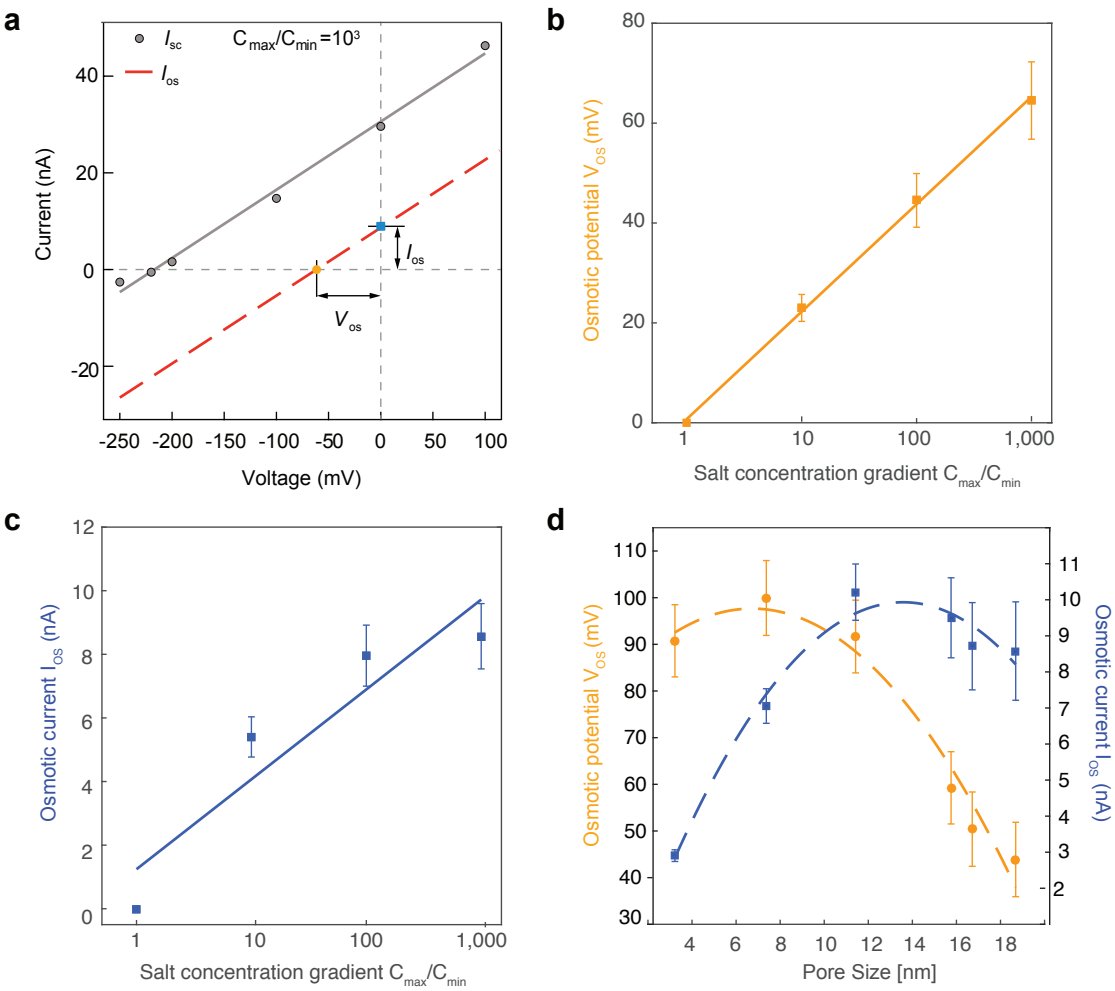

Figure 3.3 – Osmotic power generation. **a**, Current-voltage characteristics for a 15 nm nanopore in 1 M / 1 mM KCl salt gradient condition. Contribution from the redox reaction on the electrodes is subtracted (Figure S3.1) and leads to the red dashed line which represents pure osmotic contribution. I_{sc} and V_{oc} are the short circuit current and open circuit voltage, whereas I_{os} and V_{os} are the osmotic current and potential. **b**, Generated osmotic potential, as a function of salt gradient. C_{cis} is set to be 1 M KCl and C_{trans} is tunable from 1 mM to 1 M KCl. Solid line represents linear fitting to the equation Equation 3.2. **c**, Osmotic current vs. salt gradient. Solid line fits to the linear part. **d**, Osmotic potential and current as a function of pore size. Dashed lines (a guide to the eye) show the trend as the pore size is changed. Error bars come from the corresponding error estimation (section 3.4). *This Figure was published in Nature, 2016, Feng et al.*[171]

We have shown that MoS_2 nanopores are promising candidates for investigating osmotic power generation for future renewable blue energy. The giant generated power can be mainly attributed to the ultimate atomic-scale thickness of the MoS_2 membrane. These results also provide new avenues for studying other types of membrane-based processes, such as water desalination[178] or proton transport.[193] On the other hand, the nanopore generator may also find applications for other ultra-low power devices, with potential use in future electronics.

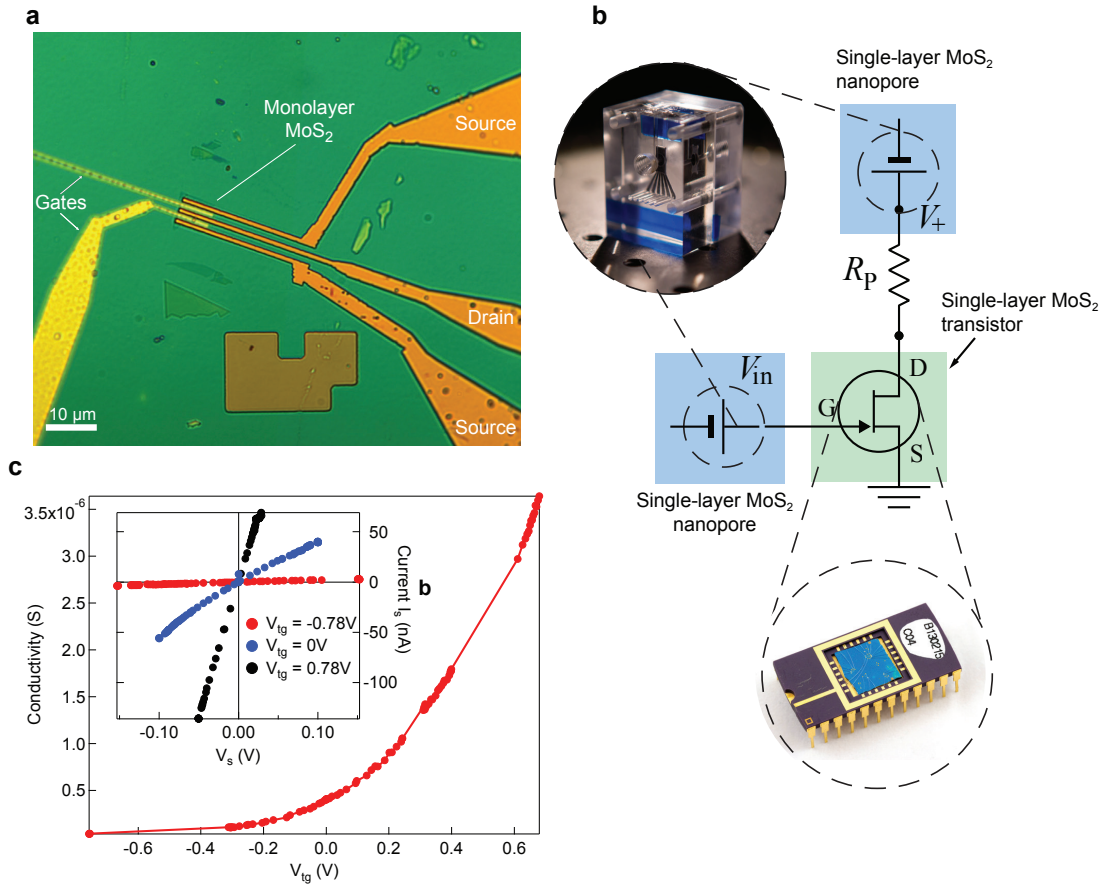

Figure 3.4 – Demonstration of a self-powered nanosystem. a, Optical image of the fabricated MoS_2 transistor with a designed gate, drain and source electrodes. **b**, Circuit diagram of the self-powered nanosystem where the drain-source supply for MoS_2 transistor is provided by a MoS_2 nanopore while a second nanopore device operates as the gate voltage source. R_p, pore resistance. V_{in}, gate voltage, V^+, drain-source voltage. G, gate. S, source. D, drain. **c**, Powering all the terminals of the transistor with nanopore generators. V_{tg}, top gate voltage. *This Figure was published in Nature, 2016, Feng et al.*[171]

3.4 Methods

3.4.1 Nanopore fabrication

The MoS_2 nanopores used in this work are fabricated either using the recently reported atomic-scale nanopore fabrication technique based on ECR[30] or electron irradiation under TEM.[28] Prior to nanopore fabrication, we create freestanding MoS_2[154] membrane. Briefly, potassium hydroxide (KOH) wet etching is used to prepare silicon nitride (SiN_x) membranes (10 µm × 10 µm to 50 µm × 50 µm, 20 nm thick). Focused ion beam (FIB) or e-beam lithography (followed by reactive ion etching (RIE)) is used to drill a 50 nm to 300 nm opening on the membrane. chemical vapor deposition (CVD)-grown single-layer MoS_2 membranes are suspended on the FIB drilled opening window by transferring from sapphire growth

substrates.[154] TEM irradiation can be applied to drill a single pore and image the pore. ECR is done by applying a step-like transmembrane potential to the membrane and monitoring the transmembrane ionic current with a FEMTO DLPCA-200 amplifier (FEMTO Messtechnik GmbH) with a custom-made feedback control on transmembrane conductance. Nanopores are formed when reaching the critical voltage of MoS_2 oxidation (>0.8 V). Then the pore size is calibrated using current-voltage (IV) characteristics.

3.4.2 Nanofluidic measurements

Nanofluidic transport experiments are performed using the setup described previously.[28] The nanopore chips are mounted in the custom-made poly(methyl methacrylate) (PMMA) chamber, and then wetted with H_2O:ethanol solution (1:1). Nanofluidic measurements are performed by taking the I-V characteristics of the nanopore in salty solutions of KCl (Sigma Aldrich, various ionic concentration or pH conditions) using an Axopatch 200B patch-clamp amplifier (Molecular Devices, Inc. Sunnyvale, CA). A pair of chlorinated Ag/AgCl electrodes which has been rechlorinated regularly is used to apply voltage and measure the current. In addition, the electrode potential differences in solutions of different concentration were calibrated with a saturated Ag/AgCl reference electrode (Sigma Aldrich). To measure osmotic power generation, the reservoirs are filled with solutions of different concentrations with a range from 1 mM to 1 M. Measurements are performed at various pH conditions. Optimized generation was found for pH = 11. First, we measure the I-V response and the measured short circuit current is obtained from the interception of the curve at zero voltage, while the measured open-circuit voltage is found from zero current interception. Next, to get the pure osmotically-driven contribution, we subtract the contribution from an electrode-potential difference due to redox potential in different concentrations, as shown in Figure S3.1. For all the experiments, we performed cross-checking measurements including the changing direction of pH and concentration to make sure the nanopores are not significantly enlarged during the experiments. Most MoS_2 pores are generally stable during hours of experiments due to their high mechanical strength and stability within the ±600 mV bias range. For this reason, we strongly recommend the use of small supporting FIB opening windows (50 nm to 300 nm) for suspended membranes.

3.4.3 Characterization of single-layer MoS_2 transistors

Single-layer MoS_2 transistors were fabricated using a procedure similar to previously published reports.[113] For electrical measurements, we used Agilent 5270B SMU, SR-570 low noise current preamplifier, and Keithley 2000 DMM. For electrical measurements we have used Agilent 5270B SMU, SR-570 low noise current preamplifier and Keithley 2000 DMM (input impedance $>10^{10}$ Ω). All measurements were performed in ambient conditions in dark. Improved efficiency of power conversion in nanopores is obtained by using a combination of pure room-temperature ionic liquids $BminPF_6$ and zinc chloride solution. We compare the performance of single-layer MoS_2 transistor in two cases: (i) we use two nanopores to apply

V_{tg} and V_s, while using current amplifier and voltmeter to control the current and voltage drop across the device (schematic of the setup is presented on Figure S3.8a, (ii) we use source-meter unit (SMU) to perform standard two-contact measurements. In case (i) we used voltage dividers to change the source and gate voltage on the device (not shown on schematics). Furthermore, we compare the case (i) and (ii). Although the characteristics of our transistor with both setups are similar, we comment on the difference in the ON state conductivity. We attribute it to the slow response of the device in case (i) of nanopore measurements. The change of transistor resistance by application of gate voltage leads to impedance change of the device and thus the applied effective voltage V_{dev} (measured with a voltmeter connected in parallel). Nanopore reacts on change of impedance with certain stabilization time (from 10 s to 100 s). This appears to be a hysteretic effect and influences the conductivity vs. gate voltage measurements. In case (ii) on the other hand $V_{dev} = V_s$ is constant. There are a number of secondary effects, which might, in turn, influence the measured values of two-probe conductivity. In relatively short channel devices applied V_s might partially contribute to gating of the channel and furthermore to modification of contact resistance. This could be understood comparing the values of V_s (around 100 mV) and V_{tg} (780 mV). We also do not exclude slight doping variations and hysteretic effects due to the filling of trap states inside the transistor channel. On the other hand, driving a device to the ON state and stabilizing the current for a reasonable amount of time, we could get a very good match in drain-source current-voltage I_s-V_s characteristics, as shown on Figure S3.8c. We thus conclude that although there are differences in performance in both cases which originate mainly from the slow response time of nanopore.

We extracted the resistance and the power of the nanopore with ionic liquid BminPF$_6$. From the consideration of the simple resistor network, sketched on Figure S3.8d (inset), we could extract the output power as a function of load resistance R_{load}. We fit our dependence with the model, which assumes the constant V_{out} and R_{pore}:

$$\text{Power} = \frac{V_{out}^2 R_{load}}{(R_P + R_{load})^2} \tag{3.3}$$

and found good fit with the $V_{out} = 0.83$ V, which is close to measured voltage $V_{out} = 0.78$ V and nanopore impedance $R_P = (9.4 \pm 2.1)$ MΩ as shown in Figure S3.8d.

3.4.4 Data analysis

All data analysis has been performed using custom-made Matlab (R2016a) code. First, current-voltage characteristics have been recorded using an Axopatch 200B amplifier either by using an automatic or manual voltage switch. The current trace was then segmented into pieces of constant voltage. The mean $\mu(v)$ and standard deviation $\sigma(v)$ of the stable part of each segment is extracted and an I-V plot generated. The error bars on the I-V plots are the standard

deviation described above. All I-V characteristics were linear. In order to propagate the error correctly, we used a linear fitting method.[170] Using this method, we can extract a, b, σ_a and σ_b of the first order polynomial $I(V) = b \cdot V + a$. The conductance is the slope b of the I-V and a describes the offset. The height of the error-bars reported for conductance measurements is $2 \cdot \sigma_b$. The osmotic power generation is reported using osmotic current I_{os} and osmotic voltage V_{os}. Starting from the linear fit values of the I-V plot, we can calculate the measured current and voltage: $I_{\text{meas}} = a$ and $V_{\text{meas}} = \frac{a}{b}$. These measured values have to be adjusted for the electrode potential: $V_{\text{os}} = V_{\text{meas}} - V_{\text{redox}}$ and $I_{\text{os}} = \frac{V_{\text{os}}}{V_{\text{meas}}} \cdot I_{\text{meas}}$. Assuming an uncertainty of the redox potential σ_{redox} estimation of 5 %, we can propagate the errors using the following formulas:[194]

$$\sigma_{V_{os}} = \sqrt{\left(\frac{1}{b}\sigma_a\right)^2 + \left(\frac{a}{b^2}\sigma_b\right)^2 + \sigma_{\text{redox}}^2} \tag{3.4}$$

$$\sigma_{I_{os}} = \sqrt{\sigma_a^2 + (V_{\text{redox}}\sigma_b)^2 + b^2\sigma_{\text{redox}}^2} \tag{3.5}$$

The error bars reported in osmotic voltage and current plots are calculated using above relations.

3.4.5 Computational simulations: molecular dynamics and continuum models

MD simulations were performed using the LAMMPS package.[195] A MoS_2 membrane was placed between two KCl solutions as shown in Figure S3.4a. A fixed graphene wall was placed at the end of each solution reservoir. A nanopore was drilled in MoS_2 by removing the desired atoms. The accessible pore diameter, considered in most of the simulations, is 2.2 nm with a surface charge density of $-0.4694\,\text{C}\,\text{m}^{-2}$. The system dimensions are 6 nm × 6 nm × 36 nm in x, y, and z, respectively. The SPC/E water model was used and the SHAKE algorithm was applied to maintain the rigidity of each water molecule. The Lennard Jones cutoff distance was 12 Å. The long-range interactions were computed by the particle particle particle Mesh (PPPM).[196] Periodic boundary conditions were applied in the x and y directions. The system is non-periodic in the z direction. For each simulation, first, the energy of the system was minimized for 10,000 steps. Next, the system was equilibrated in constant number, pressure and temperature (NPT) ensemble for 2 ns at a pressure of 1 atm and a temperature of 300 K to reach the equilibrium density of water. Graphene and MoS_2 atoms were held fixed in space during the simulations. Then, NVT simulations were performed where the temperature was maintained at 300 K by using the Nosè-Hoover thermostat with a time constant of 0.1 ps.[197,198] Trajectories of atoms were collected every picosecond to obtain the results. For accurate mobility calculations, however, the trajectories were stored every ten femtoseconds. We also use continuum based 2D PNP model. In this model, we neglect the contribution of H^+ and OH^- ions in the current calculation as its concentration is much lower compared to the bulk concentration of the ionic species. Hence, the water dissociation effects are not considered

in the numerical model. Further, we assume that the ions are immobile inside the Steric layer and do not contribute to the ionic current. We also do not model the Faradaic reactions occurring near the electrode. Finally, we also assume that the convective component of current originating from the fluid flow is negligible and does not contribute to the non-monotonic osmotic current observed in the experiments. We validate this assumption by performing detailed all-atom MD simulations and predict the contribution of electroosmotic velocity in comparison to the drift velocity of the ions. Under these assumptions, the total flux of each ionic species (Γ_i) is contributed by a diffusive component resulting from the concentration gradient and an electrophoretic component arising due to the potential gradient as given by $\Gamma_i = -D_i \nabla c_i - \Omega_i z_i F c_i \nabla \phi$, where F is Faraday's constant, z_i is the valence, D_i is the diffusion coefficient, Ω_i is the ionic mobility, c_i is the concentration of the ith species and ϕ is the electrical potential. Note that the ionic mobility is related to the diffusion coefficient by Einstein's relation, $\Omega_i = \frac{D_i}{RT}$, where R is the ideal gas constant and T is the thermodynamic temperature. The mass transport of each ionic species is: $\frac{dc_i}{dt} = -\nabla \cdot \Gamma_i$. The individual ionic current (I_i) across the reservoir and the pore is calculated by integrating their respective fluxes over the cross-sectional area, i.e., $I_i = \int z_i F \Gamma_i dS$. The total ionic current at any axial location is calculated as, $I = \sum_{i=1}^{m} z_i F \Gamma_i dS$, where S is the cross-sectional area corresponding to the axial location and is the number of ionic species. In order to determine the electric potential along the system, we solve the Poisson equation, $\nabla \cdot (\epsilon_r \nabla \phi) = -\frac{\rho_e}{\epsilon_0}$, where ϵ_0 is the permittivity of free space, ϵ_r is the relative permittivity of the medium and ρ_e is the net space charge density of the ions defined as, $\rho_e = F \sum_{i=1}^{m} z_i F c_i$. We provide the necessary boundary conditions for the closure of the problem. The normal flux of each ion is assumed to be zero on all the walls so that there is no leakage of current. To conserve charge on the walls of the pore, the electrostatic boundary condition is given by, $\mathbf{n} \cdot \nabla \phi = \frac{\sigma}{\epsilon_0 \epsilon_r}$, where $\mathbf{n}$ denotes the unit normal vector (pointing outwards) to the wall surface and σ is the surface charge density of the walls. The bulk concentration of the *cis* reservoir is maintained at $C_{\max}$ and the bulk concentration on the *trans* reservoir is maintained at $C_{\min}$. As we are interested to understand the osmotic short-circuit current, I_{sc}, we do not apply any voltage difference across the reservoirs. Thus, the boundary conditions at the ends of the *cis* and *trans* are specified as, $c_i = C_{\max}, \phi = 0$ and $c_i = C_{\text{in}}, \phi = 0$. The coupled PNP equations are numerically solved using the finite volume method in OpenFOAM (OpenField Operation and Manipulation). The details regarding the solver implementation are discussed in our earlier works.[199–201] The simulated domain consists of a MoS_2 nanopore of length L_n and diameter d_n varying from 2.2 nm to 25 nm. The simulated length of the reservoir is $L_{\text{cis}} = L_{\text{trans}} = 100$ nm and the diameter of the reservoir is 50 nm. KCl buffer solution is used in the simulation. The bulk concentration of the *cis* reservoir was fixed at 1 M and the concentration in the *trans* reservoir was systematically varied from 1 mM to 1 M. The simulation temperature is T = 300 K. The bulk diffusivities of K^+ and Cl^- are 1.96×10^{-9} m^2 s^{-1} and 2.03×10^{-9} m^2 s^{-1}. The dielectric constant of the aqueous solution is assumed to be $\epsilon_r = 80$. We also assume zero surface charge density on the walls of the reservoir, as the reservoir is far away from the nanopore to have an influence on the transport. Unless otherwise stated, the charge on the walls of the MoS_2 nanopore is assumed to be $\sigma_n = -0.4694$ C m^{-2}, consistent with the surface charge calculated

from our MD simulations.

3.5 Supplementary Figures and Tables

Reverse electrodialysis cell	P ($W\,m^{-2}$)	Membrane thickness
Weinstrin and Leitz, 1976[202]	0.17	1 mm
Audinos, 1983[203]	0.40	3 mm
Turek and Bandura, 2007[203]	0.46	0.19 mm
Suda et al., 2007[203]	0.26	1 mm
Veerman et al., 2009[203]	0.95	0.2 mm
Kim et al., 2010[189]	7.7	0.14 mm
Siria et al., 2013[176]	4000	1 µm
This work	10^6	0.65 nm
Multilayer MoS_2 (MD)	30000	7.2 nm

Table S3.1 – Membrane thickness vs. power generation. *This Figure was published in Nature, 2016, Feng et al.*[171]

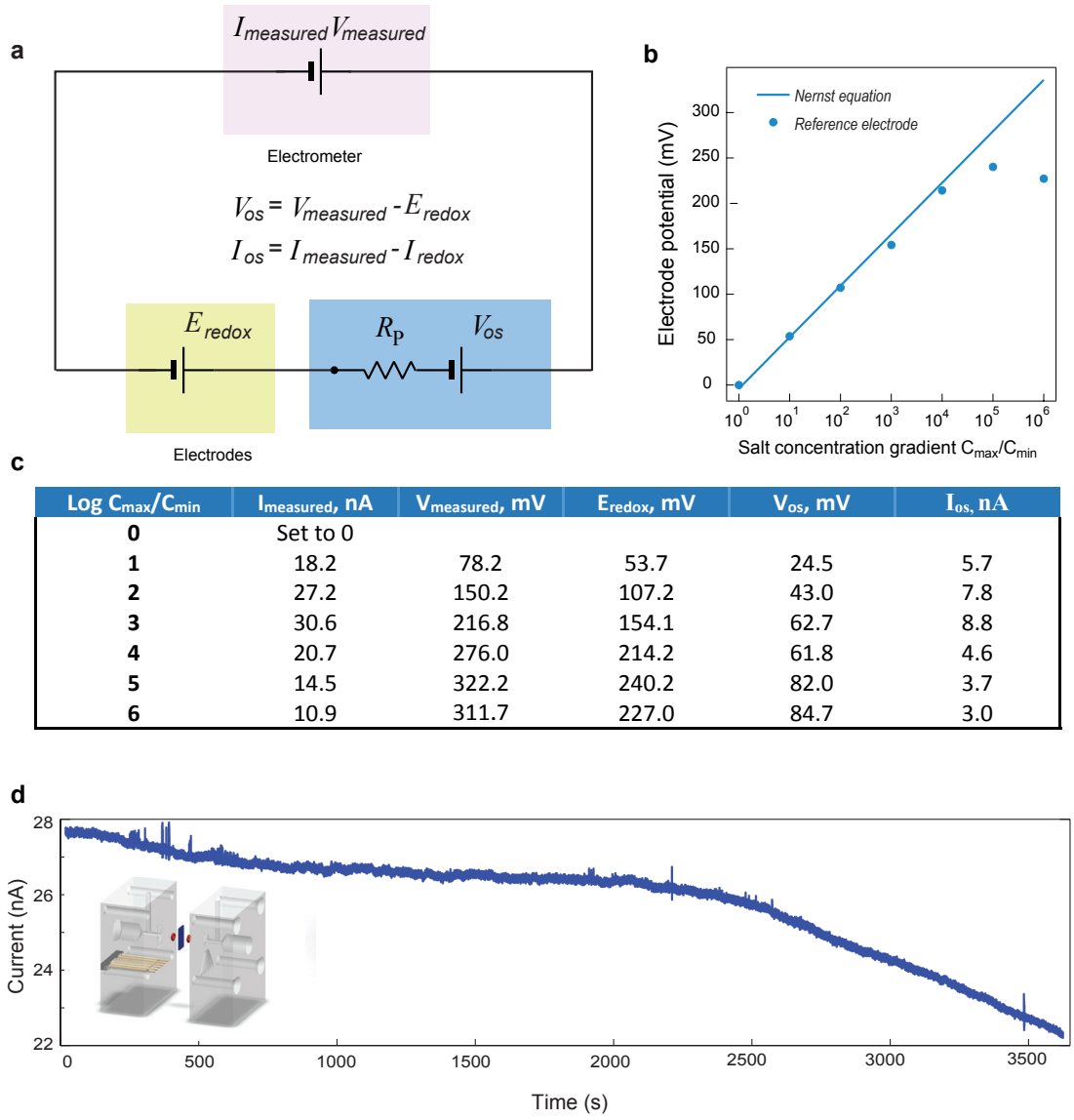

Log C_{max}/C_{min}	$I_{measured}$, nA	$V_{measured}$, mV	E_{redox}, mV	V_{os}, mV	I_{os}, nA
0	Set to 0				
1	18.2	78.2	53.7	24.5	5.7
2	27.2	150.2	107.2	43.0	7.8
3	30.6	216.8	154.1	62.7	8.8
4	20.7	276.0	214.2	61.8	4.6
5	14.5	322.2	240.2	82.0	3.7
6	10.9	311.7	227.0	84.7	3.0

Figure S3.1 – The subtraction of electrode contribution and stability of nanopore generator. **a**, Schematic diagram that details the contributions to the overall measured current. Osmotic contribution is obtained by subtracting electrode potential contribution. **b**, Electrode contribution: Values obtained from Nernst equation (line) and measured electrode redox potential difference by reference electrode (dots). **c**, Data table used for the subtraction. **d**, One-hour ionic current trace displaying a stability of a 14 nm pore in 1 M KCl/1 mM KCl. Inset, the design of the fluidic cell. *This Figure was published in Nature, 2016, Feng et al.*[171]

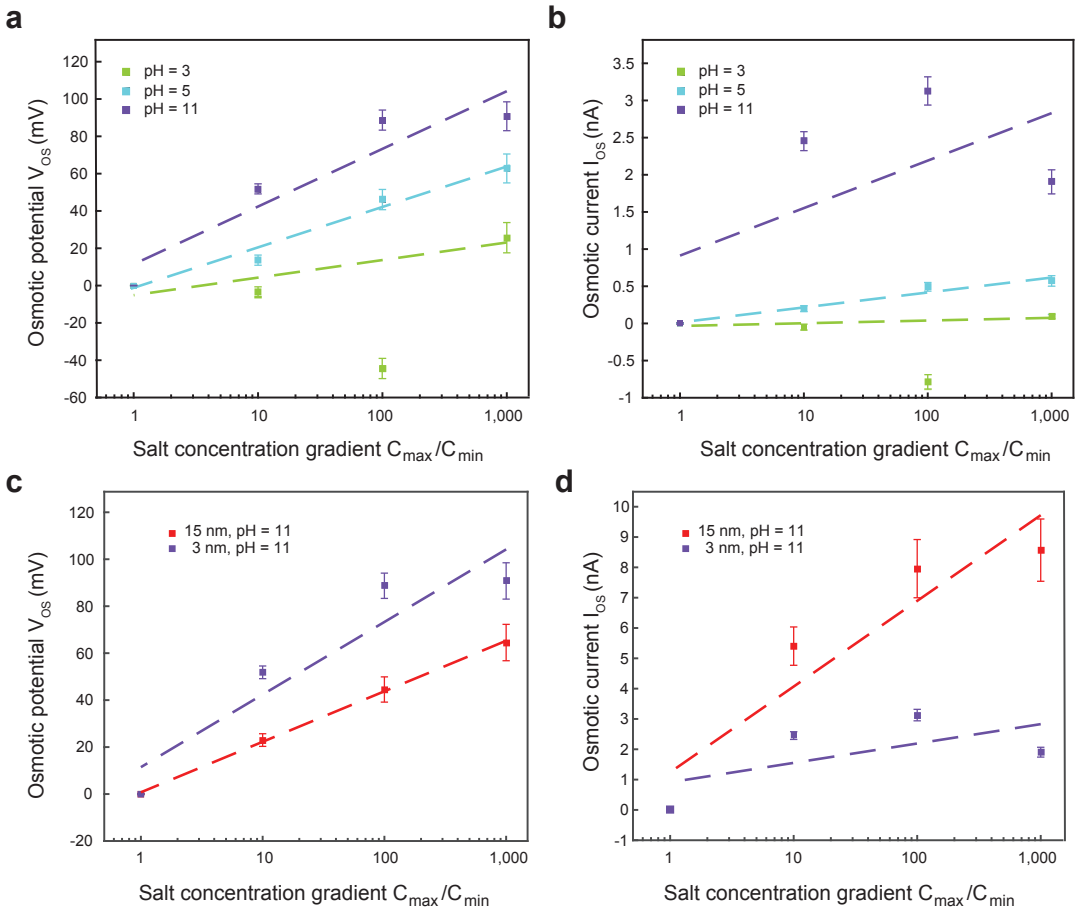

Figure S3.2 – pH and pore size-dependent osmotic power generation. **a** (potential) and **b** (current), Power generation for a 3 nm pore under different pH conditions (3, 5, 11) and under different concentration gradient conditions. We noticed the power generation at pH 3 is very low and may fluctuate to negative which indicates the pore charge is relatively low. A possibility for the point at negative voltage is the fluctuation to positive pore surface charges. **c** (potential) and **d** (current), Power generation for two pores (3 nm and 15 nm) at pH 11 and under different concentration gradient conditions. *This Figure was published in Nature, 2016, Feng et al.*[171]

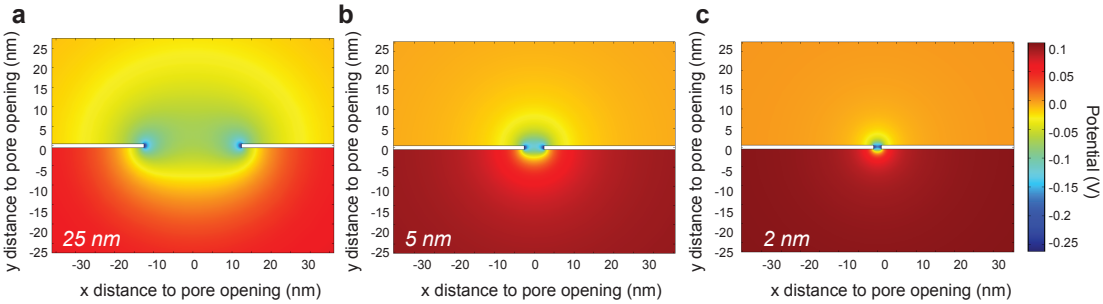

d

C_{min}/C_{max}	$V_{measured}$, mV	E_{redox}, mV	V_{os}, mV	Ion selectivity
1mM/10mM	100.6	46.9	53.7	0.92
10mM/100mM	104.4	53.5	50.9	0.86
10mM/1M	153.3	107.2	46.1	0.78
1mM/100mM	183.0	100.4	82.6	0.7
100mM/1M	67.3	53.7	13.6	0.23

Figure S3.3 – Ion selectivity: ideal cation selectivity. The calculated surface potential distribution of MoS_2 nanopores of 25 nm (shown in **a**), 5 nm (shown in **b**), and 2 nm (shown in **c**) under a fixed surface charge density. **d**, Ion selectivity at different salt gradient conditions. The ion selectivity also depends on the Debye length when the concentration gradient ratio is fixed and with the combination of 10 mM/1 mM in a 5 nm pore, the ion selectivity approaches nearly 1, indicating the ideal cation selectivity. *This Figure was published in Nature, 2016, Feng et al.*[171]

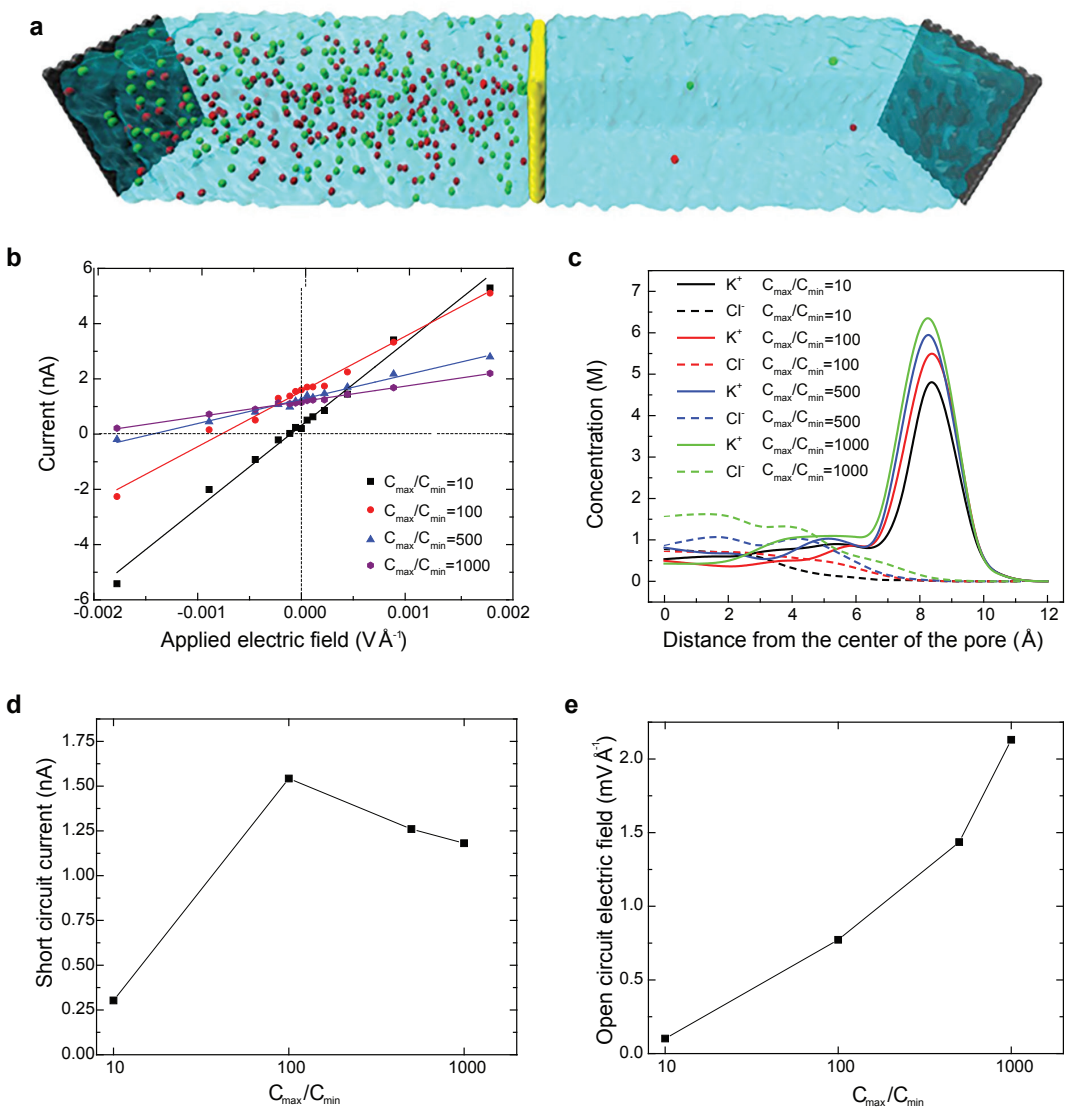

Figure S3.4 – MD simulated power generation at various concentration gradient ratio. a, Schematic of a typical simulation box. **b**, Current as a function of the applied electric field for a single-layer MoS_2 for different concentration ratios. **c**, K^+ and Cl^- concentrations as a function of the radial distance from the center of the pore for different concentration ratios. **d**, Short circuit current as a function of the concentration ratio. **e**, Open circuit electric field as a function of the concentration ratio. *This Figure was published in Nature, 2016, Feng et al.*[171]

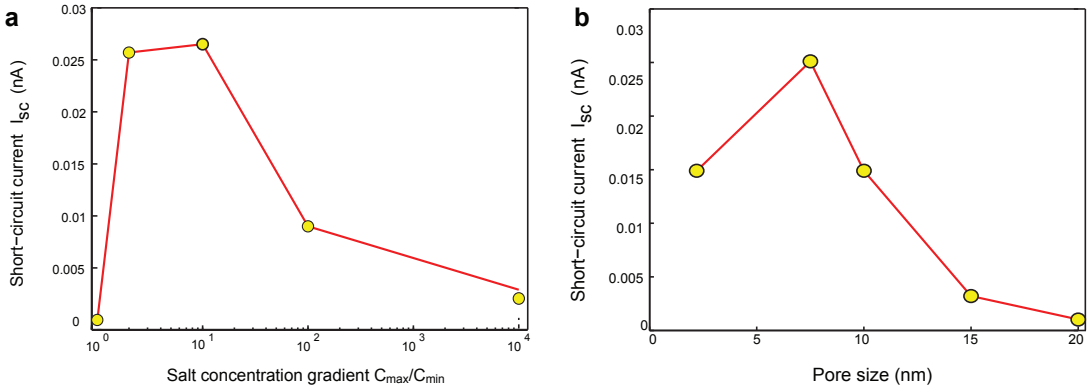

Figure S3.5 – Continuum based PNP model. a, Variation of short-circuit current, I_{sc} to concentration gradient ratio. The diameter of the nanopore is $d_n = 2.2$ nm. **b**, Variation of short-circuit current, I_{sc} as a function of the nanopore diameter. The salinity concentration ratio is fixed at 1000. The surface charge of the nanopore is $\sigma_n = -0.046\,94\ \mathrm{C\,m^{-2}}$. *This Figure was published in Nature, 2016, Feng et al.*[171]

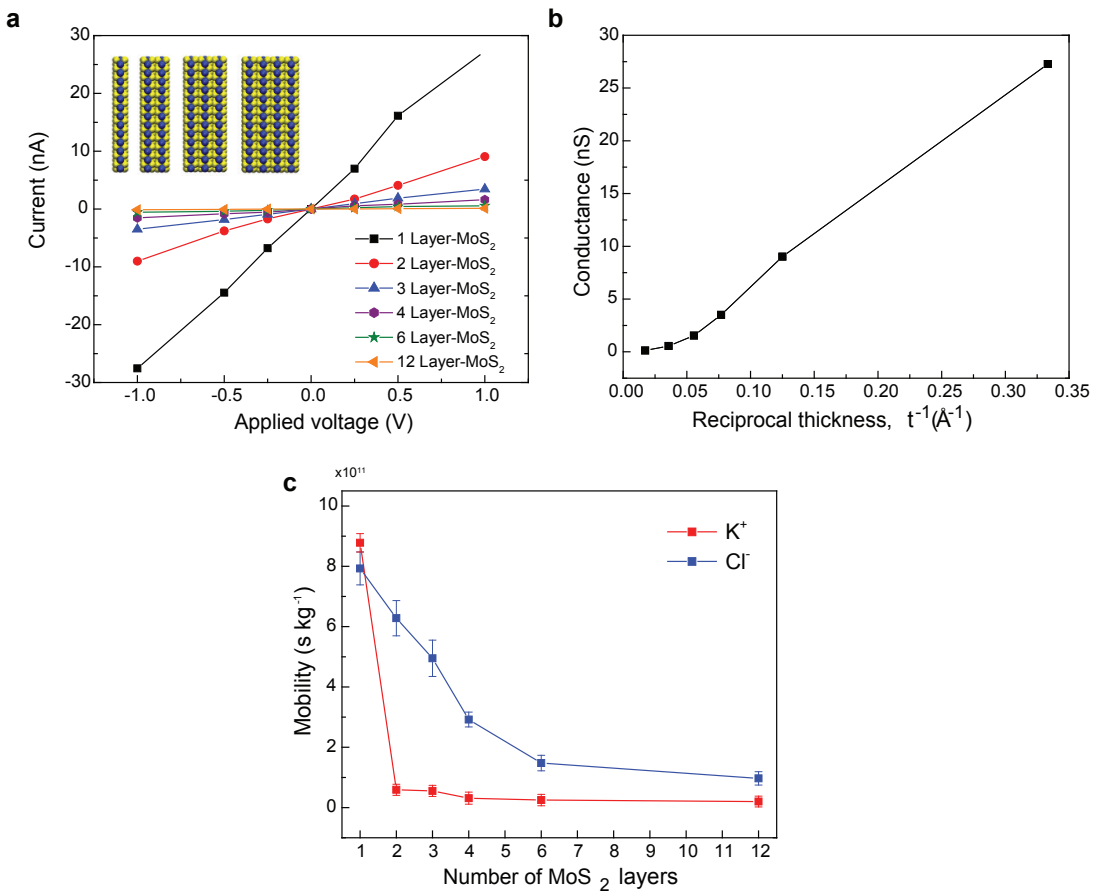

Figure S3.6 – MD modeled conductance as a function of thickness. a, I-V curves for six membranes with a different number of MoS_2 layers across a symmetric 1 M KCl solution. **b**, Conductance of the nanopore as a function of the reciprocal thickness of the membrane (t^{-1}). **c**, Average mobility of each ion for different layers of MoS_2 membranes. *This Figure was published in Nature, 2016, Feng et al.*[171]

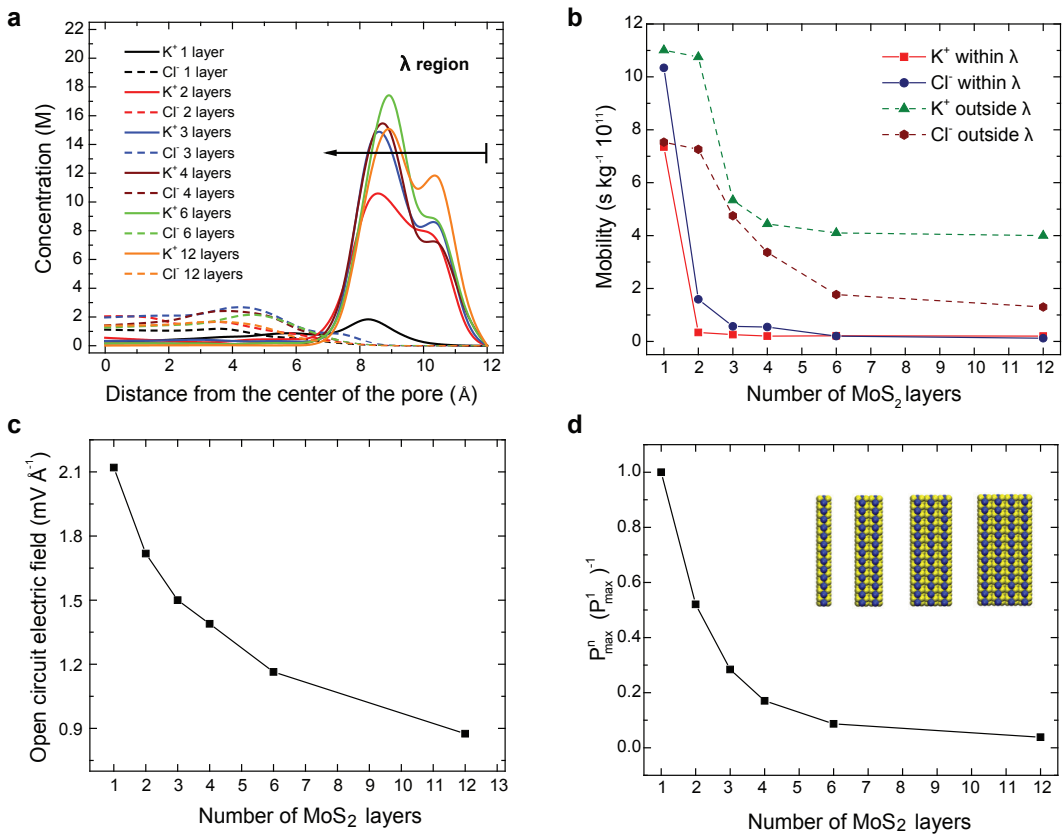

Figure S3.7 – Simulated power generation vs. thickness. a, K^+ and Cl^- concentrations as a function of the radial distance from the center of the pore for single and multi-layer membranes. The λ region near the charged wall of the pore is representative of the ionic double layer. **b**, The mobility of each ion type within and outside the λ region for different layers of membranes. **c**, The open circuit electric field across the membrane for a different number of MoS_2 layers. **d**, The ratio of the maximum power from multilayer membranes to the maximum power generated by a single-layer MoS_2. *This Figure was published in Nature, 2016, Feng et al.*[171]

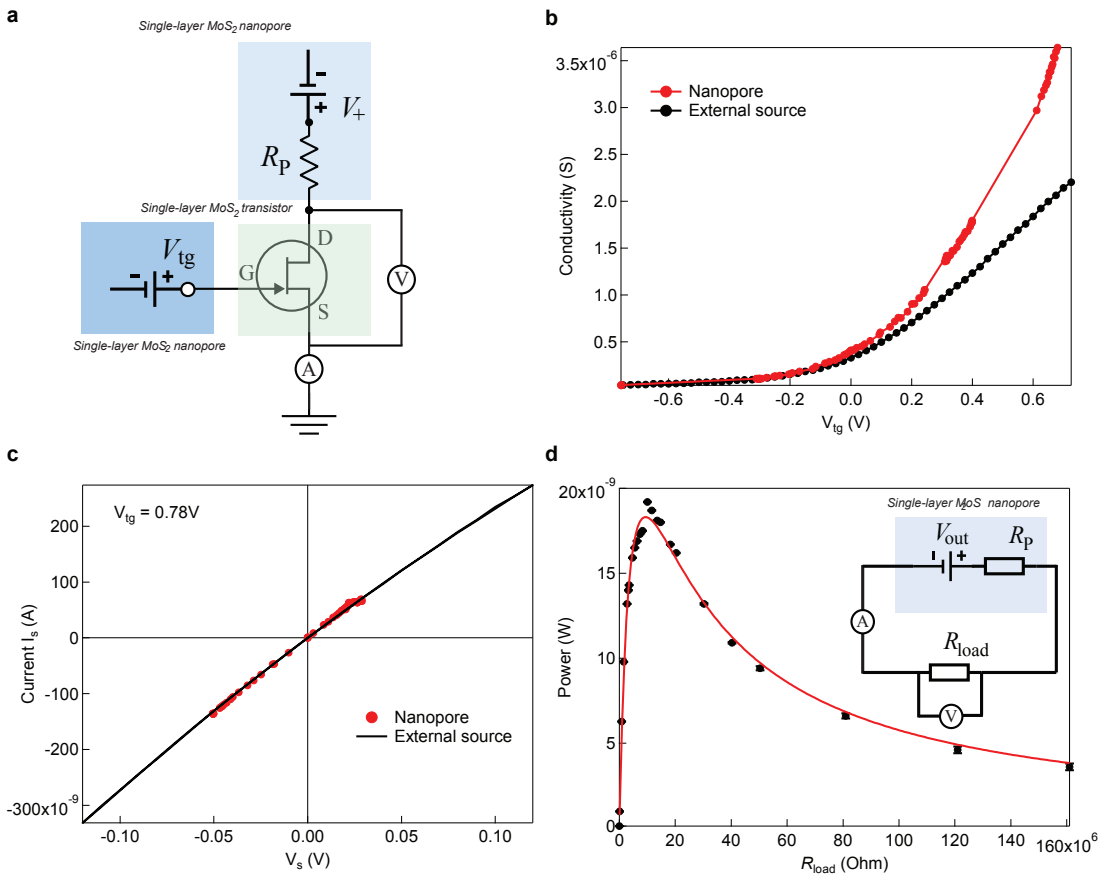

Figure S3.8 – Characterization of a single-layer MoS_2 transistor with nanopores and SMU a, Schematic of electrical measurements with two nanopores (V_+ and V_{tg}). The voltage drop across the transistor channel is monitored with the voltmeter V, current is measured with current amplifier A. **b**, Comparison of nanopore measurements and standard two-probe measurements with an external source. **c**, Current-voltage characteristics at $V_{tg} = 0.78$ V after current stabilization, measured with both setups. **d**, Power of nanopore in $BminPF_6/ZnCl_2$ as a function of load resistance R_{load}. Inset, schematic of measurements. *This Figure was published in Nature, 2016, Feng et al.*[171]

4 Light-Enhanced Blue Energy

This chapter is the preprint version of:

Michael Graf[1], Martina Lihter[1], Dmitrii Unuchek[2], Aditya Sarathy[3], Jean-Pierre Leburton[3], Andras Kis[2], Aleksandra Radenovic[1]. **Light Enhanced Blue Energy Generation using MoS_2 Nanopores.** Joule (2019)

If not otherwise noted, all figures and the associated data are my own work. M.G. and A.R. conceived the idea and designed all experiments. M.G., M.L., and A.R. wrote the manuscript. M.G. and M.L. performed the measurements. M.G. performed the data analysis. M.G. and M.L. fabricated the nanopore devices. D.U. performed PL measurements under A.K.'s supervision. M.G. and A.S. built the COMSOL models.

4.1 Summary

Blue energy relies on the chemical potential difference generated between solutions of high and low ionic strength and would provide a sun-and-wind independent energy source at estuaries around the world. Converting this osmotic energy into electrical current through reverse-electrodialysis relies on ion-selective membranes. A novel generation of these membranes is based on atomically thin molybdenum disulfide (MoS_2) membranes to decrease the resistance to current flow to increase the power output. Typically, to achieve good ion permeability ratios, alkaline conditions are used to boost the surface charge in solution. By exploiting the photo-excitability of MoS_2 membranes, we are able to raise the ion selectivity of the membrane by a factor of 5 while staying at a neutral pH level. The observed effect is due to a change in the surface charge caused by light-induced charge generation. Furthermore, we find that the behavior of small nanopores is dominated by surface conductance. We introduce a formalism based on the Dukhin number to quantify these effects in the case of a

[1]Laboratory of Nanoscale Biology, Institute of Bioengineering, School of Engineering, EPFL, 1015 Lausanne, Switzerland
[2]Laboratory of Nanoscale Electronics and Structures, Institute of Electrical Engineering and Institute of Materials Science and Engineering, School of Engineering, EPFL, 1015 Lausanne, Switzerland
[3]Department of Electrical and Computer Engineering, University of Illinois at Urbana-Champaign, USA

concentration gradient system. As a consequence, the charges created by light illumination of the membrane provoke two important changes: first, the surface charge at the pore rim increases, leading to an enhanced ion selectivity and therefore larger osmotic voltage (effect stronger in small pores). Second, the surface charge of the membrane increases, which in turn enhances the surface conductance and therefore increases the osmotic current (effect stronger in large pores). The combination of these effects might be able to efficiently boost the energy generation with arrays of nanopores with varying pore sizes.

4.2 Introduction

The term blue energy embodies all the attempts to harvest energy coming from the spontaneous and irreversible mixing of sea-water and river-water. The chemical potential difference between two liquids of different salt concentration holds immense amounts of energy: 2.3 MJ of theoretical energy is buried in each cubic meter of water.[204] Extracting this chemical potential energy can be achieved by reverse-electrodialysis, which relies on the direct electrical conversion of an ion current generated through stacks of cation and anion-selective membranes.[204] Ion exchange membranes for reverse electrodialysis are typically made from polymers that contain charged functional groups responsible for rejecting ions. An ideal membrane should be as thin as possible in order to decrease the resistance and increase the power output. Recent advances in 2D-material growth and processing allowed the development of free-standing membranes using ultra-thin materials like graphene or transition metal dichalcogenides (TMDs),[205] such as MoS_2. Controlled drilling in these materials using a transmission electron microscopy (TEM) or the electrochemical reaction (ECR) described in subsection 2.6.2 (page 50) allows the creation of single nanopores. Single-nanopores in MoS_2 have recently been successfully used to generate nanowatts of power (Figure 3.3 (page 69)). The relatively strong negative charge of the pore rim and the electrical double layer (EDL)-overlap in small pores results in ion repulsion. These combined effects are responsible for an efficient ion-selectivity which manifests in a measured osmotic potential. However, persistence of high ion-selectivity for relatively big pores (>10 nm) has been observed. This intriguing effect has not been completely understood so far.[206]

Using single-layer MoS_2 we can engineer a reverse-electrodialysis membrane with the highest single pore power to date (Figure 3.3). However, these highly efficient power conversions have been performed in extremely alkaline conditions (pH 11) to increase the surface charge of the material and improve the ion-selectivity (subsection 3.4.2 (page 71)).[176] The results obtained in such basic environments are not easily transferable to real-world operating conditions, where estuaries and seawater have pH values around 7.4. If these novel membranes pertain to have a winning chance of being applicable in reverse-electrodialysis applications, alternative ways of tuning the surface charge without compromising their thickness need to be developed. For this purpose, another natural resource, sunlight, can be used to generate charges in the material.

The presence of a visible range direct band gap in the single-layer TMDs makes them very attractive for optoelectronics applications.[207] We highlight MoS_2 as it shows very strong photogating effects allowing significant modulation of the charge carrier density by illumination with external light.[124,208] This photogating effect is responsible for the relatively slow but ultrahigh sensitivity of MoS_2 photodetectors.[209]

In this work, we investigate the possibility of tuning the surface charge with light in single-layer MoS_2 nanopores. We show that the observed changes in the efficiency of the generated osmotic power are due to photon absorption and the generation of charge carriers within the material. To the best of our knowledge, this is the first demonstration of a light-induced efficiency boost for osmotic power harvesting. Furthermore, we optimize the light intensities and the excitation wavelength to maximize the power output, while avoiding any material damage that could be possible due to photo-oxidation.[32,210] The light intensities used fall within ranges that are easily attainable in solar applications. In the end, we analyze why bigger pores can maintain a high ion-selectivity. We illustrate that the osmotic potential (and thus ion-selectivity) depends on the interplay between surface conductance and bulk conductance, which in small nanopores results in reduced osmotic potential compared to bigger pores. We present a formalism based on the Dukhin number[57] to estimate the pore-size dependence of the osmotic potential that, for the first time, explains qualitatively the data observed in this paper and in previous studies using high aspect-ratio nanopores.[171,176]

4.3 Results

4.3.1 Experiment

Figure 4.1a shows the experimental set-up. We fabricated freestanding MoS_2 membranes by transferring chemical vapor deposition (CVD) grown material on top of an opening in silicon nitride (SiN_x) membrane (typically 50 nm to 100 nm). Subsequently, a nanopore is fabricated either by TEM drilling (Figure 4.1b) or by the ECR method. The membranes are then mounted in a flow-cell. A concentration gradient of 1 mM / 100 mM potassium chloride (KCl) is applied between the two compartments to approach real-world values of the ion-concentration estuaries and ocean.[211] Two Ag/AgCl electrodes connected to a current amplifier measure the ionic current (Figure 4.1a). We used two diode-lasers at 643 nm (red) and 475 nm (blue) wavelengths to irradiate the membrane surface during the experiment. Figure 4.2 illustrates the alignment and the flow-cell set-up in detail. The energies of the two excitation wavelengths are above the single-layer MoS_2 optical bandgap which is around 1.83 eV, i.e. 676 nm in wavelength.[119] Specifics on the laser spot size and power measurements can be found in Figure S4.1 and Table S4.1. Excitation power densities for the 643 nm and 475 nm wavelength were calculated to be $P_0 \cdot 15.05\,\mathrm{W\,cm^{-2}}$ and $P_0 \cdot 27.25\,\mathrm{W\,cm^{-2}}$, respectively, where P_0 was the power set in the control-software.

The lasers were aligned perpendicular to the membrane by adjusting the position of the flow-

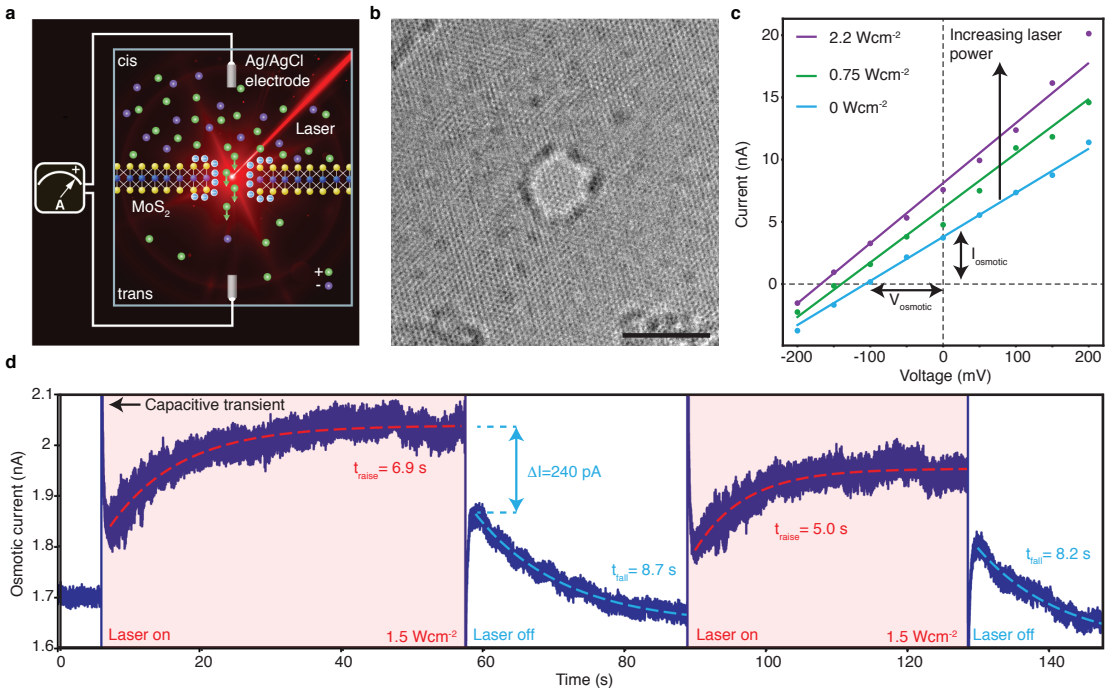

Figure 4.1 – Experimental overview. a, Schematics of the experimental set-up: Laser light is used to photogate the MoS_2 and thus modulate the surface charge of the nanopore. **b**, A typical nanopore drilled through a MoS_2 membrane by focusing the beam of a TEM using an acceleration voltage of 80 kV. **c**, I-V characteristics at a concentration gradient of 1000 using different laser intensities. **d**, Time trace of the osmotic current while switching the laser on and off (643 nm, 1.5 W cm^{-2}). The half-life values have been extracted by fitting to a single-exponential function. *This Figure was published in Joule, 2019, Graf et al.*[212]

cell to maximize the light transmitted through the membrane (Figure 4.2c-d). We first set out to investigate the stability of the MoS_2 membrane. We found that a laser flux as low as 3 W cm^{-2} was sufficient to slowly increase the pore size in MoS_2 or create additional holes or defects (Figure S4.4). Therefore, we restricted all of our subsequent laser irradiation to values below 1.5 W cm^{-2} in order to allow a margin of error and to reduce any misinterpretation of the results due to pore size changes.

4.3.2 Laser induced surface charge changes

The osmotic current (the current at zero potential) and the osmotic potential (the potential needed to zero the current) is found by measuring the linear current response in a voltage range of –200 mV to 200 mV (I-V). All reported values were corrected for the contribution of the electrode potential difference (Table S4.2). Qualitatively, during the laser irradiation, we observe an enhanced osmotic potential (Figure 4.1c). Increases in osmotic potential are related to larger ion selectivity. This could potentially be caused by stronger surface charges on the rim of the nanopore which enhances the repulsion of Cl^- ions. To cross-check this interpretation, we performed finite element model (FEM) simulations and observe a similar

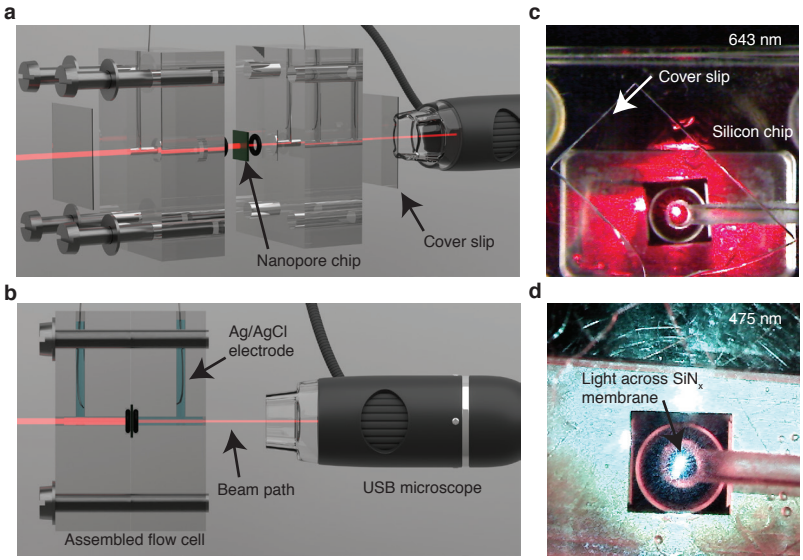

Figure 4.2 – Experimental set-up. a, Two parts of a poly(methyl methacrylate) (PMMA) flow-cell are screwed together to sandwich the nanopore chip (indicated by an arrow) between two O-rings. After filling the flow-cell with electrolyte, the two inlets are sealed with a coverslip (indicated by an arrow). A USB microscope is used to monitor the laser beam. **b**, Side view of the experimental set-up. The Ag/AgCl electrodes are placed outside of the laser beam path. **c**, Example alignment using the 643 nm laser. The laser light only passes across the nanopore chip when the beam is properly aligned to the SiN_x membrane. the ideal position of the nanopore chip is found by maximizing the transmitted light. **d**, An example alignment using the 475 nm laser. *This Figure was published in Joule, 2019, Graf et al.*[212]

trend when increasing the surface charge of the pore (Figure S4.2).

Further, we investigate the ionic current response to laser irradiation. Light-induced generation of charges in MoS_2 is not instantaneous. This can be directly observed in the photocurrent of MoS_2 photodetectors. When light hits the material, a characteristic rise time of the photocurrent is measured. Similarly, when the light is turned off, a decay in the current is observed.[209] The slow part of the photo-response is associated with the photogating effect.[208] Since the ionic current is influenced by the surface charge of the membrane, we expect it to follow a similar trend. To compare the dynamics of the observed electrical photocurrent to the ion current variations in our system, we record a time trace while the shutter of a 643 nm laser (1.5 W cm^{-2}) was alternately opened and closed (Figure 4.1d). When turning the laser on, a rapid current jump is followed by a slow increase of the osmotic current. When the laser is turned off, another rapid current jump, followed by a slow decay back to the initial current prior to the laser illumination is observed. The capacitive transient visible on the current trace is associated with the underlying silicon substrate.[213,214] We can fit the decay to an exponential function and extract the half-life of the current-increase (t_{raise} = 5 s to 7 s) and the current decrease (t_{fall} = 8 s to 9 s). These values are comparable to the reported electrical current measurements (t_{raise} = 4 s and t_{fall} = 9 s).[209]

4.3.3 Osmotic power generation

Next, we created nanopores of 3 nm and 10 nm size, respectively, using the ECR method. Dehydration and non-linear current-voltage characteristics in small nanopores[215,216] could complicate the interpretation of the experimental results. Therefore, we use a starting pore size of 3 nm. The larger 10 nm pore was previously determined to be the optimal pore size for power generation (Figure 3.3d). First we estimated the pore size in symmetrical 1 M KCl condition by fitting the I-V to Equation 1.2 (page 13) (Figure 4.3a).[54] We then performed the experiment in gradient condition by exposing the membrane to the laser light. To ensure that all observed differences are due to light irradiation and not to any time-related effect, such as pore size increase or pore clogging, a binary illumination condition (on/off) was used to cycle between a dark state and an illuminated state until we recorded at least 10 I-Vs for each condition. The obtained values of the osmotic current and potential are presented as boxplots in Figure 4.3b-c. For the small nanopore, the osmotic current is increasing significantly for both wavelengths tested. Similarly, the large nanopore shows a significant increase with the red and blue laser. The median of the osmotic potential of the 3 nm pore increase from 73 mV in the dark state to 92 mV (blue laser) and 98 mV (red laser), whereas the 10 nm pore did not show any significant difference in osmotic potential. Consistently with previously published work,[171,206] we observe an increased osmotic potential for the larger 10 nm pore compared to the 3 nm one.

Figure 4.4 shows the power generated by the device (product of the osmotic current and potential). All power increases were statistically significant. The power increases with laser illumination by 19 % (red, d = 10 nm), 15 % (blue, d = 10 nm), 131 % (red, d = 3 nm) and 71 % (blue, d = 3 nm). These results show a clear relationship between the efficiency of the membrane and the wavelength of the light used to illuminate the membrane. Furthermore, the calculated flux for the red laser (742 mW cm^{-2}) is nearly half the value of the blue laser (1300 mW cm^{-2}). It becomes therefore clear that the 643 nm laser is substantially more efficient in the generation of optical charges.

4.3.4 Estimation of the surface charge

To further investigate the influence of the laser light on the surface charge of our nanopore system, we performed conductance measurements at different electrolyte conductivities in symmetrical condition. Again, a 3 nm and a 10 nm pore were used with both laser wavelengths. We fit the obtained data to the conductance model proposed by Lee et al. (Figure S4.3a-d),[57] which takes into account the surface charge of the nanopore system (details on the calculations can be found in subsection 4.6.4). We calculate a surface charge in the range of 10 mC m^{-2} to 50 mC m^{-2}, which increases substantially upon laser illumination (Figure S4.3e-h).

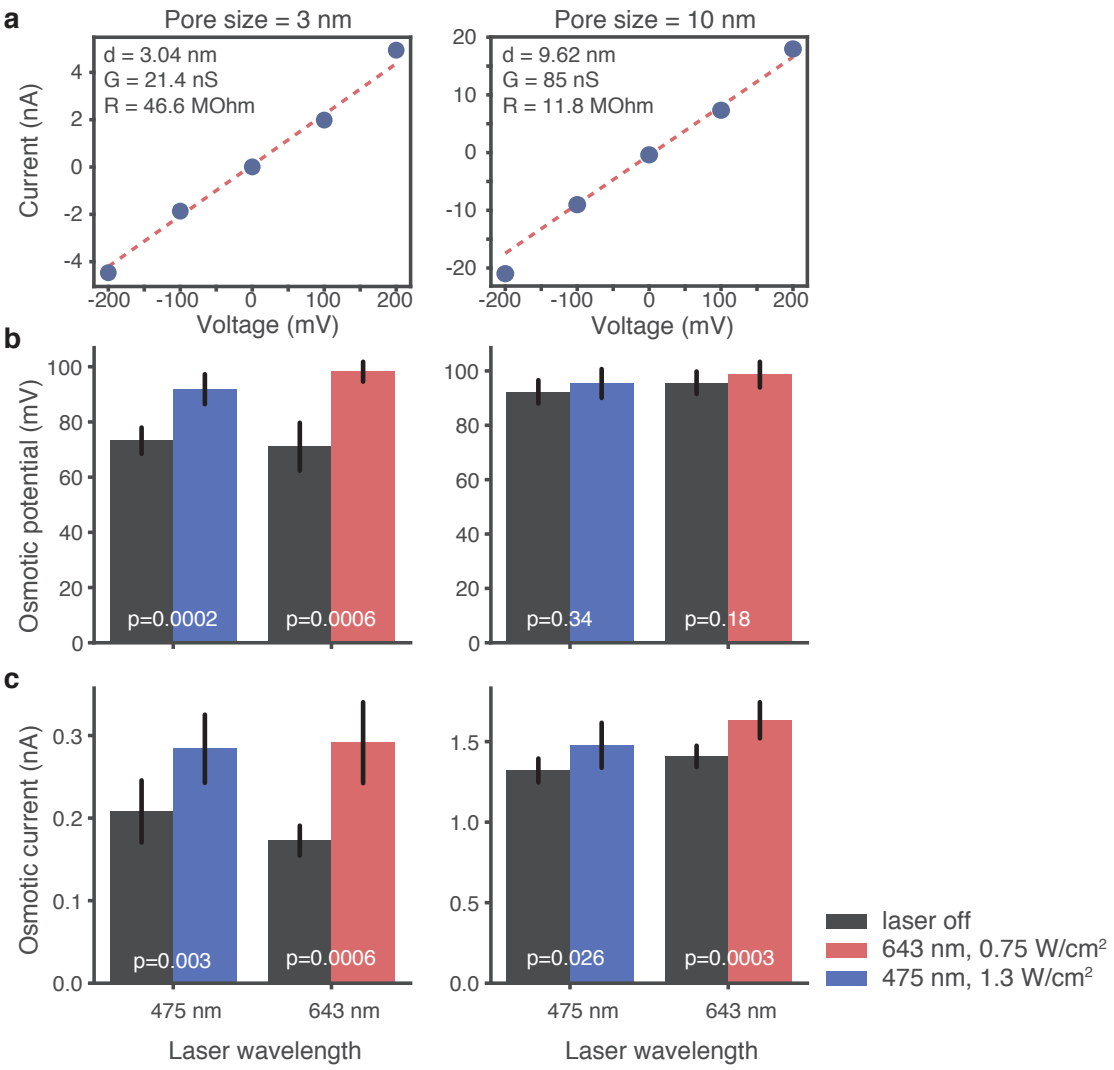

Figure 4.3 – Effect of laser light on the osmotic energy conversion for a 3 nm and 10 nm pore. a, The I-V relationship for a 3 nm (left) and a 10 nm (right) pore at 1 M KCl. The osmotic potential (**b**) and current (**c**) generated by a 3 nm (left) and 10 nm (right) MoS_2 nanopore as a function of laser light (grey: laser off, color: laser on) and wavelength (red: 643 nm, blue: 475 nm). The height of the bar denotes the mean value, whereas the error bar is the standard deviation of the dataset. n=10 for all the measurement groups for the 3 nm pore, n=11 for the 643 nm laser for pore size 10 nm and dark state, n=12 for 475 nm laser and its dark state. P-values reported are calculated using the Wilcoxon rank-sum test and test for the alternative hypothesis that samples from the dark state distribution are more likely to be smaller than samples from the illuminated distribution. All p-values are highly significant ($p < 0.05$), except for osmotic potential values for the 10 nm pore. Between the two dark-states all $p > 0.05$ except in the case of the osmotic current ($p = 0.02$) and power ($p = 0.03$) of the 10 nm pore. The mean values for each distribution are reported in Table S4.3. The values of the osmotic power can be found in Figure 4.4. *This Figure was published in Joule, 2019, Graf et al.*[212]

4.3.5 Photoluminescence

We further investigate this difference in optical response for these two wavelengths and have performed micro-photoluminescence (μ-PL) measurements of MoS_2 deposited on the

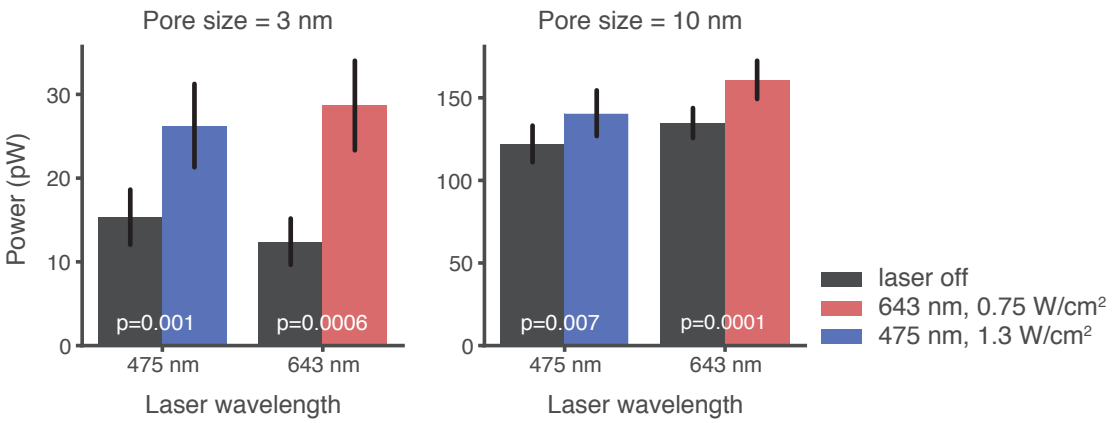

Figure 4.4 – Effect of laser light on the osmotic power for a 3 nm and 10 nm pore. The osmotic power generated by a 3 nm (left) and 10 nm (right) MoS_2 nanopore as a function of laser light (grey: laser off, color: laser on) and wavelength (red: 643 nm, blue: 475 nm). More details can be found in the caption of Figure 4.3. *This Figure was published in Joule, 2019, Graf et al.*[212]

membrane and in the vicinity of the membrane. A bright field image of the area considered for the photoluminescence (PL) measurements is shown in Figure 4.5a. The white dashed rectangle depicts the 20 x 20 μm^2 area used to generate the PL maps shown in Figure 4.5c and e with 488 nm and 647 nm excitation wavelength correspondingly. These maps represent spatial distribution of the PL intensity at 665 nm emission wavelength. The observed inhomogeneity of the PL strength over the MoS_2 flakes which arises due to the two reasons: First, incident light experiences different interference which depends on the substrate. Thus, there is a strong difference of the light absorption by the MoS_2 on top of the 20 nm thick SiN_x membrane compared to the similar crystal deposited on the SiN_x/silicon dioxide (SiO_2)/Si substrate. This effect is clearly visible in the bright field image and leads to the respective difference in µ-PL intensity of MoS_2 in and out of the SiN_x membrane (spectra 3 and 4 in Figure 4.5d, f). Second, the modulation of intensity and position of the µ-PL peak inside the single crystal (spectra 1-2-3 and 5-6 in Figure 4.5d) is associated with the CVD growth process. Apart from these two side effects, the main results of these measurements are clear when the two maps are compared to each other. The MoS_2 PL intensity is 8 times higher when a 647 nm laser is used for excitation. This is consistent with previous reports.[217] Even though MoS_2 absorption is lower in the case of the red laser, the energy of incident photons is closer to the excitonic resonance making optical excitation more efficient and optical effects more pronounced, including the photogating effect schematically depicted in Figure 4.5b. Therefore, efficient optical generation of charges in MoS_2 under the 647 nm excitation is responsible for the results summarized in Figure 4.3 and Figure 4.4.

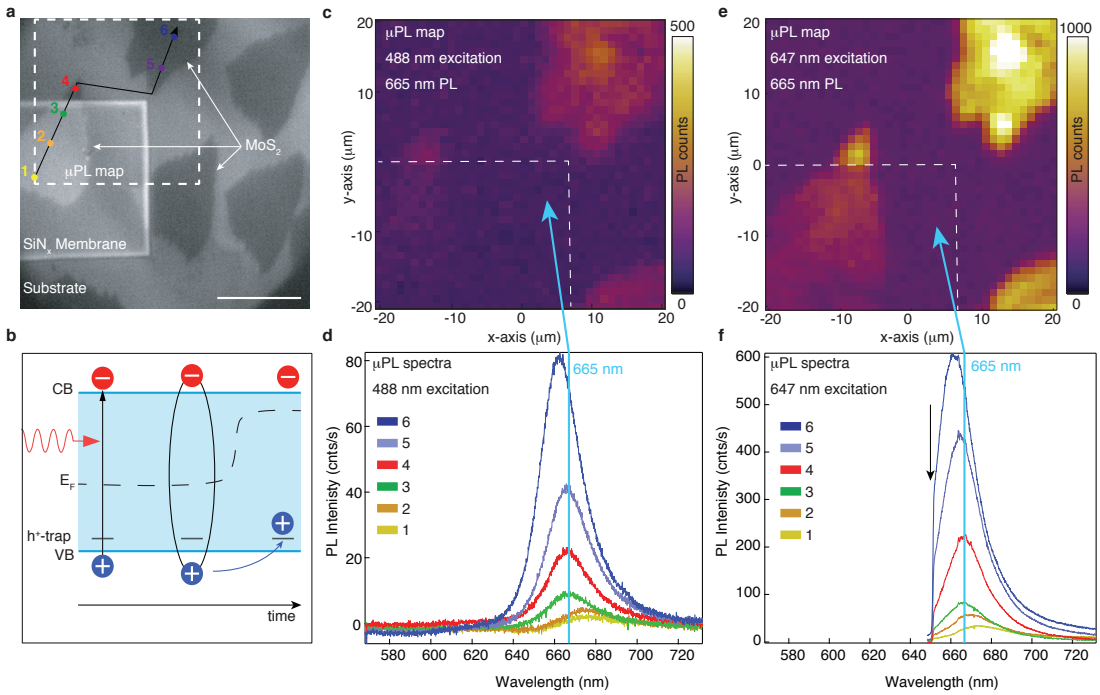

Figure 4.5 – Photoluminescence measurements. **a**, Optical image of the device area used for the photoluminescence measurements. The dashed rectangle represents the position of the μ-PL maps in **c** and **e**. Color points show position for μ-PL spectra in **d** and **f**. Scale bar is 20 μm. **b**, Schematic depiction of the photogating effect in a single-layer MoS_2, when trapped photoexcited holes shift the Fermi level closer to the conduction band (CB). **c** and **e** μ-PL maps acquired at high energy (488 nm) and near-resonant (647 nm) excitations correspondingly. Both maps demonstrate PL intensity distribution at 665 nm emission wavelength. Resonance excitation results in an 8-fold PL intensity enhancement. The dashed rectangles shows edges of the membrane. **d** and **f** Corresponding μ-PL spectra. Black arrow represents near-resonant excitation at 647 nm wavelength. *The data was acquired and processed by Dmitrii Unucheck from LANES, EPFL. This Figure was published in Joule, 2019, Graf et al.*[212]

4.4 Discussion

4.4.1 Heat

As previously reported by Hwang et al.,[218] heat can influence the gradient driven energy conversion by increasing the surface charge density and ionic mobility. The authors see a steep change of the slope of the I-V characteristics with changing temperature, whereas in this study we merely see an offset (Figure 4.1), suggesting that our mechanism cannot be explained by heat-induced conductivity changes. Furthermore, Figure 4.3c clearly shows an increased effect with the 643 nm laser, even though the energy provided is nearly half than that of the 475 nm laser. If the effect would be dominated by heating one would expect a more prominent effect using the more energetic 475 nm illumination. In subsection 4.6.1 we provide a detailed and thorough analysis on how heat can influence different parameters in our system such as EDL thickness, surface potential, and viscosity. Furthermore, through FEM simulations we

estimate a maximum of 4 °C of temperature increase in our system (all details are provided in subsection 4.6.1) which is not enough to cause the observed response in current and voltage. We, therefore, conclude that heat does not play a relevant role in explaining the experimental data.

4.4.2 Evidence for increased surface-charge density

The ionic current measurements performed in this work illustrate an enhancement in osmotic voltage (Figure 4.1c) during laser irradiation. This indicates that the surface-charge density increases, which is consistent with the results obtained by FEM simulations (Figure S4.2). Furthermore, conductance measurements with and without light confirm the increase in surface charge upon light irradiation (Figure S4.3). Upon the absorption of a photon, an electron-hole pair is generated. Photoexcited holes from the valence band can then be further trapped by defects in the MoS_2. This shifts the Fermi level closer to the conduction band (like a local electrostatic n-doping) and brings more mobile electrons to the surface, which in turn becomes effectively more negatively charged. In other words, the light illumination does not generate additional electrons but makes deeply entombed electrons available at the surface. This photogating mechanism is consistent with previous work on silicon nitride nanopores showing that light can induce surface charge changes by exciting electrons in the ground state and making them available at the surface.[219]

As previously mentioned, the ionic current response to laser illumination shows similar behavior as the current generated in MoS_2 photodetectors. The half-lifes of the current-increase (t_{raise} = 5 s to 7 s) and the current decrease (t_{fall} = 8 s to 9 s) are similar as in the reported electrical current measurements (t_{raise} = 4 s and t_{fall} = 9 s).[209] The same dynamic response in the measured ionic current indicates a strong relationship with the same charge generation mechanism observed in photodetectors. The above observations indirectly confirm that the effects we are measuring are the consequence of light-induced surface charge changes. Figure 4.4d thus demonstrates that light illumination can indeed increase the generated osmotic power.

Ionic current measurements also show that the 643 nm laser is more efficient for power generation than 475 nm one, even though lower intensities were used (Figure S4.3). This fact is consistent with our PL measurements and the literature,[217] and also originates from the charge generation mechanism. As already mentioned, this is due to more efficient optical generation of charges with 643 nm excitation since the energy of incident photons is closer to the excitonic resonance.

4.4.3 Surface vs. bulk conductances

We are intrigued by the fact that the osmotic voltages are higher in the larger nanopore (Figure 4.3c, 3 nm, and 10 nm pore), even though the ion selectivity should be smaller due to a

smaller EDL-overlap. Experimental artifacts are unlikely since this behavior has been observed in other studies involving ultra-thin nanopores (Figure 3.3 (page 69)d),[171,206] though the origin of the effect was not resolved. To further investigate this counterintuitive behavior, we performed finite element simulations for different pore sizes. Consistent with decreasing EDL-overlap, we always observed a decrease of the osmotic voltage with larger pores, independently of the surface charge assigned to the membrane (Figure S4.5a-d).

We suspect that small nanopores do not follow bulk conductance rules since deviations in conductance from bulk predictions have been observed in nanopores with high aspect ratios $\frac{L}{D} < 1$, where D is the pore diameter and L is the membrane thickness.[57] As a result, small nanopores might sense a modified chemical potential difference. In subsection 4.6.2, we derive a framework based on the Dukhin formalism that qualitatively explains the observed effect. The result shows that two competing mechanisms (Figure 4.6) determine the ionic current through a nanopore of diameter D: the surface conductance and the bulk conductance. The importance of each contribution can be estimated through the Dukhin number Du:

$$Du = \frac{4 l_{Du}}{D} \tag{4.1}$$

, where l_{Du} is the Dukhin length approximated by $l_{Du} \approx \frac{\sigma}{2 c_s e}$ with c_s the bulk ion concentration, e the elementary charge and σ the surface charge. The Dukhin number of the 3 nm pore is 3.5, suggesting a large surface conductance contribution, whereas the 10 nm pore has $Du = 1$ (equal contributions). The classical Goldman-Hodgkin-Katz (GHK) equation[220] can estimate the osmotic potential when the bulk conductance dominates, but overestimates the potential when the surface conductance becomes important. In this case, the ion concentration within the EDL plays a larger role than the bulk concentration (Figure 4.7a). We qualitatively estimated the osmotic potential for any pore size by weighing the GHK equation with the Dukhin number (Figure 4.7b, solid blue line):

$$E_{\text{total}} = \frac{RT}{F}\left[R_b \cdot \ln\left(\frac{P_{K^+/Cl^-} \cdot c_{\text{cis}} + c_{\text{trans}}}{P_{K^+/Cl^-} \cdot c_{\text{trans}} + c_{\text{cis}}}\right) + R_s \cdot \ln\left(\frac{P_{K^+/Cl^-} \cdot c_{K^+}^{\text{cis}} + c_{Cl^-}^{\text{trans}}}{P_{K^+/Cl^-} \cdot c_{K^+}^{\text{trans}} + c_{Cl^-}^{\text{cis}}}\right)\right] \tag{4.2}$$

Where P_{K^+/Cl^-} is the permeability ratio, R_b and R_s are the contribution ratios of the bulk conductance and surface conductance that satisfy $R_s + R_b = 1$ and are estimated using the Dukhin number: $R_b = \frac{1}{1+Du}$ and $R_s = \frac{Du}{1+Du}$. The ion concentration within the EDL of the charged membrane is denoted as: $c_{K^+}^{\text{trans}}$, $c_{Cl^-}^{\text{trans}}$, $c_{Cl^-}^{\text{cis}}$ and $c_{K^+}^{\text{cis}}$. This effectively scales the osmotic potential with the surface and bulk contributions. The trend observed in the experiments is qualitatively reproduced by this modified GHK equation. Strikingly, the highest osmotic potential is found for a pore size of ≈ 9 nm which is similar to the values observed experimentally (Figure 3.3d).

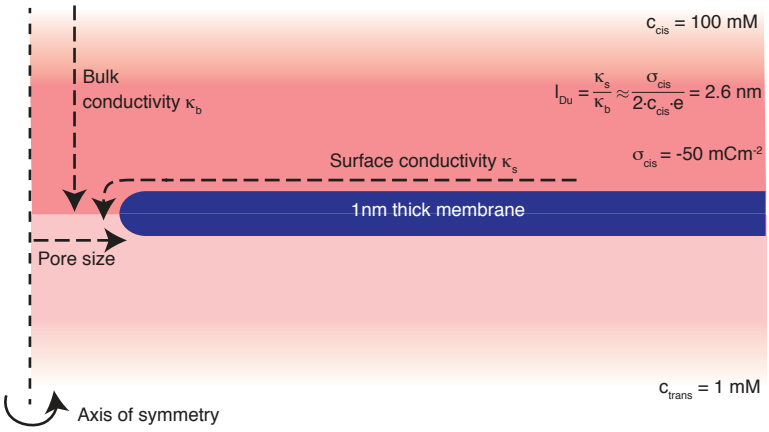

Figure 4.6 – Surface conduction contribution. Illustration of bulk and surface conductance contributions. The values of the Dukhin length l_{Du} and the surface charge of the *cis* and *trans* side have been estimated assuming a concentration gradient of c_{cis} = 100 mM, c_{trans} =1 mM. *This Figure was published in Joule, 2019, Graf et al.*[212]

4.4.4 Consequence of the light boosting

The surface conduction highly dominates the smaller 3 nm nanopore. This decreases the effective concentration gradient sensed by the nanopore. As a consequence, the osmotic potential is lower than what would be expected from bulk predictions. The larger the nanopore becomes, the less it is dominated by surface conduction, emphasizing the bulk gradient and therefore increasing the effective chemical potential difference. We have shown that light can double the osmotic power in small nanopores and increase the power output of larger pores by up to 20 %. Since the power is a product of osmotic voltage and osmotic current it can be affected by either parameter.

During light-exposure of the pore two changes are occurring simultaneously: first, the surface charge at the pore rim increases, leading to an enhanced ion selectivity (by enhancing the repulsion of anions) and therefore larger osmotic voltage. Second, the surface charge of the membrane increases, which in turn enhances the surface conductance and therefore increases the osmotic current. The first effect dominates in small pores, while the second effect dominates in bigger pores. This can be seen by the astonishing increase of the osmotic potential in small nanopores. In larger pores this difference is less pronounced and results only in a small improvement of the ion selectivity. However, even though the effect on the ion selectivity is small in the large pore, the enhanced surface conductance during light illumination (due to large l_{Du}) increases the ionic current substantially (Figure 4.3c). This effect is becoming increasingly important as the pore size increases and helps to maintain good power generation in large nanopores. Along the same line, recent work has analytically shown that strong surface conductance generates a dynamic ion selectivity, which is defined through Dukhin, rather than EDL, overlap and is responsible for the maintenance of good ion selectivity in larger pores.[221]

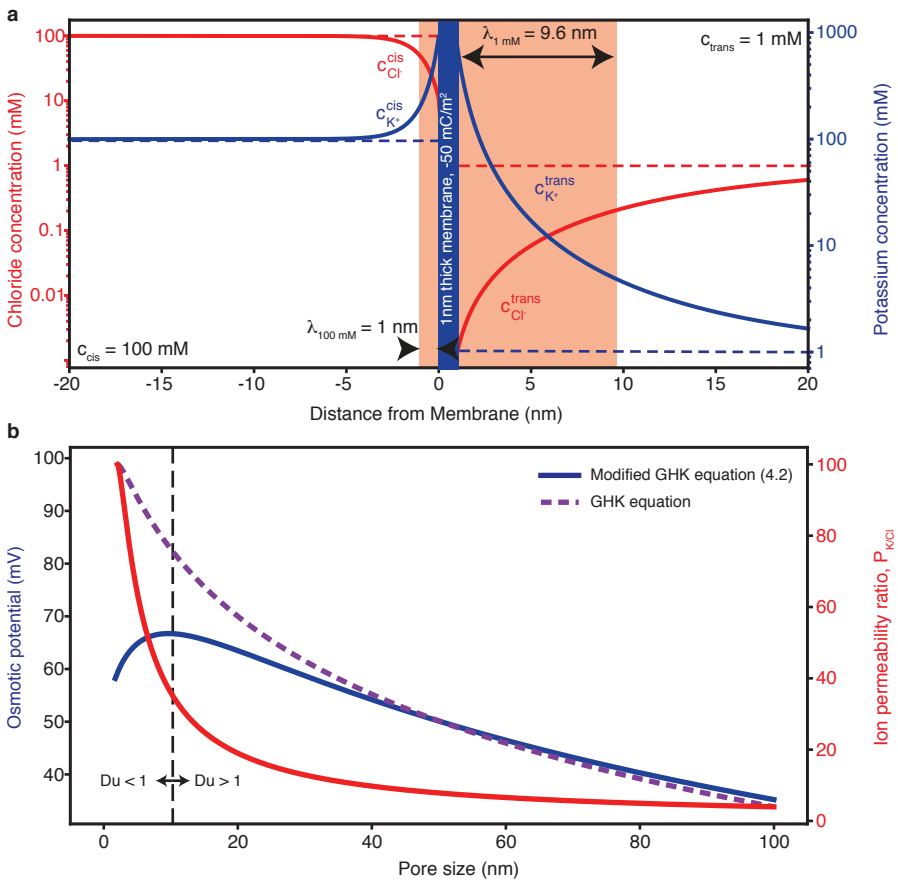

Figure 4.7 – Modified GHK model. **a**, Simulated potassium (blue) and chloride (red) concentration distribution from a charged wall with surface charge $\sigma_{\text{cis}} = -50\,\text{mC}\,\text{m}^{-2}$. The bulk concentration levels of potassium and chloride c_{cis} and c_{trans} are indicated with the blue and red dashed lines. The red box shows the EDL length over which ions have been averaged for the calculation of the effective ion concentration in the case of a surface conductance dominated system. **b**, The reversal potential calculated from the modified GHK model (Equation 4.2) is denoted with a solid blue line and plotted versus pore size (D>2 nm). This model scales the two competing effects through prefactors weighing the bulk contribution and the surface contribution. The values of the prefactors are a function of the pore size D and are calculated through the Dukhin number Du. The dashed blue line shows the non-modified GHK equation. The ion permeability assumed for the calculations is plotted in red on the secondary y-axis and is estimated from a geometrical consideration of EDL-overlap (see subsection 4.6.2). The vertical black line at around 10 nm pore size shows where the Dukhin number passes 1, i.e. at which pore size the system switches from a surface conductance dominated system to a bulk conductance dominated system. *This Figure was published in Joule, 2019, Graf et al.*[212]

4.4.5 Outlook

To increase the osmotic current, arrays of nanopores will have to be fabricated on a large-scale. We suggest achieving this through a non-specific large scale defect creation method, such as oxygen plasma,[47] ion bombardment[222] or chemical etching.[223] This will produce a large pore size distribution, where small and large nanopores are present on the membrane at the same time. Light-induced charge generation will render both nanopores more efficient. This

is especially important since the power density does not increase linearly with the porosity of the membrane due to the importance of the surface conductance.[224]

Increasing the reactivity of MoS_2 to light could provide a way of further boosting the permeability ratio in small nanopores, but equally important, help to maintain a good selectivity and strong surface current in larger nanopores. Self-assembled gold nanoparticles or plasmonic nanoshells could be used to induce a surface plasmon resonance and thus increase the charge creation.[225,226] Aluminum nanocavities can improve the absorbance of the light to nearly 70 %,[227] but would increase the membrane thickness. A better option might be to use a single-layer of hexagonal boron-nitride (h-BN) for that purpose.[228]

In a real-world application, one could imagine boosting the osmotic power generation during daytime by directing sunlight onto the membranes. Typical irradiance levels of sunlight are about 100 mW cm^{-2} at sea level making it easy to achieve here reported power densities by focusing the sun's light using standard concentrators used in solar cells.[229] The most common salt in ocean water is NaCl. We do not expect measurable difference between the model (KCl) system and real-world conditions due to nearly identical selectivity ratios of K^+ and Na^+ reported in graphene nanopores.[206]

To our knowledge, this is the first observation that laser light can modulate the ion selectivity of MoS_2 nanopores through a photogating effect and thus increase the osmotic power generated through reverse electrodialysis. Furthermore, we developed a novel formalism to qualitatively explain the data observed in thin nanopores.

4.5 Methods

4.5.1 Nanopore fabrication

The fabrication of the devices has been previously described in chapter 2 (page 35). In summary, we prepared silicon nitride membranes by using conventional photolithography and anisotropic etching of silicon in potassium hydroxide (KOH). We then used e-beam lithography and reactive ion etching with a mixture of CHF_3 and SF_6 gases to etch through SiN_x and SiO_2 to create 50 nm sized holes in the nitride membrane.

Single crystal MoS_2 was grown using CVD on sapphire substrates. We then spin-coat PMMA on this substrate and do a water-based transfer to the target substrate (subsection 2.4.1 (page 45)). The devices are then soaked in Acetone and baked overnight at 400 °C with a flow of argon (100 sscm) and hydrogen (10 sscm) in order to remove the majority of PMMA residues. The devices are then placed into a transmission electron microscope (FEI Talos, Hillsboro, Oregon, USA) at an acceleration voltage of 80 kV to assess the integrity and cleanliness of the sample. If the sample passes the quality control, a nanopore of the desired size is drilled by focusing the electron beam to the smallest possible spot. The devices are then mounted into a custom made PMMA flow-cell using two rubber O-rings to ensure a good seal. The two

chambers are subsequently flushed with an ethanol-deionized (DI) water mixture (50/50) in order to properly wet the nanopore. The input channels are then sealed off by a coverslip to create a flat water-glass interface. This avoids light scattering and greatly improves the alignment precision. The flow-cell is then placed on a xy-stage in a custom-made Faraday cage and aligned to the laser beam. The laser electronics (iBeam smart, Toptica Photonics, Gräfelfing, Germany) are placed outside the metal cage to avoid noise increases. The beam is inserted into the cage through a hole in the box. On the opposite side of the flow-cell, a small USB microscope is placed to observe the light transmitted through the nitride membrane. The flow-cell can then be carefully aligned using the xy-stage. The point where the most light penetrates the nitride membrane was considered to be the ideal position.

An Axopatch 200B in combination with a custom made LabView program is used to measure and record the current through the nanopore. Pore sizes were checked by comparing current-voltage characteristics in symmetrical salt concentration, i.e., 1 M / 1 M KCl at the start and the end of the experiments. All pore sizes were estimated by substituting the conductance in the well-established conductance model described in Equation 1.2 (page 13). For all measurements, we used the potassium chloride (K^+/Cl^-) ion pair due to their nearly identical bulk mobilities. All our buffers have been adjusted to a pH of 7.4, except for the 1 mM dilution, which was adjusted, but unbuffered.

All laser powers reported are the values that have been entered by the user in the software (iTopas, Toptica Photonics, Gräfelfing, Germany). A table of the theoretical vs. measured output power can be found in Table S4.1. Roughly, the measured power was about 90 % (643 nm) and 98 % (475 nm) of the entered value. In practice, the power reaching the membrane is less, due to scattering at the coverslip and in the PMMA flow-cell. The laser fluxes were calculated by dividing the corrected output power P_c by the approximate area that has been measured using a slit scanning beam profiler (BP104-VIS, Thorlabs, Newton, New Jersey, United States). The correction factor was determined by measuring the laser power using a FieldmaxII-TOP (Coherent, Santa Clara, United States) and reported in Table S4.1. The loss is roughly 10 % for 643 nm and 2 % for 475 nm. We can thus calculate the fluxes as follows: $I = (1 - \text{loss}) P_0 \frac{1}{\pi X_{4-\sigma} Y_{4-\sigma}}$, $I_{643\,\text{nm}} = P_0 \cdot 15.05\,\text{W}\,\text{cm}^{-2}$, $I_{475\,\text{nm}} = P_0 \cdot 27.25\,\text{W}\,\text{cm}^{-2}$

4.5.2 Optical measurements

µ-PL spectra were performed in air at room temperature using the laser light focused to the diffraction limit with a beam size of about 1 µm. The incident power was 90 µW for both excitation wavelengths. The emitted light was acquired using a spectrometer (Andor) and the laser line was removed with a long-pass 488 nm (650 nm) edge filter in the case of 488 nm (647 nm) excitation. The presented µ-PL maps were obtained by scanning the sample using the nano-positioning stage (Mad City Labs Nano-Drive). Bright field image was acquired by a CCD camera (Andor Ixon).

4.5.3 Data analysis

The I-V traces were recorded at a reduced sampling rate 6250 Hz with a lowpass filter set to 1 kHz. The voltage polarity switched when the voltage ramps to avoid charging of the membrane, i.e. 0 mV, 100 mV, –100 mV, 200 mV and –200 mV. Each voltage step lasts for 10 s. The traces are then segmented through detecting the current transient when the voltage was switched. Each extracted part is fit to a simple exponential function $I(t) = I_0 \cdot e^{-b \cdot x} + I_{\text{stable}}$. The considered current value corresponds to the stable current at infinite time. The standard deviation of this fit $\sigma_{\text{exp-fit}}$ is extracted by taking the square root of the covariance matrix. We then perform a linear fit of the obtained current-voltage values. By using York's method we can propagate the previously calculated errors correctly through the linear fit.[170] We can now extract the parameters of the current-voltage relationship $I(V) = G \cdot V + I_0$, where G is the conductance. The measured osmotic current is defined as I_0, the measured osmotic voltage is $\frac{I_0}{G}$. The redox potential of the Ag/AgCl electrodes are then removed from the measured osmotic voltage to yield the effective voltage $V_{\text{osm}} = \frac{I_0}{G} - E_{\text{redox}}$. The electrode potential of the Ag/AgCl electrodes has been measured for the buffers used in the experiments using a reference electrode. Table S4.2 reports the measured and theoretical voltages. The deviations to the theoretical values most probably come from the uncertainty of preparation of such dilute solutions.

The effective osmotic current is then calculated as $I_{\text{osm}} = V_{osm} \cdot G$. The osmotic power is defined as: $P_{\text{osm}} = V_{\text{osm}}^2 \cdot G$.

4.5.4 COMSOL numerical modeling – heat

COMSOL 5.3a was used for all finite element simulations. The COMSOL model was built by keeping all dimensions as close to reality as possible. The silicon chip was defined as 380 µm thick and 5 x 5 mm^2. The back side contained a 520 µm large, pyramidical opening penetrating through the chip and leaving a 52 µm large membrane area on the front side. The silicon chip is encompassed by a 10 mm cubic PMMA flowcell, which has two 1 mm large channels that provide the liquid contact to the silicon chip. The heat transfer in solids module is used. Initial temperatures were set at 20 °C. We then apply the power from the laser in two steps by using the *Deposited Beam Power* module. 1st, we apply a Gaussian distributed beam (centered in the middle of the membrane, standard deviation 250 µm) of a power of 70 % of the laser power (simulating the silicon absorbance) to the area outside of the membrane. 2nd, we apply a second beam (same center and standard deviation) of a power of 10 % of the laser power (nitride absorbance) to the membrane only. *Heat transfer in Solids and Fluids* modules are used to model the transfer of heat along the silicon chip, the PMMA, and the liquid. Furthermore, the *Diffuse Surface* module is used to take into account the radiative heat source. The finite element simulation is then run for different laser power. As a boundary condition for the temperature, the edge of the PMMA flow-cell was set to be at 20 °C.

4.5.5 COMSOL numerical modeling – nanopore

We simulated the stationary ion distribution around a monolayer MoS_2 membrane by solving the Poisson-Nernst-Planck (PNP) equations given by:

$$\nabla^2 = \frac{eF}{\epsilon}(K^+ - Cl^-) \tag{4.3}$$

$$\nabla \cdot J_{K^+} = \nabla \cdot [-FD_{K^+}\nabla K^+ - \frac{F^2 D_{K^+}}{RT} K^+ \nabla\phi] = 0 \tag{4.4}$$

$$\nabla \cdot J_{Cl^-} = \nabla \cdot [-FD_{Cl^-}\nabla Cl^- - \frac{F^2 D_{Cl^-}}{RT} Cl^- \nabla\phi] = 0 \tag{4.5}$$

Where ϕ is the electrostatic potential at every point in space. This potential along with the current densities of the respective ionic species (J_i) is dependent on the concentration of the ionic species (i = K^+/Cl^-), the respective diffusion coefficients (D_i) and the temperature T. F is Faraday's constant while R is the universal gas constant and ϵ is the relative permittivity. Equation 4.3 refers to the self-consistent Poisson equation that computes the electrostatic potential in the presence of the solute ions while Equation 4.4 and Equation 4.5 refer to the Nernst-Planck equation describing the electrodiffusion in terms of concentration of the ionic species across the membrane. Since we are interested in the steady-state distributions of the ions in the vicinity of the nanopore, the current continuity equations are set to 0. A modified version of the above equations was used to explore the ionic distribution around nanopores in salt concentration gradients by Xie et al.[104]

The Equations (4.3) to (4.4) were solved simultaneously using COMSOL 5.3a using the *Transport of Diluted Systems* module coupled to the *Electrostatics* module. We fixed the salt gradient to be 1 mM on the trans side and 100 mM on the cis side, by defining the corresponding concentration as the boundary conditions on the top and bottom walls. Similarly, the boundary conditions on the electric field were set by defining the upper wall of the cis side as a ground whereas the bottom wall of the trans side was set to the applied voltage. The surface charge of the pore rim was set to 2 times the surface charge of the top and bottom surface to address the higher reactivity of the pore rim. We then sweep through different pore sizes, surface charges and applied voltages. By measuring the net ionic current through the nanopore for different applied voltages, we can simulate the current-voltage relationships. We can then use the same method as applied to the experimental data to extract the osmotic current and voltage. A similar setup was utilized by Rollings et al.[230] to investigate ion selectivity in graphene nanopores.

The continuum PNP model described above is quite useful to investigate electrodiffusion

of charged species in ion channels, however, there are a few known shortcomings. These include the neglect of finite volume effect of the ionic particles and correlation effects (such as ion-ion interactions and steric effects). While there have been a few known corrections and modifications to the PNP theory, they have not been considered in our model. Alternately, many other ab-initio methods can also be used to investigate electrodiffusion in narrowly confined ion channels such as molecular dynamics (MD), brownian dynamics (BD) and Monte-Carlo simulations. Each of these methods offers their own unique advantages to analyze ionic flows at varying length scales which we are yet to explore.

4.6 Supplementary Data

4.6.1 Heat discussion

Water heating

First, we set out to estimate the heating effect of the laser power when it penetrates through water. We used the following equation derived by[231] to estimate the steady state change of temperature ΔT: $\Delta T = \frac{\alpha}{2\pi \cdot C} \cdot [\ln(\frac{2\pi \cdot R}{\lambda}) - 1] \cdot P$, where α is the absorption coefficient (0.0114 for 475 nm and 0.322 for 643 nm[232]), λ the wavelength of the laser used, P the laser power (150 mW, full theoretically possible power), C the thermal conductivity of water (0.60 W m^{-1} K) and R the distance to the surface of the flow-cell. For both wavelengths, the temperature increases are below 0.01 °C, which means that we can neglect any heating effects of the water.

Chip heating

Since we are working with a non-focused laser of about 1 mm spot size (Figure S4.1) we irradiate not only the silicon nitride membrane but also some of the silicon that is found outside the membrane. To estimate the heat produced by this system we simulated the geometry in COMSOL. We designed a 50 µm squared, 20 nm thick nitride membrane in a 5 mm dice of silicon. Water is placed in a circular fashion on top and on the bottom of the chip. A 10 x 10 mm^2 PMMA block is placed around the system and the outer boundaries of this block have been set to room temperature. An illustration of the simulated geometry can be found in Figure S4.6a. The silicon nitride aperture and the silicon are treated separately using two instances of the deposited beam power module. Since the silicon nitride is transparent, we assume an absorbance value of only 10 % as previously calculated.[233] On the other hand, the absorbance of the silicon part was set to 70 %, since 30 % of the light gets reflected on its polished surface[234] (Figure S4.6b). The spot size to calculate the power flux was set to 1 mm, whereas the deposited Gaussian beam profile was set to a standard deviation of 250 µm to correspond to the commonly used 4-σ value of beam width. The resulting temperature profile in the case of a 1.5 mW cm^{-2} intensity can be found in Figure S4.6c. Figure S4.6d shows the temperature distribution along the z-axis of the nanopore chip for different laser powers. A small peak is found at the nitride membrane. In general, the highest possible temperature

increase at its peak value is about 4 °C. These values are absolute upper limits since we do not take into account any losses happening due to scattering on the PMMA flow-cell and intensity losses when the light penetrates the glass slide covering the flow-cell. We can expect that the real temperature increases to be substantially lower than the values estimated here.

Viscosity effect

In this part, we estimate and rule out the influence of temperature on the observed results. Here, we ignore any influence of the surface charge and concentrate on the temperature dependence of the KCl conductivity. Electrolytic conductivity (σ) values of KCl (concentrations ranging from 10 mM to1 M) in a temperature (T) range of 0 °C to 50 °C were extracted from the NIST standards for electrolytic conductivity.[235] Since the conductivity-temperature relationship is linear in this range, we extracted parameters a and b from: $\sigma = a \cdot T + b$. We can then extract the temperature corresponding to a certain nanopore conductance using: $T = \frac{\sigma - b}{a}$, where $\sigma = G \cdot \left[\frac{4l}{\pi d^2} + \frac{1}{d}\right]^{-1}$.[54] In these calculations, we assume that the pore diameter and length does not change. We used a suspended MoS_2 layer in a 50 nm nitride hole. In this configuration, the MoS_2 layer reaches until the nitride edge producing a pore of diameter 50 nm and a thickness of 21 nm (20 nm nitride + ≈ 1 nm MoS_2). The advantage of this configuration is its higher temporal stability. In Figure S4.7 we measured the conductance of this nanopore at different symmetric salt concentrations of 1 M, 100 mM, and 10 mM. If we apply the same temperature analysis, we observe that higher temperature differences are needed to explain the data at a low salt concentration (up to 60 °C). This is not consistent with the reasonable assumption that the laser heating is independent of the ion concentration. There must be another, concentration-dependent variable at play: the surface charge.

Chemical potential

Other than viscosity changes, heat also influences the chemical potential difference. We can express the osmotic voltage observed in Figure 4.3b in a simplified way using the reversal potential: $\mathrm{V_{diff}} = \mathrm{S(\Sigma)_{is}} \frac{\mathrm{RT}}{\mathrm{F}} \ln\left[\frac{\mathrm{a^{cis}_{KCl}}}{\mathrm{a^{trans}_{KCl}}}\right]$, where V_{diff} is the measured osmotic potential, $S(\Sigma_{\mathrm{is}})$ is the ion selectivity and the logarithmic expression the concentration gradient. To estimate the pure thermal effect, we assume that the laser is not influencing the ion selectivity, so we set $S(\Sigma_{\mathrm{is}})$ is to a fixed value (selectivity in the dark state) and vary T in order to obtain the values measured. In the case of the smaller, 3 nm pore, a temperature differences of 118 °C and 73.9 °C are needed to explain the change due to a 643 nm and 475 nm laser irradiation. For exactly the same laser conditions these values drop to 11.5 °C and 6.5 °C for the 10 nm pore. Realistically, no difference should be seen between the two cases since an enlarged nanopore does not influence how the laser heats the system. Furthermore, the values obtained for the small nanopore are at least an order of magnitude away from anything we could expect from the previous estimation.

Electrical double layer thickness

In order to estimate the influence of the temperature on the EDL we analytically calculate the thickness of the EDL for different temperature (Figure S4.8a). The thickness of the EDL corresponds to the Debye length. With the Debye-Hückel approximation we can calculate the Debye length λ as:[236] $\frac{1}{\lambda} = k = \left(\frac{e^2 \sum_i n_i^\infty z_i^2}{\epsilon_0 \epsilon_r k_b T}\right)^{\frac{1}{2}}$, where κ is the Debye-Hückel parameter, ϵ_r the relative permittivity of water, ϵ_0 the permittivity of vacuum, k_B Boltzmann's constant, T temperature, n_i the bulk volume density, z_i the valence (in the case of KCl: $\sum_i n_i^\infty z_i^2 = 2n^\infty$ and e the electron charge. Since ϵ_r depends on the temperature as well we can use an analytical approximation to calculate its value.[237] Since the EDL length actually decreases a few picometers per °C of increased temperature, we cannot expect to see any improvement of the pore ion selectivity due to temperature changes and EDL thickness.

Surface charge

The surface charge of MoS_2 in water is estimated through the following chemical equilibrium:

$$MoS_2 + H_2O \rightleftharpoons MoS_2 - OH^- + H^+ \tag{4.6}$$

We can estimate the diffuse layer electrostatic potential Φ_s (Zeta potential) of the surface by:[175,238] $\Phi_s = \frac{K_B T}{e}\left(\ln \frac{-\sigma}{e\Gamma + \sigma} + \ln(10)(\mathrm{pK} - \mathrm{pH})\right)$, where σ is the surface charge and Γ the density of reactive sites. The pK of nanocrystalline MoS_2 has been measured to be around 3.1.[188] We estimate the surface potential at different temperatures and pH using a pK value of 3.1 and a surface charge value of $-50\,\mathrm{mC\,m^{-2}}$. The surface potential changes with temperature, but the rate of this change is highly dependent on the pH as calculated in Figure S4.8c. For instance, at pH 7 the rate is just below $1\,\mathrm{mV\,K^{-1}}$ whereas at pH 4 the rate is only about $640\,\mu\mathrm{V\,K^{-1}}$. Such an increase in surface potential might well improve the repulsion of cations and therefore increase the ion selectivity. Assuming we get a temperature increase of 10 °C then we could expect a 10 mV stronger surface potential. To put this value into context we can estimate the pH change needed to induce the same increase in surface potential. From Figure S4.8d we can see that the surface potential reduces 58 mV per pH unit. In order to get a 10 mV decrease, we would thus need a pH change of roughly 0.2, which is well within the error of our buffer system, especially at low dilutions.

Electrode potential

Last but not least, the redox potential generated at the interface of the Ag/AgCl electrode with the ionic solution also depends on the temperature. Depending on the salt concentration the potential can increase between $200\,\mu\mathrm{V\,K^{-1}}$ to $600\,\mu\mathrm{V\,K^{-1}}$ (Figure S4.8b). This is relevant if the whole system is heated and has to be considered if one wants to calculate the effective

osmotic power generated by the membrane. In the case of laser irradiation, we can neglect any influences originating from the redox potential since we are not affecting the temperature that far away from the membrane.

4.6.2 Derivation of the modified GHK equation

4.6.3 Surface conduction domination

Deviations in conductance from bulk predictions have been observed in nanopores with high aspect ratios $\frac{L}{D} < 1$[57] and were linked to a large contribution of the surface conductivity, described as the ratio between surface and bulk conductivity: $l_{Du} = \frac{\kappa_s}{\kappa_b}$, where κ_s is the surface conductivity and κ_b the bulk conductivity. The Dukhin length, l_{Du}, can be approximated using the surface charge σ and the bulk ion concentration c_s as: $l_{Du} \approx \frac{\sigma}{2c_s e}$. The surface charge of the MoS_2 membrane was fixed to –50 mC m^{-2} as previously estimated (Figure 3.2 (page 66)). The Dukhin lengths on both sides are then 2.6 nm and 26 nm respectively (Figure 4.6a). Since this formalism has been developed for symmetrical salt concentrations, we set the effective Dukhin length to 2.6 nm and thus provide the lower limit of the effect by underestimating the surface conduction effect. To further quantify the contributions of the surface and bulk conductances to the ionic current inside the pore we refer to the Dukhin number which is defined as: $Du = \frac{4l_{Du}}{D}$, where D is the pore diameter.[57] The Dukhin number of the 3 nm pore is 3.5 suggesting a large surface conductance contribution, whereas the 10 nm has $Du = 1$ (equal contributions). In order to calculate the osmotic voltage in the surface conductance dominated regime, we need to know the distribution of the ions in the vicinity of the membrane: $c_{K^+}^{\text{trans}}$, $c_{Cl^-}^{\text{trans}}$, $c_{Cl^-}^{\text{cis}}$ and $c_{K^+}^{\text{cis}}$. Using FEM simulations we estimate these ion concentrations as a function of distance to a charged membrane (Figure 4.7a). The bulk concentrations of potassium (K^+) and chloride (Cl^-) are identical and simply denoted as c_{cis} and c_{trans}. We rewrite the GHK equation to account for the surface conductance as well as the bulk conductance:

$$E_{\text{total}} = \frac{RT}{F}\left[R_b \cdot \ln\left(\frac{P_{K^+/Cl^-} \cdot c_{\text{cis}} + c_{\text{trans}}}{P_{K^+/Cl^-} \cdot c_{\text{trans}} + c_{\text{cis}}}\right) + R_s \cdot \ln\left(\frac{P_{K^+/Cl^-} \cdot c_{K^+}^{\text{cis}} + c_{Cl^-}^{\text{trans}}}{P_{K^+/Cl^-} \cdot c_{K^+}^{\text{trans}} + c_{Cl^-}^{\text{cis}}}\right)\right] \tag{4.7}$$

Where P_{K^+/Cl^-} is the permeability ratio, R_b and R_s are the contribution ratios of the bulk conductance and surface conductance that satisfy $R_s + R_b = 1$ and are estimated using the Dukhin number: $R_b = \frac{1}{1+Du}$ and $R_s = \frac{Du}{1+Du}$, effectively scaling the reverse potential to surface and bulk contributions. We estimate the permeability values P_{K^+/Cl^-} by geometrically estimating the area affected by the EDL inside the pore:

$$P_{K^+/Cl^-}(D) = P_{\max}\frac{A_{\text{EDL}}}{A_{\text{total}}} = P_{\max}\frac{\pi(\frac{D}{2})^2 - \pi(\frac{D}{2} - \lambda)^2}{\pi(\frac{D}{2})^2} \tag{4.8}$$

, which can be simplified to:

$$P_{K^+/Cl^-}(D) = 4\lambda \cdot P_{\max}\frac{D - \lambda}{D^2} \tag{4.9}$$

The Debye length, λ, was defined as 1 nm inside the nanopore. The value of the maximal permeability ratio, $P_{\max}$ was chosen to be 100 to best reflect the values obtained through FEM simulations (Figure S4.5a) and experimental studies.[206]

4.6.4 Surface charge measurements

In order to estimate the influence of the laser light on the MoS_2 surface charge, we performed conductance measurements in KCl electrolyte with different conductivities. The analysis of the surface charge is based on the work of Lee et al.,[57] who developed an analytical expression of the nanopore conductance G by taking into account the surface conductance:

$$G = \kappa_b \left[\frac{4l}{\pi d^2} + \frac{1}{1 + 4\frac{l_{Du}}{d}} + \frac{2}{\alpha d + \beta l_{Du}} \right]^{-1} \tag{4.10}$$

, where κ_b is the bulk conductivity, l the pore thickness, D the pore diameter and the geometrical factors $\alpha = \beta = 2$. As previously mentioned l_{Du} is the Dukhin length defined as $l_{Du} = \frac{\kappa_s}{\kappa_b}$. We prepared dilutions of KCl electrolyte with the following measured conductivities κ_b: 0.0303 S m^{-1}, 0.0311 S m^{-1}, 0.0347 S m^{-1}, 0.0605 S m^{-1}, 0.3123 S m^{-1}, 1.447 S m^{-1} and 11.03 S m^{-1}. We then measured the ionic conductance of our nanopore system for a 3 nm and a 10 nm pore with and without laser illumination (λ = 643 nm and λ = 475 nm). The conductance is estimated from the slope of the linear I-V characteristics. All measurements were taken in triplicates. In Figure S4.3a-d we show the obtained conductance values for each conductivity (circles). The error bars range from minimal to maximal measured value, emphasizing the reproducibility of the measurement. We use this measured relationship between nanopore conductance and KCl conductivity to estimate the surface conductance κ_s of Equation 4.10. This is done through a curve fit. The fit (dashed line) and the obtained values for the surface conductance are reported in Figure S4.3a-d. We can calculate the surface charge σ for a given κ_s through the relationship:

$$\sigma = 2 \cdot c \cdot e \frac{\kappa_s}{\kappa_b} \tag{4.11}$$

,where c is the ion concentration and e the elementary charge. We know that preparing very low dilutions of KCl can be very challenging in practice, we estimate the effective ion concentration for a given buffer from the measured conductivity κ_b. We use the Kohlrausch's law to convert the conductivities to ion concentration:[239]

$$\Lambda = \Lambda^0 - (A + B\Lambda^0)\sqrt{c} \tag{4.12}$$

, where Λ is the molar conductivity ($\Lambda = \frac{\kappa_b}{\kappa_c}$, A = 60.20 and B = 0.229 constants and Λ_0 = 149.79 m^2 S mol^{-1} the molar conductivity at infinite dilution. Figure S4.3c-h shows the resulting surface charges for the different conditions. The apparent increase of the surface charge for the high κ_b value is due to a simplification in Equation 4.11, which leads to an overestimation of the surface charge in highly concentrated KCl solutions.[57] The error bars S_σ are estimated

through propagating the errors using the variance formula:

$$S_\sigma = \sqrt{(\frac{2e\kappa_s}{\kappa_b})^2 \cdot S_c^2 + (\frac{2ce}{\kappa_b})^2 \cdot S_{\kappa_s}^2 + (\frac{2ce\kappa_s}{\kappa_b^2})^2 \cdot S_{\kappa_b}} \tag{4.13}$$

, where S_{κ_b} is the error in the conductivity measurement (estimated to be 5 %), S_{κ_s} the uncertainty of the fit and S_c the error in estimating the ion concentration (estimated to be 10 %).

4.6.5 Supplementary figures and tables

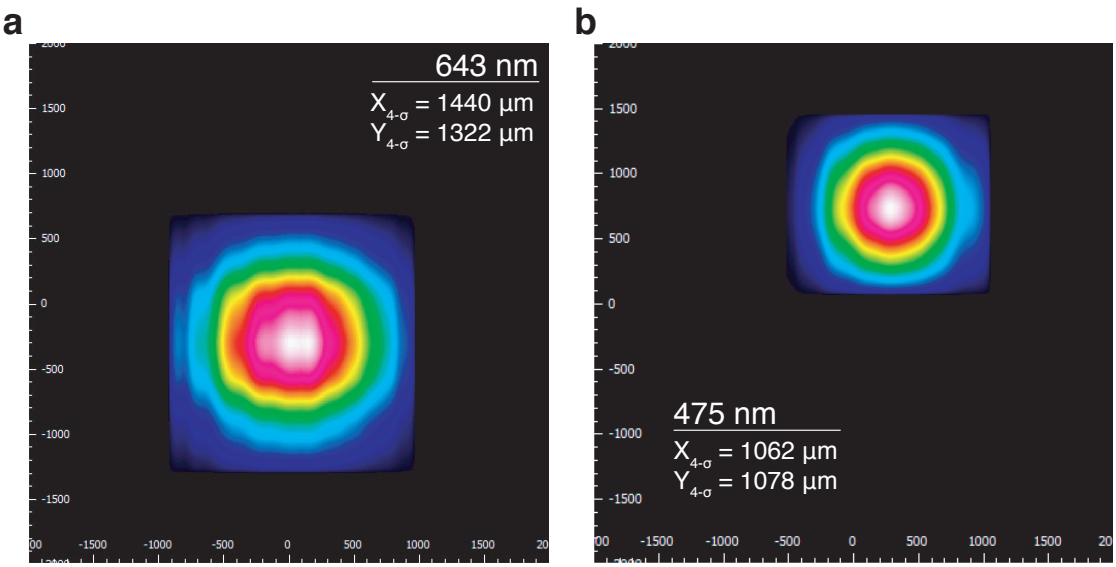

Figure S4.1 – Laser spot size. Measured laser spot sizes for the two diode lasers with wavelenghts 643 nm (**a**) and 475 nm (**b**). *This Figure was published in Joule, 2019, Graf et al.*[212]

Set power [mW]	Real power 643 nm [mW]	Real power 475 nm [mW]
150	135.9	-
140	127.1	-
130	117.9	-
120	109.1	-
100	91.7	98.3
50	47.1	49.1
20	19.89	19.6
10	10.7	9.76
1	1.8	-

Table S4.1 – Laser powers. The *set power* is the power value entered in the program. The real power is the corresponding power measured with a power meter.

Salt concentration	Absolute potential	Potential difference	Theoretical potential difference
1 M	31.7 mV	0 mV	0 mV
10 mM	82.9 mV	51.2 mV	58.6 mV
100 mM	135 mV	103.3 mV	117.13 mV
1 mM	185 mV	153.3 mV	175.7 mV

Table S4.2 – Electrode potentials. The potential differences are given with respect to 1 M.

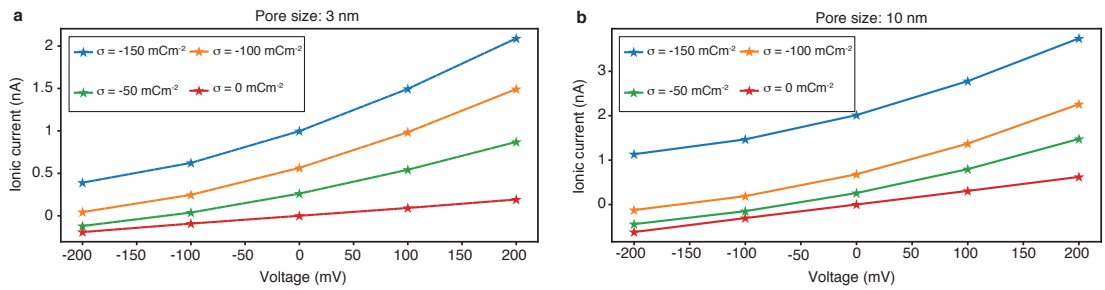

Figure S4.2 – Simulated effect of the surface charge. Simulated I-V characteristics for the 3 nm (**a**) and 10 nm (**b**) pore. The experimentally observed upwards shifts (Figure 4.1**c**) of the I-Vs is reproduced by this COMSOL model. *This Figure was published in Joule, 2019, Graf et al.*[212]

	643 nm		475 nm	
10 nm pore	Dark	752 mW cm^{-2}	Dark	1.3 W cm^{-2}
Osmotic Current	1.41 nA	1.63 nA	1.32 nA	1.48 nA
Osmotic Voltage	95.64 mV	98.63 mV	92.30 mV	95.37 mV
Osmotic Power	134.72 pW	160.85 pW	122.09 pW	140.66 pW
3 nm pore				
Osmotic Current	172.76 pA	291.34 pA	207.99 pA	283.98 pA
Osmotic Voltage	71.03 mV	98.20 mV	73.21 mV	91.86 mV
Osmotic Power	12.41 pW	28.67 pW	15.33 pW	26.27 pW

Table S4.3 – Overview of results. Mean values of the dataset reported in Figure 4.3 and Figure 4.4

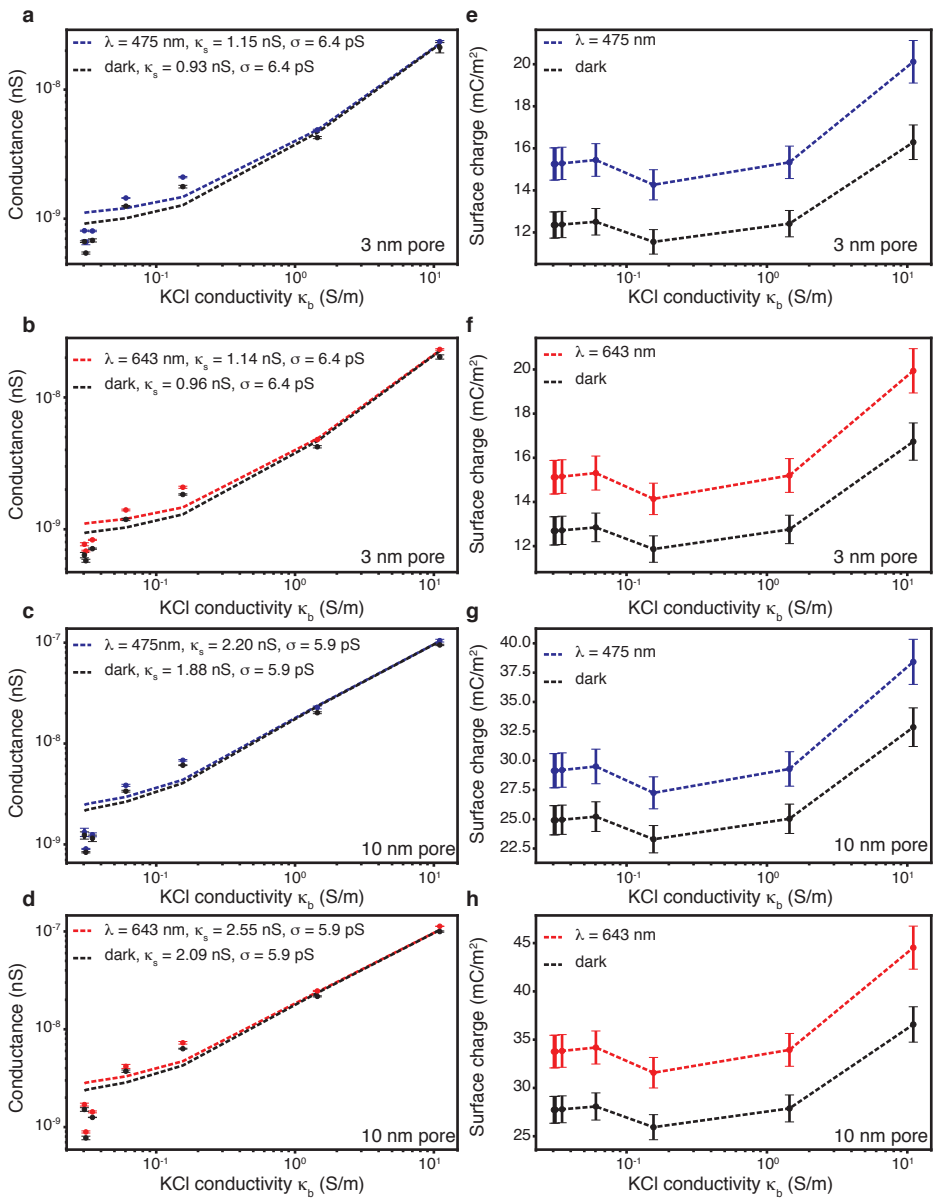

Figure S4.3 – Surface charge measurements. a-d, Conductance measurements (triplicates) of a 3 nm (**a-b**) and a 10 nm (**c-d**) pore for different KCl conductivities and different laser wavelengths (**a**, **c**: 475 nm, **b**, **d**: 645 nm). The dashed lines denote the fit of the conductance equation (Equation 4.10) to extract the surface conductance κ_b. These values are then used to calculate the surface charge at each measurement point (**e-h**). The error bars in **a-d** are the spread of the datapoints of the triplicate measurement. In **e-h** the error bars are estimated through error propagation. A detailed analysis and information on the error propagation can be found in subsection 4.6.4. The flux of the 643 nm and the 475 nm laser were 0.75 W m^{-2} and 1.3 W m^{-2}, respectively. *This Figure was published in Joule, 2019, Graf et al.*[212]

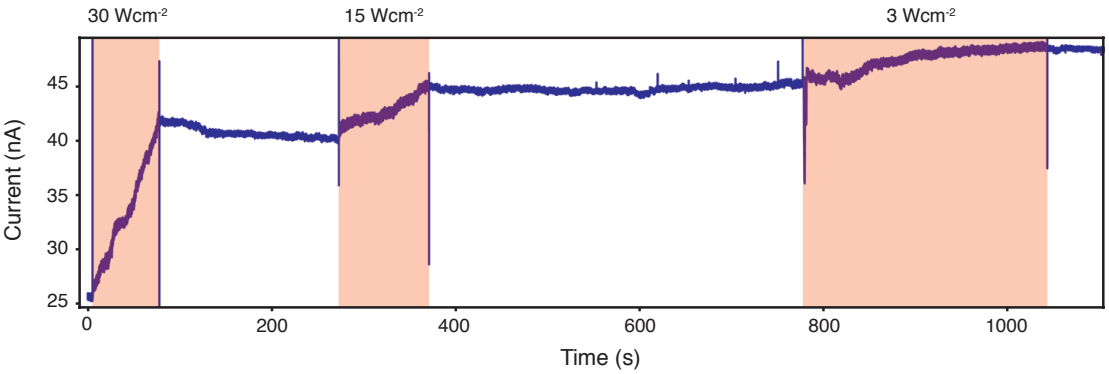

Figure S4.4 – Photo-oxidation. Enlargement of the nanopore for different photon fluxes for the 643 nm laser. *This Figure was published in Joule, 2019, Graf et al.*[212]

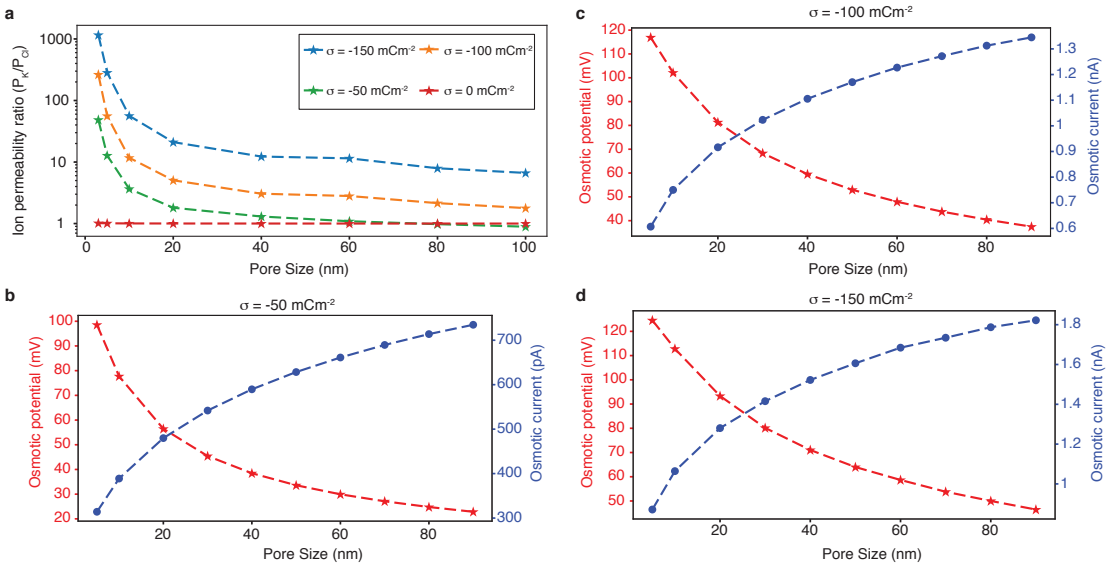

Figure S4.5 – Permeability ratio simulations. **a**, Simulated permeability ratio. **b**-**d**, Osmotic voltage and current for versus pore sizes for surface charges of $-50\,\mathrm{mC\,m^{-2}}$ (**b**), $-100\,\mathrm{mC\,m^{-2}}$ (**c**) and $-150\,\mathrm{mC\,m^{-2}}$ (**d**). *This Figure was published in Joule, 2019, Graf et al.*[212]

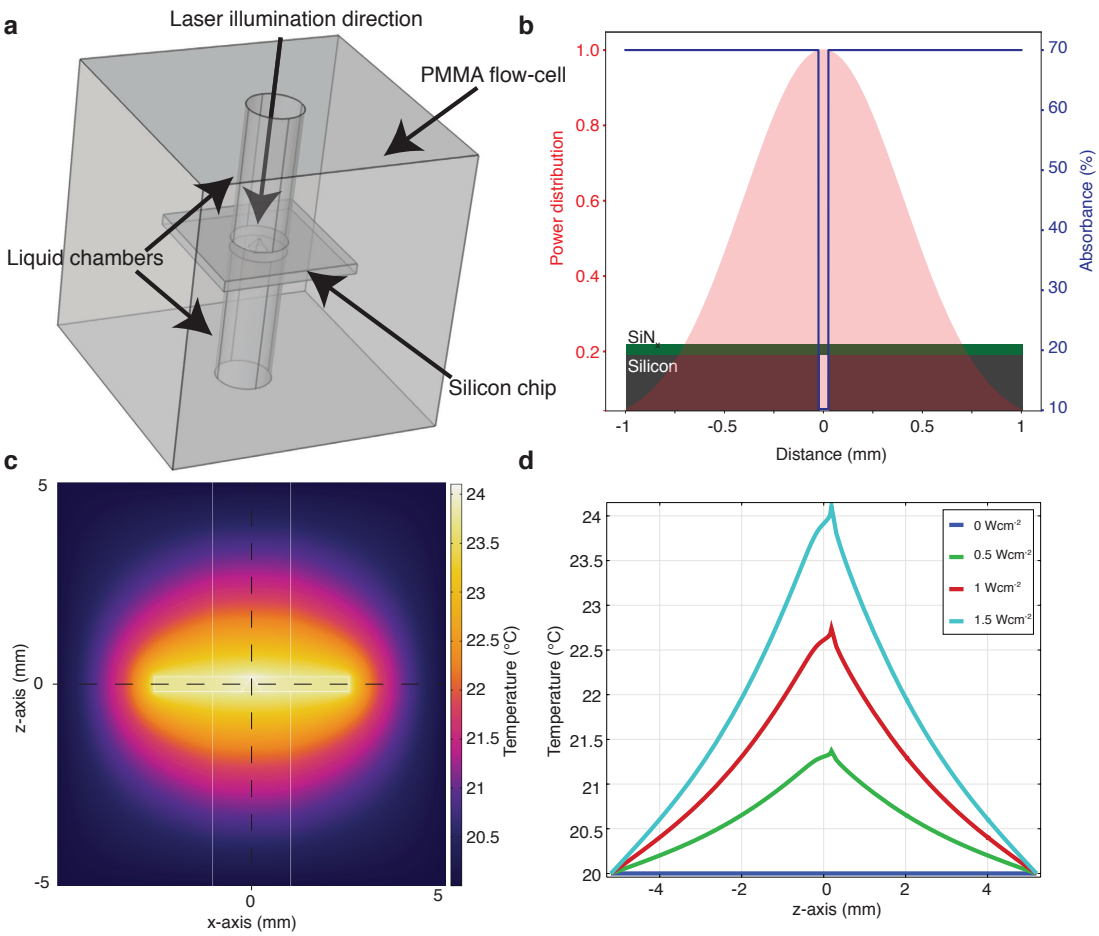

Figure S4.6 – FEM simulation of the heat produced by the laser. a, The geometry of the model used to reproduce as closely as possible the experimental situation. **b**, Illustration of the power distribution irradiating the surface of the chip (red) and the different absorbance values over the surface. **c**, Heat map of the z-x axis of the system. **d**, The temperature profile along the z-axis and through the centre of the membrane. *This Figure was published in Joule, 2019, Graf et al.*[212]

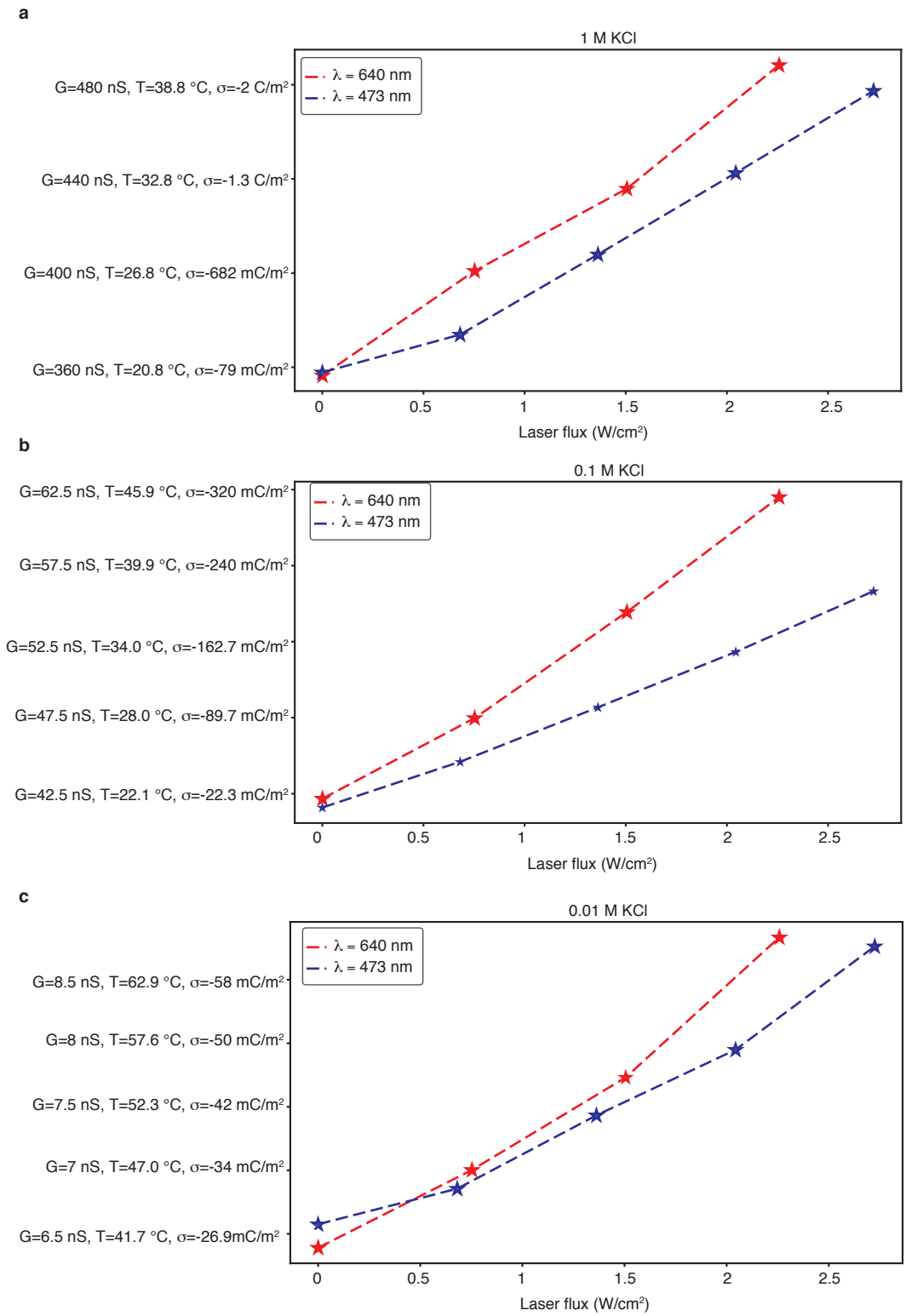

Figure S4.7 – Heat calculation. Laser Influence on the conductance of a silicon nitride nanopore at concentrations of 1 M (**a**), 100 mM (**b**) and 10 mM (**c**) KCl. The conductance G is measured, whereas the temperature T and the surface charge σ are calculated according to the main text in order to estimate the necessary temperature or surface charge change to explain the observed data. *This Figure was published in Joule, 2019, Graf et al.*[212]

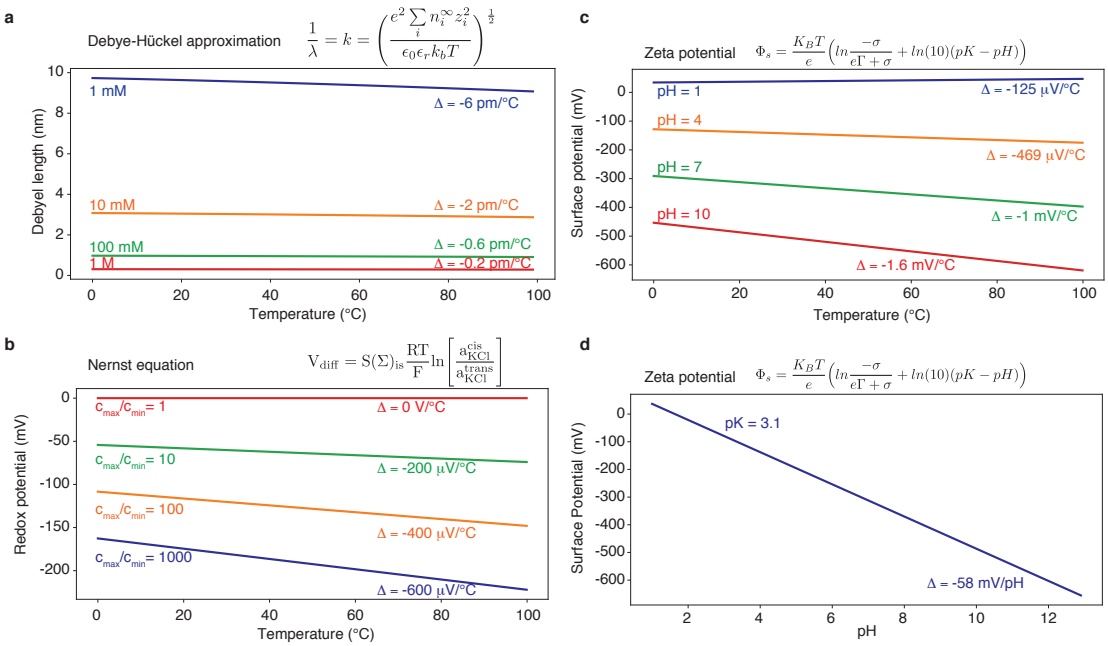

Figure S4.8 – Analytical heat estimation. a, Debye length vs temperature for different ionic dilutions. The data has been calculated using the Debye-Hückel approximation[236] and an analytical estimation of the dielectric constant of water.[237] **b**, Nernst potential vs. temperature for different concentration gradients. **c**, The surface potential vs temperature for different pH values. **d**, The surface potential as a function of pH for assuming a pK of 3.1. *This Figure was published in Joule, 2019, Graf et al.*[212]

5 Transverse Detection of DNA in a MoS_2 Nanopore

5.1 Summary

Classical nanopore sensing relies on the measurement of the ion current passing through the nanopore. Whenever a molecule electrophoretically translocates through the narrow constriction, it modulates the ion current. This approach allows the precise measurements of single molecules. However, the access resistance limits the spatial resolution in ionic sensing. This limitation can potentially be overcome by an alternative sensing scheme taking advantage of the current across the membrane material itself. In this work, I present the fabrication of an electrically contacted molybdenum disulfide (MoS_2) nanoribbon with a freestanding part where a nanopore can be drilled. I show proof-of-concept data on supported nanoribbons. Correlated signals were recorded in both measurement channels. The results point towards a field-effect sensing scheme where the charges of the molecule are directly sensed by the nanoribbon. I will discuss different sensing schemes such as local potential sensing and direct charge sensing. Furthermore, I show that the fabrication of contacted, freestanding MoS_2 ribbons is reliable and I describe the challenges that arise in the fabrication and usage of these devices.

5.2 Introduction

Solid-state nanopores have become a versatile tool to analyze single-molecules of deoxyribonucleic acid (DNA) or proteins. A small hole in a thin membrane separates two compartments filled with saline solution. A transmembrane voltage generates an electric field around the nanopore. This field captures charged molecules in solution and electrophoretically drives them through the orifice. In the hope of achieving single-base resolution for sequencing, ultrathin membranes based on graphene[23–25] and MoS_2 have been investigated as a mean to provide a spatial resolution approaching the inter-base distance.[28,29] However, the sensing length of a nanopore in an ultrathin material does not correspond to the physical thickness of the membrane due to the domination of the access resistance. This is a physical limit

common to all ionic current measurements using nanopores and originates from the passage of ions from the bulk to the confined space of the nanopore. To overcome this limitation, a different sensing method is needed. Nonetheless, extending the sensing signal by an independent readout, would not render the nanopore obsolete but change its function. The nanopore would then act as a localizer, bringing single-molecules from free diffusion in solution to a well-defined location (the nanopore). Combining nanopores with fluorescently tagged analytes provides an optical readout system, where the responsibility of the nanopore is solely the single-molecule loading of the analyte.[85,213,240–243] Another example of a device where the nanopore is used merely as a DNA loading tool to improve an existing technology is presented by Larkin et al.[244] Nanopores placed on the bottom of optical cavities improve the single-molecule real-time (SMRT) DNA sequencing by voltage-induced DNA loading.[244] Other than optical readouts, two alternative approaches have been addressed in the literature: tunneling electrodes and field-effect sensing.

5.2.1 Tunneling electrodes and field-effect sensing

Electrodes that can measure the current across passing nucleotides were first theoretically investigated by Zwolak et al.[88] For this process to work, electrodes should be placed immediately at the nanopore mouth to achieve the small distance needed for electron tunneling to work. Experimental attempts to fabricate such devices showed that to achieve true tunneling detection, the distance between the electrodes needs to be smaller than 2.5 nm.[92–94] Even though nanofabrication methods have improved substantially over the years, it is still extremely challenging to achieve the precision needed using conventional nanofabrication methods. One possible approach to create a tiny nanogap is the use of break junctions through mechanically bending the substrate.[245–249]

Instead of trying to measure the tunneling current directly between an electrode and a nucleotide, a recognition molecule can be used to link the two. This would allow a chemical bond between the electrode and the nucleotide through Watson-Crick recognition.[96] Electron-tunneling junctions have shown differences in peak current when single nucleotides formed short hydrogen bonds with the recognition adapter fused to an electrode.[91] However, devices integrating a recognition tunneling electrode with a nanopore have not yet been realized.

The first nanopore-field-effect-sensor was based on silicon nanowires and showed that the local potential around a nanopore can be measured during DNA translocation.[104] When graphene emerged, it sparked interest as a membrane material in nanopore sensors.[23–25] Compared to the silicon nitride (SiN_x) membranes, the graphene membrane is more conductive and thus allows current to pass. The possibility of measuring simultaneously the ionic current and the sheet current motivated researchers to create hybrid devices. Graphene can acquire a bandgap when sculpted to a nanoribbon, therefore becoming a field-effect sensor.[250] Different research groups have attempted to measure simultaneously the ionic current and the graphene sheet current during DNA translocation through a nanopore.[101–103] However,

difficulties in the fabrication of the nanoribbons, device yield, and capacitive cross-talks have severely limited the use of these sensors.

When MoS_2 was first introduced as a membrane material for nanopore experiments,[28] the intrinsic bandgap of the material[113] has drawn the attention of theorists for its potential use of the sheet current for DNA sequencing.[105,106] Furthermore, a functionalized MoS_2 field-effect transistor (FET) has been shown to be very sensitive in detecting ultralow concentrations of analytes. When compared to 2D-graphene FET devices, a MoS_2-FET performed 74-times better in detecting biomolecule absorption,[251] emphasizing the potential practicality of this intrinsic semiconductor.

Here, I present a hybrid nanopore-FET device based on monolayer MoS_2. I will discuss the design, challenges in the fabrication and present the measured data. To better understand the observed signals I will qualitatively discuss possible sensing mechanisms.

5.3 Device Fabrication

5.3.1 Design principles

Before describing the fabrication of the device, I would like to shortly summarize the most important design decisions that we defined initially.

Ribbon To restrict the electron flow to the region of interest, we need to sculpt the MoS_2 crystal into a thin ribbon. This is important to increase the sensitivity of the device.[106] However, dimensions that are too small might introduce a higher proportion of defective sites, which could impede the conductance.[252]

Freestanding The MoS_2 membrane should be freestanding, to maintain a high ionic current and signal-to-noise ratio (SNR). Further, the field drop occurring at a thin nanopore is stronger, which can increase the chance of observing a gating effect.[253] Last, the carrier mobility in freestanding MoS_2 is substantially higher than on the supported counterpart.[254]

Alignment Different fabrication steps need to be precisely aligned with each other. Ideally, an alignment precision of less than 100 nm is required.

Large-Scale Ideally, most fabrication steps should be done on a wafer-scale to increase device yield.

Reproducibility The fabrication, as well as the practical usage of the final device, should be as easy as possible to increase reproducibility.

Obviously, to maintain good sensitivity, the dimensions of the ribbon should be as small as possible. On the other hand the smaller the dimensions the more challenging the fabrication

process becomes. Especially the alignment between different steps will become very difficult if the ribbon width approaches sizes of about 200 nm. For a proof-of-principle device, I have fixed the width of the ribbon to be 500 nm and the length to 2 µm.

A schematic representation of the proposed nanopore-FET device is shown in Figure 5.1a, with its equivalent electronic circuit depicted in Figure 5.1b. The goal is to design a narrow ribbon of MoS_2 (500 nm x 2 µm) on top of an aperture in a conventional SiN_x membrane. The ribbon is then contacted with metal leads to provide the source and drain contacts. A dielectric material then needs to be deposited on the metal to electrically insulate the contacts from the electrolyte. A thick dielectric layer limits the cross-talk induced by capacitive coupling[102] and avoids any electrochemical reactions between the metal and the electrolyte. Figure 5.1c and d show transmission electron microscopy (TEM) images of finished devices as a proof of the successful fabrication process. To increase the yield of the devices, we fabricate three ribbons per membrane, from which only one (the middle ribbon, Figure 5.1c) has a freestanding part. The two supported ribbons, designed as a control, also act as a backup and are used for experiments in a supported configuration. Suspending the MoS_2 over an aperture has two reasons: first, the ultrathin nature of the MoS_2 membrane allows for very high signal-to-noise in the ionic channel due to improved ion flow. Second, the thinner the membrane and the smaller the nanopore the larger the voltage drop provoked by DNA translocations will be.[253] The FET will, therefore, benefit from larger conductance modulations and the chances of detecting translocation events will be increased. In ideal conditions (pore diameter, D = 1.3 nm and membrane thickness, L = 0.6 nm) a potential change of 100 mV due to the translocation of DNA has been previously calculated.[253] For these reasons, I aimed to keep the MoS_2 membrane freestanding.

5.3.2 Summary of the fabrication steps

A more complete description of the fabrication steps and the equipment used can be found in section A.3 (page 178). The following is a short summary of the fabrication steps involved.

The basis of the device is a SiN_x membrane containing a 50 nm to 100 nm aperture created by e-beam lithography (EBL) and reactive ion etching (RIE) of the SiN_x layer. On this hole, a chemical vapor deposition (CVD) grown, single-crystal MoS_2 layer is transferred using a PMMA wet transfer approach (subsection 2.4.1 (page 45)) suspended and contacted via Ti/Au electrodes (EBL and e-beam assisted metal evaporation). The crystal is then etched into a thin ribbon using EBL and RIE (O_2 gas) to restrain the current flow to the area of interest. An area selective insulation is deposited on the metal leads using EBL and atomic layer deposition (ALD). In all EBL steps, a three-step alignment scheme is used to achieve the alignment precision needed (<50 nm, see subsection 5.3.3). A computer-aided design (CAD) summarizing the different fabrication steps can be found in Figure 5.2a. An optical micrograph of the finished device can be found in Figure 5.2b. Finally, a TEM as opposed to electrochemical reaction (ECR) is then used to drill a nanopore into the suspended part of

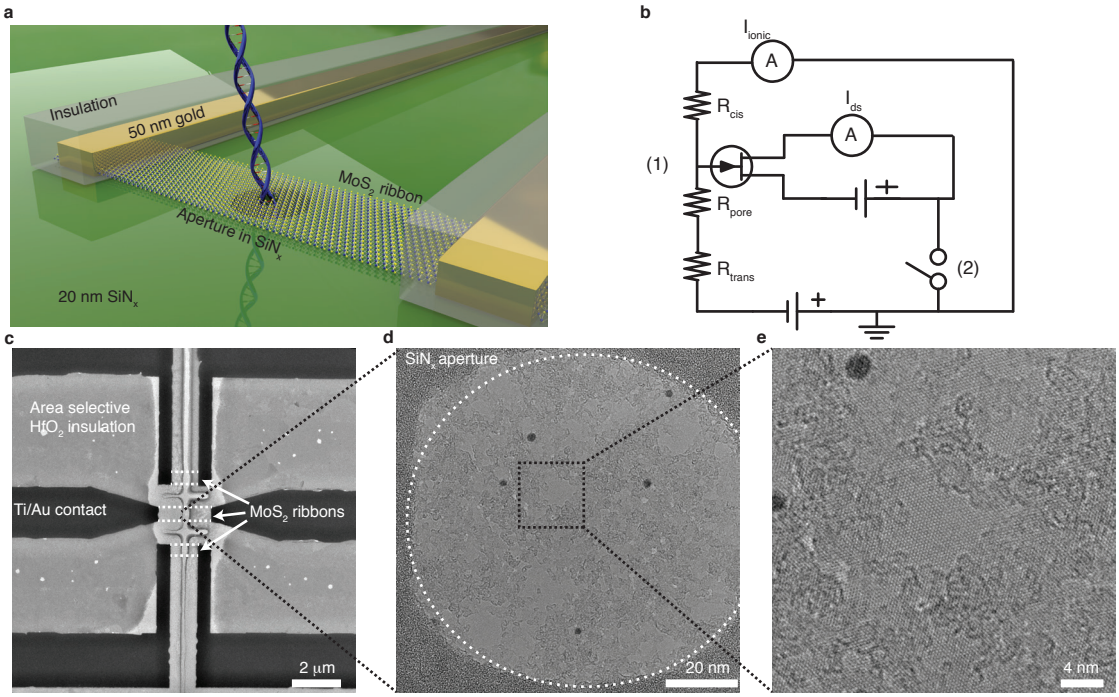

Figure 5.1 – Device design summary. a, A schematic of the proposed FET-nanopore device. Metal leads contact the monolayer MoS_2 crystal, which is subsequently etched into a ribbon. A layer of insulation around the electrodes avoids cross-talk and insulates the metal from the electrolyte. An aperture in the SiN_x membrane provides a part where the MoS_2 is freestanding. A nanopore can then be drilled through this freestanding part using a TEM. The translocating DNA will then simultaneously modulate the ionic current as well as the transverse current. **b**, The equivalent electrical circuit describing the two subcircuits, denoted here as ionic and transverse. The MoS_2 ribbon is represented by a transistor at the vicinity of the nanopore (1). To avoid current leakages we developed electronics to decouple the two grounds of the set-up (2). **c**, A TEM image of a finished device. Three ribbons are placed on the SiN_x membrane. The middle ribbon contains a suspended part. **d**, The suspended part of the middle ribbon. Crystalline monolayer MoS_2 is visible between patches of poly(methyl methacrylate) (PMMA) contamination.

the crystal (Figure 5.1d). At this stage the TEM also serves to characterize the device. After so many fabrication steps, especially in the initial stage when PMMA contaminations were substantial, it was crucial to inspect the integrity of the devices through TEM imaging. After a steep learning curve, we are at a point where the devices are clean enough for nanopore drilling using ECR.

Just before the experiment, a silicone elastomer is painted around the membrane to reduce the capacitance of the chip and provide additional insulation between the metal leads and the electrolyte (subsection 2.3.4 (page 41)).

To connect the device to the macroscopic world, the fabricated chip is glued to a custom-made printed circuit board (PCB) using double-sided polyimide tape and sandwiched by a custom made PMMA flow-cell (Figure 5.2c). A thin cylindrical access-pillar brings the buffer to the nanopore device, while keeping the wires dry (Figure 5.2d). The PCB is then connected

through a custom wired secure digital (SD) card connector to the set-up.

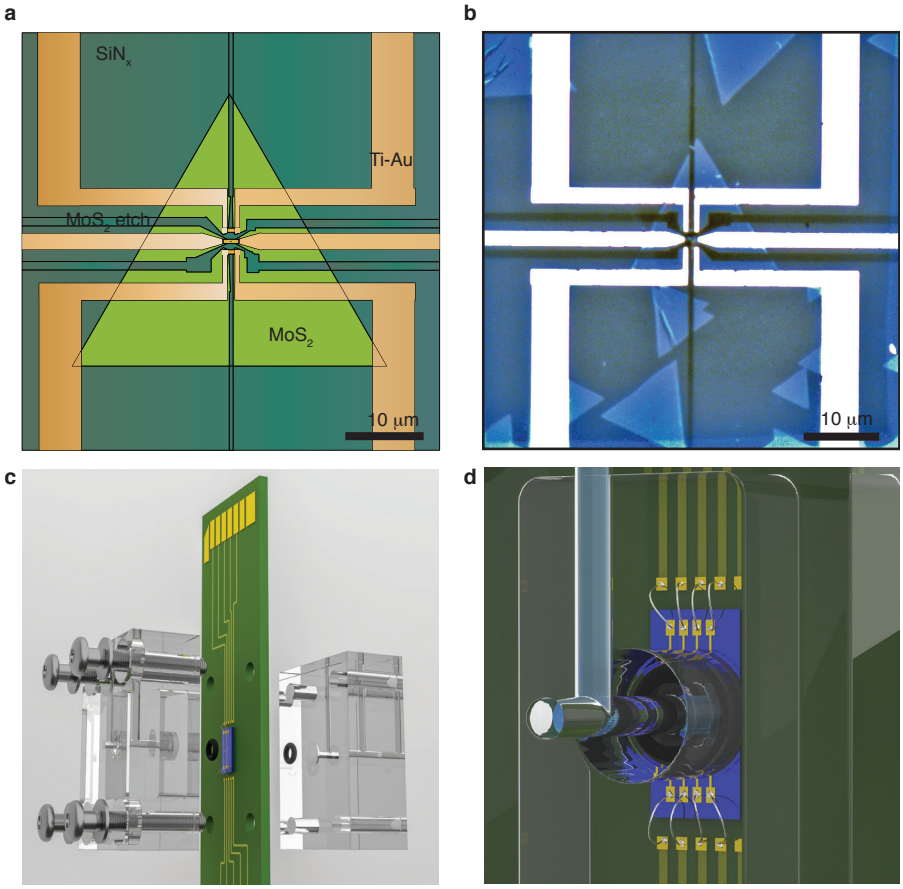

Figure 5.2 – Fabrication. a, CAD design schematics. In summary, a single-crystal of MoS_2 is transferred onto an aperture 50 nm to 100 nm in a SiN_x membrane. The crystal is then contacted through a Ti-Au electrode. A subsequent step etches the MoS_2 crystal into 500 nm wide ribbons connecting the two leads of each electrode. **b**, An optical micrograph taken before the electrodes were insulated. The dark lines are the etching patterns used to generate the ribbons. **c**, A render of the flow-cell set-up: the silicon chip containing the nanopore-FET is mounted on a custom made PCB and contacted through wire bonding. The chip is then sandwiched between two custom machined PMMA pieces and secured by screws. **d**, A close-up view of the assembled nanopore-chip. A pillar in the flow-cell brings the electrolyte to the surface while keeping the wires between the PCB and the chip dry.

5.3.3 Alignment of subsequent EBL steps

A three-step alignment is used in all EBL steps to precisely align the location of the aperture with the electrode deposition, the ribbon etching and the insulation (Figure 5.3). First, a pre-alignment marker containing an array of 50 µm squared pads at increasing distances of 1 µm is used to roughly align the 12 x 12 mm^2 sized substrate. Since every marker is at an increasing distance from its neighboring markers, the system can back-calculate the exact location of the center-marker from any three markers within the array. This is very useful since the whole array is about 1 mm in size. To run the alignment, any coordinate (with respect to

the holder) inside the array will result in correct pre-alignment. This greatly simplifies the manual alignment and measurements on the EBL holders. Second, alignment markers at each edge of the chip perform a global alignment by correcting for offset, scale, rotation, and keystone. Third, just before the pattern gets written, the last set of alignment markers just next to the SiN_x membrane is fine-tuning the alignment. This process allows alignment precisions greater than 50 nm judged by the shifts between the aperture in the SiN_x membrane and the MoS_2 nanoribbon (Figure 5.4a-c).

Together with the definition of the edges by the EBL as well as the resolution of the resist the alignment precision acts as the limiting step for the dimensions of the nanoribbon. The dimensions I chose for the ribbons (500 nm x 2 µm) are on the conservative side and I am confident that it is technically possible to fabricate much smaller ribbons.

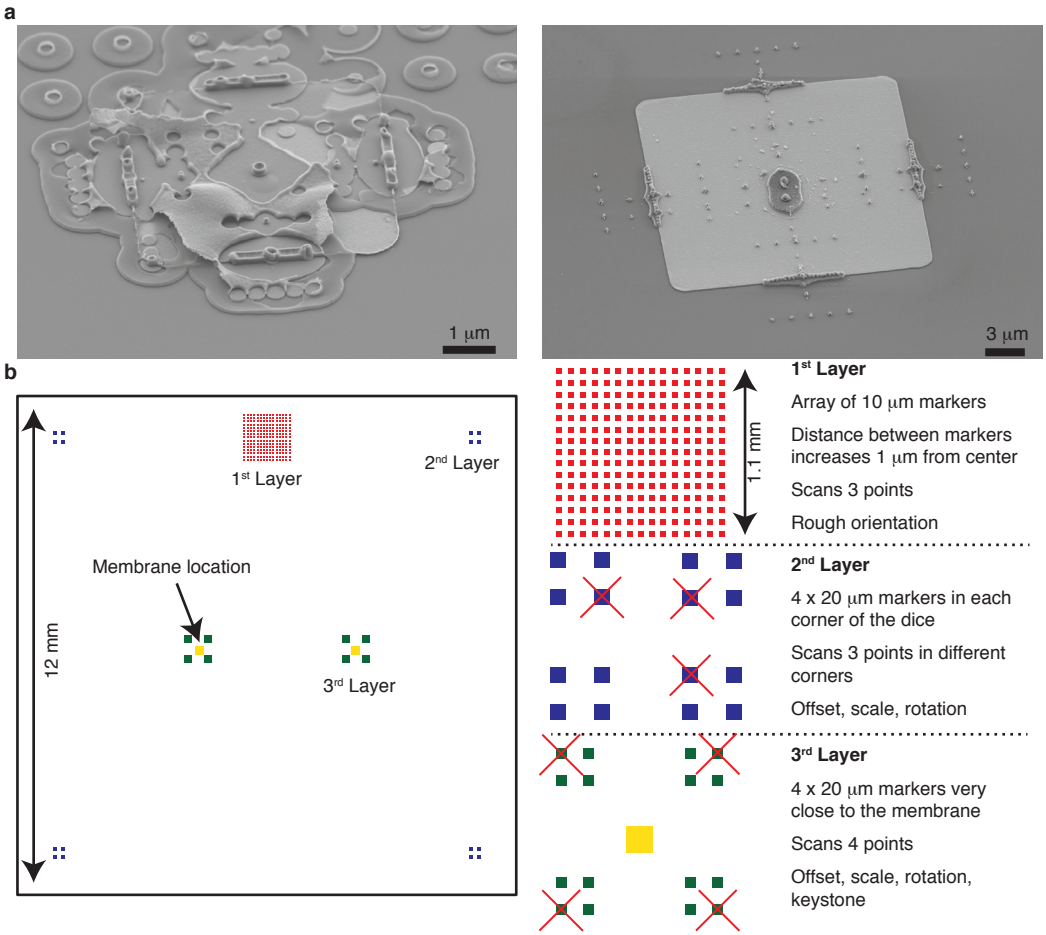

Figure 5.3 – Three-step EBL alignment. a, Scanning electron microscopy (SEM) images of the alignment markers. By scanning across the squared marker, the electron beam precisely detects the edges of the alignment markers. During the process, the resist gets activated and will be removed at the scanned locations during the development. After metal evaporation and lift-off, the scanning pattern of the EBL system becomes visible. **b**, Visual explanation of the three-step alignment scheme. 1st layer: An array of 10 µm markers. The distance between the markers increases by 1 µm from the center pad. This is used to roughly align the system (offset, scale and rotation) since the array is large (1 mm) the coordinates given by the user do not need to be precise. The lithography system will be able to back-calculate the center-pad from anywhere within the array. 2nd layer: One marker in each corner of the chip is scanned to generate a more precise global map (offset, scale, rotation, and keystone). 3rd layer: Another set of alignment markers is placed in the vicinity of the SiN_x nanopore and scanned immediately before writing the pattern.

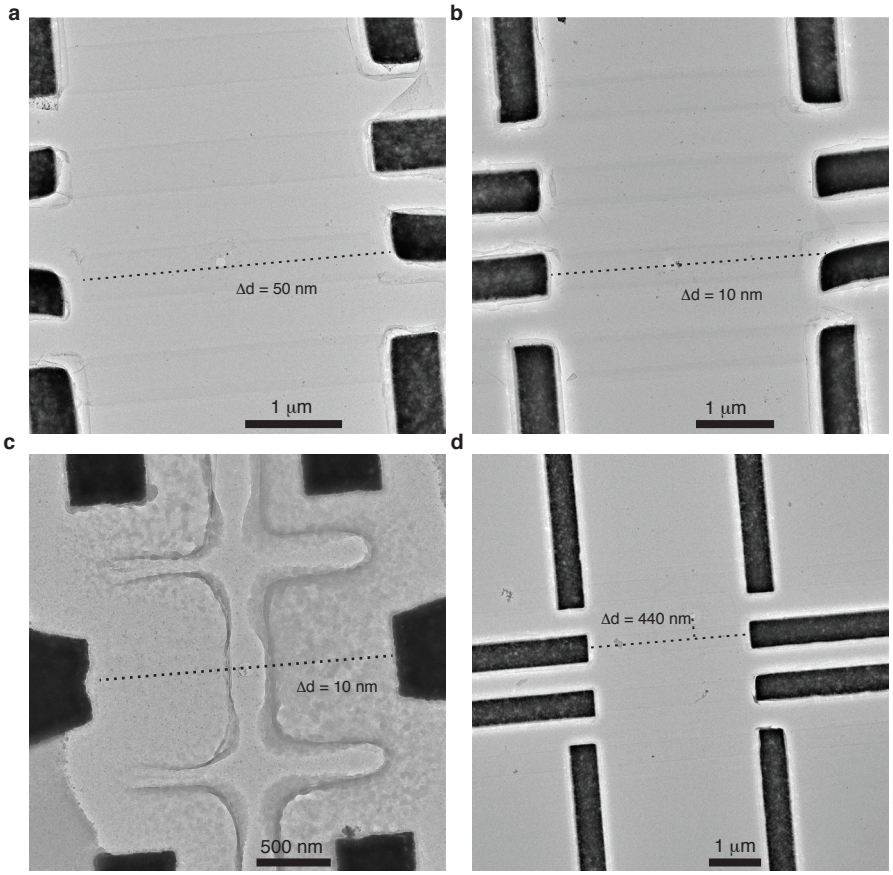

Figure 5.4 – Alignment precision. **a-c**, Successful three-step alignment. The observed shifts are typically 10 nm to 50 nm, which is well within the width of the MoS_2 ribbon (≈450 nm after etching). **d**, An example of unsuccessful alignment. The 3rd step failed on this device, subsequently, the global alignment is used and the ribbon is misaligned by 440 nm, emphasizing the importance of the three-step alignment scheme.

5.4 Results

After multi-step fabrication, I proceed with the electrical characterization of the devices. The device geometry does not allow for an electrical gate. All conductance measurements in dry condition were performed by contacting the drain-source pads with probe-needles mounted on a micro-manipulator and aligned using a microscope. To confirm that the measured entity is indeed the transverse current through MoS_2, I used the light (white LED) of the alignment microscope to photogate the transistor.

5.4.1 Conductance measurements

First, I measure the conductivity of metalized MoS_2 crystals in ambient condition with an electrical probe-station. In dark state, I record a conductance of 3.27 nS (Figure 5.5a). By illuminating the device with the white LED, the conductance increases to 18.3 nS, which can be explained by strong photogating of the transistor.[209] I then repeat the measurement for the same device, but lithographically etch the MoS_2 to a 500 nm x 2 µm small ribbon. The conductance due to the confinement drops to 72 pS in the dark-state and increases to 556 pS using light (Figure 5.5b). It is important to note that the conductance of small MoS_2 ribbons is very low in air and in the absence of a backgate.[252] Furthermore, the conductance depends highly on the environment, where small changes in the humidity-level can lead to very high conductance changes.[255] To test the proper functioning of the fabricated ribbons, we performed conductance measurements of MoS_2 ribbons in a vacuum. A 100-fold increase is observed in vacuum (Figure S5.2a). The conductance can even be pushed to the µA range by thermal annealing at high vacuum (Figure 5.5c). However, once the ribbon is in contact with air again, the conductance drops rapidly (Figure S5.2b). Although the gating of MoS_2 in room temperature ionic liquid (RTIL) is well understood,[256,257] the performance of MoS_2 devices directly in contact with an aqueous salt solution has not been well documented. Furthermore, our nanopore set-up has little in common with classical ionic liquid gating of transistors, since we apply ionic voltages across a monolayer MoS_2 membrane. In this case, we are changing the electrical field around the nanopore through the applied voltage, which, if large enough, should have an effect on the ribbon conductance.

Our devices are meant to perform in liquid. Therefore, the performance of the FET in ionic solution and under a transmembrane voltage is measured next.

5.4.2 Ionic gating

To better understand the behavior of the device in liquid, the drain-source currents of the freestanding FET (middle ribbon) are measured while different ionic voltages are applied. Figure 5.5d shows the transconductance (drain-source current (I_{ds}) vs. applied transmembrane-voltage (V_{tm})) for symmetric, 1 M / 1 M (*cis*/*trans*) potassium chloride (KCl), and asymmetric, 10 mM / 1 M (*cis*/*trans*) salt concentrations. When diluting the *cis*-side salt concentration

to 10 mM, the transconductance improves slightly from 44 nS to 51 nS. This can possibly be explained by investigating the potential distribution around the nanopore. To gain better insight into this effect, I performed finite element simulations of the potential distribution around a 10 nm nanopore in a 1 nm thick membrane. As expected, in 1 M / 1 M (*cis*/*trans*) I find a symmetric voltage drop across the membrane (Figure 5.5e). However, when lowering the salt concentration to 10 mM on the *cis*-side, the *trans*-side potential extents relatively far into the *cis*-side, increasing the overall potential that could affect the ribbon conductance (Figure 5.5f). A large asymmetry in the transverse I-V at 1 M / 1 M KCl conditions can also be found in Figure S5.3a, whereas the concentration gradient of 10 mM / 1 M does not show an asymmetric transverse I-V (Figure S5.3b).

Unfortunately, freestanding MoS_2 ribbons are unstable when simultaneously measuring ionic and transverse currents. Electrical discharges on the drain-source leads or unwanted circuit couplings can potentially induce breakage of the MoS_2 membrane. I therefore used a TEM to drill a nanopore into a non-supported ribbon to create a more stable device configuration (Figure 5.6a).

5.4.3 DNA translocations

I first measure the transmembrane conductance of the MoS_2 nanopore in 1 M KCl. The I-V characteristic in Figure 5.6b reveals an ionic conductance of roughly 11 nS. Using a thickness of 21 nm and the conductivity of 1 M KCl of 10.5 S m^{-1} I confirm that the conductance corresponds well to the pore size observed in the TEM.[54] Next, I sweep the drain-source voltage to probe the MoS_2 ribbon current in 1 M KCl (Figure 5.6c). A fairly large ribbon conductance of 1 µS is observed. Next, I added 80 nucleotides (nt) long single-stranded DNA (ssDNA) and attempted to simultaneously record the ionic and the transverse current. Figure 5.6d shows a representative extract of the events recorded. Distinct current drops with about 15 % blockage are visible on the ionic current trace. Estimating the expected conductance change due to ssDNA translocation is not straightforward since the polymer is extremely flexible (see subsection 1.5.1 (page 16)) and can translocate in a multitude of different shapes.[18,54] Previous studies have found long passage times of 50 nt ssDNA in gold-coated pores. This effect was explained by physisorption of bases with the gold surface.[258,259] A similar mechanism occurs on the MoS_2 membrane, where Van der Waals forces between the nucleobases and the basal plane of MoS_2 is responsible for the interaction.[260] Lower adsorption is found for double-stranded DNA (dsDNA).[260] Further, molecular dynamics (MD) simulations have shown that ssDNA can interact with a MoS_2 surface, whereas dsDNA shows nearly no sticking behaviour. Unfortunately, no correlated signals were visible on the transverse channel in 1 M KCl. To increase the local potential and the Debye length around the nanopore, we lowered the salt concentration to 10 mM / 100 mM (*cis*/*trans*). Correlated signals started to appear on the transverse current. A total of 759 correlated events were recorded. Figure 5.6e shows a representative collection of the recorded events. The ionic events mainly consist of a current decrease followed by a very short current increase. This is consistent with previous work in

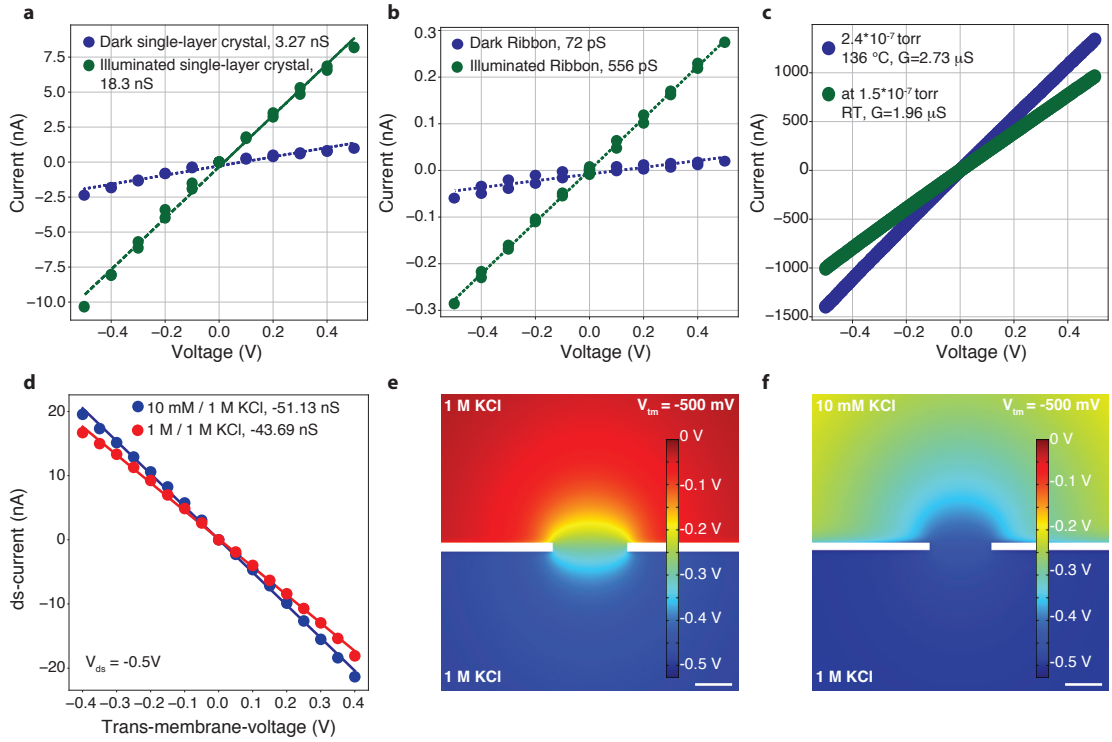

Figure 5.5 – Conductance measurements. a, Conductance of a metallized MoS_2 crystal suspended on an aperture in a SiN_x membrane in dark state (blue) and LED-illumination (green). **b**, Conductance of the same device when the full crystal is etched into a 500 nm x 2 µm ribbon in dark-state (blue) and with light (green). **c**, Conductance of the ribbon after annealing overnight at 136 °C in a vacuum of 2.4×10^{-7} torr. **d**, I-V characteristics of the MoS_2 ribbon when different transmembrane voltages are applied in symmetrical 1 M KCl condition (red) and concentration gradient of 10 mM/1 M (*cis*/*trans*) (blue), COMSOL simulations of the potential distribution at 1 M/1 M (**e**) and 10 mM/1 M (*cis*/*trans*) (**f**). The scale bar is 5 nm.

low-salt concentration, where the initial dip in current is assigned to access resistance probing or blocking of the pore and the current overshoot is assigned to an increase of ions in the nanopore due to mobile counterions along the DNA molecule and is associated with the actual translocation.[81,163] The current decrease on the transverse channel seems to be correlated to the part where the DNA probes the access resistance and returns back to the baseline once the translocation starts.

5.4.4 Decoupling the grounds

Previous reports of transverse currents in graphene nanoribbons have shown strong derivative signals on the sheet current, induced by the ionic signal.[102] Although the data obtained in Figure 5.6e does not resemble the derivative signals reported, some cross-talk could still occur. For example, on another device (Figure S5.1a and b) with bad insulation current leakages between the two channels occurred, effectively copying the ionic signal onto the transverse

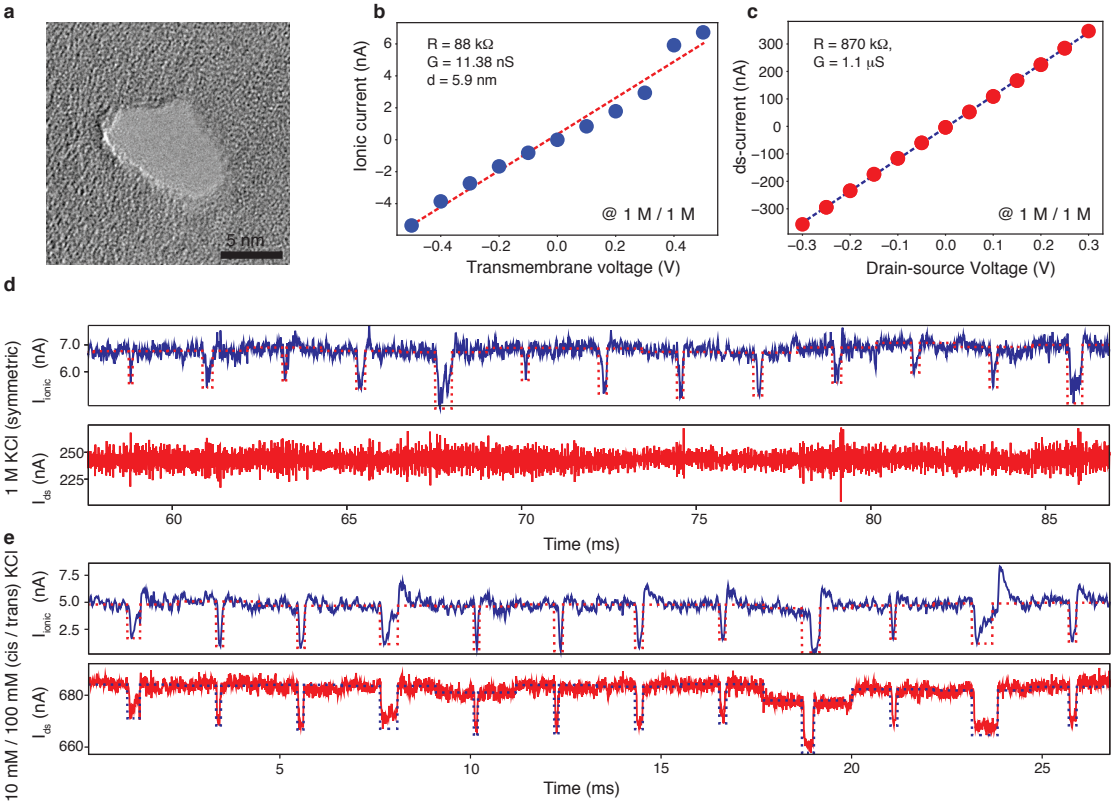

Figure 5.6 – Experimental data of 80 nt ssDNA translocation. a, A TEM image of the nanopore drilled through MoS_2 and the SiN_x membrane. **b**, Ionic I-V performed at 1 M KCl confirming the pore size obtained in **a**. **c**, Drain-source current (I_{ds}) vs. drain-source voltage (V_{ds}) at 1 M KCl. **d**, Concatenated signal traces representative of the dataset at 1 M KCl. **e**, Concatenated signal traces representative of the dataset at 10 mM / 100 mM (*cis*/*trans*) KCl. Both channels are sampled at 100 kHz, whereas the ionic channel had an analog low-pass of 10 kHz and the transverse channel an analog low-pass of 50 kHz. The dashed lines denote the fit used to estimate the current drop and the dwell time.

channel (Figure S5.1c). Furthermore, on another device, strong random noise spikes appeared on the ionic channel (no analyte added to the chamber), which translated to perfect derivative signals on the transverse channel (Figure 5.11). To avoid current leakages and capacitive couplings, we developed a novel electronic circuit, which decouples and electrically insulates the two circuits, similarly to the set-up presented in Heerema et al.[103]

Figure 5.7a shows a schematic representation of the experimental set-up. The circuit amplifying the ionic current is grounded to the Faraday cage and uses an Axopatch 200B amplifier to apply the transmembrane voltage and measure the ionic current. The main ground is depicted in blue color in the schematics. We then designed two decoupling components to electrically isolate the transverse current circuit: first, a voltage isolator propagates the voltage applied on the data acquisition (DAQ) card to the MoS_2 ribbon without propagating the ground, making the ground effectively floating (green, dashed lines). A Femto grounded to this floating potential is then used to amplify the current through the ribbon. This amplified voltage output is then connected to a differential amplifier, which is grounded to the main ground and copies

the signal to the DAQ card input. To reduce the noise induced by the floating potential, all the components are powered by lead-acid batteries placed inside the Faraday cage. The isolating performance of this set-up was assessed by connecting it to a custom test board that attempts to simulate the two circuits by placing two 10 MΩ resistors on each side of the circuit and interconnecting them with another 10 MΩ resistor. The insets of Figure 5.7b and c show the schematics of the test board. The resistance to current leakages from one circuit to another was tested by either sweeping the transmembrane voltage and recording the transverse current (Figure 5.7b) or sweeping the transverse voltage and recording the transmembrane current (Figure 5.7c). The resistance between voltages originating from the transverse circuit to the ionic circuit is 75 GΩ, which emphasizes the strong isolation. However, currents originating from the ionic circuit can leak towards the transverse circuit with a resistance of 1.8 GΩ.

5.4.5 Second dataset

The new electronic set-up was tested using a device with a small nanopore of about 2.5 nm in diameter in a supported ribbon (Figure 5.8). To test the influence of the charge of the analyte, we translocated three analytes of different charge: 1 kilobase pairs (kbp) dsDNA (negative), polylysine (positive) and polyethylene glycol (PEG) (neutral, average molecular weight (mw): 20×10^3 g mol^{-1}). All measurements are done in a concentration gradient of 10 mM / 1 M. A concatenated extract of the data obtained from these measurements can be found in Figure 5.9. The ionic current became quite large over time, suggesting that the contamination around the aperture visible in Figure 5.8 partially dissolved to create a second ionic current path. Figure 5.9a reports the correlated signals obtained when translocating 1 kbp dsDNA. The ionic signal is a current drop without overshoot and the transverse signal is a current decrease of the same length. After carefully washing the flow-cell the neutrally charged PEG molecules were added. These molecules cannot be translocated electrophoretically. To induce an electroosmotic flow dragging the molecules through the orifice, a negative transmembrane voltage was applied. Strong current decreases indicate successful translocations of PEG molecules (Figure 5.9b). However, most of the time no correlated transverse signals were visible. Last, the positively charged polylysine molecules were added. To translocate the positively charged analyte the ionic voltage was reversed again. During translocation of polylysine the ionic signal is characterized by short current decreases, whereas the transverse signal shows current increases Figure 5.9c.

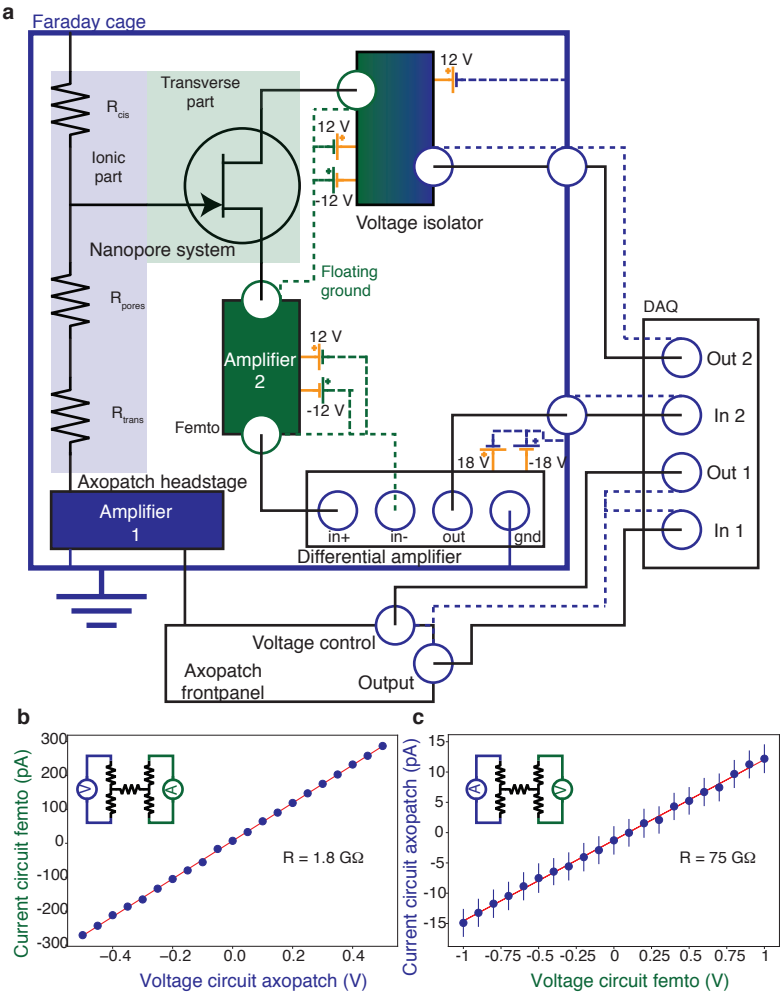

Figure 5.7 – Electrical set-up. a, A large Faraday cage serves as the ground (depicted in blue) of the ionic current measurement circuit closed via an Axopatch 200B amplifier. The second circuit used to measure the drain-source current through the transistor is isolated from the common ground through a voltage isolator and a differential amplifier, effectively creating a circuit between a floating potential (depicted in green) and the second amplifier (Femto Messtechnik). All components in this circuit are powered by lead-acid batteries placed inside the Faraday cage. In the schematics, the batteries and their grounding connections are depicted with a DC-voltage source symbol. We made a test circuit to assess the isolation capacity of the two circuits (depicted in the insets of b and c). Each resistor symbol corresponds to a 10 MΩ resistor. The resistance towards current leakages is then measured by recording the current of one circuit (b: transverse circuit, c: ionic circuit) while the voltage is swept on the other circuit (b: ionic circuit, c: transverse circuit). The differential amplifier was designed by Sanjin Marion (LBEN, EPFL) and Damir Altus (Institute of physics, Zagreb). Damir Altus built the differential amplifier.

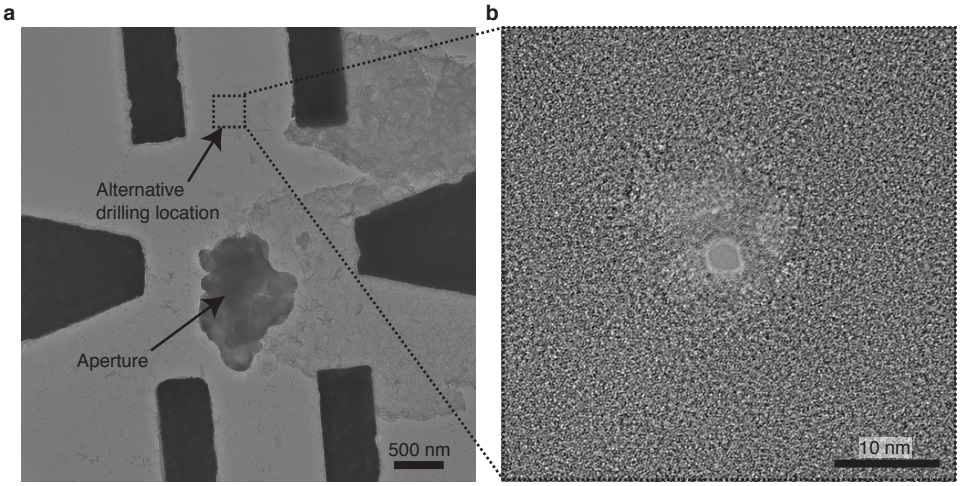

Figure 5.8 – TEM image of the device. **a**, TEM image of the device used to produce the data in Figure 5.9. The aperture was contaminated rendering the device impossible to use as a freestanding MoS_2 membrane. **b**, Alternatively, a small nanopore was drilled into the top ribbon.

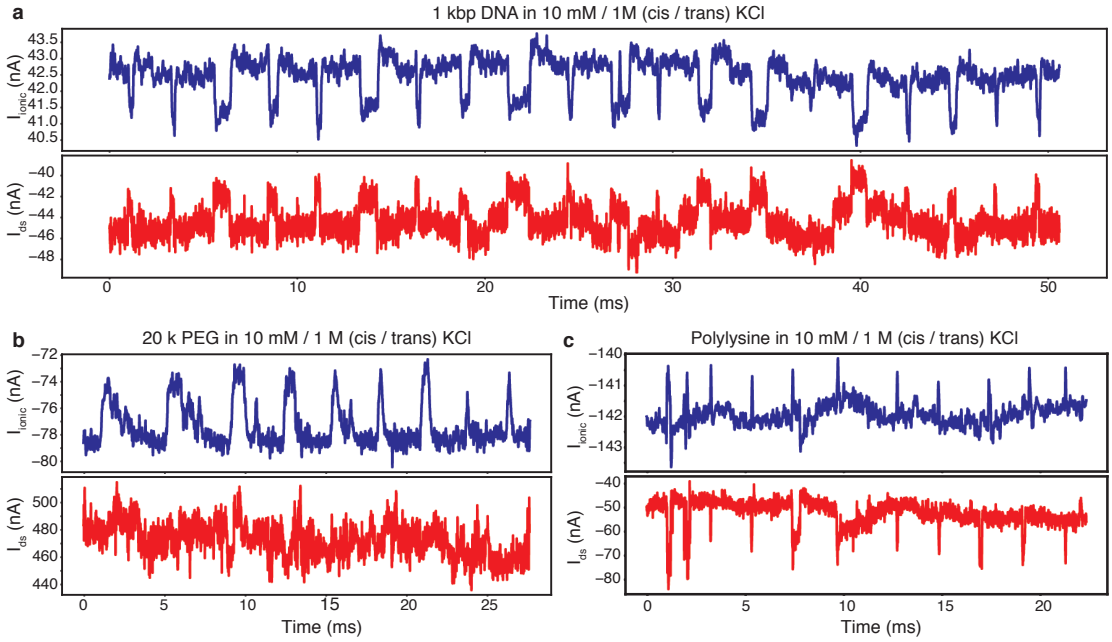

Figure 5.9 – Translocation data for differently charged analytes. **a**, 1 kbp dsDNA translocations. **b**, PEG (mw = 20×10^3 g mol^{-1}) translocations. Since the molecule is neutrally charged the ionic voltage is inverted to induce an electroosmotic flow that drives the analyte through the pore. **c**, Translocations of polylysine molecules. The transmembrane voltage is reversed again to drive the positively charged polymer through the nanopore using the electrophoretic force.

5.5 Discussion

5.5.1 Yield

I faced several fabrication-related challenges (described in detail in section 5.6). In total, I fabricated approximately 200 devices. The fabrication of about 100 devices was needed to optimize the fabrication steps. After optimization, about 50 devices reached the final fabrication step. Most devices were eliminated during the process due to breakage of the SiN_x membrane or problems during PMMA lift-off. Out of these 50, only about 20 devices were clean enough and had intact ribbons (judged from TEM images). Often, cracked ribbons (Figure S5.4) were making the devices unusable. The origin of the ribbon cracking is unknown but could originate from thermal expansions of the EBL resist (PMMA) during baking. Another common issue is contaminations in the vicinity of the aperture (Figure S5.5). These contaminations might be due to capillary-force induced accumulation or originate from the RIE and potassium hydroxide (KOH) etching processes. Lastly, devices with clean freestanding MoS_2 layers tend to break rapidly once both measurement channels were connected, suggesting large current discharges can occur. From these 20 devices, only 3 devices allowed recording of translocation events. This low yield is consistent with previous efforts in fabricating nanopore-FET devices,[101–104] emphasizing the difficulty of the fabrication.

5.5.2 Sensing principle

In this section, I will discuss the hypothetical origins of the observed signals. Unfortunately, the literature on FET-nanopore devices is quite sparse. I have mentioned these papers throughout this thesis and at this point, I will only shortly summarize the conclusions drawn from these experiments.

Silicon nanowire on SiN_x, Xie et al., 2011[104] Correlated events recorded at 10 mM / 1 M KCl, but not at 1 M / 1 M. The amplitude of the FET signal scales with the amplitude of the ionic signal. The total ionic current of 3 FET-nanopore pairs is the sum of their individual signal. The origin of the signal was assigned to a local potential change due to DNA translocation.

Graphene on SiN_x, Traversi et al., 2013[101] 125 correlated events recorded in 10 mM KCl. Sensing principle adapted from Xie et al.

Graphene on SiN_x, Puster et al., 2015[102] Transverse channel shows derivative signals at 1 M KCl, no transverse signals at 10 mM (or buried in noise). No field effect changes were observed.

Graphene, Heerema et al., 2018[103] 1400 correlated events at 1 M KCl. Comparable SNR in both channels. Origin of the signal is assigned to local potential change (Xie et al.) or DNA charge sensing.

Judging from the literature, there seems to be a consensus that an electrostatic gating involving a change of local potential due to DNA insertion is the most popular explanation of the observed signals.[101,104] However, only Xie et al. were able to investigate the behavior of their system carefully enough to make a conclusion on the most likely sensing principle. Heeremea et al. discuss that the direct charge sensing of the DNA backbone could explain their experimental data as well.[103]

The transconductance describes the conductance changes induced by changing the potential around the nanopore via the transmembrane voltage. It should, therefore, be possible to get a very rough estimation of the expected conductance drop due to a voltage change induced by the translocation of a molecule. In the next paragraphs, I will try to roughly estimate the expected signal caused by the translocation of DNA. The estimation of the voltage drop due to local potential change is largely based on the work by Parkin et al.,[253] whereas the estimation of the voltage drop through direct charge sensing is inspired by Heerema et al.[103]

Local potential sensing

One possible sensing scheme is the detection of the local electrical potential as described by Xie et al.[104] Here, the translocation of a molecule generates an electric field drop around the nanopore, which effectively gates the FET. The experimental data reported in Figure 5.6 shows a clear dependence of the transverse signal on the salt concentration. As previously explained by Xie et al., in 1 M / 1 M KCl the electric field drops symmetrically at the nanopore (see Figure 5.5e), whereas concentration gradients, such as 10 mM / 100 mM enlarge the resistance in one compartment, extending the electrical field drop further into the *cis*-chamber, as shown in the finite element model (FEM) simulations of the potential distribution (Figure 5.5f). The translocation of analytes can, therefore, induce potential changes at distances further away from the nanopore, effectively gating a larger surface of the ribbon. The data presented in Figure 5.6 could be explained by a local charge sensing mechanism. However, the transconductance value of that particular device was very low (3.5 nS).

In a local potential sensing scheme, the current drop ΔI_{ds} on the FET can be described by:[253]

$$\Delta I_{\mathrm{ds}} = g_{\mathrm{tm,\,pore}} \Delta V_{\mathrm{molecule}} \tag{5.1}$$

, where $g_{\mathrm{tm,\,pore}}$ is the effective transconductance at the nanopore and $\Delta V_{\mathrm{molecule}}$ is the voltage change induced by the translocating molecule. The effective transconductance scaled with the access resistance at the entrance of the pore can be expressed as:[253] $g_{\mathrm{eff}} = \frac{dI_{\mathrm{ds}}}{dV_{\mathrm{en}}}$, where I_{ds} is the drain-source current and V_{en} is the potential at the pore entrance. Using the model in Figure 5.5d, we can estimate $V_{\mathrm{en}} \approx \frac{3}{5} V_{\mathrm{ion}}$, where V_{ion} is the applied transmembrane voltage. Using the transconductance value, we can calculate the effective transconductance: $g_{\mathrm{eff}} = \frac{5}{3} \cdot 3.5\,\mathrm{nS} = 5.8\,\mathrm{nS}$. An absolut upper limit for the voltage drops induced by the translocation of DNA can be fixed to 100 mV.[253] Then the expected current change in the FET is $I_{\mathrm{ds}} = 100\,\mathrm{mV} \cdot 5.8\,\mathrm{nS} \approx 0.5\,\mathrm{nA}$, which is very low and not resolvable given the high noise noise of the system

(subsection 5.5.5). However, the model used here does not take into account the charge of the molecule itself and bases the voltage changes solely on the perturbation of the electric field due to the DNA.

Sensing the charge of the molecule

In this sensing scheme, we hypothesize that the charge of the molecule gates the transistor. Monolayer MoS_2 typically behaves like a n-type FET.[113] The charge of DNA backbone is negative, and we would, therefore, expect a drop in the drain-source current of the MoS_2-FET. The absence of any FET-signal at a salt concentration of 1 M KCl can be explained by a strong charge screening. In water, the distance at which electrostatic effects persist can be expressed by the Debye length, estimated through $\lambda_D = \frac{3.04 \cdot 10^{-10}}{\sqrt{c}}$, where c is the KCl concentration.[236] In 1 M KCl the Debye length is roughly 0.3 nm, whereas, at the more dilute 10 mM case, the Debye length extents to 3 nm.[236] The charge of the DNA backbone has, therefore, an effect on a larger surface of the ribbon. Another factor to consider is the interaction of ssDNA on the MoS_2 surface. MD simulations have shown that ssDNA as opposed to dsDNA can adsorb on the MoS_2 surface through Van der Waals forces, starting with the adsorption of the two ends.[107] This Van der Waals forces combined with the electrophoretic force immobilizes the ssDNA shortly before being dragged through the nanopore by the electric field. During that time, a large amount of the DNA molecule is in close contact with the MoS_2 ribbon(Figure 5.10b), effectively gating the transistor and provoking the transverse current decrease observed. Brownian motion then moves the trapped molecule (Figure 5.10c) until the DNA molecule translocates and increases the intrapore ion concentration by bringing additional counterions into the pore (visible as an overshoot in the ionic current) (Figure 5.10d). While the DNA is inside the nanopore it is invisible to the MoS_2-FET as all the charges are screened by the SiN_x layer.

Additionally, the experiments reported in Figure 5.9b show that the neutrally charged PEG molecule does not induce a transverse signal, providing additional evidence of a direct charge sensing scheme. The positively charged polylysine molecules provoke a current increases, which is consistent with an n-type FET.

The current change due to the charge of a molecule can be estimated using the capacitance of the MoS_2-liquid interface C_i per area and the effective charge of the molecule Q_{eff} acting on a surface A, using the following relationship:[103]

$$\Delta I_{\text{ds}} = g_{\text{eff}} \frac{Q_{\text{eff}}}{C_i A} \tag{5.2}$$

We can roughly estimate the capacitance C_i by combining the contribution of the electrical double layer (EDL), C_{EDL} and the quantum capacitance C_q:[261]

$$\frac{1}{C_i} = \frac{1}{C_q} + \frac{1}{C_{\text{EDL}}} = \frac{C_{\text{EDL}} + C_q}{C_{\text{EDL}} C_q} \tag{5.3}$$

Combining Equation 5.3 with Equation 5.2 yields the final expression of the expected current drop ΔI_{ds}:

$$\Delta I_{ds} = g_{eff} \frac{Q_{eff}(C_{EDL} + C_q)}{C_{EDL} C_q A} \tag{5.4}$$

The quantum capacitance in 2D-systems can be calculated using the relationship:[261] $C_q = \frac{e^2 m^*}{\pi \hbar^2}$, where $\hbar = 1.05 \times 10^{-34}$ J s is the reduced Planck constant, $e = 1.6 \times 10^{-19}$ C the elementary charge and $m^* = 9.11 \times 10^{-31}$ kg the rest mass of an electron. The value of the quantum capacitance is therefore: $C_q = 0.67\,\mathrm{F\,m^{-2}}$.

The capacitance due to the EDL can be estimated through: $C_{EDL} = \frac{\epsilon \epsilon_0}{\lambda}$, where $\lambda = 3$ nm is the Debye length at 10 mM KCl,[236] $\epsilon_0 = 8.85 \times 10^{-12}\mathrm{F\,m^{-1}}$ the permittivity of vacuum and $\epsilon \approx 80$, the permittivity of the electrolyte used. Finally the value for the EDL capacitance can be calculated as: $C_{EDL} = 0.24\,\mathrm{F\,m^{-2}}$. Using Equation 5.3, we can calculate the total capacitance to be $C_i = 0.17\,\mathrm{F\,m^{-2}}$. Using the transconductance of the device used in Figure 5.6 (≈ 3.5 nS), we can estimate the expected current change through Equation 5.4: $\Delta I_{ds} \approx 3\,\mathrm{nA}\,e^{-1}\,\mathrm{nm^{-2}}$. Theoretically, the 80 nt long ssDNA used in the experiment should have a charge of 80 e. The experimental data shows typical current drops of about 15 nA, suggesting that about 5 elementary charges are sensed per nm^2.

Looking at the above analysis, the only value that can vary is the capacitance of the EDL. The expected current-drop is therefore proportional to the Debye length and inversely proportional to the dielectric constant of the solvent: $\Delta I_{ds} \propto \frac{\lambda}{\epsilon \epsilon_0}$. For example, in 1 M KCl, the Debye length is only 0.3 nm,[236] which would lead to an expected current drop of $\Delta I_{ds} \approx 1\,\mathrm{nA}\,e^{-1}\,\mathrm{nm^{-2}}$. This could potentially explain the absence of any transverse signal in high-salt conditions. Furthermore, another solvent, such as RTILs could lower the dielectric constant ϵ_0 and therefore increase the amplitude of the current modulation. For example, typical dielectric constant values in RTILs range between 10 to 20,[262] which could boost the current modulation to $\Delta I_{ds} \approx 20\,\mathrm{nA}\,e^{-1}\,\mathrm{nm^{-2}}$. Additionally, recent experiments have revealed that RTILs have a remarkably long ranged screening length.[263]

Judging from the results of the two calculations (local charge sensing versus direct charge sensing) it would seem that direct charge sensing can induce larger effects than local potential sensing. However, these estimations are very rough and the reality is probably better reflected through a combination of local potential changes and direct charge sensing. Another complicating factor is the 2D-nature of the semiconducting material, which makes it extremely sensitive to surface effects. For instance, ions are believed to scatter mobile electrons in the material, therefore decreasing the field-effect mobility.[264]

Furthermore, the translocation data measured with PEG molecules is not consistent with a local potential sensing mechanism, since the neutrally charged molecule should also induce a local potential change during the translocation (Figure 5.9b). Additionally, DNA translocations

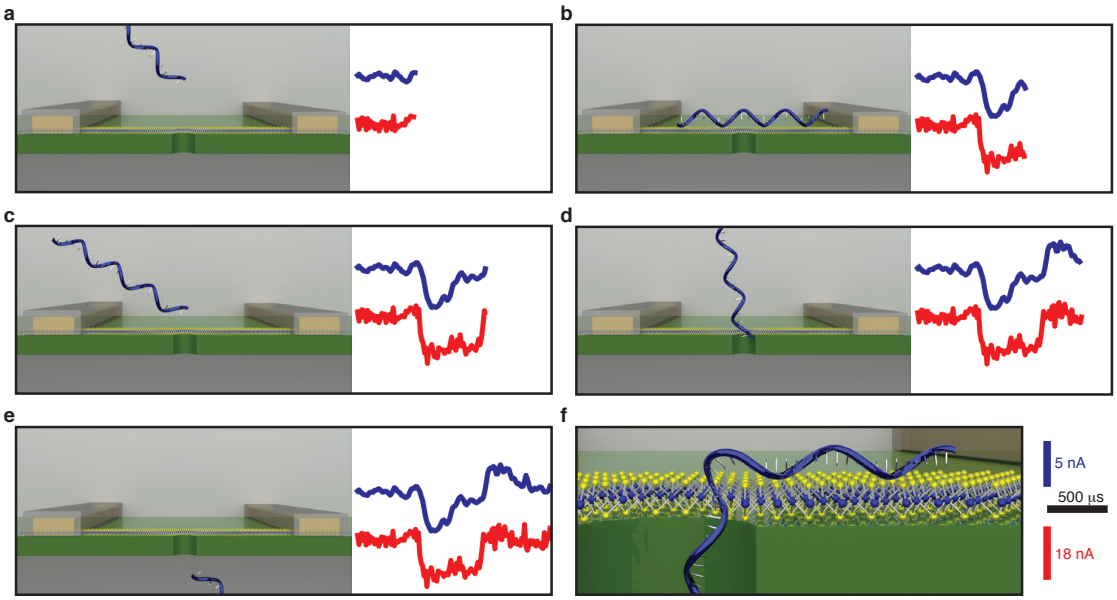

Figure 5.10 – Translocation dynamics. Depiction of a typical correlated event. The ionic current is depicted in blue, whereas the transverse current is drawn in red. **a**, The DNA molecule is approaching the nanopore by diffusion. **b**, The strong electric field around the nanopore, as well as interactions with MoS_2 surface trap the DNA molecule and immobilize it at the pore mouth. **c**, Thermal motion causes the molecule to move across the surface until one end is electrophoretically drawn into the nanopore. **d**, Once the DNA molecule translocates through the nanopore, the potential change (or the charge of the molecule) is not visible anymore and the transverse current returns to baseline. **e** During the translocation, the ionic current overshoots due to the counterions that the ssDNA brings into the nanopore. Once the molecule is released into the *trans*-side chamber, the ionic current returns to the pre-event baseline value. **f**, Close-up illustration on how the ssDNA could interact with the pore system.

produce current decreases, whereas polylysine translocations produce current increases. A change in the polarity of the FET signal would not be compatible with local potential sensing.

Unfortunately, the number of devices that yielded meaningful experimental data was small. It is therefore difficult to comment on the reproducibility of the observed behavior. For this reason, it is also not obvious to conclude whether charge-sensing or local potential sensing is responsible for the observed signals. A careful analysis of the signal amplitudes at different applied ionic voltages might be able to resolve this question. If the FET signal scales with the ionic signal/applied voltage, then a local potential sensing mechanism is more realistic. In a pure charge sensing regime, the transverse signal might still depend on the transmembrane voltage due to electrolyte gating, but it should scale differently.

I have discussed both, the local potential sensing and the direct charge sensing, but a short discussion on capacitive coupling is needed as well.

Cross-talk

During previous measurements on graphene nanoribbons, Puster et al.[102] have found strong capacitive coupling between the ionic translocation signal and an electrode in the vicinity of the electric field (even a pure gold pad at ground 20 nm away from the nanopore). In this case, the drain-source current takes the shape of the derivative of the ionic current, indicating a capacitive coupling.[102] Furthermore, the capacitive signals do not scale with V_{ds}, which means that a field-effect response cannot be responsible for the signal. Applying a higher drain-source voltage increases the current but does not influence the signal amplitudes. In my configuration the metal leads contacting the MoS_2 ribbon are 1 µm away from the nanopore. The potential change introduced by a molecule inserted at the nanopore decays exponentially with distance from the nanopore. It is therefore extremely unlikely that potential changes can be sensed by the contacting electrodes themselves. Furthermore, the cross-talk reported by Puster et. al. vanished with decreasing salt concentration (10 mM). The signal on the MoS_2-FET seems to appear only at salt concentrations below 100 mM and is not visible at higher concentrations.

We have observed derivative signals on the transverse channel originating from the ionic current circuit on one device only (Figure 5.11). However, these signals are likely random current spikes since they appeared before the addition of an analyte. Although the data presented in Figure 5.6 points towards a field-effect induced mechanism, a cross-talk artifact can still not be completely excluded at this time.

5.5.3 Signal comparison

Figure 5.12 shows current-drop vs. dwell time scatter plots of the ionic and the transverse channel. There are no distinct subpopulations visible in the current drops. As previously reported, the dwell time exhibits a log-normal distribution suggesting that very short events are missed.[36] Furthermore, the amplitudes of the current drops and dwell times observed in the two channels correlate very well (Pearson's correlation coefficient of 0.7 and 0.63 respectively, Figure 5.13a and b). The correlation of the amplitudes of the two signals is compatible with both local potential sensing and direct charge sensing. Physically, deeper ionic current dips might be caused by a stronger interaction at the pore mouth, which would increase the voltage drop in the local potential measurement scheme as well as improve the direct charge sensing scheme due to a decreased distance to the surface

5.5.4 Signal improvement through the transverse channel

The question remains whether the transverse channel can actually provide an improved signal compared to the ionic channel. First, to estimate the potential improvements of the transverse sensing scheme we can compare the SNR values between the signals of the two channels. To fairly compare the signal between the channels, I digitally filtered the transverse signal to

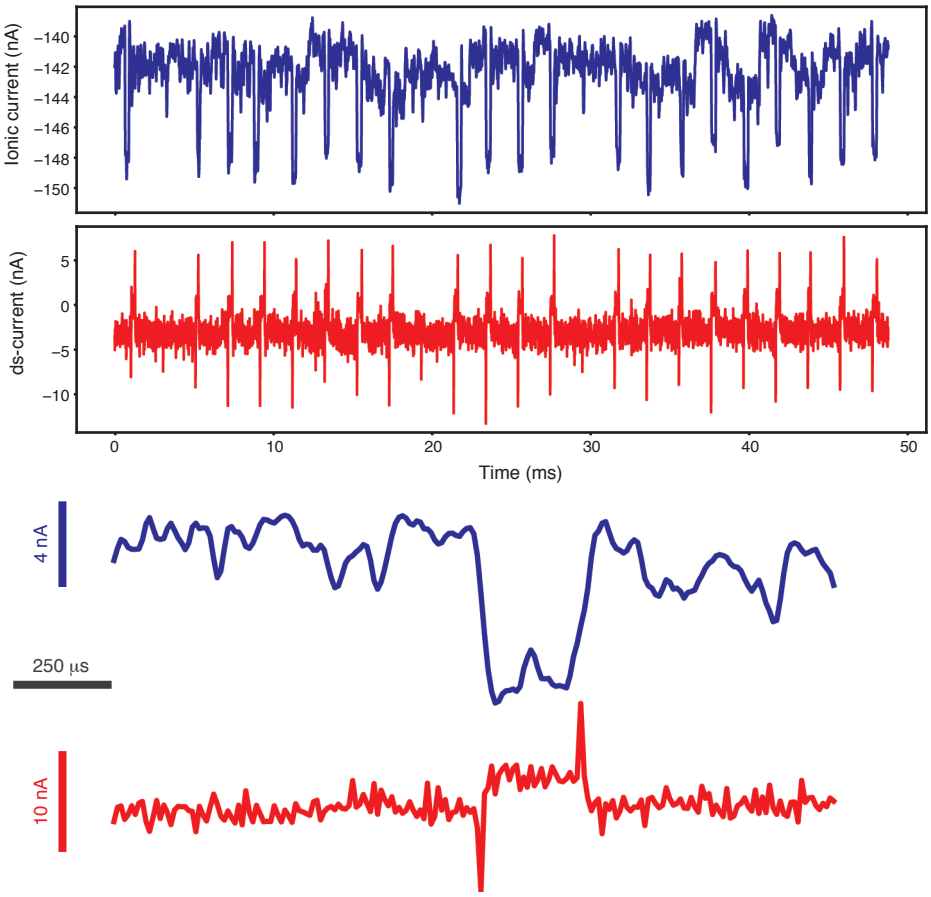

Figure 5.11 – Example of cross-talk. Random current spikes in the absence of analyte caused strong capacitive coupling to the transverse channel in this particular device.

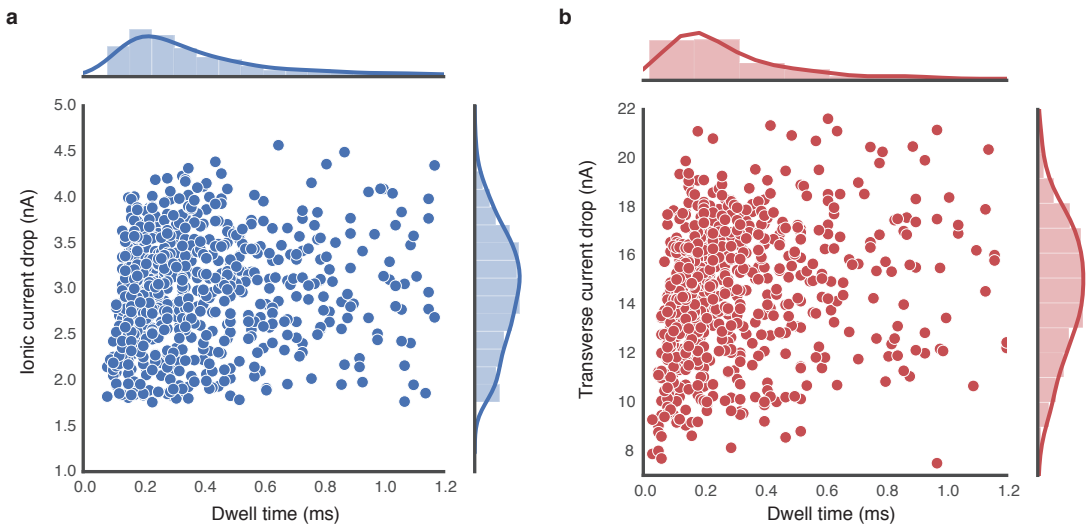

Figure 5.12 – Scatter plots of the translocations. **a**, The current drops of the ionic channel vs. the dwell time. **b**, The current drops of the transverse channel vs. the dwell time. n = 759

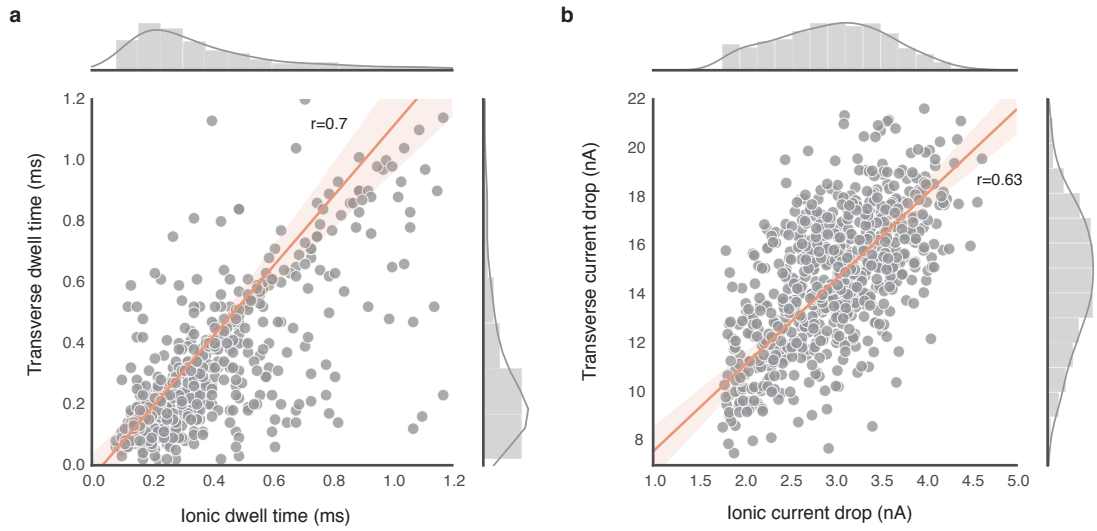

Figure 5.13 – Correlation between the channels. **a**, The current drops of the transverse channel vs. the current drop of the ionic channel. **b**, The dwell time of the transverse channel vs. the dwell time of the ionic channel. A regression (solid red line) is drawn through the data-points. The shaded region around the regression line illustrates the confidence interval of 95 %. n = 759

match the low-pass cutoff of 10 kHz of the ionic channel before calculating the SNR values. The SNR was defined as: SNR = $\frac{\Delta I}{\sigma_{\text{baseline}}}$, where ΔI is the observed current drop and σ_{baseline} the standard deviation of the baseline upstream of that ΔI. Figure 5.14 shows the probability density function (PDF) and boxplots of the two cases. The transverse current has a 40 % higher SNR ($p < 0.01$). The median of the SNR of all 759 correlated events presented in Figure 5.6 is 7.7 for the ionic current and 10.7 for the transverse current. This increase in SNR illustrates the potential improvements that the transverse measurement scheme can offer and could pave the way to higher bandwidth recordings, where noise typically masks translocation events.

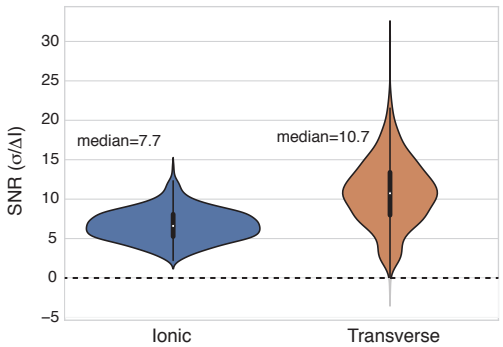

Figure 5.14 – Signal-to-noise ratio. The standard deviation is divided by the current drop of each event of the dataset presented in Figure 5.6. The standard deviation is calculated using 500 points (5 ms) before the event. The SNR increases on average 30 %. To illustrate the underlying distribution, the PDF of the SNR-data is outlined around the boxplot. The Mann-Whitney U test reveals that one population has greater values than the other with a confidence of $p < 0.01$.

5.5.5 Noise

The simultaneous measurement using the two circuits increases the noise of the system. Figure 5.15 shows the typical baseline values of the two channels in high-salt (1 M / 1 M KCl) and low-salt condition (10 mM / 100 mM KCl). The standard deviation of the ionic current increases in low-salt from 0.5 nA to 0.8 nA. The noise on the transverse current, however, decreases substantially from 8.6 nA to 3.1 nA. The increase of the ionic noise with lower salt concentration is consistent with previous reports[143] and is associated with the low-frequency 1/f noise. The noise power of the 1/f noise scales inversely with the number of charge carriers.[143] On the transverse channel, a strong noise reduction is observed with lower salt concentration, which is in contrast to the graphene-FET device presented by Puster et al.,[102] where the noise on the transverse channel increased with lower salt concentrations.

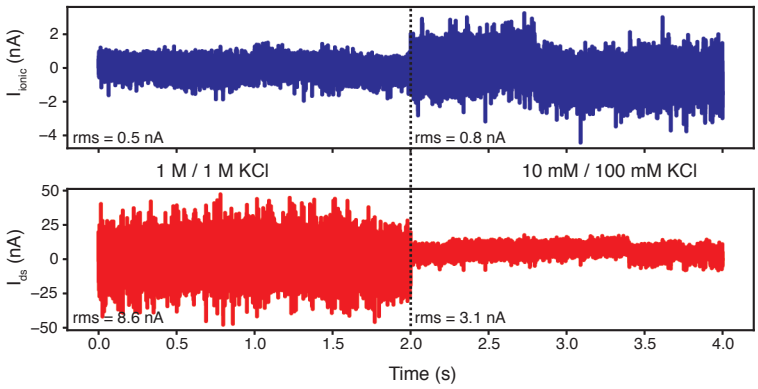

Figure 5.15 – Noise performance. Mean-corrected baseline currents for the ionic and transverse channel in 1 M / 1 M KCl and 10 mM / 100 mM KCl. The root mean square (rms) values are displayed on the respective parts of the plot.

5.5.6 Stability

The stability of MoS_2 membranes is in general not as good as SiN_x membranes. Electrical discharges originating from the flow-cell can easily break the ultrathin membrane (see subsection 2.3.3 (page 41)). Connecting the transverse circuit leads to an increased risk of damage of the freestanding MoS_2 through higher noise and potential current spikes or discharges. Furthermore, the isolating circuit places the ground of the transverse channel and the ground of the ionic channel to arbitrary potentials, which might further increase the risk of electrical discharges. It would, therefore, be useful to implement control of the potentials of the two grounds. However, connecting the two grounds with a potentiometer would, in turn, defy the purpose of the isolating circuit by allowing current leakages.

The amount of contamination (usually PMMA) of the freestanding part of the MoS_2 layer defines strongly how stable the layer is: large amounts of PMMA can have a stabilizing effect, but introduce an unwanted increase in thickness and might further uncontrollably dope the transistor.[265]

Besides the material itself, many studies in 2D-materials have shown the importance of the contact resistance on the performance of the device.[149,266,267]

5.5.7 Metal contacts

2D-FETs are extremely sensitive since charge carriers are confined to the atomically thin semiconductor. Therefore, the mobile charge carriers are very uniformly controlled by the gate voltage (in our case, local potential changes or charge sensing). However, a major bottleneck in 2D-transistors is the contact resistance of the source and drain leads. Metal evaporation of the contacts is a high-energy process, which can cause chemical bonds with the MoS_2 layer. This can induce a strong Fermi level pinning, which can be beneficial or disadvantageous for the drain-source conduction without applied back gate voltage.[268] Furthermore, if the voltage-drop across the metal lead is comparable to the applied ds-voltage, then source choking prevents the injection of more charge carriers into the material.[269]

For these reasons, I believe that one of the major bottlenecks of the device described here is the contact between the MoS_2 ribbon and the contacting metal. If evaporating the contacting metal changes the Fermi level, then we are exposed to a process which randomly defines the conductance level of the ribbon (in absence of a back gate). To avoid this phenomenon, metal pads supported on a polydimethylsiloxane (PDMS) film could be transferred on top of the MoS_2 ribbon.[268] This would ensure that the MoS_2 ribbon is undamaged and more reproducible conductances should be achievable through this method.

5.5.8 Gating

In addition to the metals contacts, other external factors can influence the conductance of the devices. These dopants can be gases in the air or ions in solution. Many devices that I fabricated showed very low conductances in air or electrolyte environment. Typically, large back gate voltages are used to control the Fermi level of 2D-transistors to bring them to the *on* state. Controlling the number of charge carriers in our device set-up is not trivial. Back-gate voltages are typically applied through the underlying silicon substrate. In the case of a nanopore-FET device this is not practical since the transistor is placed on top of a freestanding membrane of SiN_x. Very large back gate voltages would thus be needed to effectively gate the isolated transistor. Furthermore, adding additional electrodes for gate controls would complicate the electrical set-up further and increase the risk of parasitic noise and signals.

A recent study has shown that a corrugated SiN_x layer can improve the carrier mobility strongly.[254] Alternatively, dopants such as potassium or benzyl viologen can improve the concentration of mobile charge carriers.[270,271] A less invasive method of effectively gating MoS_2 transistors is light. Light above the bandgap energy can excite electrons in the valence band to render the transistor more conductive.[209] In Figure 5.16, I measured the photo-response of a MoS_2 ribbon in liquid. The current can increase five-fold upon light irradiation,

encouraging further investigation of light as an effective booster for these types of devices. However, photooxidation processes on the atomically thin layer when placed in the electrolyte can cause damage to the ribbon.[210] Further, the laser light increases the noise on the ionic channel. Although, this could be solved by using low noise substrates.[214]

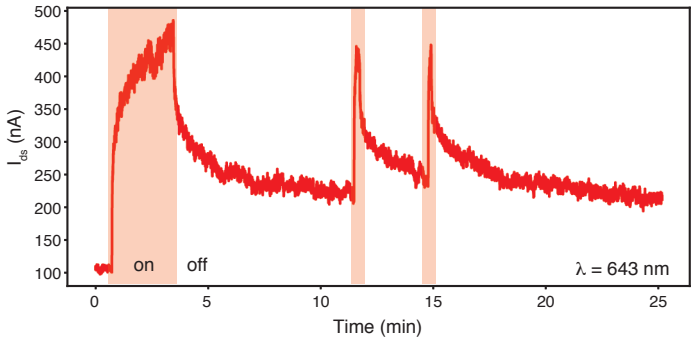

Figure 5.16 – Photogating of a MoS_2-nanopore FET. Here the light of a 643 nm diode laser (more information in Figure S4.1 (page 105)) was aligned with the SiN_x membrane of a finished FET-nanopore device, placed into aqueous solution. The transverse current of the nanoribbon is measured while the shutter of the laser is opened and closed.

5.5.9 TEM induced damage

Normal imaging of the finished devices in a TEM greatly affects the conductivity of the MoS_2 ribbons. In Figure 5.17 the conductance values before and after TEM imaging are shown. A conductance decrease of up to three orders of magnitude was observed for the ribbon with the freestanding part. This is probably due to a larger electron dose since the freestanding part is of most interest and therefore imaged the longest. Parkin et al. have performed in-situ conductance measurements on SiN_x supported MoS_2 and have observed strong conductance decreases during the electron irradiation.[272] The effect of the electron beam is irreversible, which suggest physical damage to the layer. Most probably, sulfur vacancies are responsible for the reduction in the mobility.[272]

During the development of the process flow, the TEM was the only tool to investigate the integrity of the devices. Since contamination issues have been largely resolved in recent batches we can use the ECR method to create the nanopores to avoid damage to the MoS_2 layer.

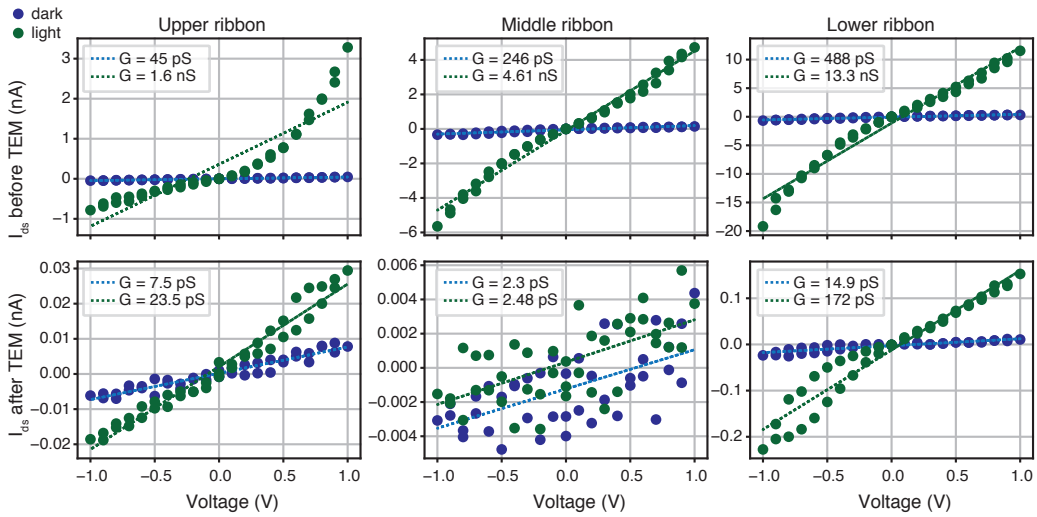

Figure 5.17 – Influence of TEM irradiation on MoS_2 conductance. The conductances of the three ribbons (columns) are measured before (top row) and after imaging in TEM (bottom row). Blue dots are the measured current values in dark condition, whereas the green dots are the measured current values during irradiation with white light. The conductance values are extracted by fitting the data linearly (dotted line).

5.6 Challenges

5.6.1 Fabrication challenges

I have shown that we can achieve clean freestanding MoS_2 membranes even after a lengthy fabrication process with multiple PMMA coatings. I found that the timing of each step and the age of the PMMA is crucial for achieving a clean lithography processes. In the best case, a processing step should be done within 24 h from coating with PMMA to its removal. Furthermore, serial dilution of the devices in warm acetone (60 °C) helps to achieve residue-free devices.[50] However, to reach the current state of fabrication I faced a few unexpected challenges that needed to be solved. In the next few paragraphs, I will summarize the most important challenges that occurred during the fabrication process.

First, the SiN_x membrane on which the metal contacts are deposited can deform with temperature changes or vacuum suction (as used in spin-coating to fix the chips to the spinning chuck). After these deformations of the SiN_x membrane, we observed delamination of the metal layer. Experimentally, this has been mainly observed for Ti / Pt (5 nm / 50 nm) layers. Unfortunately, this effect was difficult to spot since the delamination is not visible in the optical microscope or during TEM imaging, due to the perpendicular vantage point. Tilted SEM images, however, provided an alternative viewpoint and revealed that the metal contacts were delaminating on the membrane (Figure 5.18a). However, Ti / Au (5 nm / 50 nm) did not produce any delamination (Figure 5.18b). We suspect that the high elastic modulus of thin platinum (140 GPa, compared to 69 GPa for gold[273]) was responsible for the delamination effect as explained in the caption of Figure 5.18c and d.

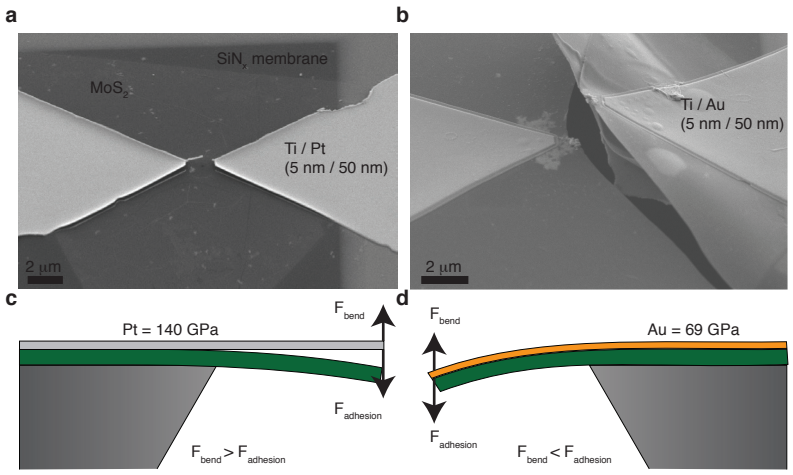

Figure 5.18 – Delamination of metal contacts. a, Choice of metal when working on a thin SiN_x membrane is crucial. **a**, A layer of Ti-Pt (5 nm / 50 nm) detached on the SiN_x membrane. **b**, Using Ti-Au contacts, the detachment is not observed. We suspect that the detachment is due to a difference in the bendability of the material. For example, the elastic modulus of thin film Pt is 140 GPa,[273] which means it will be much stiffer. **c**, When the membrane deforms, the force resisting the bending overcomes the adhesion force to the surface and as a result, the membrane detaches. **d**, In the case of Au, however, the Young modulus is only 69 GPa,[273] which allows easier bending and reduces the chance of overcoming the adhesion force. Therefore, the electrodes can easily follow small movement or vibrations of the SiN_x membrane occurring during spin-coating (vacuum suction) as well as thermal expansion and contraction.

Second, it is very challenging to achieve a good quality area-selective insulation of the metal electrodes. The most obvious approach would be the use of EBL and e-beam assisted evaporation at room temperature of an insulating material, such silicon dioxide (SiO_2). However, I have found that evaporated oxides are easily dissolved in an electrolyte solution such as 1 M KCl. This is probably related to the quality of the layer, which might be more mesh-like instead of a dense, smooth film. Further, I have tried the EBL resist hydrogen silsesquioxane (HSQ),[274] which turns into a SiO_2-like material after exposure and allows extremely precise patterning on the SiN_x-membrane due to the absence of backscattered electrons (Figure 5.19e-f). Unfortunately, exposed HSQ rapidly dissolves in KCl solution (Figure 5.19e-f). Lastly, we explored the possibility of coating our devices using ALD. We found that 20 nm alumina (Al_2O_3) is not stable in the experimental conditions. However, 20 nm thick hafnium dioxide (HfO_2) layers have good stability and we did not observe any degradation of the layer over-time. Unfortunately, high-quality ALD films are deposited at high temperatures (> 200 °C), which makes area-selective patterning challenging.[275] In some cases, we observed strong reflowing of the PMMA resist, when depositing HfO_2 at a temperature of 200 °C (Figure 5.20a and b) in other cases the reflow was not sufficient to render the device unusable (Figure 5.1c and Figure 5.20c-d).

Third, to etch the MoS_2 crystal into a ribbon, EBL and RIE etching using oxygen plasma is typically used. However, we have found that the PMMA layer typically gets burnt by the short (< 10 s) RIE exposure. This burnt layer redeposits on the chip surface during dissolution in

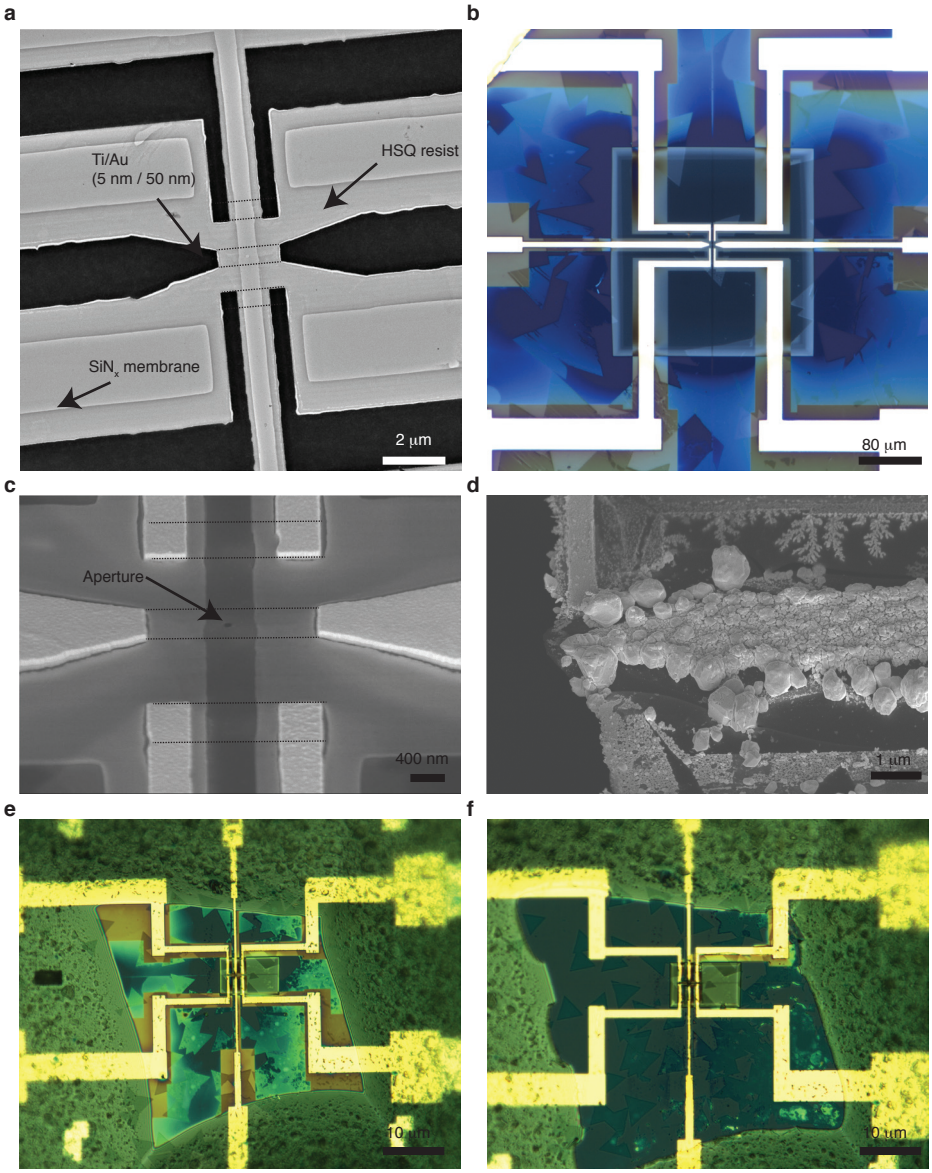

Figure 5.19 – HSQ as an electrical insulation material. **a**, A TEM image of a finished device using HSQ insulation. **b**, Optical micrograph of the same device. HSQ is a very sensitive EBL resist, therefore, electron-backscattering leads to crosslinking visible as a contrast-gradient outside of the membrane. Fortunately, the SiN_x membrane is largely transparent to electrons and backscattering does not occur inside membrane area. **c**, A tilted SEM image illustrating the topology of the HSQ coated devices. **d**, During the experiment in KCl solution, the HSQ seems to dissolve and redeposit on the electrodes. **e**, Optical micrograph of the device before experiment (the thick layer around the membrane is silicone elastomer applied to further improve insulation). **f**, The same device after the experiment. The contrast due to HSQ is completely lost, which suggest dissolution of the material during the experiment.

acetone and becomes impossible to remove (Figure 5.21a and b). We suspect that the issue is generated by stray gases other than oxygen. In an ideal case, no residues should be seen on the surface of the device (as shown in Figure 5.2).

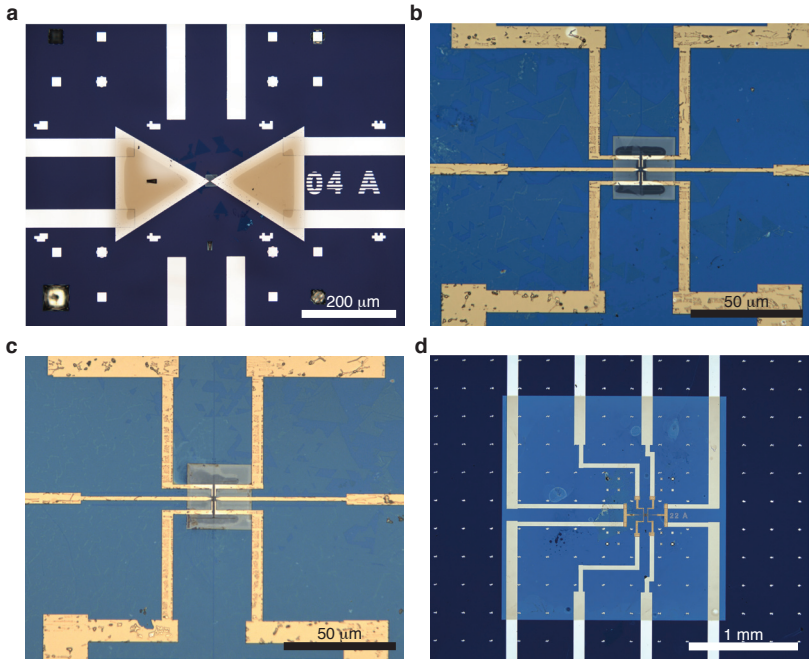

Figure 5.20 – PMMA reflow during ALD a The triangular metal leads were patterned by EBL in PMMA resist. The contrast gradient is a function of HfO_2 thickness. **b**, Compared to **c**, the membrane shows dark regions that lack HfO_2 coverage. **a-c** show that the resist melts in the temperatures used in the ALD furnace (200 °C) and reflows onto the patterned area, protecting it from the deposition. **d**, Large-scale impression of the HfO_2 coating (blue).

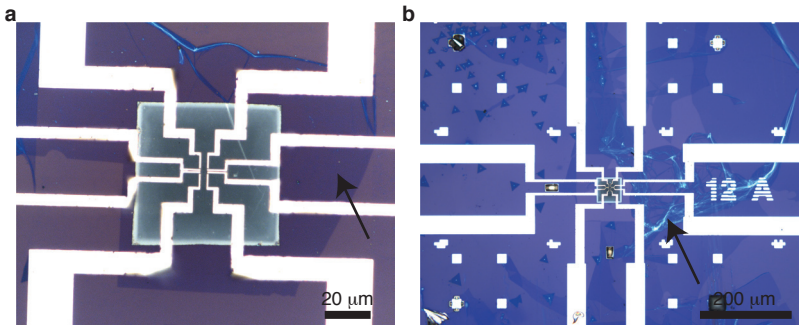

Figure 5.21 – Oxygen RIE. Burnt PMMA (indicated by the arrows) redeposits on the membrane (**a**) and the chip (**b**) after dissolution in acetone.

5.7 Conclusion and Outlook

I have shown that the fabrication of freestanding MoS_2 ribbons containing a nanopore is technically possible. However, the stability of these ribbons when both measurement channels were connected remains to be solved. By using suspended MoS_2 ribbons, we have shown that correlated transverse signals can be obtained. The nature of these signals, however, is at the moment speculative and I provided different possible explanations. Ionic signals are highly dominated by capacitive noise at higher frequencies, the FET measurement scheme

could, therefore, be beneficial to achieve high signal-to-noise ratios at bandwidths up to 100 MHz.[253] By pushing more charge carriers into the conduction band, we believe that much higher signal-to-noise ratios than reported here can be achieved. It is, therefore, crucial to find suitable methods to gate the ribbons to take full advantage of the field effect sensing capabilities of monolayer MoS_2.

The morphology of the two signals might allow us to decouple two distinct parts of the translocation process. Since the FET only senses the molecule when it is close to the MoS_2 surface, we can effectively only detect the moment before the translocation when the DNA is in close contact to the MoS_2 surface. Comparing the signals of the two channels might help to interpret the ionic current traces and decouple access resistance probing from the actual translocation.

An alternative to the ionic current readout could greatly simplify the design of nanopore sequencing devices. A chip made of 2D-field effect transistors would allow extremely dense packing of nanopores with the limit set only by the current nanofabrication methods. Furthermore, the technologies needed for this dense fabrication are already widely used in semiconductor manufacturing. Since the transmembrane voltage would then be used uniquely to bring analytes to the nanopore, electrical insulation between individual nanopores is not important.

Lastly, such a device configuration might also overcome resolution limitations associated with the importance of the access-resistance in ionic current. In biological nanopores, the access resistance increases the read-length to 4 nucleotides at a time.[8] This means, that there are 256 distinct nucleotide configurations that make up the ionic current blockage. In practice, this complicates the base calling and is partly responsible for the low accuracy of nanopore sequencing devices.

5.8 Supplementary Figures and Tables

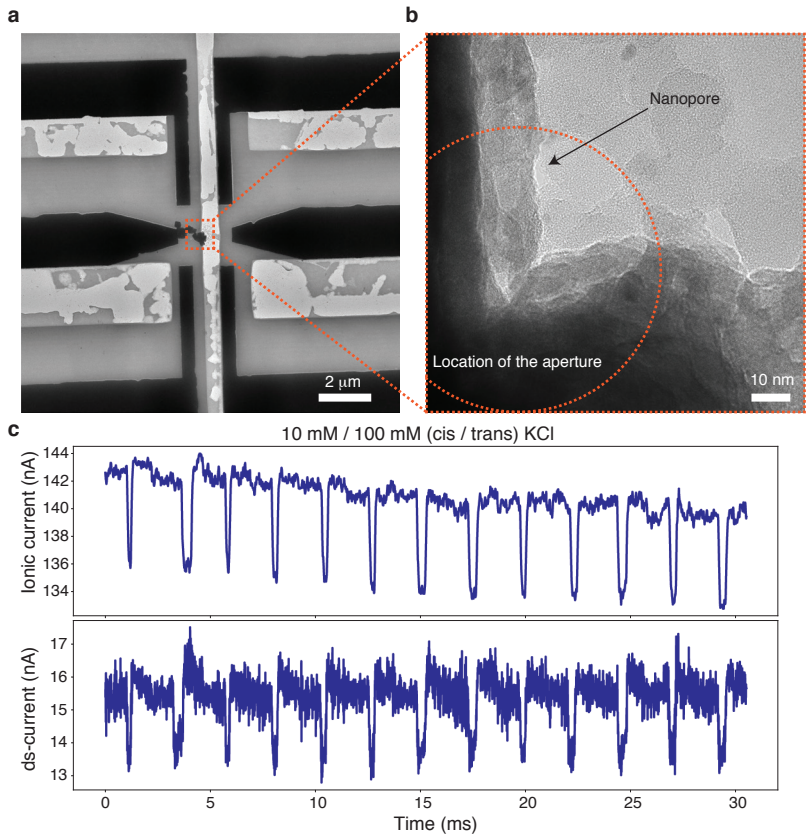

Figure S5.1 – Bad electrode insulation. a, TEM image of the device used to record the data in **c**. The aperture was partially clogged only leaving a small part open. There was a small hole in the MoS_2 (**b**). **c**, 1 kbp dsDNA translocation signals. The HSQ insulation on this device was removed after a short time in electrolyte (Figure 5.19**e** and **f**). The large current on the ionic channel suggests that a current leakage due to poor electrode insulation occured.

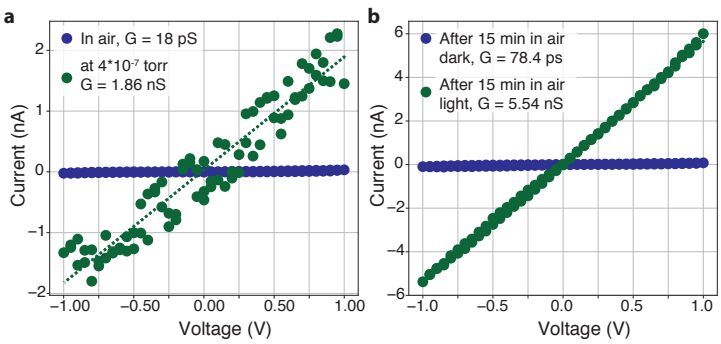

Figure S5.2 – Supplementary conductance measurements. a, Ribbon conductance in air (blue) and in a vacuum of 4×10^{-7} torr (green). **b**, Conductance 15 min after the vacuum measurements in dark state (blue) and with illumination (green).

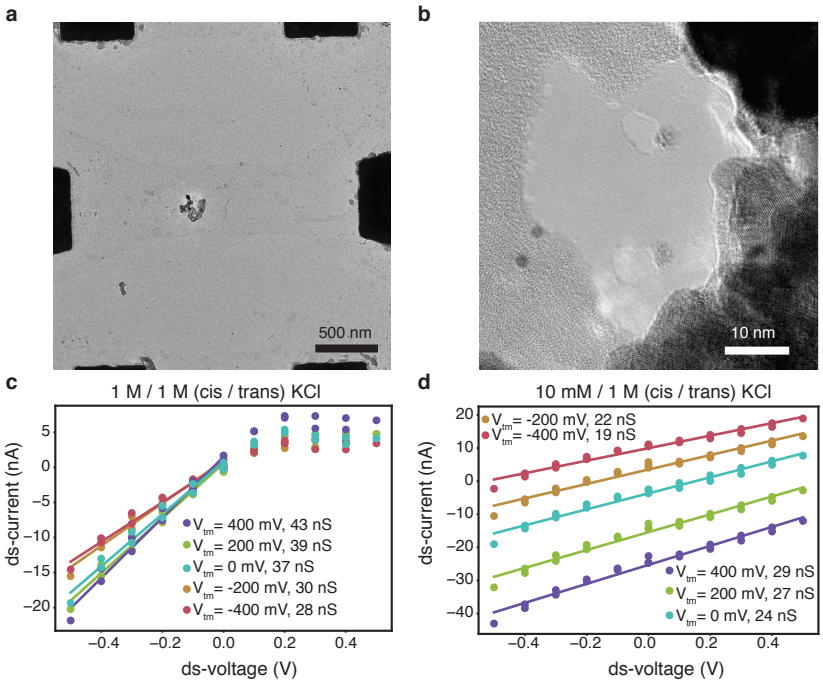

Figure S5.3 – Supplementary ionic gating. **a**, TEM image of the device used to measure the data in Figure 5.5. **b**, Close-up view of the freestanding part of the ribbon. **c**, I_{ds} vs. V_{ds} for different transmembrane voltages V_{tm} in 1 M / 1 M KCl. **d**, I_{ds} vs. V_{ds} for different transmembrane voltages V_{tm} in 10 mM / 1 M KCl.

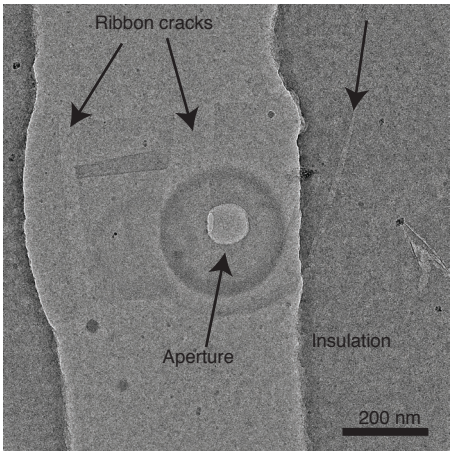

Figure S5.4 – Ribbon cracking after fabrication. A TEM image of a finished device. The darker contrast on both sides of the aperture is the insulation used to protect the metal leads from the electrolyte solution. Three large cracks are observed in the MoS_2 ribbon, which make the device unusable. The cracks might originate from the transfer process, or from a defective coating of PMMA during the EBL used to etch the ribbons.

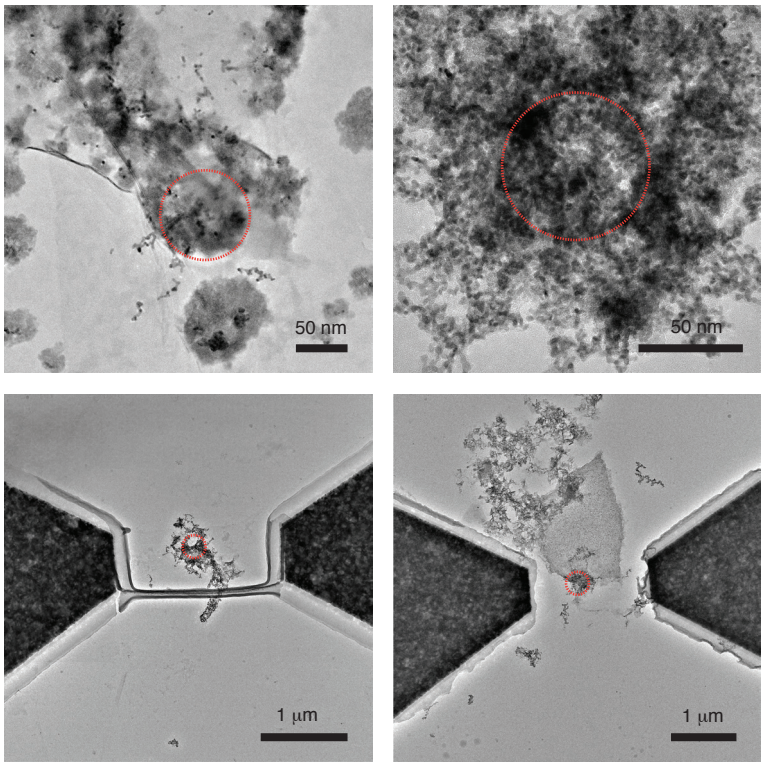

Figure S5.5 – A selection of contaminated SiN_x apertures. A collection of TEM images showing a contaminated freestanding MoS_2 part. The red dashed circles indicate the location of the aperture in the SiN_x membrane.

6 Outlook and Conclusion

This chapter is largely subjective and reflects my personal experience. First I will shortly discuss the impact of the advances presented in this thesis. I then will attempt to put the technologies into a larger context. Further, I will convey my subjective opinion on future developments. We have discussed three major subjects in this thesis: fabrication, energy conversion, and field-effect transistor (FET)-sensing.

6.1 Fabrication

At the start of my PhD, the state of the art fabrication method relied on focused ion beam (FIB)-drilling to create 100 nm to 500 nm large holes in silicon nitride (SiN_x) membranes fabricated through photolithography (Figure 6.1a). A poly(methyl methacrylate) (PMMA) mediated dry-transfer method was then used to place molybdenum disulfide (MoS_2) on top of the previously drilled aperture.

After countless afternoons in the cleanroom drilling apertures one-by-one using FIB I realized that this was neither a very efficient nor a scalable method of making holes in SiN_x membranes. Furthermore, to fabricate the FET-devices, precise knowledge of the location of the drilled aperture is needed in order to properly align subsequent e-beam lithography (EBL) steps, such as ribbon etching and insulation of the metal contacts. I used to take high-resolution scanning electron microscopy (SEM) images to determine the location of the FIB drilled aperture, then aligned it to the EBL design in the CAD software. Obviously, the alignment precision was very poor using this method, as illustrated in Figure 6.1b. It became quickly clear to me that the fabrication of a MoS_2-FET-nanopore cannot be done in a reliable way using this process flow. I, therefore, set out to develop a process flow allowing to create the apertures using EBL and reactive ion etching (RIE). There are two advantages in using an EBL system to create the apertures: first, the location is very precisely defined. Second, a whole wafer containing 72 membranes can be processed in minutes (compared to 10 min for a single aperture using FIB).

The transfer was the second bottleneck that frustrated me in the fabrication of MoS_2 devices.

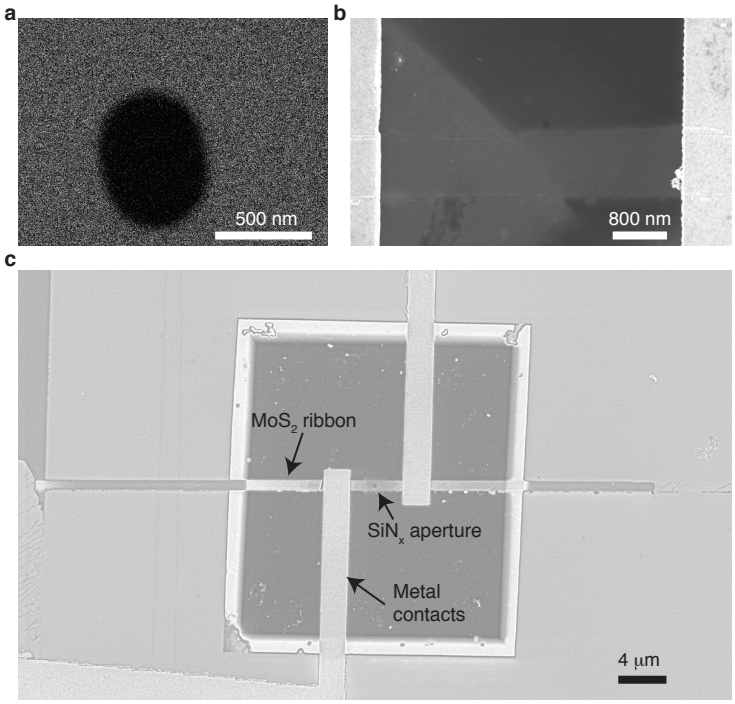

Figure 6.1 – Early process-flow. a, A FIB drilled aperture in a SiN_x membrane. The image was taken with a FIB-SEM in the center for micronanotechnology (CMI). **b**, The MoS_2 ribbon is misaligned with respect to the aperture. The image was taken with an SEM in the CMI. **c**, The first prototype of a MoS_2-FET-device using FIB made SiN_x apertures and EBL for shaping the ribbon. The image was taken with an SEM in the CMI.

The dry transfer method relied on using large areas of chemical vapor deposition (CVD)-grown material, reducing the throughput to a point where only a few transfers could be made with a single growth substrate. To make MoS_2 nanopore devices it is very important to align the aperture in the SiN_x membrane with the single-layer crystal of MoS_2. Although there was some degree of control on the alignment, misalignment was a very common occurrence. Once misaligned, it was not possible to change the location of the MoS_2 crystal. The supply of high-quality MoS_2 crystals was very limited and I got quickly frustrated by the wasteful use of this precious resource. I, therefore, built a new transfer microscope set-up and developed a transfer method allowing to make hundreds of devices from a single growth substrate (discussed in section 2.4 (page 44)).

As a result of these efforts, we can now fabricate a large number of MoS_2 devices reliably. The transfer method is still the limiting factor since the substrates can now be easily fabricated at the wafer scale. A skilled user can make about 30 devices a day with our current process flow.

I think that the fabrication of the substrates (SiN_x membranes with apertures) has already reached the maximal potential. All the steps involved are standard microfabrication processes already widely used in the semiconductor industry. It would, therefore, be easy to scale this process to any desired size. The MoS_2 transfer, however, has a lot of room for improvement.

To date, transfers are still done on a chip-scale. For a truly high-throughput fabrication, the MoS_2 needs to be transferred at the wafer scale. For this to happen, two developments are important: first, homogeneous monolayer growth using CVD or metal-organic CVD (MOCVD) on a wafer scale needs to be realized. Second, the transfer method needs to be able to bring the MoS_2 crystal from the growth substrate to the target substrate without compromising the quality. An alternative approach which would allow to create high-quality devices would be the direct growth of MoS_2 on the target substrate. Although direct growth of MoS_2 over apertures in SiN_x has been shown,[156] difficulties in controlling the process and therefore reproducing the results have limited its use. Direct growth would also avoid another major bottleneck of the transfer: polymer contamination. The transfer methods presented in this thesis rely on polymer transfer using PMMA or polydimethylsiloxane (PDMS). These polymers introduce unwanted contamination of the layer. Therefore it will be important to develop polymer-free transfer methods.

To conclude, large scale growth and transfer in combination with electrochemical reaction (ECR)[30] would allow relatively simple mass production of MoS_2-nanopore devices.

6.2 Blue Energy

The first application of the MoS_2 nanopore system was the sensing of analytes such as DNA.[28,29] My colleague, Jiandong Feng, was doing experiments with MoS_2 nanopores when I jokingly asked him: *Can we create a reaction inside a nanopore to generate power?* I imagined creating a nano-sized nuclear-reaction inside the nanopore, whereas he actually came up with a practical and simple answer to my question by using a chemical potential difference to create power.

The first realization was that our biosensor system is naturally ion-selective due to the strong surface charge of the material. There are two major applications of ion-selective membranes: desalination of seawater through reverse osmosis and energy conversion with a concentration gradient through reverse electrodialysis. Reverse osmosis has already been widely studied and is currently broadly used to produce drinking water in water-stressed countries. Reverse osmosis is becoming an increasingly important technology in water purification due to its higher energy efficiency than traditional desalination methods based on evaporation. We have not experimentally investigated the use of MoS_2 for reverse osmosis yet, but theorists have predicted high water flux and good ion rejection in MoS_2 membranes.[48] Given the importance of access to high-quality drinking water in the future, it would be very important to study the potential of nanoporous MoS_2 membranes for water desalination.

The second application, the energy conversion through reverse electrodialysis, is still in very early development. This energy is currently untapped and is lost at estuaries around the world. Therefore, this technology would provide another addition to the portfolio of clean energy sources. So far, a pilot power station in the Netherlands is evaluating the commercial viability of the technique. The efficiency of the ion-selective membranes will define whether

this technology is successful or not. Conventional ion-exchange membranes are based on thick polymer matrices and can achieve power densities of only about 1 W m^{-2}.

Since the efficiency of the ion transport is inversely proportional to the thickness of the membrane, our mono-atomic membranes could potentially provide the ultimate ion transport efficiency. The first step was to understand the generated osmotic current and potential for a single nanopore system. We found that a very large single-pore power was achievable with this system. Furthermore, we carefully investigated the dependence on pore size, pH values, and salt concentration.

In order to achieve high power, alkaline solutions were used to boost the surface charge of the MoS_2 pore, which in turn increased the ion selectivity. However, in real-world conditions, pH levels are neutral. It was, therefore, important to find alternative ways of tuning the surface charge without affecting the pH of the solution.

I was installing a laser set-up to my Faraday cage (Figure 6.2) to photogate my MoS_2-nanopore FETs (Figure 5.16 (page 139)) when I had the idea to use the laser source to investigate its influence on osmotic power generation. Monolayer MoS_2 is an intrinsic semiconductor with a bandgap of 1.8 *e*V (688 nm). In theory, any light illumination with a wavelength below 688 nm should influence the electronic state of the material. The idea was that if the surface charge increases during laser illumination, I could combine two natural resources to create something more efficient and compatible with the natural environment. I was using two diode lasers at two different wavelengths (blue and red) to evaluate the influence of the color of the light. Measuring the ion current generated in the dark state and the illuminated state revealed up to five times enhancement of the osmotic power during light illumination. We found that the enhancement is due to two factors: first, the ion selectivity is enhanced due to increased charges at the pore rim. This results in a larger osmotic voltage. Second, the charge of the surface (surrounding the pore) is also increased, which increases the surface conductance and therefore increases the osmotic current.

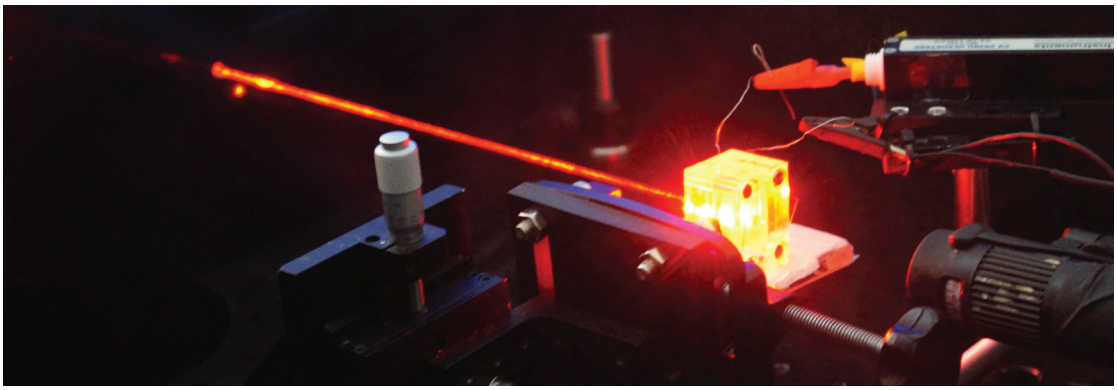

Figure 6.2 – Impression of the blue energy set-up. The laser blue-energy conversion in action. Photo-credits: Vytautas Navikas, LBEN, EPFL

The illumination intensities I used in this study were quite low, therefore the surface charge

boost should be easily achievable with natural sunlight and simple light concentrators.

The most interesting question that remains unclear, is how the single-pore power is translated into a porous membrane. We have discussed the importance of the surface conductance in subsection 4.4.3 (page 92) and it becomes obvious that the surface around the pore is crucial. As a consequence, the more pores that are introduced into a membrane the less surface is available between the pores. In other words, when increasing the porosity, the power density does not increase linearly. In fact, recent simulations by Cao et al.[224] suggest that the power density actually starts to decrease after a certain porosity. We can use these results to estimate the power density of the devices presented in this thesis. A porosity, ϕ, of about 1 % was calculated to be the most efficient for thin nanopores.[224] The power density Cao et al. obtained with thin membranes is about 10 % of the linear extrapolation of a single-pore. For a porosity of $\phi = 1$ % we have the following amount of nanopores per m^2 membrane: $n = \phi \frac{A_{\text{total}}}{\pi(\frac{d}{2})^2}$. Assuming a pore size of $d = 10$ nm we would have around $n = 1.27 \times 10^{14}$ nanopores per m^2. The power density, ϱ, can then be calculated using $\varrho = n \cdot P_{\text{singlepore}} \cdot F_{\text{linear}}$, where $P_{\text{singlepore}}$ is the single pore power (about 150 pW, Figure 4.4 (page 90)) and F_{linear} is the fraction of the linear extrapolation of a single pore. Using these numbers, we calculate a power density of about 2000 W m^{-2}. Using smaller nanopores allows for a slightly larger amount of pores for the same porosity, therefore also increasing the final power density.

Given these very conservative calculations, I believe that our technology can surpass the power density of conventional ion-exchange membranes (1 W m^{-2}) by at least three orders of magnitudes. However, to reach the stage of practical applications, there is still a lot of work needed to improve mechanical stability and large area scaling of the nanoporous MoS_2 membranes. To give mechanical stability, the ultra-thin MoS_2 layer needs to be supported on a larger substrate. One possible configuration is a silicon wafer containing a dense array of SiN_x membranes (Figure 6.3a), which are easily and cheaply fabricated through photolithography and KOH etching. Another photolithography step (with reactive ion etching) can then be used to create a dense array of apertures into the SiN_x membranes. MoS_2 is then transferred on this wafer, creating ultrathin MoS_2 membranes spanning the apertures in the SiN_x (Figure 6.3b). To make the final nanopore array into the MoS_2, several methods can be used, such as chemical etching[223] or laser-induced etching[210] (Figure 6.3b).

Another possible implementation of an energy harvesting device using MoS_2 membranes could be inspired by the work of hydrogel stacking by Schroeder et al.[276] By stacking high-salinity gels and low-salinity gels between cation- and anion selective gels an electrical current can be generated. Since this approach is based on flexible gels, it allows large arrays to work in parallel by cleverly folding the layers. Improving the ion-selectivity of these devices could further improve the achievable power density. Here, MoS_2 membranes could be used in combination with hydrogels to increase the ion selectivity.

Climate change is perhaps the biggest issue for our civilization and it might alter the progress and prosperity of the human species. We might soon reach a point where a reduction or

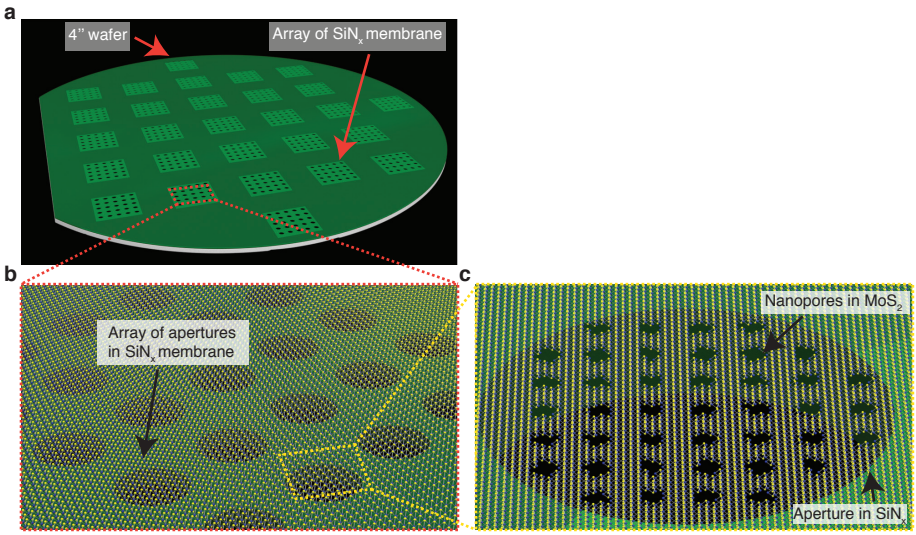

Figure 6.3 – Blue energy design proposal a, An array of SiN_x membranes can be created on a 4" wafer by conventional photolithography and KOH wet-etching. An array of apertures created through lithography and RIE can provide the structural support for the MoS_2. **b**, Zoom into one of the SiN_x membranes with suspended MoS_2. **c**, A zoom into one aperture in SiN_x, where an array of nanopores was fabricated into the MoS_2 membrane.

even a complete stop of fossil fuels alone is not sufficient to stabilize the climate and mitigate the negative effects caused by increased temperatures. Most measures to counteract global warming rely on reducing the amount of fossil fuel used. Energy production is, therefore, one important part that needs to be addressed when tackling climate change. I believe that clean energy can only be achieved by a highly diverse and decentralized portfolio of energy sources. However, geographic and climatic differences around the world do not allow the efficient use of each of these energy sources anywhere and anytime in the world. I hope that our contribution to effective ion-selective membranes can have a positive impact on the future energy portfolio.

6.3 Transverse Detection

The design, fabrication, and use of MoS_2-nanopore FET device was the main goal of my thesis. As described in section 5.6 (page 140), there were many obstacles along the way, which slowed the progress substantially. Especially intimidating was the knowledge that cross-talk artifacts are a big problem and that it would, therefore, require extraordinary proof to convince myself and the experts of the field that a field effect occurs. On the other hand, only a small number of people have worked on such devices in the past, opening possibilities of discovering something new. This gave me the motivation and persistence needed to attempt to tackle the difficult fabrication of these devices.

The recent popularity of Oxford nanopore's handheld DNA sequencer based on biological

nanopores shows the potential of nanopore platform for DNA sequencing. Oxford nanopore's technology is still in its early stages but already works surprisingly well. It allowed sequencing in remote areas without access to large sequencing facilities. Doubtless, nanopores will play a major role in future sequencing technologies. Even though nanopore sequencing can provide extreme long read lengths, the error rates are still much higher than conventional sequencing methods. Therefore, a large array of nanopores with individual readouts is needed to cover DNA sequences multiple times in order to improve the accuracy. To achieve this, every single nanopore needs to be electrically isolated from each other, requiring complicated nanofluidic channels bringing analyte and buffer to the individual nanopores. This greatly limits the density of devices currently achievable.

The current flow-cell used in Oxford nanopore's technology MinIon sequencer is roughly 1 cm x 2 cm in size. It contains 512 individually addressable nanopores that are electrically insulated from each other through microfluidics. Therefore, the pore density is about 250 pores cm^{-2}. This value is probably close to the practical limit of this system. Nanolithography might be able to push the boundary further. However, by shrinking the dimensions, the volume of each analysis-chamber will also shrink. At some point the depletion of the ions during the experiment would become so important that a single run could only last for a short time. For these reasons I believe that it will not be possible to increase the pore density much further with the current technology.

The nanopore-FET device described in this thesis shows that an alternative to the ionic current readout could greatly simplify the design of nanopore sequencing devices. A chip made of 2D-FETs would allow extremely dense packing of nanopores with the limit set only by the current nanofabrication method. To get a rough comparison with the MinIon we could assume that we place a FET device every 10 µm. Such a configuration yields 10^6 pores cm^{-2}, which would easily overcome the limitations posed by the MinIon system. Furthermore, except MoS_2 growth and transfer, all technologies needed for this dense fabrication are already widely used in semiconductor manufacturing. Since the transmembrane voltage would solely be used to bring analytes to the nanopore, electrical insulation between individual nanopores would become obsolete.

Furthermore, I have shown that the signal-to-noise ratio (SNR) of the FET current is superior to the ionic current. As a consequence, higher bandwidths than currently used for ionic current sensing can be used for recording signals. As a consequence, DNA molecules can be threaded through the nanopore at higher speeds, effectively increasing the DNA sequencing speed.

Lastly, such a device configuration might also overcome resolution limitations associated with the dominating access-resistance in ionic current. In biological nanopores, the access resistance increases the read-length to four nucleotides at a time. This means, that there are 256 distinct nucleotide configurations that make up the ionic current blockage. In practice, this complicates the base calling and is partly responsible for the low accuracy of nanopore sequencing devices. If an alternative sensing mechanism can decrease the number of simul-

taneously measured nucleotides, then the accuracy of the base-calling algorithms could be greatly improved.

A better understanding of the sensing principles of these MoS_2 based nanopore-FET devices is needed in order to advance into practical applications. To understand the devices better, more experiments need to be conducted, which requires devices that are stable for longer measurement periods. At the current stage, the fabrication of the devices has become largely routine, all the involved steps are set-up and optimized. The main part that still needs some attention is the stability of freestanding devices. I suspect that improper use or suboptimal design of the electronic set-up can induce current discharges and facilitate the breakage of the freestanding MoS_2 layer. To the best of my knowledge, nothing is known about the structural integrity of a freestanding MoS_2 layer in aqueous solution when a drain-source current is passed through it. Therefore it would also be advisable to more carefully study the fundamental behaviors of these transistors in aqueous solution.

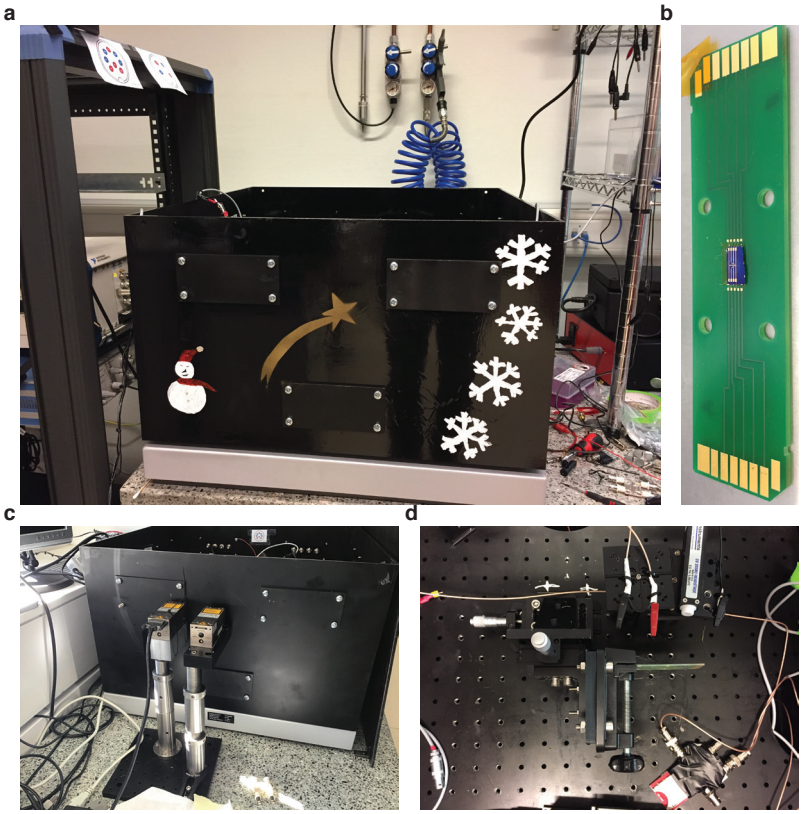

Figure 6.4 – Impression of FET-nanopore set-up a, The steel box built for the nanopore FET project is made of two levels. The bottom level contains all the batteries needed to power the electronic components. The top level is a hole-plate inspired from optical set-ups which allows to build configurations using existing components. **b**, A nanopore chip wire-bond to a custom made PCB board. **c**, Laser sources are kept outside of the Faraday cage and are injected via holes in the box. **d**, Measurement part of the set-up.

This project turned out to be highly interdisciplinary and gave me the opportunity to learn

new things about micro- and nano-fabrication, electronics, amplifiers, materials-science, solid-state physics and even metal-work (Figure 6.4). Looking at the results obtained so far, the usefulness of a nanopore-FET sensor seems questionable at first. But I am convinced that with continued research effort these devices can be fabricated in a reliable and reproducible way. I believe that once the technology is more mature it will definitely provide advantages over ionic current measurements. It might even be used in future sequencing devices due to its ability to create denser arrays of pores.

The nanopore field, in general, is not that young anymore and most of the fundamental physics of ion transport has been discovered. However, the discovery of more and more 2D-materials continues rapidly, providing the nanopore field with membranes that have interesting physical properties spanning insulators, conductors and semiconductors. Not only the band-gap of a 2D-material is interesting, but also the composition of the crystal structure can induce surprising properties, such as triangularly shaped nanopores in hexagonal boron-nitride (h-BN).[31] Further, I think that the membrane material has a large influence on the behavior of ions under confinement (as shown with room temperature ionic liquid (RTIL)[277]), opening possibilities to study fundamental nanofluidics. I believe that the nanopore field should work closely with material scientists to expand the horizon of possible membrane materials to discover new avenues in fundamental nanofluidics, biosensing, as well as ion-exchange applications.

A Appendix

A.1 Materials

A.1.1 Reagents

This is a list of materials used in the fabrication of MoS_2 devices as described in chapter 2 (page 35) and put into step-by-step instructions in section A.2. This list of materials has been published here:

M. Graf et al. "Fabrication and practical applications of molybdenum disulfide nanopores". In: *Nature Protocols* 14.4 (2019), pp. 1130–1168. DOI: 10.1038/s41596-019-0131-0.

- 4-inch double-side polished (DSP) silicon substrates (Doping: N-Type, Orientation: < 100 >, Resistivity: 1 Ω cm to 20 Ω cm, Thickness: 400±10 µm) (Nova Electronic Materials)
- PELCO ESD Safe SV Carbon Wafer Tweezers (Ted Pella, cat. no. 5048-SV)
- SPR 220 3.0 photoresist (MicroChem)AZ 300 MIF Developer (EMD Performance Materials Corp). ⚠ It is a potential irritant and corrosive to metals. Wear proper eye protection and gloves while handling. It should be discarded in an appropriate waste disposal container.
- ZEP 520A electron beam photoresist (ZEON). ⚠ It is a highly flammable liquid. Keep away from heat and static discharge. While handling, wear proper eye and face protection.
- 45 % (w/w) Potassium hydroxide solution (Fisher Scientific, cat. no. SP236-500). ⚠ It is highly corrosive and irritant. It should be handled with proper eye protection and gloves. It should be discarded in an appropriate waste disposal container.
- 29 % (w/w) Ammonium hydroxide solution (Fisher Scientific, cat. no. NC1297835). ⚠ It is highly corrosive and irritant. It should be handled with proper eye protection and gloves. It should be discarded in an appropriate waste disposal container.

- 30 % (w/w) Hydrogen peroxide (Fisher Scientific, cat. no. H325-4). ⚠ It is highly corrosive and may cause severe burns. It should be handled with proper eye protection and gloves. It is discarded in an appropriate waste disposal container.
- 49 % (w/w) Hydrofluoric Acid (Fisher Scientific, cat. no. 08-901-806). ⚠ It is highly corrosive, toxic and fatal. It must be handled with face protection shields and neoprene gloves to prevent any exposure to skin. It must be handled within a laminar cabinet. It must be disposed of in an appropriate waste disposal container.
- Hydrochloric acid (Fisher Scientific, cat. no. 50-012-11). ⚠ It is highly corrosive and irritant acid. It must be handled with face protection shields and neoprene gloves to prevent any exposure to skin. It must be handled within a laminar cabinet. It must be disposed of in an appropriate waste disposal container.
- Remover 1165 (MicroChem). ⚠ It can cause eye, skin and respiratory irritation. It should be handled with proper eye protection and gloves within a laminar cabinet It must be disposed of in an appropriate waste disposal container.
- Nanostrip (VWR, cat. no. 10135-756). ⚠ It is highly corrosive, irritant and toxic. It must be handled with proper eye protection and gloves within a laminar cabinet. It must be disposed of in an appropriate waste disposal container.
- ProTEK PS Primer (Brewer Science). ⚠ It can cause irritation when in contact with eyes and skin. It should be handled with proper eye protection and gloves within the laminar cabinet. It should be discarded in an appropriate waste disposal container.
- ProTEK PSB-23 (Brewer Science). ⚠ May cause drowsiness or dizziness. It should be handled with proper eye protection and gloves within a laminar cabinet. It should be discarded in an appropriate waste disposal container.
- Ethyl lactate (Sigma Aldrich, cat. no. W244015). ⚠ It is flammable, oxidizing and corrosive. It can cause serious irritation when in contact with eyes and skin. It should be handled with proper eye protection and gloves within a laminar cabinet. It should be discarded in an appropriate waste disposal container.
- Hexyl acetate (Sigma Aldrich, cat. no. 108154)
- 2-Propanol (Fisher Scientific, cat. no. 50-012-02). ⚠ 2-Propanol vapors can cause eye, skin and respiratory irritation. It should be handled with proper eye protection and gloves within a laminar cabinet. It should be discarded in an appropriate waste disposal container.
- Potassium chloride (KCl, ≥ 99 %; Sigma-Aldrich, cat. no. P9333), for preparing the translocation buffer.
- Ethylenediaminetetraacetic acid solution (EDTA, pH8, Sigma-Aldrich, cat.no. 03690), for preparing the translocation buffer

- Thermo Scientific NoLimits 2 kilobase pairs (kbp) DNA Fragment (0.5 µg µl^{-1}) in TE Buffer (10 mM Tris-HCl pH 7.6, 1 mM EDTA)
- Ambion 1M Tris (pH 8, Thermo Fisher Scientific, cat. No. AM9856), for preparing buffer for translocation experiments
- RBS™25 solution (Sigma-Aldrich, cat. No. 83460), for cleaning the PMMA flow-cells. ⚠ RBS 25 solution should be handled with proper eye protection and gloves since it can cause eye damage and skin irritation. It should be discarded in an appropriate waste disposal container.
- Poly(methyl methacrylate), PMMA, Mr = 450, 8 % (w/v) in Anisol (Micro Resist Technology GmBH, Berlin, Germany)
- Sylgard 184 silicone base and a Sylgard curing agent
- KWIK-CAST Silicone (World Precision Instruments)
- Milli-Q water (0.2 µm filtered)
- Ethanol (Thommen-Furler AG)
- Acetone (Thommen-Furler AG), for cleaning. ⚠ Acetone is irritant for eyes and skin and can be hazardous if inhaled. It should be handled with proper eye protection and gloves within a laminar flow cabinet. It should be discarded in an appropriate waste disposal container.
- Isopropanol (Thommen-Furler AG), for cleaning

A.1.2 Equipment

Clean room equipment

- RCA Wet Bench (Reynolds Tech)
- Silicon Etch Wet Bench (Reynolds Tech)
- Spectroscopic Ellipsometer (J. A. Woollam, model no. M-2000 DI)
- LPCVD Furnace (Tystar Corp., model no. Mini-Tytan 4600)
- High-Purity Oxidation and Diffusion Furnace (Tystar Corp., Tytan)
- HMDS Vapor Prime System (Yield Engineering Systems)
- Spinner and Hotplate (Brewer Science, model no. CEE 100CB)
- Spinner (CEE Apogee)

- Laser Pattern Generator (Heidelberg, model no. DWL 2000)
- i-Line Stepper (ASML, model no. PAS5500/275D)
- Contact Aligner (Suss MicroTec MA8)
- Direct-Write Electron Beam Lithography System (JEOL, model no. JBX 6300-FS)
- Reactive Ion Etcher (Unaxis 790)
- Deep Silicon Etcher (Unaxis Shuttleline DSEII)
- Spin Rinse Dryer (Semitool PSC-101)
- Backside LED illuminated Wet Etching Wafer Holder (AMMT)
- Ion Beam Sputtering Cluster Tool (4 Wave)
- Parametric Test Station (Keithley, model no. 4200 SCS)
- PDMS Dispenser (STANGL Semiconductor Equipment AG, Germany)
- Thinky Mixer (THINKY ARE 250, Japan)
- Hot-air oven (VWR VENTA-Line)
- Weighing pan (Scout™Pro)

Wet lab equipment

- Clean glass slides (Thermo Scientific)
- Clean-Room-Paper (VWR, Nonwoven Wipers)
- Hot-plate (CORNING PC-400D)
- Micropipettes (RAININ Pipet-Lite XLS)
- Microtips (VWR ZAP®SLIK™Aerosol Tips)
- Tweezers (ideal-tek 1-259cf.SA), plastic tips
- Razor blades (Apollo Solingen Germany)
- Insulin Syringes U100 (1 ml, VWR, cat. no. CODA621640), for injection of the buffers into the flow-cell
- Hypodermic Needle 26 G (0.45 x 10 mm BD Microlance, VWR, cat. no. 613-5155), a needle that fits into the flow-cell
- Syringe Filters Whatman Anotop 10 Plus (0.02 µm, Sigma-Aldrich, cat. no. WHA68093002), for filtering Milli-Q/EtOH and buffer solutions before injection into the flow-cell

- Syringe Filters PES-20/25 (0.20 µm, Chromafil Xtra, cat. no. 729240), for filtering Poly(methyl methacrylate), PMMA

Other materials

- Silver Wire (0.2 mm diameter, Advent Research Materials, cat. No. AG5488), for preparing Ag/AgCl electrodes
- Teflon chucks
- flow-cell, see subsection 2.7.3 (page 55))
- O-rings (2 mm inner diameter, 1 mm thickness, Kubo Tech AG, Effretikon, Switzerland, cat. No. 0101-001081)

Instrumentation

- Axopatch 200B (Molecular Devices, Inc. Sunnyvale, CA), for measuring the current (<100 kHz)
- Chimera VC100, for measuring the current (<2 MHz)
- FEMTO DLCPA-200, for measuring the current (different amplifications are provided)
- NI-PXI-4461 (National Instruments, Austin TX, USA), to digitize the analog data from Axopatch 200B and FEMTO DLPCA-200
- NI-PXI 8336 (National Instruments, Austin TX, USA), fiber optic interface to communicate with the computer
- NI-PXI-1042Q (National Instruments, Austin TX, USA), chassis to hold NI-PXI-4461 and NI-PXI 8336
- Simple voltage source for the chlorination of silver wire
- Transmission electron microscope (FEI Talos, Hillsboro, OR, USA), for imaging and drilling nanopores
- Custom made TEM holder
- Furnace with argon and hydrogen gas flow

Transfer microscope

- 5x Long working distance objective (LMPLFLN5x, Olympus, Tokyo, Japan)
- 50x Long working distance objective (LMPLFLN50x, Olympus, Tokyo, Japan)

- Halogen lamp power supply (TH4-200, Olympus, Tokyo, Japan)
- Halogen lamp (U-LH100L-3-7, Olympus, Tokyo, Japan)
- Microscope base (BXFM, Olympus, Tokyo, Japan)
- Camera (AVT PIKE F-505C, Allied Vision Technologies, Stadtroda, Germany)
- Vacuum and heating stage (taken from chip-to-chip bonder, Idonus, Neuchatel, Switzerland)
- Hypodermic Needle 26G (0.45 x 10 mm BD Microlance, VWR, cat. no. 613-5155), screws onto the M4 screw of the sample holder post and provides connection to microcapillary
- Laser-based micropipette puller P-2000 (Sutter Instruments)
- Pulled microcapillary (Sutter Instruments P2000, Novato, CA, USA), for pulling microcapillaries. Alternatively, pre-pulled capillaries can be bought.
- XYZ Translation Stage with Standard Micrometers (Thorlabs, cat. no. PT3), for holding the needle
- XY Stage (Thorlabs, cat. no. XRN25P-K1/M), for holding the sample
- Post holder (Thorlabs, cat. no. PH1), for attaching the needle holder to the XYZ stage
- Stainless steel post (Thorlabs, cat. no. TR2), acts as the needle holder in combination with an M4 screw

Software

- Nanolithography Toolbox (Center for Nanoscale Science and Technology CNST, NIST)
- LabView 2017 (National Instruments, Austin TX, USA), to write the acquisition software

A.2 Protocol

This protocol has been published here:

M. Graf et al. "Fabrication and practical applications of molybdenum disulfide nanopores". In: *Nature Protocols* 14.4 (2019), pp. 1130–1168. DOI: 10.1038/s41596-019-0131-0.

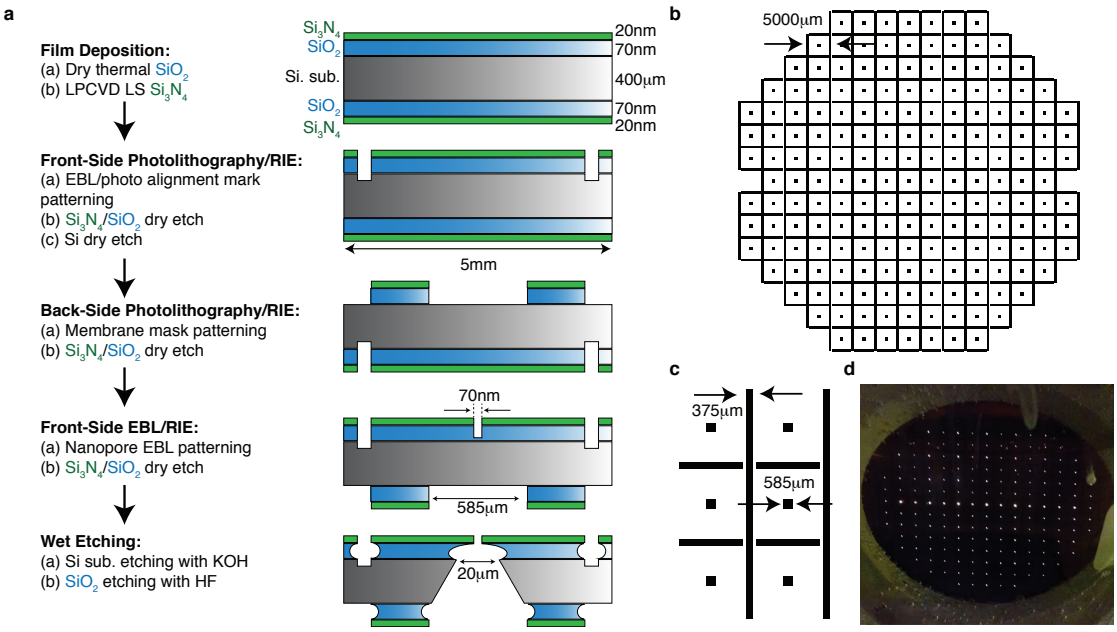

Figure A1.1 – Fabrication. **a**, The clean-room process flow. **b**, The backside-lithography design. **c**, Dimensions of the membrane openings and the dicing lines. **d**, Backside illumination during potassium hydroxide (KOH) etching to verify the membrane formation. *This Figure was published in Nature Protocols, 2019, Graf et al.*[50]

A.2.1 Fabrication of silicon nitride chips. Timing 2 d to 3 d

⚠ Fabrication is performed in a clean room facility ISO 14644-1 Class 7. Figure A1.1a summarizes the fabrication process.

Step 1 Generate the lithography patterns (alignment marks, membranes, and nanopores) with Nanolithography Toolbox and generate photolithography reticles with a laser pattern generator.

> Membrane pattern mask dimension (585 x 585 µm^2) and the width of the trenches (375 µm) (Figure A1.1b-c) were chosen to generate ≈ 20 x 20 µm^2 square membranes and trenches etched 2/3 into 400 µm-thick silicon substrate upon completion of anisotropic KOH etch. This allows individual devices to be easily separated by cleaving the pieces from patterned arrays without the need for wafer scribing and dicing, thereby reducing sample handling during the fabrication process.

Step 2 Clean a batch of 4-inch silicon wafers using RCA clean as follows: Clean the wafers at 80 °C in H_2O:NH_4OH:H_2O_2 (5:1:1) for 10 min followed by a rinse in deionized (deionized (DI)) water. Clean the wafers at 80 °C in H_2O:HCl:H_2O_2 (6:1:1) for 10 min followed by a rinse in DI and spin dry.

Step 3 Grow 70 nm of dry thermal SiO_2 at 1000 °C in an oxidation and diffusion furnace and verify the SiO_2 film thickness using spectroscopic ellipsometry.

Step 4 Deposit 20 nm of low-stress silicon nitride (LS SiN_x) on oxidized wafers and an additional silicon wafer monitor in a low pressure chemical vapor deposition (LPCVD) furnace and verify the LS SiN_x film thickness on the monitor wafer using spectroscopic ellipsometry.

> Put aside one wafer in order to test the quality of the nitride membrane (Step 31-Step 36).

Step 5 Vapor prime the wafer in hexamethyldisilazane (HMDS) to improve photoresist adhesion.

Step 6 Spin-coat one side of the wafer with positive photoresist SPR 220 3.0 at 3,000 rpm (1,000 rpms^{-1} ramp-up rate) for 60 s, and soft-bake the wafer on a hot plate at 115 °C for 90 s.

> Do not put the wafer directly on the vacuum chuck on the spinner as it could scratch the surface. Use a 4” wafer chuck to prevent surface damage. Clean all surfaces such as microscope stages, heating plates, wafer cooling plates on which the wafer is placed to avoid scratching the thin films. Handle the wafers only with ESD safe non-scratching tweezers.

Step 7 Expose the wafer in an i-line stepper at 200 mJ cm^{-2} to define stepper alignment marks.

Step 8 Post-exposure soft-bake the wafer on a hot plate at 115 °C for 90 s.

Step 9 Develop with MIF-300 AZ developer for 90 s, rinse it with DI water for 60 s, and dry with a nitrogen gun.

Step 10 Descum the wafer in an oxygen plasma (O_2 30 sccm, 40 mtorr, 100 W, 60 s).

Step 11 Etch the LS SiN_x/silicon dioxide (SiO_2) layers using a reactive-ion etcher. Etch the 20 nm LS SiN_x first with CHF_3 30 sccm, O_2 2 sccm, 15 mTorr, 150 W, for 180 s. Consecutively, etch through 70 nm SiO_2 into silicon substrate with CF_4 30 sccm, 40 mtorr, 150 W, for 120 s. After etching, remove the photoresist with Remove 1165, rinse in DI water. The etched marks will be easily recognizable by stepper optics after the etch.

⚠ Always clean the etch chamber and check the etch rates on monitor pieces.

Step 12 Repeat Step 5-Step 11 to define electron-beam lithography (EBL) alignment marks. The local-alignment marks are positioned in the corners of the chips (Figure A1.1), outside of the area exposed to liquid when the sample is placed in the flow-cell to avoid current leakage through the exposed substrate during ionic current and DNA translocation measurements.

Step 13 Etch EBL marks with deep silicon etcher. First etch with C_4F_8 1 sccm, Ar 40 sccm, SF_6 60 sccm, 22 mtorr, 12 W, 900 W ICP, for 4 s and then with C_4F_8 1 sccm, Ar 40 sccm, SF_6 120 sccm, 23 mtorr, 12 W, 900 W ICP, for 4 s. Repeat this step four times to create ≈3.5 µm deep trenches into the silicon substrate that will be easily recognizable with EBL electron optics.

Step 14 Repeat Step 5-Step 11 to define the membrane patterns and trenches (Figure A1.1b-c) at the other side of the wafer. Back-side-align the pattern to the stepper alignment marks.

Step 15 Spin-coat the front-side of the wafer (the side with alignment marks) with ZEP 520A EBL resist at 4,000 rpm (1,000 $rpms^{-1}$ ramp up rate) for 60 s, and hard-bake the resist on a hot plate at 180 °C for 15 min.

⚠ It is recommended to filter the EBL resist to remove impurities that could create nanoscale pin-holes in LS SiN_x/SiO_2 during nanopore etching in Step 19.

Step 16 Expose the wafer in electron beam at 1000 µC cm^{-2} to define 70 nm nanopores into the resist. Use deep-etched EBL marks to locally align nanopore patterns to the center of membranes.

Step 17 Cold-develop at 4 °C in hexyl acetate for 90 s, rinse in 2-propanol for 30 s and dry the wafer with a nitrogen gun.

Step 18 Descum the wafer in an oxygen plasma (O_2 30 sccm, 40 mtorr, 100 W, 10 s).

Step 19 Etch the nanopores into LS SiN_x with CF_4 30 sccm, 40 mtorr, 150 W, 9 loops, 60 s each. After etching, remove the photoresist with hot (100 °C) Remover 1165, rinse in DI water and spin dry.

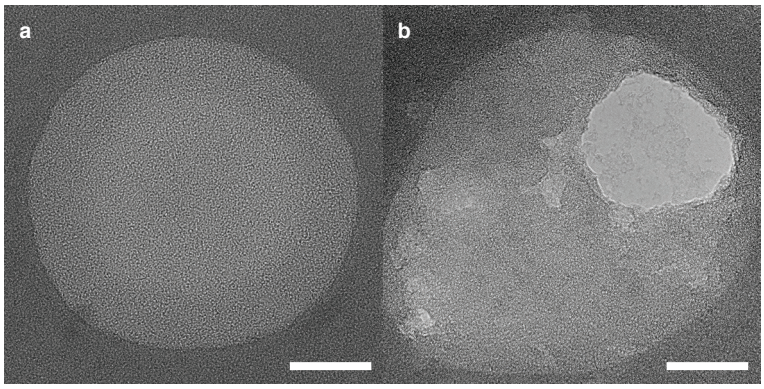

Figure A1.2 – Insufficient etching of the aperture. **a**, Unsuccessful etching of aperture in the SiN_x membrane. The scale bar is 20 nm. **b**, MoS_2 monolayer transferred on an incompletely etched SiN_x aperture. The scale bar is 20 nm. *This Figure was published in Nature Protocols, 2019, Graf et al.*[50]

⚠ Always clean the etch chamber and check the etch rates on monitor pieces. If nanopores are not open (Figure A1.2a) or only partially open (Figure A1.2b), increase the etching time or the number of loops.

Step 20 Remove the residual impurities with RCA clean as described in Step 2.

Step 21 Spin ProTEK Primer at 1,000 rpm (1,000 $rpms^{-1}$ ramp-up rate) for 60 s, bake hot-plate at 110 °C for 60 s, and bake on hot-plate at 220 °C for 5 min. Then spin ProTEK PSB-23 at 1,500 rpm (1,000 $rpms^{-1}$ ramp-up rate) for 60 s, bake hot-plate at 110 °C for 120 s.

Step 22 Expose negative tone mask with the membrane array and trenches in a contact aligner at 500 mJ cm^{-2}.

Step 23 Post-exposure soft-bake the wafer on a hot plate at 110 °C for 120 s.

Step 24 Develop in ethylene lactate for 60 s.

Step 25 Post-development hard-bake the wafer on a hot plate at 220 °C for 180 s.

Step 26 Descum the wafer in an oxygen plasma (O_2 30 sccm, 40 mtorr, 100 W, 155 s).

Step 27 Mount the wafer protected with ProTeK into a holder so that the membrane patterns and trenches are facing outward and are exposed to the etching solutions. Etch the silicon substrate in at 80 °C, constantly stirring the 45 % (w/w) KOH:DI water (1:1) solution. Terminate the etch after ≈ 4 h 30 min when the substrate becomes transparent to the back-side illuminating LED light. Rinse the holder with the wafer in DI water. Backside-illuminated wafer with released membranes in the etching solution is shown in Figure A1.1d.

⚠ The thickness of the wafers varies, which requires adjustments to the etch-time. It is important to know when to stop etching to get the desired membrane dimensions. A wafer holder with LED illuminated or transparent back-side that allows illuminating the wafer from the back while it is in the etching solution to see when the membranes become transparent is very useful.

Step 28 Remove the wafer from the holder, dry it gently with a nitrogen gun, and measure the membrane dimensions under a calibrated microscope with NIS-Elements Viewer to ensure their dimensions are ≈20 x 20 μm^2.

⚠ Handle the wafer with released membranes and etched trenches with extreme caution in this and the following steps as it is quite fragile. Never sonicate or spin-dry the wafers.

Step 29 Remove ProTEK in hot Nanostrip, rinse in DI water, and do RCA clean as described in Step 2.

Step 30 Etch the wafer in HF for 10 s to remove the remaining SiO_2 underlayer, rinse it with DI water and dry it gently with a nitrogen gun. Inspect the membrane with an optical microscope. Repeat RCA clean if impurities are present.

A.2.2 Optional: Fabrication of a test wafer for leakage analysis. Timing: 1 d to 2 d

⚠ This section (Step 31-Step 36) describes the procedures for preparing a test wafer to test the current leakage. For details, see subsection 2.3.5 (page 42)

Step 31 Take one wafer from the batch prepared in Step 1-Step 4.

Step 32 Perform lithography as described in Step 14, defining only membrane patterns and trenches.

Step 33 Perform Step 20-Step 27 to release the membranes.

Step 34 Deposit 50 nm of gold by biased target deposition (BTD) at 45° on both the membrane side and the back-side of the wafer using a sputtering cluster tool. The back-side of the wafer is shown in Figure 2.3 (page 42)a.

⚠ BTD technique traditionally used in the fabrication of tunnel junctions is utilized to ensure good sidewall coverage in the KOH etched vias and to prevent interface mixing and formation of defects in SiN_x/SiO_2 layers.

Step 35 Separate the individual chips by carefully cleaving, effectively creating 180 large-area metal-insulator-metal (MIM) junctions shown in Figure 2.3b.

⚠ Handle the pieces with extreme caution with non-scratching tweezers while avoiding touching the metalized surfaces which can create defects in SiN_x/SiO_2 thin-film layers.

Step 36 Measure the voltage-current characteristics with parametric test station.

⚠ Apply silver paint on the gold layer to avoid defect creation with electrical probes during measurements.

A.2.3 Transfer

Step 37 Transfer of MoS_2 on SiN_x membrane can be achieved in two ways as follows (see section 2.4 (page 44)). Follow Option A for transfer using PMMA and Option B for transfer using PDMS.

(A) Transfer of MoS_2 using PMMA. Timing: ≈15 min per device with ≈ 12 h cleaning procedure

i Filter poly(methyl methacrylate) (PMMA, Mr=450, 8 % (w/v) in anisole) using 0.2 µm filter.

ii Place the CVD grown MoS_2 on sapphire substrate (see subsection 2.3.6 (page 43)) on a spin-coater with vacuum suction and add ≈ 200 µl to 300 µl of PMMA followed by spin-coating at 2500 rpm for 1 min.

⚠ It is ideal to perform this step-in a clean laminar flow cabinet to avoid any particulate contamination.

iii Place the PMMA/MoS_2/sapphire substrate on a hot-plate preheated at 180 °C for 5 min.

⏸ The substrate can be stored in a clean dust-free environment. The best is to use it within a week.

iv Using a scalpel, manually scratch the spin-coated PMMA on the MoS_2/sapphire substrate orderly to leave behind small PMMA patches (c.a. 1 x 0.5 mm^2) covering the MoS_2.

⚠ The scratching should be delicate and uniform. Unavoidably, scratching sometimes removes MoS_2 along with the PMMA layer leaving behind some defective monolayers at the edges of the patch. However, each PMMA patch harbors monolayer MoS_2 that can be used to transfer on SiN_x membranes.

v Place a drop of Milli-Q water (≈ 10 µl) at the edge of a PMMA patch to be transferred.

⚠ Do not put a large drop of water (>20 µl) as it will be difficult to track the detachment progress. If you accidentally put a larger volume of the drop, you can use a small clean-room paper to suck out the drop carefully and re-do the step with a smaller volume.

vi Using a microcapillary attached to a micromanipulator, approach one of the edges of the PMMA patch and slowly peel the edge of the patch so that the water starts to penetrate from below the patch.

⚠ Slowly approach the edge of the patch. Collision with the substrate might bend or break the microcapillary.

vii After approximately half of the patch is detached, slowly remove the microcapillary from below and re-align it on the top of the patch, press gently and slowly start detaching the rest of the patch from the substrate.

viii Once the entire patch is detached, it floats on the air-water interface. Slowly approach the microcapillary through the water-drop from the bottom of the floating PMMA/MoS_2 patch and lift it out of the water-drop.

⚠ One can use bright-field illumination or dark-field mode under the optical microscope to search for the detached patch.

ix Align the SiN_x membrane on which the MoS_2 is to be transferred and place a drop of Milli-Q water (≈ 10 µl) c.a. 1 mm to 2 mm away from the membrane.

x Slowly approach the microcapillary with PMMA/MoS_2 patch from top of the water droplet so that it detaches from the microcapillary and unfolds on the drop (usually floating at the edge).

xi Slowly remove the microcapillary from below and re-align it on the top of the free-floating patch and press it gently on the PMMA/MoS_2 patch guiding it towards the membrane.

⚠ While maneuvering the PMMA/MoS_2 patch avoid direct contact of the microcapillary tip to the SiN_x membrane. This is to avoid the SiN_x membrane damage due to scratching by the microcapillary tip.

xii Carefully align the monolayer MoS_2 on top of the membrane and set the temperature of the sample holder to ca. 50 °C without releasing the microcapillary. Let the water evaporate from the area between the patch and the membrane, thereby rendering MoS_2 attached to the membrane. Release the microcapillary from the patch and keep the substrate with a freshly transferred MoS_2/PMMA patch on pre-heated hot-plate at 180 °C for 5 min.

⚠ It is important to check if the PMMA patch misaligns during the drying process.

⏸ The samples can be stored in a dust-free environment for up to 24 h until they are cleaned in xiii-xv. It is however advisable to clean the chips as soon as possible.

xiii Chip cleaning (xiii-xv): Place the chips in a Teflon chip's holder into closed beaker with acetone. Heat it to ≈ 60 °C on a heat plate and leave it for 60 min. Quickly transfer the chips into the next beaker with hot acetone (≈ 60 °C) leaving it on a heat plate for another 60 min. Transfer the chips into another beaker with hot acetone (≈ 60 °C), but then turn off the heating and leave the chips in acetone until it cools down to ambient temperature (≈ 25 °C). Continue the washing by transferring the chips into isopropyl alcohol (IPA) and Milli-Q water both at ambient temperature and for 30 min.

⚠ Since membranes are very fragile avoid any abrupt temperature changes which could eventually cause cracking. Also avoid complete drying of the chips while transferring them from one beaker to another. This will prevent drying of the impurities on the membrane.

xiv Carefully dry the chips with a very gentle nitrogen flow directed in parallel with the chip surface. While doing this hold the chip under 45° in respect to the ground so that the water droplet can easily flow away from the membrane toward the edges of the chip.

⏸ The samples can be stored in a dust-free environment for ca. 1 week until they are baked/annealed in xv. It is, however, advisable to anneal the chips as soon as possible to successfully remove polymer residues.

xv Place the substrates in an alumina boat with MoS_2 facing the top and anneal it in a furnace at 400 °C in Ar/H_2 flow (100 sccm / 10 sccm) for 8 h.

xvi Confirm successful transfer using an optical microscope with at least 50x magnification. See the micrograph in Figure 2.1 (page 37)b (bottom) for an example of a successfully transferred MoS_2 layer on a SiN_x membrane.

⏸ The samples can be stored in a dust and moisture-free environment for up to four weeks.

(B) Transfer of MoS_2 using PDMS. Timing: ≈ 10 min per device with ≈ 5 h to 6 h preparation

⚠ Step 37B(i-v) should be performed in a clean room facility ISO 14644-1 Class 6 or Class 7.

i Preparation of PDMS stamps (i-iv): Using a PDMS dispenser, add Sylgard 184 silicone base and Sylgard curing agent in a ratio of 10:1 (w/w). 20 g of base and 2 g of curing

agent is sufficient for making a thin layer of about 1 mm to 1.5 mm of PDMS on a clean silicon wafer.

ii Mix the contents in a mixer (THINKY) for about 1 min at 2000 rpm and defoam for 2 min for about 2200 rpm.

⚠ It is important to mix the base and the curing agent homogenously to avoid any sticky residues or uncured PDMS base.

iii Degas the contents using a desiccator for about 30min.

iv Place a clean silicon wafer in petri dishes and pour degassed PDMS over it very slowly. Keep the remaining PDMS for future use in Step 37B(vi) . One can degas again for 10 min to make sure it is free of entrapped air bubbles. Bake the PDMS at 80 °C for 4 h.

⏸ The baked PDMS can be kept at room temperature for a few weeks until used.

v Cut small pieces of PDMS stamps (1 mm to 2 mm) using clean razor blades.

⚠ Detach the PDMS stamps slowly to avoid PDMS breakage. Excessive force will introduce cracks on the PDMS.

vi On a clean glass slide, dispense a small drop of uncured PDMS from iv and place the flat PDMS stamp on it. Make sure that the side of the cured PDMS stamp that was facing the silicon wafer now is on the top-side. Bake the glass slide with PDMS at 80 °C for about 20 min.

⚠ Keep the PDMS stamps in a clean and dust-free environment.

⏸ The PDMS stamps can be kept for weeks before use. They can be kept in a moisture-free environment.

vii Transfer of MoS_2 using the PDMS stamp (vii-viii): First align the MoS_2 grown on a sapphire substrate (see section 2.4 (page 44)) under the optical microscope (facilitated with vacuum suction) and then align a PDMS stamp (attached to a glass slide) using a micromanipulator (XYZ) over the area of interest.

viii Using micromanipulator stage, slowly bring down the PDMS stamp until it interacts with the MoS_2/sapphire surface.

⚠ A slightly tilted glass-slide helps to interact with the MoS_2 surface. While using a micromanipulator, try to make the PDMS stamp completely interact with the MoS_2 surface with least compression on PDMS stamp. Typically, higher pressure leads to cracks in the MoS_2 and potentially introduces a larger number of PDMS residues on the MoS_2 surface after transfer.

ix Place a drop of Milli-Q water (c.a. 5 µl to 10 µl) around the edges of the PDMS stamp using a syringe needle or a small micropipette tip.

⚠ If the PDMS stamp is too thin (<1 mm), the area is inaccessible to a needle or micropipette tip thereby making it inaccessible to drop water around the PDMS/MoS_2 edge.

x Using the micromanipulator slowly lift-up the PDMS stamp which enables the intercalation of water between the sapphire substrate and the MoS_2, facilitating the transfer of MoS_2 directly onto the stamp.

⚠ If the water does not penetrate, use the micro-manipulator to lower the stamp again and gently poke the edge of the water/PDMS stamp interface so that the water penetrates from the edge.

xi After the lift-off, focus on the area under the PDMS stamp to look for the MoS_2 triangle that is to be transferred to the target substrate.

xii Align the target substrate having a SiN_x membrane to the MoS_2 triangle and slowly lower the stamps making sure that the triangle follows the vertical axis of the alignment with the membrane.

xiii After attachment of the MoS_2/PDMS stamp on the SiN_x membrane, slowly raise the stamp so that the desired MoS_2 gets printed on the membrane.

xiv Confirm successful transfer using an optical microscope with at least 50x magnification. See the micrograph in Figure 2.1 (page 37)b (bottom) for an example of a successfully transferred MoS_2 layer on a SiN_x membrane

A.2.4 Nanopore formation

Step 38 For creating nanopores using TEM imaging and drilling, follow Option A. For nanopore formation using ECR, follow Option B. (see section 2.6 (page 49)).

(A) TEM imaging and drilling. Timing: 30 min

⚠ This section can be skipped in case of pore generation through ECR.

i Set the microscope to TEM mode, lower the high tension to 80 kV.

⚠ Imaging should be performed at low acceleration voltage and high vacuum to avoid damage to the sample.

ii First go to the lowest magnification to find the membrane. Then zoom in to find the opening in SiN_x. If it is not visible, go out of focus to increase the contrast until you see it.

iii Set the beam spot size to 5 or 6 (first condenser lens or C1) and do the general alignment

iv Go to a higher magnification (SA mode, 630 k) always spreading the beam and keeping the electron current density below ≈0.05 pA nm^{-2}, i.e. at 630 k magnification the current should not exceed 300 pA.

v Do the alignment close to the SiN_x opening.

vi Go to the suspended MoS_2 region and check the live FFT signal to make sure there is a MoS_2 monolayer.

vii Correct objective astigmatism and put the sample into the focal plane.

viii Find the clean MoS_2 region where you want to drill a hole and put it into the center of the field of view.

ix Quickly contract the beam to the smallest spot. If the layer is very clean the damage will start immediately. Slightly spread the beam to observe the pore growth.

⚠ If the process of contracting the beam is too slow, the whole suspended area can get easily damaged.

x Once the pore has reached the desired size, blank the beam.

xi Spread the beam again to reduce the electron current density and unblank it.

xii Take a high-resolution image of the created pore.

(B) Nanopore formation using ECR drilling. Timing: 30 min

i Load a clean chip with MoS_2 transferred on the membrane into a sample holder or groove between two parts of the PMMA flow-cell (Figure 2.10 (page 56)a-b).

⚠ Before starting the following steps, please refer to subsection 2.7.4.

ii Place an O-ring in a groove dedicated to the flow-cell followed by carefully placing the chip on the O-ring. Now, place another O-ring on the chip followed by carefully aligning and gently screwing another part of the flow-cell.

iii Prepare a single Ag/AgCl electrode of ca. 10 cm with both ends chlorinated (as described in subsection 2.7.6 (page 56)) and insert each end of the electrode through the top electrode outlet in each of the flow-cell chambers (Figure 2.10 (page 56)b).

⚠ This step is vital to avoid any electrical discharge on the MoS_2 membrane.

iv Prepare a Milli-Q water/EtOH (0.02 µm filtered) mixture at a volumetric ratio of 1:1. Ultrasonicate the solution while degassing under vacuum for 40min.

v Inject a Milli-Q water/EtOH mixture (1:1, 0.02 µm filtered and degassed) from the liquid injection ports. Keep the flow-cell for wetting.

vi Continuously inject the Milli-Q water/EtOH mixture from the liquid injection port.

⚠ This step is essential to remove most of the air bubbles from the buffer solution.

vii Using a syringe needle, steadily suck out the wetting solution from either side of the flow-cell chambers via liquid injection port and inject degassed buffer.

viii Prepare a pair of Ag/AgCl electrodes (ca. 10 cm) and insert individual electrodes each from the top electrodes/outlet into each of the PMMA chambers. The MoS_2/SiN_x facing side is referred to as *cis side*, and the other side is referred to as *trans side*.

ix Before starting the following steps, please also refer to the precautions in subsection 2.7.4 (page 55) to avoid any discharge on the membrane.

x Connect the chlorinated Ag/AgCl electrodes on the cis-side to the ground electrode, the trans-side is connected to the active terminal to complete the circuit.

⚠ Connect the ground lead first, the active lead should be connected afterward.

xi The amplifier will short-circuit at this point due to the Ag/AgCl bridge still connecting the two chambers. Remove the bridge now without removing the active and ground electrodes.

xii Record the leakage current at a transmembrane voltage of 100 mV using a FEMTO DLPCA-200 amplifier for c.a. 2 min.

xiii Increase the transmembrane voltage step-wise (100 mV steps, 10) to 25) and notice the increase in the current.

xiv Increase the voltage until there is a sudden increase in the current (typically for voltages higher than 800 mV) which implies that one has reached a critical voltage (see subsection 2.10.2 (page 60)).

xv To check whether a nanopore has been formed apply a lower transmembrane potential of 100 mV and compare it with the previous leakage current recorded at Step 31.

xvi Record an I-V curve across a transmembrane potential of 0 mV to 800 mV at a step size of 50 mV with a dwell time of 10 s.

xvii Extract the conductance and linearity of the I-V (as shown in subsection 2.6.3 (page 50)), to calculate the pore diameter.

⚠ The acquisition software should be set-up to show the conductance rather than the current. In such a way the user can precalculate the target conductance for a given pore size and stop the process once the value is reached.

A.2.5 Precision painting. Timing: 10 min

Step 39 Dispense a small volume (50 µl to 100 µl) of elastomer mix from commercial KWIK-CAST (WPITM Silicone elastomer).

Step 40 Thoroughly mix both the elastomer contents for 30 s. The elastomer cures very quickly after mixing (c.a. 3 min). Hence it is advised to use the elastomer mix quickly before it cures.

Step 41 Take a minimal amount of the mix onto a bristle attached to a micromanipulator holder.

Step 42 Align the SiN_x membrane under the optical microscope and start applying the elastomer mix by *painting* it around the membrane area using the bristle.

⚠ While applying the elastomer mix, it is better to start far away from the SiN_x membrane so that the mixture does not flow over the membrane.

Step 43 Keep applying the elastomer mix quickly before it dries off (≈3 min). If the elastomer dries before completion, prepare another fresh mix and continue.

A.2.6 DNA translocations. Timing: 2 h to 3 h, depending on the experiment

⚠ Before starting the following steps, please refer to the precautions in subsection 2.7.4 (page 55) to avoid any discharge on the membrane.

Step 44 Prepare DNA/buffer mix by dissolving DNA stock (e.g., 2 kbp dsDNA, 0.5 $\mu g\,\mu l^{-1}$) in 1 M KCl - 10 mM Tris - 1 mM EDTA buffer (0.02 µm filtered and degassed, adjusted to pH 7.5) in a volumetric ratio of 1:50 in a polymerase chain reaction (PCR) tube to reach a final DNA concentration of about 10 $ng\,\mu l^{-1}$.

Step 45 Incubate the DNA/buffer mix at 40 °C for 10 min on a PCR machine or block heater.

Step 46 Use a micropipette to gently load the mix into the cis-chamber of the flow-cell.

Step 47 Set-up the flow-cell and apply a transmembrane voltage of 100 mV to 400 mV.

Step 48 Acquire the data using a custom-made LabView program (as mentioned in section 2.8 (page 57)) and an amplifier (e.g., Axopatch 200B).

A.3 FET Process Flow

We start with a 380 µm 4" Si-wafer (p-type, boron doped, 0.01 Ω cm to 0.02 Ω cm with 60 nm SiO_2 and 20 nm LPCVD low stress SiN_x on both sides (Active Business Company GmbH, Brunnthal, Germany). Standard photolithography processes are used to created 32 dices (each containing two devices). On the frontside, contact electrodes (10 nm Cr, 50 nm Pt) and alignment markers are prepatterned. On the backside, the silicon nitride is etched (RIE, C_2F_6, Alcatel 601, Alcatel Micro Machining Systems) to open 520 µm squares. Electron beam lithography (Vistec EBPG5000, Vistec Electron Beam GmbH, Jena, Germany) and RIE etching (RIE, C_2F_6, Alcatel 601, Alcatel Micro Machining Systems) is used to create 50 nm holes at the center position of the future membrane. The previously deposited alignment markers are used to generate a three-step alignment scheme increasing the alignment precision substantially (subsection 5.3.3 (page 118)). The wafer is then diced into 12 x 12 mm^2 chips. The dices are subsequently placed into hot KOH (25 %, 80 °C, 5 h) to open a freestanding 20 nm thick SiN_x membrane containing the previously created 50 nm hole. CVD (home-made furnace) grown MoS_2 is then transferred from a sapphire chip to the 50 nm hole using PMMA supported lift-off (subsection 2.4.1 (page 45)). Alignment of a single crystal triangle to the supporting hole is done in DI water under an optical microscope and a glass capillary on a micro-manipulator. Electrode contacts are subsequently patterned using e-beam lithography and Ti-Au-Pt (5 nm, 50 nm and 5 nm) was evaporated using a Lab 600H (Leybold Optics, Bühler AG, Alzenau Germany). Titanium was the most optimal material to decrease the contact resistance with MoS_2.[266] In order to restrain the electron flow to the region of the nanopore we used e-beam lithography and reactive ion etching with O_2 gas (Oxford Plasmalab System 80, Oxford-Instruments, Abingdon, UK) to create 500 nm wide ribbons. We made three ribbons on every device, but only one is placed above the supporting hole. In such a configuration we can use the additional ribbons for the non-supported experiments in case the supporting hole contains impurities. Nanopores are then drilled using a FEI Talos TEM (FEI, Hillsboro, Oregon, United States) in HR-TEM mode. The chip is then painted outside of the membrane with a silicone elastomer (Kwik-Cast, world precision instruments). The finished chips are then wire-bound to a custom-made PCB board, which allows easy plugging into a SD card reader. A custom-made flow cell is used to sandwich the PCB board and isolate the two reservoirs. A Faraday cage is used to isolate the measurements from stray electromagnetic fields. 80 nucleotides (nt) deoxyribonucleic acid (DNA) strands were purchased from Microsynth (Switzerland). 1 kbp DNA was purchased from (Thermo-Fisher). polyethylene glycol (PEG) was purchased from (Sigma). Polylysine was purchased from (Sigma). The potassium chloride (KCl) solutions contained 1 mM ethylenediaminetetraacetic acid (EDTA) and were buffered with 10 mM tris(hydroxymethyl)aminomethane (Tris) and adjusted to a pH of 7.4.

Table A1.1 – Complete process flow for the FET device

Step	Description	Cross-Section After Process
1	Substrate: Double Side polished, Boron-doped Si (100) wafers with resistivities of 10 mΩ cm to 20 mΩ cm, Thickness: SiO_2 60 nm, low stress LPCVD Si_3N_4: 20 nm	
2	Photolithography 1 PR: AZ1512HS on LOR, ACS200 Mask n. 1 on MA6Gen3	
3	Metal evaporation and lift-off Machine: LAB 600 Material: Cr 10 nm / Pt 50 nm E-beam markers and coordinate system	
4	Photolithography 2, Backside PR: AZ1512HS, ACS200 Mask n. 2 on MA6Gen3	
5	RIE of SiN_x and SiO_2, PR stripping Machine: Alcatel 601 Recipe: Therm. at 20 °C, 10 s C_2F_6 PR stripping: TEPLA GIGA-BATCH, 10 min	

6	E-beam litho and RIE Material: ZEP as photoresist Window size 50 nm to 100 nm Machine: Alcatel 601 Recipe: Therm. at 20 °C, 10 s C_2F_6 PR stripping: TEPLA GIGA-BATCH, 10 min	
7	Dicing Disco DAD	
8	KOH etching (done in LBEN) Recipe: 5 h in 25 % KOH (250 g of salt in 1 l of DI water) at 80 °C	
9	Monolayer MoS_2 fabrication, CVD grown	
10	MoS_2 Transfer, PMMA, Done in LBEN	
11	E-beam litho: Electrodes for connecting MoS_2 Material: PMMA as photoresist Electrodes connecting MoS_2 flake	
12	Metal evaporation and lift-off Machine: LAB 600 Material: Ti 5 nm / Au 50 nm, Lift-off in acetone	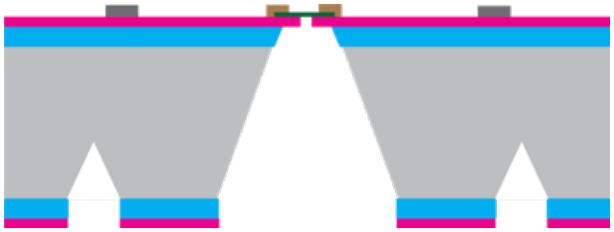

13	E-beam litho: Ribbons Material: PMMA as photoresist 1 µm x 500 nm wide ribbons of MoS_2	
14	MoS_2 Etching and resist stripping Machine: Plasmalab System 80, Material: 100 sscm O_2 10 s, Lift-off in acetone	
15	TEM drilling Pore FEI Talos	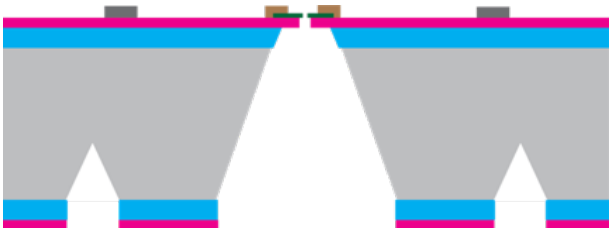

Bibliography

[1] W. Coulter. *Means for counting particles suspended in a fluid.* U.S. Patent 2,656,508. 1953. URL: www.google.com/patents/US2656508.

[2] M. Wanunu. "Nanopores: A journey towards DNA sequencing". In: *Physics of Life Reviews* 9.2 (2012), pp. 125–158. DOI: 10.1016/j.plrev.2012.05.010.

[3] M. D. Graham. "The Coulter Principle: Foundation of an industry". In: *JALA: Journal of the Association for Laboratory Automation* 8.6 (2003), pp. 72–81. DOI: 10.1016/S1535-5535(03)00023-6.

[4] R. W. DeBlois, C. P. Bean, and R. K. Wesley. "Electrokinetic measurements with submicron particles and pores by the resistive pulse technique". In: *Journal of Colloid And Interface Science* 61.2 (1977), pp. 323–335. DOI: 10.1016/0021-9797(77)90395-2.

[5] D. Deamer, M. Akeson, and D. Branton. "Three decades of nanopore sequencing". In: *Nature Biotechnology* 34.5 (2016), pp. 518–524. DOI: 10.1038/nbt.3423.

[6] J. J. Kasianowicz, E. Brandin, D. Branton, and D. W. Deamer. "Characterization of individual polynucleotide molecules using a membrane channel". In: *Proceedings of the National Academy of Sciences* 93.24 (1996), pp. 13770–13773. DOI: 10.1073/pnas.93.24.13770.

[7] E. A. Manrao et al. "Reading DNA at single-nucleotide resolution with a mutant MspA nanopore and phi29 DNA polymerase". In: *Nature Biotechnology* 30.4 (2012), pp. 349–353. DOI: 10.1038/nbt.2171.

[8] A. H. Laszlo et al. "Decoding long nanopore sequencing reads of natural DNA". In: *Nature Biotechnology* 32.8 (2014), pp. 829–833. DOI: 10.1038/nbt.2950.

[9] I. M. Derrington et al. "Subangstrom single-molecule measurements of motor proteins using a nanopore". In: *Nature Biotechnology* 33.10 (2015), pp. 1073–1075. DOI: 10.1038/nbt.3357.

[10] M. Jain et al. "Nanopore sequencing and assembly of a human genome with ultra-long reads". In: *Nature Biotechnology* 36.4 (2018), pp. 338–345. DOI: 10.1038/nbt.4060.

[11] N. J. Loman, J. Quick, and J. T. Simpson. "A complete bacterial genome assembled de novo using only nanopore sequencing data". In: *Nature Methods* 12.8 (2015), pp. 733–735. DOI: 10.1038/nmeth.3444.

[12] T. Hoenen et al. "Nanopore Sequencing as a Rapidly Deployable Ebola Outbreak Tool." In: *Emerging infectious diseases* 22.2 (2016), pp. 331–4. DOI: 10.3201/eid2202.151796.

[13] Nasa. *First DNA Sequencing in Space a Game Changer*. 2016. URL: https://www.nasa.gov/mission_pages/station/research/news/dna_sequencing (visited on 12/05/2018).

[14] J. Li et al. "Ion-beam sculpting at nanometre length scales". In: *Nature* 412.6843 (2001), pp. 166–169. DOI: 10.1038/35084037.

[15] J. Li, M. Gershow, D. Stein, E. Brandin, and J. A. Golovchenko. "DNA molecules and configurations in a solid-state nanopore microscope". In: *Nature Materials* 2.9 (2003), pp. 611–615. DOI: 10.1038/nmat965.

[16] A. J. Storm, J. H. Chen, H. W. Zandbergen, and C. Dekker. "Translocation of double-strand DNA through a silicon oxide nanopore". In: *Physical Review E - Statistical, Nonlinear, and Soft Matter Physics* 71.5 (2005), p. 51903. DOI: 10.1103/PhysRevE.71.051903.

[17] A. J. Storm, J. H. Chen, X. S. Ling, H. W. Zandbergen, and C. Dekker. "Fabrication of solid-state nanopores with single-nanometre precision". In: *Nature Materials* 2.8 (2003), pp. 537–540. DOI: 10.1038/nmat941.

[18] S. W. Kowalczyk, M. W. Tuijtel, S. P. Donkers, and C. Dekker. "Unraveling single-stranded DNA in a solid-state nanopore". In: *Nano Letters* 10.4 (2010), pp. 1414–1420. DOI: 10.1021/nl100271c.

[19] H. Kwok, K. Briggs, V. Tabard-Cossa, and V. Tabard Cossa. "Nanopore fabrication by controlled dielectric breakdown". In: *PLoS ONE* 9.3 (2014), e92880. DOI: 10.1371/journal.pone.0092880.

[20] T. Gilboa, A. Zrehen, A. Girsault, and A. Meller. "Optically-Monitored Nanopore Fabrication Using a Focused Laser Beam". In: *Scientific Reports* 8.1 (2018), p. 9765. DOI: 10.1038/s41598-018-28136-z.

[21] H. Yamazaki, R. Hu, Q. Zhao, and M. Wanunu. "Photothermally Assisted Thinning of Silicon Nitride Membranes for Ultrathin Asymmetric Nanopores". In: *ACS Nano* (2018), acsnano.8b06805. DOI: 10.1021/acsnano.8b06805.

[22] C. Ying et al. "Formation of Single Nanopores with Diameters of 20–50 nm in Silicon Nitride Membranes Using Laser-Assisted Controlled Breakdown". In: *ACS Nano* 12.11 (2018), pp. 11458–11470. DOI: 10.1021/acsnano.8b06489.

[23] G. F. Schneider et al. "DNA Translocation through Graphene Nanopores". In: *Nano Letters* 10.8 (2010), pp. 3163–3167. DOI: 10.1021/nl102069z.

[24] S. Garaj et al. "Graphene as a subnanometre trans-electrode membrane". In: *Nature* 467.7312 (2010), pp. 190–193. DOI: 10.1038/nature09379.

[25] C. A. Merchant et al. "DNA translocation through graphene nanopores". In: *Nano Letters* 10.8 (2010), pp. 2915–2921. DOI: 10.1021/nl101046t.

[26] C. J. Shearer, A. D. Slattery, A. J. Stapleton, J. G. Shapter, and C. T. Gibson. "Accurate thickness measurement of graphene". In: *Nanotechnology* 27.12 (2016), p. 125704. DOI: 10.1088/0957-4484/27/12/125704.

[27] G. F. Schneider et al. "Tailoring the hydrophobicity of graphene for its use as nanopores for DNA translocation". In: *Nature Communications* 4.1 (2013), p. 2619. DOI: 10.1038/ncomms3619.

[28] K. Liu, J. Feng, A. Kis, and A. Radenovic. "Atomically thin molybdenum disulfide nanopores with high sensitivity for dna translocation". In: *ACS Nano* 8.3 (2014), pp. 2504–2511. DOI: 10.1021/nn406102h.

[29] J. Feng et al. "Identification of single nucleotides in MoS_2 nanopores". In: *Nature Nanotechnology* 10.12 (2015), pp. 1070–1076. DOI: 10.1038/nnano.2015.219.

[30] J. Feng et al. "Electrochemical reaction in single layer MoS_2: Nanopores opened atom by atom". In: *Nano Letters* 15.5 (2015), pp. 3431–3438. DOI: 10.1021/acs.nanolett.5b00768.

[31] K. Liu et al. "Geometrical Effect in 2D Nanopores". In: *Nano Letters* 17.7 (2017), pp. 4223–4230. DOI: 10.1021/acs.nanolett.7b01091.

[32] G. Danda et al. "Monolayer WS_2 Nanopores for DNA Translocation with Light-Adjustable Sizes". In: *ACS Nano* 11.2 (2017), pp. 1937–1945. DOI: 10.1021/acsnano.6b08028.

[33] M. Mojtabavi, A. Vahid-Mohammadi, W. Liang, M. Beidaghi, and M. Wanunu. "Single-Molecule Sensing Using Nanopores in Two-Dimensional Transition Metal Carbide (MXene) Membranes". In: *ACS Nano* (2019), acsnano.8b08017. DOI: 10.1021/acsnano.8b08017.

[34] I. M. Derrington et al. "Nanopore DNA sequencing with MspA". In: *Proceedings of the National Academy of Sciences* 107.37 (2010), pp. 16060–16065. DOI: 10.1073/pnas.1001831107.

[35] C. G. Brown and J. Clarke. "Nanopore development at Oxford Nanopore". In: *Nature Biotechnology* 34.8 (2016), pp. 810–811. DOI: 10.1038/nbt.3622.

[36] C. Plesa et al. "Fast translocation of proteins through solid state nanopores". In: *Nano Letters* 13.2 (2013), pp. 658–663. DOI: 10.1021/nl3042678.

[37] J. Larkin, R. Y. Henley, M. Muthukumar, J. K. Rosenstein, and M. Wanunu. "High-bandwidth protein analysis using solid-state nanopores". In: *Biophysical Journal* 106.3 (2014), pp. 696–704. DOI: 10.1016/j.bpj.2013.12.025.

[38] L. J. Steinbock et al. "Probing the size of proteins with glass nanopores". In: *Nanoscale* 6.23 (2014), pp. 14380–14387. DOI: 10.1039/c4nr05001k.

[39] E. C. Yusko et al. "Real-time shape approximation and fingerprinting of single proteins using a nanopore". In: *Nature Nanotechnology* 12.4 (2017), pp. 360–367. DOI: 10.1038/nnano.2016.267.

[40] L. Restrepo-Pérez, C. Joo, and C. Dekker. "Paving the way to single-molecule protein sequencing". In: *Nature Nanotechnology* 13.9 (2018), pp. 786–796. DOI: 10.1038/s41565-018-0236-6.

[41] L. Restrepo-Pérez, S. John, A. Aksimentiev, C. Joo, and C. Dekker. "SDS-assisted protein transport through solid-state nanopores". In: *Nanoscale* 9.32 (2017), pp. 11685–11693. DOI: 10.1039/c7nr02450a.

[42] E. Kennedy, Z. Dong, C. Tennant, and G. Timp. "Reading the primary structure of a protein with 0.07 nm^3 resolution using a subnanometre-diameter pore". In: *Nature Nanotechnology* 11.11 (2016), pp. 968–976. DOI: 10.1038/nnano.2016.120.

[43] J. Bush et al. "The nanopore mass spectrometer". In: *Review of Scientific Instruments* 88.11 (2017), p. 113307. DOI: 10.1063/1.4986043.

[44] S. W. Kowalczyk et al. "Single-molecule transport across an individual biomimetic nuclear pore complex". In: *Nature Nanotechnology* 6.7 (2011), pp. 433–438. DOI: 10.1038/nnano.2011.88.

[45] M. Elimelech and W. A. Phillip. "The future of seawater desalination: Energy, technology, and the environment". In: *Science* 333.6043 (2011), pp. 712–717. DOI: 10.1126/science.1200488.

[46] K. Hata et al. "Water-assisted highly efficient synthesis of impurity-free single-walled carbon nanotubes." In: *Science (New York, N.Y.)* 306.5700 (2004), pp. 1362–4. DOI: 10.1126/science.1104962.

[47] S. P. Surwade et al. "Water desalination using nanoporous single-layer graphene". In: *Nature Nanotechnology* 10.5 (2015), pp. 459–464. DOI: 10.1038/nnano.2015.37.

[48] M. Heiranian, A. B. Farimani, and N. R. Aluru. "Water desalination with a single-layer MoS_2 nanopore". In: *Nature Communications* 6.1 (2015), p. 8616. DOI: 10.1038/ncomms9616.

[49] Z. Jia, B. Wang, S. Song, and Y. Fan. "Blue energy: Current technologies for sustainable power generation from water salinity gradient". In: *Renewable and Sustainable Energy Reviews* 31 (2014), pp. 91–100. DOI: 10.1016/j.rser.2013.11.049.

[50] M. Graf et al. "Fabrication and practical applications of molybdenum disulfide nanopores". In: *Nature Protocols* 14.4 (2019), pp. 1130–1168. DOI: 10.1038/s41596-019-0131-0.

[51] A. J. Storm et al. "Fast DNA translocation through a solid-state nanopore". In: *Nano Letters* 5.7 (2005), pp. 1193–1197. DOI: 10.1021/nl048030d.

[52] B. Lu, F. Albertorio, D. P. Hoogerheide, and J. A. Golovchenko. "Origins and consequences of velocity fluctuations during DNA passage through a nanopore". In: *Biophysical Journal* 101.1 (2011), pp. 70–79. DOI: 10.1016/j.bpj.2011.05.034.

[53] J. E. Hall. "Access resistance of a small circular pore". In: *The Journal of General Physiology* 66.4 (1975), pp. 531–532. DOI: 10.1085/jgp.66.4.531.

[54] S. W. Kowalczyk, A. Y. Grosberg, Y. Rabin, and C. Dekker. "Modeling the conductance and DNA blockade of solid-state nanopores". In: *Nanotechnology* 22.31 (2011), p. 315101. DOI: 10.1088/0957-4484/22/31/315101.

[55] C. Hyun, R. Rollings, and J. Li. "Probing access resistance of solid-state nanopores with a scanning-probe microscope tip". In: *Small* 8.3 (2012), pp. 385–392. DOI: 10.1002/smll.201101337.

[56] W. Si et al. "Investigation on the interaction length and access resistance of a nanopore with an atomic force microscopy". In: *Science China Technological Sciences* 60.4 (2017), pp. 552–560. DOI: 10.1007/s11431-016-0494-7.

[57] C. Lee et al. "Large apparent electric size of solid-state nanopores due to spatially extended surface conduction". In: *Nano Letters* 12.8 (2012), pp. 4037–4044. DOI: 10.1021/nl301412b.

[58] M. D. B. Pérez et al. "Improved model of ionic transport in 2-D MoS_2 membranes with sub-5 nm pores". In: *Applied Physics Letters* 114.2 (2019), p. 023107. DOI: 10.1063/1.5061825.

[59] R. Pethrick. "Polymer physics. Edited by Michael Rubinstein and Ralph H Colby Oxford University Press, Oxford, 2003. ISBN 019852059X. pp 440". In: *Polymer International* 53.9 (2004), pp. 1394–1395. DOI: 10.1002/pi.1472.

[60] J.-L Barrat and J.-F Joanny. "Persistence Length of Polyelectrolyte Chains". In: *Europhysics Letters (EPL)* 24.5 (1993), pp. 333–338. DOI: 10.1209/0295-5075/24/5/003.

[61] A. McMullen, H. W. De Haan, J. X. Tang, and D. Stein. "Stiff filamentous virus translocations through solid-state nanopores". In: *Nature Communications* 5 (2014). DOI: 10.1038/ncomms5171.

[62] H. Chen et al. "Ionic strength-dependent persistence lengths of single-stranded RNA and DNA". In: *Proceedings of the National Academy of Sciences* 109.3 (2012), pp. 799–804. DOI: 10.1073/PNAS.1119057109.

[63] J. Kang, J. Jung, and S. K. Kim. "Flexibility of single-stranded DNA measured by single-molecule FRET". In: *Biophysical Chemistry* 195 (2014), pp. 49–52. DOI: 10.1016/J.BPC.2014.08.004.

[64] E Haas, M Wilchek, E Katchalski-Katzir, and I. Z. Steinberg. "Distribution of end-to-end distances of oligopeptides in solution as estimated by energy transfer." In: *Proceedings of the National Academy of Sciences of the United States of America* 72.5 (1975), pp. 1807–11. DOI: 10.1073/pnas.72.5.1807.

[65] M. Murphy, I. Rasnik, W. Cheng, T. M. Lohman, and T. Ha. "Probing Single-Stranded DNA Conformational Flexibility Using Fluorescence Spectroscopy". In: *Biophysical Journal* 86.4 (2004), pp. 2530–2537. DOI: 10.1016/S0006-3495(04)74308-8.

[66] J. Abels, F. Moreno-Herrero, T. van der Heijden, C. Dekker, and N. Dekker. "Single-Molecule Measurements of the Persistence Length of Double-Stranded RNA". In: *Biophysical Journal* 88.4 (2005), pp. 2737–2744. DOI: 10.1529/BIOPHYSJ.104.052811.

[67] S. B. Smith, L Finzi, C Bustamante, and S Smith. "Direct mechanical measurements of the elasticity of single DNA molecules by using magnetic beads." In: *Science (New York, N.Y.)* 258.5085 (1992), pp. 1122–6. DOI: 10.1126/science.1439819.

[68] N. L. Goddard, G. Bonnet, O. Krichevsky, and A. Libchaber. "Sequence Dependent Rigidity of Single Stranded DNA". In: *Phys. Rev. Lett.* 85 (11 2000), pp. 2400–2403. DOI: 10.1103/PhysRevLett.85.2400.

[69] Bernard Tinland, Alain Pluen, Jean Sturm, and G. Weill. "Persistence Length of Single-Stranded DNA". In: 30.30 (1997), pp. 5763–5765. DOI: 10.1021/MA970381+.

[70] A. Y. L. Sim, J. Lipfert, D. Herschlag, and S. Doniach. "Salt dependence of the radius of gyration and flexibility of single-stranded DNA in solution probed by small-angle x-ray scattering". In: *PHYSICAL REVIEW E* 86 (2012), p. 21901. DOI: 10.1103/PhysRevE.86.021901.

[71] M. Wanunu, W. Morrison, Y. Rabin, A. Y. Grosberg, and A. Meller. "Electrostatic focusing of unlabelled DNA into nanoscale pores using a salt gradient". In: *Nature Nanotechnology* 5.2 (2010), pp. 160–165. DOI: 10.1038/nnano.2009.379.

[72] N. C. Stellwagen, C. Gelfi, and P. G. Righetti. "The free solution mobility of DNA". In: *Biopolymers* 42.6 (1997), pp. 687–703. DOI: 10.1002/(SICI)1097-0282(199711)42:6<687::AID-BIP7>3.0.CO;2-Q.

[73] A. E. Nkodo et al. "Diffusion coefficient of DNA molecules during free solution electrophoresis". In: *ELECTROPHORESIS* 22.12 (2001), pp. 2424–2432. DOI: 10.1002/1522-2683(200107)22:12<2424::AID-ELPS2424>3.0.CO;2-1.

[74] M. Von Smoluchowski. "Versuch einer mathematischen Theorie der Koagulationskinetik kolloider Lösungen". In: *Zeitschrift für physikalische Chemie* (1916).

[75] P. Chen et al. "Probing single DNA molecule transport using fabricated nanopores". In: *Nano Letters* 4.11 (2004), pp. 2293–2298. DOI: 10.1021/nl048654j.

[76] S. W. Kowalczyk and C. Dekker. "Salt and Voltage Dependence of the Conductance Blockade Induced By Translocation of DNA and RecA Filaments Through Solid-State Nanopores". In: *Nanopores for Bioanalytical Applications : Proceedings of the International Conference* (2012), pp. 24–31. DOI: 10.1039/9781849735278-00024.

[77] G. M. Skinner, M. van den Hout, O. Broekmans, C. Dekker, and N. H. Dekker. "Distinguishing Single- and Double-Stranded Nucleic Acid Molecules Using Solid-State Nanopores". In: *Nano Letters* 9.8 (2009), pp. 2953–2960. DOI: 10.1021/nl901370w.

[78] M. Wanunu, J. Sutin, B. McNally, A. Chow, and A. Meller. "DNA Translocation Governed by Interactions with Solid-State Nanopores". In: *Biophysical Journal* 95.10 (2008), pp. 4716–4725. DOI: 10.1529/BIOPHYSJ.108.140475.

[79] S. W. Kowalczyk and C. Dekker. "Measurement of the docking time of a DNA molecule onto a solid-state nanopore". In: *Nano Letters* 12.8 (2012), pp. 4159–4163. DOI: 10.1021/nl301719a.

[80] R. M. M. Smeets et al. "Salt dependence of ion transport and DMA translocation through solid-state nanopores". In: *Nano Letters* 6.1 (2006), pp. 89–95. DOI: 10.1021/nl052107w.

[81] D. M. Vlassarev and J. A. Golovchenko. "Trapping DNA near a solid-state nanopore". In: *Biophysical Journal* 103.2 (2012), pp. 352–356. DOI: 10.1016/j.bpj.2012.06.008.

[82] Y. Zhang et al. "Ionic current modulation from DNA translocation through nanopores under high ionic strength and concentration gradients". In: *Nanoscale* 9.2 (2017), pp. 930–939. DOI: 10.1039/c6nr08123a.

[83] S. W. Kowalczyk, D. B. Wells, A. Aksimentiev, and C. Dekker. "Slowing down DNA Translocation through a Nanopore in Lithium Chloride". In: *Nano Letters* 12.2 (2012), pp. 1038–1044. DOI: 10.1021/nl204273h.

[84] D. Fologea, J. Uplinger, B. Thomas, D. S. McNabb, and J. Li. "Slowing DNA translocation in a solid-state nanopore". In: *Nano Letters* 5.9 (2005), pp. 1734–1737. DOI: 10.1021/nl051063o.

[85] B. McNally et al. "Optical Recognition of Converted DNA Nucleotides for Single-Molecule DNA Sequencing Using Nanopore Arrays". In: *Nano Letters* 10.6 (2010), pp. 2237–2244. DOI: 10.1021/nl1012147.

[86] A. Demuro and I. Parker. "Optical patch-clamping". In: *The Journal of general physiology* 126.3 (2005), pp. 179–92. DOI: 10.1085/jgp.200509331.

[87] B. N. Anderson et al. "Probing solid-state nanopores with light for the detection of unlabeled analytes". In: *ACS Nano* 8.11 (2014), pp. 11836–11845. DOI: 10.1021/nn505545h.

[88] M. Zwolak, M. D. Ventra*, and M. Di Ventra. "Electronic signature of DNA nucleotides via transverse transport". In: *Nano Letters* 5.3 (2005), pp. 421–424. DOI: 10.1021/nl048289w.

[89] J. Lagerqvist, M. Zwolak, and M. Di Ventra. "Fast DNA sequencing via transverse electronic transport". In: *Nano Letters* 6.4 (2006), pp. 779–782. DOI: 10.1021/nl0601076.

[90] M. Tsutsui, M. Taniguchi, K. Yokota, and T. Kawai. "Identifying single nucleotides by tunnelling current". In: *Nature Nanotechnology* 5.4 (2010), pp. 286–290. DOI: 10.1038/nnano.2010.42.

[91] S. Chang et al. "Electronic signatures of all four DNA nucleosides in a tunneling gap". In: *Nano Letters* 10.3 (2010), pp. 1070–1075. DOI: 10.1021/nl1001185.

[92] A. P. Ivanov et al. "DNA tunneling detector embedded in a nanopore". In: *Nano Letters* 11.1 (2011), pp. 279–285. DOI: 10.1021/nl103873a.

[93] M. Carminati, G. Ferrari, A. P. Ivanov, T. Albrecht, and M. Sampietro. "Design and characterization of a current sensing platform for silicon-based nanopores with integrated tunneling nanoelectrodes". In: *Analog Integrated Circuits and Signal Processing* 77.3 (2013), pp. 333–343. DOI: 10.1007/s10470-013-0193-9.

[94] A. Fanget et al. "Nanopore integrated nanogaps for DNA detection". In: *Nano Letters* 14.1 (2014), pp. 244–249. DOI: 10.1021/nl403849g.

[95] S. Lindsay et al. "Recognition tunneling". In: *Nanotechnology* 21.26 (2010), p. 262001. DOI: 10.1088/0957-4484/21/26/262001.

[96] J. He, L. Lin, P. Zhang, and S. Lindsay. "Identification of DNA basepairing via tunnel-current decay". In: *Nano Letters* 7.12 (2007), pp. 3854–3858. DOI: 10.1021/nl0726205.

[97] S. Huang et al. "Identifying single bases in a DNA oligomer with electron tunnelling". In: *Nature Nanotechnology* 5.12 (2010), pp. 868–873. DOI: 10.1038/nnano.2010.213.

[98] T. Nelson, B. Zhang, and O. V. Prezhdo. "Detection of Nucleic Acids with Graphene Nanopores: Ab Initio Characterization of a Novel Sequencing Device". In: *Nano Letters* 10.9 (2010), pp. 3237–3242. DOI: 10.1021/nl9035934.

[99] K. K. Saha, M. Drndić, and B. K. Nikolić. "DNA Base-Specific Modulation of Microampere Transverse Edge Currents through a Metallic Graphene Nanoribbon with a Nanopore". In: *Nano Letters* 12.1 (2012), pp. 50–55. DOI: 10.1021/nl202870y.

[100] A. Girdhar, C. Sathe, K. Schulten, and J.-P. Leburton. "Graphene quantum point contact transistor for DNA sensing". In: *Proceedings of the National Academy of Sciences* 110.42 (2013), pp. 16748–16753. DOI: 10.1073/pnas.1308885110.

[101] F. Traversi et al. "Detecting the translocation of DNA through a nanopore using graphene nanoribbons". In: *Nature Nanotechnology* 8.12 (2013), pp. 939–945. DOI: 10.1038/nnano.2013.240.

[102] M. Puster et al. "Cross-Talk between Ionic and Nanoribbon Current Signals in Graphene Nanoribbon-Nanopore Sensors for Single-Molecule Detection". In: *Small* 11.47 (2015), pp. 6309–6316. DOI: 10.1002/smll.201502134.

[103] S. J. Heerema et al. "Probing DNA Translocations with Inplane Current Signals in a Graphene Nanoribbon with a Nanopore". In: *ACS Nano* 12.3 (2018), pp. 2623–2633. DOI: 10.1021/acsnano.7b08635.

[104] P. Xie, Q. Xiong, Y. Fang, Q. Qing, and C. M. Lieber. "Local electrical potential detection of DNA by nanowire-nanopore sensors". In: *Nature Nanotechnology* 7.2 (2012), pp. 119–125. DOI: 10.1038/nnano.2011.217.

[105] A. B. Farimani, K. Min, and N. R. Aluru. "DNA base detection using a single-layer MoS_2". In: *ACS Nano* 8.8 (2014), pp. 7914–7922. DOI: 10.1021/nn5029295.

[106] A. Sarathy and J. P. Leburton. "Electronic conductance model in constricted MoS_2 with nanopores". In: *Applied Physics Letters* 108.5 (2016), p. 53701. DOI: 10.1063/1.4941237.

[107] H. Qiu, A. Sarathy, K. Schulten, and J.-P. Leburton. "Detection and mapping of DNA methylation with 2D material nanopores". In: *npj 2D Materials and Applications* 1.1 (2017), p. 3. DOI: 10.1038/s41699-017-0005-7.

[108] K. S. Novoselov et al. "Two-dimensional atomic crystals". In: *Proceedings of the National Academy of Sciences* 102.30 (2005), pp. 10451–10453. DOI: 10.1073/pnas.0502848102.

[109] P. Blake et al. "Making graphene visible". In: *Applied Physics Letters* 91.6 (2007), p. 63124. DOI: 10.1063/1.2768624.

[110] M. M. Benameur et al. "Visibility of dichalcogenide nanolayers". In: *Nanotechnology* 22.12 (2011), p. 125706. DOI: 10.1088/0957-4484/22/12/125706.

[111] G. Rubio-Bollinger et al. "Enhanced Visibility of MoS_2, $MoSe_2$, WSe_2 and Black-Phosphorus: Making Optical Identification of 2D Semiconductors Easier". In: *Electronics* 4.4 (2015), pp. 847–856. DOI: 10.3390/electronics4040847.

[112] Nobel. *Nobel Media AB. Press release. Nobel Prize 2019.* URL: https://www.nobelprize.org/prizes/physics/2010/press-release/ (visited on 02/25/2019).

[113] B. Radisavljevic, A. Radenovic, J. Brivio, V. Giacometti, and A. Kis. "Single-layer MoS_2 transistors". In: *Nature nanotechnology* 6.3 (2011), pp. 147–150. DOI: 10.1038/nnano.2010.279.

[114] C. J. Shearer, A. D. Slattery, A. J. Stapleton, J. G. Shapter, and C. T. Gibson. "Accurate thickness measurement of graphene". In: *Nanotechnology* 27.12 (2016), p. 125704. DOI: 10.1088/0957-4484/27/12/125704.

[115] K. S. Novoselov et al. "Electric Field Effect in Atomically Thin Carbon Films". In: *Science* 306.5696 (2004), pp. 666–669. DOI: 10.1126/science.1102896.

[116] M. Li et al. "Experimental study and modeling of atomic-scale friction in zigzag and armchair lattice orientations of MoS_2". In: *Science and Technology of Advanced Materials* 17.2 (2016), pp. 189–199. DOI: 10.1080/14686996.2016.1165584.

[117] W. Choi et al. "Recent development of two-dimensional transition metal dichalcogenides and their applications". In: *Materials Today* 20.3 (2017), pp. 116–130. DOI: 10.1016/J.MATTOD.2016.10.002.

[118] H. F. Liu, S. L. Wong, and D. Z. Chi. "CVD Growth of MoS_2-based Two-dimensional Materials". In: *Chemical Vapor Deposition* 21.10-12 (2015), pp. 241–259. DOI: 10.1002/cvde.201500060.

[119] A. Splendiani et al. "Emerging photoluminescence in monolayer MoS_2". In: *Nano Letters* 10.4 (2010), pp. 1271–1275. DOI: 10.1021/nl903868w.

[120] H. Zhang et al. "Interference effect on optical signals of monolayer MoS_2". In: *Applied Physics Letters* 107.10 (2015), p. 101904. DOI: 10.1063/1.4930257.

[121] M. Buscema, G. A. Steele, H. S. J. van der Zant, and A. Castellanos-Gomez. "The effect of the substrate on the Raman and photoluminescence emission of single-layer MoS_2". In: *Nano Research* 7.4 (2014), pp. 1–11. DOI: 10.1007/s12274-014-0424-0.

[122] H. Nan et al. "Strong photoluminescence enhancement of MoS_2 through defect engineering and oxygen bonding". In: *ACS Nano* 8.6 (2014), pp. 5738–5745. DOI: 10.1021/nn500532f.

[123] P. Tonndorf et al. "Photoluminescence emission and Raman response of monolayer MoS_2, $MoSe_2$, and WSe_2". In: *Optics Express* 21.4 (2013), p. 4908. DOI: 10.1364/OE.21.004908.

[124] B. Miller, E. Parzinger, A. Vernickel, A. W. Holleitner, and U. Wurstbauer. "Photogating of mono- and few-layer MoS_2". In: *Applied Physics Letters* 106.12 (2015), p. 122103. DOI: 10.1063/1.4916517.

[125] S. Z. Butler et al. "Progress, challenges, and opportunities in two-dimensional materials beyond graphene". In: *ACS Nano* 7.4 (2013), pp. 2898–2926. DOI: 10.1021/nn400280c.

[126] Y.-C. Lin et al. "Wafer-scale MoS_2 thin layers prepared by MoO_3 sulfurization". In: *Nanoscale* 4.20 (2012), p. 6637. DOI: 10.1039/c2nr31833d.

[127] Y. H. Lee et al. "Synthesis and transfer of single-layer transition metal disulfides on diverse surfaces". In: *Nano Letters* 13.4 (2013), pp. 1852–1857. DOI: 10.1021/nl400687n.

[128] X. Wang, H. Feng, Y. Wu, and L. Jiao. "Controlled Synthesis of Highly Crystalline MoS_2 Flakes by Chemical Vapor Deposition". In: *Journal of the American Chemical Society* 135.14 (2013), pp. 5304–5307. DOI: 10.1021/ja4013485.

[129] A. Gurarslan et al. "Surface-energy-assisted perfect transfer of centimeter-scale monolayer and few-layer MoS_2 films onto arbitrary substrates". In: *ACS Nano* 8.11 (2014), pp. 11522–11528. DOI: 10.1021/nn5057673.

[130] H. Li et al. "A universal, rapid method for clean transfer of nanostructures onto various substrates". In: *ACS Nano* 8.7 (2014), pp. 6563–6570. DOI: 10.1021/nn501779y.

[131] H. Yu et al. "Wafer-Scale Growth and Transfer of Highly-Oriented Monolayer MoS_2 Continuous Films". In: *ACS Nano* 11.12 (2017), pp. 12001–12007. DOI: 10.1021/acsnano.7b03819.

[132] S. M. Shinde et al. "Surface-Functionalization-Mediated Direct Transfer of Molybdenum Disulfide for Large-Area Flexible Devices". In: *Advanced Functional Materials* 28.13 (2018), pp. 1–11. DOI: 10.1002/adfm.201706231.

[133] G. F. Schneider, V. E. Calado, H. Zandbergen, L. M. K. Vandersypen, and C. Dekker. "Wedging transfer of nanostructures". In: *Nano Letters* 10.5 (2010), pp. 1912–1916. DOI: 10.1021/nl1008037.

[134] M. Graf, K. Liu, A. Sarathy, J.-P. Leburton, and A. Radenovic. "Transverse Detection of DNA in a MoS_2 Nanopore". In: *Biophysical Journal* 114.3 (2018), 180a. DOI: 10.1016/j.bpj.2017.11.1005.

[135] A. Zrehen, T. Gilboa, and A. Meller. "Real-time visualization and sub-diffraction limit localization of nanometer-scale pore formation by dielectric breakdown". In: *Nanoscale* 9.42 (2017), pp. 16437–16445. DOI: 10.1039/c7nr02629c.

[136] M. Drndić. "Sequencing with graphene pores". In: *Nature Nanotechnology* 9.10 (2014), pp. 743–743. DOI: 10.1038/nnano.2014.232.

[137] S. Carson and M. Wanunu. "Challenges in DNA motion control and sequence readout using nanopore devices". In: *Nanotechnology* 26.7 (2015), p. 74004. DOI: 10.1088/0957-4484/26/7/074004.

[138] D. Branton et al. "The potential and challenges of nanopore sequencing". In: *Nature Biotechnology* 26.10 (2008), pp. 1146–1153. DOI: 10.1038/nbt.1495.

[139] J. K. Rosenstein, M. Wanunu, C. A. Merchant, M. Drndic, and K. L. Shepard. "Integrated nanopore sensing platform with sub-microsecond temporal resolution". In: *Nature Methods* 9.5 (2012), pp. 487–492. DOI: 10.1038/nmeth.1932.

[140] M. Wanunu et al. "Rapid electronic detection of probe-specific microRNAs using thin nanopore sensors". In: *Nature Nanotechnology* 5.11 (2010), pp. 807–814. DOI: 10.1038/nnano.2010.202.

[141] V. Tabard-Cossa, D. Trivedi, M. Wiggin, N. N. Jetha, and A. Marziali. "Noise analysis and reduction in solid-state nanopores". In: *Nanotechnology* 18.30 (2007), p. 305505. DOI: 10.1088/0957-4484/18/30/305505.

[142] C. Wen et al. "Generalized Noise Study of Solid-State Nanopores at Low Frequencies". In: *ACS Sensors* 2.2 (2017), pp. 300–307. DOI: 10.1021/acssensors.6b00826.

[143] R. M. M. Smeets, U. F. Keyser, N. H. Dekker, and C. Dekker. "Noise in solid-state nanopores". In: *Proceedings of the National Academy of Sciences* 105.2 (2008), pp. 417–421. DOI: 10.1073/pnas.0705349105.

[144] D. P. Hoogerheide, S. Garaj, and J. A. Golovchenko. "Probing surface charge fluctuations with solid-state nanopores". In: *Physical Review Letters* 102.25 (2009), p. 256804. DOI: 10.1103/PhysRevLett.102.256804.

[145] R. M. M. Smeets, U. F. Keyser, M. Y. Wu, N. H. Dekker, and C. Dekker. "Nanobubbles in solid-state nanopores". In: *Physical Review Letters* 97.8 (2006), p. 88101. DOI: 10.1103/PhysRevLett.97.088101.

[146] H. Arjmandi-Tash, L. A. Belyaeva, and G. F. Schneider. "Single molecule detection with graphene and other two-dimensional materials: Nanopores and beyond". In: *Chemical Society Reviews* 45.3 (2016), pp. 476–493. DOI: 10.1039/c5cs00512d.

[147] J. D. Uram, K. Ke, and M. L. Mayer. "Noise and bandwidth of current recordings from submicrometer pores and nanopores". In: *ACS Nano* 2.5 (2008), pp. 857–872. DOI: 10.1021/nn700322m.

[148] A. Balan et al. "Improving signal-to-noise performance for DNA translocation in solid-state nanopores at MHz bandwidths". In: *Nano Letters* 14.12 (2014), pp. 7215–7220. DOI: 10.1021/nl504345y.

[149] A. Balan, C. C. Chien, R. Engelke, and M. Drndic. "Suspended Solid-state Membranes on Glass Chips with Sub 1-pF Capacitance for Biomolecule Sensing Applications". In: *Scientific Reports* 5 (2015), p. 17775. DOI: 10.1038/srep17775.

[150] S. Garaj, S. Liu, J. A. Golovchenko, and D. Branton. "Molecule-hugging graphene nanopores". In: *Proceedings of the National Academy of Sciences* 110.30 (2013), pp. 12192–12196. DOI: 10.1073/pnas.1220012110.

[151] K. Matsui et al. "Static charge outside chamber induces dielectric breakdown of solid-state nanopore membranes". In: *Japanese Journal of Applied Physics* 57.4 (2018), p. 46702. DOI: 10.7567/JJAP.57.046702.

[152] A. Castellanos-Gomez et al. "Deterministic transfer of two-dimensional materials by all-dry viscoelastic stamping". In: *2D Materials* 1.1 (2014). DOI: 10.1088/2053-1583/1/1/011002.

[153] K. S. Novoselov et al. "Electric field in atomically thin carbon films". In: *Science* 306.5696 (2004), pp. 666–669. DOI: 10.1126/science.1102896.

[154] D. Dumcenco et al. "Large-Area Epitaxial Monolayer MoS_2". In: *ACS Nano* 9.4 (2015), pp. 4611–4620. DOI: 10.1021/acsnano.5b01281.

[155] J. Li and M. Östling. "Scalable Fabrication of 2D Semiconducting Crystals for Future Electronics". In: *Electronics* 4.4 (2015), pp. 1033–1061. DOI: 10.3390/electronics4041033.

[156] P. Waduge et al. "Direct and Scalable Deposition of Atomically Thin Low-Noise MoS_2 Membranes on Apertures". In: *ACS Nano* 9.7 (2015), pp. 7352–7359. DOI: 10.1021/acsnano.5b02369.

[157] X. Ma et al. "Capillary-Force-Assisted Clean-Stamp Transfer of Two-Dimensional Materials". In: *Nano Letters* 17.11 (2017), pp. 6961–6967. DOI: 10.1021/acs.nanolett.7b03449.

[158] A. Garcia et al. "Analysis of electron beam damage of exfoliated MoS_2 sheets and quantitative HAADF-STEM imaging". In: *Ultramicroscopy* 146 (2014), pp. 33–38. DOI: 10.1016/J.ULTRAMIC.2014.05.004.

[159] H. J. Park, G. H. Ryu, and Z. Lee. "Hole Defects on Two-Dimensional Materials Formed by Electron Beam Irradiation: Toward Nanopore Devices". In: *Applied Microscopy* 45.3 (2015), pp. 107–114. DOI: 10.9729/AM.2015.45.3.107.

[160] J. Hong et al. "Exploring atomic defects in molybdenum disulphide monolayers". In: *Nature Communications* 6 (2015), pp. 1–8. DOI: 10.1038/ncomms7293.

[161] A. T. Kuan, B. Lu, P. Xie, T. Szalay, and J. A. Golovchenko. "Electrical pulse fabrication of graphene nanopores in electrolyte solution". In: *Applied Physics Letters* 106.20 (2015), p. 203109. DOI: 10.1063/1.4921620.

[162] M. van den Hout et al. "Controlling nanopore size, shape and stability". In: *Nanotechnology* 21.11 (2010), p. 115304. DOI: 10.1088/0957-4484/21/11/115304.

[163] A. T. Carlsen, O. K. Zahid, J. Ruzicka, E. W. Taylor, and A. R. Hall. "Interpreting the conductance blockades of DNA translocations through solid-state nanopores". In: *ACS Nano* 8.5 (2014), pp. 4754–4760. DOI: 10.1021/nn501694n.

[164] A. Gadaleta et al. "Sub-additive ionic transport across arrays of solid-state nanopores". In: *Physics of Fluids* 26.1 (2014), p. 12005. DOI: 10.1063/1.4863206.

[165] G. J. Moody, R. B. Oke, and J. D. R. Thomas. "The influence of light on silver-silver chloride electrodes". In: *Analyst* 94 (1122 1969), pp. 803–804. DOI: 10.1039/AN9699400803.

[166] C. Raillon, P. Granjon, M. Graf, L. J. Steinbock, and A. Radenovic. "Fast and automatic processing of multi-level events in nanopore translocation experiments". In: *Nanoscale* 4.16 (2012), p. 4916. DOI: 10.1039/c2nr30951c.

[167] J. H. Forstater et al. "MOSAIC: A modular single-molecule analysis interface for decoding multistate nanopore data". In: *Analytical Chemistry* 88.23 (2016), pp. 11900–11907. DOI: 10.1021/acs.analchem.6b03725.

[168] C. Plesa and C. Dekker. "Data analysis methods for solid-state nanopores". In: *Nanotechnology* 26.8 (2015), p. 84003. DOI: 10.1088/0957-4484/26/8/084003.

[169] Z. Gu, Y.-L. L. Ying, C. Cao, P. He, and Y.-T. T. Long. "Accurate data process for nanopore analysis". In: *Analytical Chemistry* 87.2 (2015), pp. 907–913. DOI: 10.1021/ac5028758.

[170] D. York, N. M. Evensen, M. L. Martinez, and J. De Basabe Delgado. "Unified equations for the slope, intercept, and standard errors of the best straight line". In: *American Journal of Physics* 72.3 (2004), pp. 367–375. DOI: 10.1119/1.1632486.

[171] J. Feng et al. "Single-layer MoS_2 nanopores as nanopower generators". In: *Nature* 536.7615 (2016), pp. 197–200. DOI: 10.1038/nature18593.

[172] B. E. Logan and M. Elimelech. "Membrane-based processes for sustainable power generation using water". In: *Nature* 488.7411 (2012), pp. 313–319. DOI: 10.1038/nature11477.

[173] R. E. Pattle. "Production of Electric Power by mixing Fresh and Salt Water in the Hydroelectric Pile". In: *Nature* 174.4431 (1954), pp. 660–660. DOI: 10.1038/174660a0.

[174] S. Loeb and R. S. Norman. "Osmotic Power Plants". In: *Science* 189.4203 (1975), pp. 654–655. DOI: 10.1126/science.189.4203.654.

[175] F. H. J. Van Der Heyden, D. Stein, and C. Dekker. "Streaming currents in a single nanofluidic channel". In: *Physical Review Letters* 95.11 (2005), p. 116104. DOI: 10.1103/PhysRevLett.95.116104.

[176] A. Siria et al. "Giant osmotic energy conversion measured in a single transmembrane boron nitride nanotube". In: *Nature* 494.7438 (2013), pp. 455–458. DOI: 10.1038/nature11876.

[177] M. E. Suk and N. R. Aluru. "Water transport through ultrathin graphene". In: *Journal of Physical Chemistry Letters* 1.10 (2010), pp. 1590–1594. DOI: 10.1021/jz100240r.

[178] M. Heiranian, A. B. Farimani, and N. R. Aluru. "Water desalination with a single-layer MoS_2 nanopore". In: *Nature Communications* 6 (2015). DOI: 10.1038/ncomms9616.

[179] Z. L. Wang and J. Song. "Piezoelectric nanogenerators based on zinc oxide nanowire arrays". In: *Science* (2006). DOI: 10.1126/science.1124005.

[180] Z. L. Wang. "Self-powered nanosensors and nanosystems". In: *Advanced Materials* 24.2 (2012), pp. 280–285. DOI: 10.1002/adma.201102958.

[181] B. Tian et al. "Coaxial silicon nanowires as solar cells and nanoelectronic power sources". In: *Nature* 449.7164 (2007), pp. 885–889. DOI: 10.1038/nature06181.

[182] S. Xu et al. "Self-powered nanowire devices". In: *Nature Nanotechnology* 5.5 (2010), pp. 366–373. DOI: 10.1038/nnano.2010.46.

[183] W. Wu et al. "Piezoelectricity of single-atomic-layer MoS_2 for energy conversion and piezotronics". In: *Nature* 514.7253 (2014), pp. 470–474. DOI: 10.1038/nature13792.

[184] X. Liu et al. "Top-down fabrication of sub-nanometre semiconducting nanoribbons derived from molybdenum disulfide sheets". In: *Nature Communications* 4 (2013). DOI: 10.1038/ncomms2803.

[185] D. Stein, M. Kruithof, and C. Dekker. "Surface-Charge-Governed Ion Transport in Nanofluidic Channels". In: *Physical Review Letters* 93.3 (2004), p. 035901. DOI: 10.1103/PhysRevLett.93.035901.

[186] L. Bocquet and E. Charlaix. "Nanofluidics, from bulk to interfaces". In: *Chem. Soc. Rev.* 39.3 (2010), pp. 1073–1095. DOI: 10.1039/B909366B.

[187] Y. P. Shan et al. "Surface modification of graphene nanopores for protein translocation". In: *Nanotechnology* 24.49 (2013). DOI: 10.1088/0957-4484/24/49/495102.

[188] P. Ge et al. "Hydrogen evolution across nano-Schottky junctions at carbon supported MoS_2 catalysts in biphasic liquid systems". In: *Chemical Communications* 48.52 (2012), p. 6484. DOI: 10.1039/c2cc31398g.

[189] D.-K. K. Kim, C. Duan, Y.-F. F. Chen, and A. Majumdar. "Power generation from concentration gradient by reverse electrodialysis in ion-selective nanochannels". In: *Microfluidics and Nanofluidics* 9.6 (2010), pp. 1215–1224. DOI: 10.1007/s10404-010-0641-0.

[190] I. Vlassiouk, S. Smirnov, and Z. Siwy. "Ionic selectivity of single nanochannels". In: *Nano Letters* 8.7 (2008), pp. 1978–1985. DOI: 10.1021/nl800949k.

[191] L. Cao et al. "Towards understanding the nanofluidic reverse electrodialysis system: Well matched charge selectivity and ionic composition". In: *Energy and Environmental Science* 4.6 (2011), pp. 2259–2266. DOI: 10.1039/c1ee01088c.

[192] J. Wu, K. Gerstandt, H. Zhang, J. Liu, and B. J. Hinds. "Electrophoretically induced aqueous flow through single-walled carbon nanotube membranes". In: *Nature Nanotechnology* 7.2 (2012), pp. 133–139. DOI: 10.1038/nnano.2011.240.

[193] M. I. Walker, P. Braeuninger-Weimer, R. S. Weatherup, S. Hofmann, and U. F. Keyser. "Measuring the proton selectivity of graphene membranes". In: *Applied Physics Letters* 107.21 (2015). DOI: 10.1063/1.4936335.

[194] H. Ku. "Notes on the use of propagation of error formulas". In: *Journal of Research of the National Bureau of Standards, Section C: Engineering and Instrumentation* 70C.4 (1966), p. 263. DOI: 10.6028/jres.070C.025.

[195] S. Plimpton. "Fast parallel algorithms for short-range molecular dynamics". In: *Journal of Computational Physics* 117.1 (1995), pp. 1–19. DOI: 10.1006/jcph.1995.1039.

[196] R. W. Hockney and J. W. Eastwood. *Computer Simulation Using Particles.* 1983. DOI: 10.1137/1025102.

[197] S. Nosé. "A unified formulation of the constant temperature molecular dynamics methods". In: *The Journal of Chemical Physics* 81.1 (1984), pp. 511–519. DOI: 10.1063/1.447334.

[198] W. G. Hoover. "Canonical dynamics: Equilibrium phase-space distributions". In: *Physical Review A* 31.3 (1985), pp. 1695–1697. DOI: 10.1103/PhysRevA.31.1695.

[199] V. V. Nandigana and N. R. Aluru. "Understanding anomalous current-voltage characteristics in microchannel-nanochannel interconnect devices". In: *Journal of Colloid and Interface Science* 384.1 (2012), pp. 162–171. DOI: 10.1016/j.jcis.2012.06.004.

[200] V. V. R. Nandigana and N. R. Aluru. "Nonlinear Electrokinetic Transport Under Combined ac and dc Fields in Micro/Nanofluidic Interface Devices". In: *Journal of Fluids Engineering* 135.2 (2013), p. 021201. DOI: 10.1115/1.4023442.

[201] V. V. Nandigana and N. R. Aluru. "Characterization of electrochemical properties of a micro-nanochannel integrated system using computational impedance spectroscopy (CIS)". In: *Electrochimica Acta* 105 (2013), pp. 514–523. DOI: 10.1016/j.electacta.2013.05.011.

[202] R. S. Norman and F. B. Leitz. "Water Salination: A Source of Energy". In: *Science* 186.4161 (1974), pp. 350–352. DOI: 10.1126/science.186.4161.350.

[203] N. Y. Yip and M. Elimelech. "Comparison of Energy Efficiency and Power Density in Pressure Retarded Osmosis and Reverse Electrodialysis". In: *Environmental Science & Technology* 48.18 (2014), pp. 11002–11012. DOI: 10.1021/es5029316.

[204] J. W. Post, H. V. M. Hamelers, and C. J. N. Buisman. "Energy recovery from controlled mixing salt and fresh water with a reverse electrodialysis system". In: *Environmental Science and Technology* 42.15 (2008), pp. 5785–5790. DOI: 10.1021/es8004317.

[205] W. Kim and S. Nair. "Membranes from nanoporous 1D and 2D materials: A review of opportunities, developments, and challenges". In: *Chemical Engineering Science* 104 (2013), pp. 908–924. DOI: 10.1016/j.ces.2013.09.047.

[206] R. C. Rollings, A. T. Kuan, and J. A. Golovchenko. "Ion selectivity of graphene nanopores". In: *Nature Communications* 7 (2016), p. 11408. DOI: 10.1038/ncomms11408.

[207] K. F. Mak and J. Shan. "Photonics and optoelectronics of 2D semiconductor transition metal dichalcogenides". In: *Nature Photonics* 10.4 (2016), pp. 216–226. DOI: 10.1038/nphoton.2015.282.

[208] M. M. Furchi, D. K. Polyushkin, A. Pospischil, and T. Mueller. "Mechanisms of photoconductivity in atomically thin MoS_2". In: *Nano Letters* 14.11 (2014), pp. 6165–6170. DOI: 10.1021/nl502339q.

[209] O. Lopez-Sanchez, D. Lembke, M. Kayci, A. Radenovic, and A. Kis. "Ultrasensitive photodetectors based on monolayer MoS_2". In: *Nature Nanotechnology* 8.7 (2013), pp. 497–501. DOI: 10.1038/nnano.2013.100.

[210] G. Danda, P. Masih Das, and M. Drndić. "Laser-induced fabrication of nanoporous monolayer WS_2 membranes". In: *2D Materials* 5.3 (2018), p. 35011. DOI: 10.1088/2053-1583/aabb73.

[211] F. Helfer, C. Lemckert, and Y. G. Anissimov. "Osmotic power with Pressure Retarded Osmosis: Theory, performance and trends - A review". In: *Journal of Membrane Science* 453 (2014), pp. 337–358. DOI: 10.1016/j.memsci.2013.10.053.

[212] M. Graf et al. "Light Enhanced Blue Energy Generation using MoS_2 Nanopores". In: *Joule* 3 (2019). DOI: 10.1016/j.joule.2019.04.011.

[213] W. H. Pitchford et al. "Synchronized optical and electronic detection of biomolecules using a low noise nanopore platform". In: *ACS Nano* 9.2 (2015), pp. 1740–1748. DOI: 10.1021/nn506572r.

[214] Z. Roelen, J. A. Bustamante, A. Carlsen, A. Baker-Murray, and V. Tabard-Cossa. "Instrumentation for low noise nanopore-based ionic current recording under laser illumination". In: *Review of Scientific Instruments* 89.1 (2018), p. 15007. DOI: 10.1063/1.5006262.

[215] J. Feng et al. "Observation of ionic Coulomb blockade in nanopores". In: *Nature Materials* 15.8 (2016), pp. 850–855. DOI: 10.1038/nmat4607.

[216] S. Sahu, M. Di Ventra, and M. Zwolak. "Dehydration as a Universal Mechanism for Ion Selectivity in Graphene and Other Atomically Thin Pores". In: *Nano Letters* 17.8 (2017), pp. 4719–4724. DOI: 10.1021/acs.nanolett.7b01399.

[217] A. V. Kolobov and J. Tominaga. *Two-Dimensional Transition-Metal Dichalcogenides*. Vol. 239. Springer Series in Materials Science. Cham: Springer International Publishing, 2016, p. 538. DOI: 10.1007/978-3-319-31450-1.

[218] J. Hwang et al. "Thermal dependence of nanofluidic energy conversion by reverse electrodialysis". In: *Nanoscale* 9.33 (2017), pp. 12068–12076. DOI: 10.1039/c7nr04387b.

[219] N. Di Fiori et al. "Optoelectronic control of surface charge and translocation dynamics in solid-state nanopores". In: *Nature Nanotechnology* 8.12 (2013), pp. 946–951. DOI: 10.1038/nnano.2013.221.

[220] H. Miedema. "Surface potentials and the calculated selectivity of ion channels". In: *Biophysical Journal* 82.1 (2002), pp. 156–159. DOI: 10.1016/S0006-3495(02)75382-4.

[221] A. R. Poggioli, A. Siria, and L. Bocquet. "Beyond the Tradeoff: Dynamic Selectivity in Ionic Transport and Current Rectification". In: *The Journal of Physical Chemistry B* (2019), acs.jpcb.8b11202. DOI: 10.1021/acs.jpcb.8b11202.

[222] S. C. O'Hern et al. "Selective ionic transport through tunable subnanometer pores in single-layer graphene membranes". In: *Nano Letters* 14.3 (2014), pp. 1234–1241. DOI: 10.1021/nl404118f.

[223] P. Masih Das, J. P. Thiruraman, Y.-C. Chou, G. Danda, and M. Drndic. "Centimeter-Scale Nanoporous 2D Membranes and Ion Transport: Porous MoS_2 Monolayers in a Few-Layer Matrix". In: *Nano Letters* (2018), acs.nanolett.8b04155. DOI: 10.1021/acs.nanolett.8b04155.

[224] L. Cao et al. "On the Origin of Ion Selectivity in Ultrathin Nanopores: Insights for Membrane-Scale Osmotic Energy Conversion". In: *Advanced Functional Materials* 28.39 (2018), p. 1804189. DOI: 10.1002/adfm.201804189.

[225] A. Sobhani et al. "Enhancing the photocurrent and photoluminescence of single crystal monolayer MoS_2 with resonant plasmonic nanoshells". In: *Applied Physics Letters* 104.3 (2014), p. 31112. DOI: 10.1063/1.4862745.

[226] Y. Zeng et al. "Highly Enhanced Photoluminescence of Monolayer MoS ₂ with Self-Assembled Au Nanoparticle Arrays". In: *Advanced Materials Interfaces* 4.21 (2017), p. 1700739. DOI: 10.1002/admi.201700739.

[227] C. Janisch et al. "MoS_2 monolayers on nanocavities: enhancement in light–matter interaction". In: *2D Materials* 3.2 (2016), p. 025017. DOI: 10.1088/2053-1583/3/2/025017.

[228] M. K. Man et al. "Protecting the properties of monolayer MoS_2 on silicon based substrates with an atomically thin buffer". In: *Scientific Reports* 6.1 (2016), p. 1385. DOI: 10.1038/srep20890.

[229] B. Parida, S. Iniyan, and R. Goic. "A review of solar photovoltaic technologies". In: *Renewable and Sustainable Energy Reviews* 15.3 (2011), pp. 1625–1636. DOI: 10.1016/j.rser.2010.11.032.

[230] R. Rollings et al. "The effects of geometry and stability of solid-state nanopores on detecting single DNA molecules". In: *Nanotechnology* 26.4 (2015), p. 44001. DOI: 10.1088/0957-4484/26/4/044001.

[231] E. J. Peterman, F. Gittes, and C. F. Schmidt. "Laser-induced heating in optical traps". In: *Biophysical Journal* 84.2 I (2003), pp. 1308–1316. DOI: 10.1016/S0006-3495(03)74946-7.

[232] R. M. Pope and E. S. Fry. "Absorption spectrum (380–700 nm) of pure water II Integrating cavity measurements". In: *Applied Optics* 36.33 (1997), p. 8710. DOI: 10.1364/AO.36.008710.

[233] H. Yamazaki et al. "Label-Free Single-Molecule Thermoscopy Using a Laser-Heated Nanopore". In: *Nano Letters* 17.11 (2017), pp. 7067–7074. DOI: 10.1021/acs.nanolett.7b03752.

[234] M. A. Green. "Self-consistent optical parameters of intrinsic silicon at 300 K including temperature coefficients". In: *Solar Energy Materials and Solar Cells* 92.11 (2008), pp. 1305–1310. DOI: 10.1016/j.solmat.2008.06.009.

[235] J. P. Cline. "Accuracy in powder diffraction III - Part 1 - Preface". In: *Journal of Research of the National Institute of Standards and Technology* 109.1 (2004), p. iii. DOI: 10.6028/jres.109.001.

[236] R. B. Schoch, J. Han, and P. Renaud. "Transport phenomena in nanofluidics". In: *Reviews of Modern Physics* 80.3 (2008), pp. 839–883. DOI: 10.1103/RevModPhys.80.839.

[237] C. Malmberg and A. Maryott. "Dielectric constant of water from 0 to 100 C". In: *Journal of Research of the National Bureau of Standards* 56.1 (1956), p. 1. DOI: 10.6028/jres.056.001.

[238] Z. Huang et al. "The impact of membrane surface charges on the ion transport in MoS_2 nanopore power generators". In: *Applied Physics Letters* 111.26 (2017), p. 263104. DOI: 10.1063/1.5003695.

[239] P. V. Vanysek. *Equivalent Conductivity of Electrolytes In Aqueous Solution.* URL: https://sites.chem.colostate.edu/diverdi/all_courses/CRCreferencedata/equivalentconductivityofelectrolytes.pdf (visited on 02/05/2019).

[240] G. V. Soni et al. "Synchronous optical and electrical detection of biomolecules traversing through solid-state nanopores". In: *Review of Scientific Instruments* 81.1 (2010), p. 014301. DOI: 10.1063/1.3277116.

[241] H. Yamazaki, S. Kimura, M. Tsukahara, K. Esashika, and T. Saiki. "Optical detection of DNA translocation through silicon nanopore by ultraviolet light". In: *Applied Physics A* 115.1 (2014), pp. 53–56. DOI: 10.1007/s00339-013-7956-0.

[242] O. N. Assad, N. Di Fiori, A. H. Squires, and A. Meller. "Two color DNA barcode detection in photoluminescence suppressed silicon nitride nanopores". In: *Nano Letters* 15.1 (2015), pp. 745–752. DOI: 10.1021/nl504459c.

[243] T. Gilboa et al. "Single-Molecule DNA Methylation Quantification Using Electro-optical Sensing in Solid-State Nanopores". In: *ACS Nano* 10.9 (2016), pp. 8861–8870. DOI: 10.1021/acsnano.6b04748.

[244] J. Larkin, R. Y. Henley, V. Jadhav, J. Korlach, and M. Wanunu. "Length-independent DNA packing into nanopore zero-mode waveguides for low-input DNA sequencing". In: *Nature Nanotechnology* 12 (Sept. 2017), 1169 EP –.

[245] C. E. D. Chidsey and N. J. Tao. "Free Energy and Temperature Dependence of Electron Transfer at the Metal-Electrolyte Interface". In: *Science* 251.4996 (1991), pp. 919–922. DOI: 10.1126/science.251.4996.919.

[246] J. He et al. "Measuring single molecule conductance with break junctions". In: *Faraday Discuss.* 131.0 (2006), pp. 145–154. DOI: 10.1039/B508434M.

[247] M. Tsutsui, K. Shoji, M. Taniguchi, and T. Kawai. "Formation and self-breaking mechanism of stable atom-sized junctions". In: *Nano Letters* 8.1 (2008), pp. 345–349. DOI: 10.1021/nl073003j.

[248] M. Tsutsui, M. Taniguchi, and T. Kawai. "Fabrication of 0.5 nm electrode gaps using self-breaking technique". In: *Applied Physics Letters* 93.16 (2008), p. 163115. DOI: 10.1063/1.3006063.

[249] S. Caneva et al. "Mechanically controlled quantum interference in graphene break junctions". In: *Nature Nanotechnology* 13.12 (2018), pp. 1126–1131. DOI: 10.1038/s41565-018-0258-0.

[250] M. Y. Han, B. Özyilmaz, Y. Zhang, and P. Kim. "Energy Band-Gap Engineering of Graphene Nanoribbons". In: *Physical Review Letters* 98.20 (2007), p. 206805. DOI: 10.1103/PhysRevLett.98.206805.

[251] D. Sarkar et al. "MoS_2 field-effect transistor for next-generation label-free biosensors". In: *ACS Nano* 8.4 (2014), pp. 3992–4003. DOI: 10.1021/nn5009148.

[252] Y. Li et al. "Large-Scale Fabrication of MoS_2 Ribbons and Their Light-Induced Electronic/Thermal Properties: Dichotomies in the Structural and Defect Engineering". In: *Advanced Functional Materials* 28.13 (2018), p. 1704863. DOI: 10.1002/adfm.201704863.

[253] W. M. Parkin and M. Drndić. "Signal and Noise in FET-Nanopore Devices". In: *ACS Sensors* 3.2 (2018), pp. 313–319. DOI: 10.1021/acssensors.7b00708.

[254] T. Liu et al. "Crested two-dimensional transistors". In: *Nature Nanotechnology* 14.3 (2019), pp. 223–226. DOI: 10.1038/s41565-019-0361-x.

[255] M. Chen, S. Wi, H. Nam, G. Priessnitz, and X. Liang. "Effects of MoS_2 thickness and air humidity on transport characteristics of plasma-doped MoS_2 field-effect transistors". In: *Journal of Vacuum Science & Technology B, Nanotechnology and Microelectronics: Materials, Processing, Measurement, and Phenomena* 32.6 (2014), 06FF02. DOI: 10.1116/1.4897133.

[256] M. M. Perera et al. "Improved Carrier Mobility in Few-Layer MoS_2 Field-Effect Transistors with Ionic-Liquid Gating". In: *ACS Nano* 7.5 (2013), pp. 4449–4458. DOI: 10.1021/nn401053g.

[257] F. Wang et al. "Ionic Liquid Gating of Suspended MoS_2 Field Effect Transistor Devices". In: *Nano Letters* 15.8 (2015), pp. 5284–5288. DOI: 10.1021/acs.nanolett.5b01610.

[258] H. Kwok, M. Waugh, J. Bustamante, K. Briggs, and V. Tabard-Cossa. "Long Passage Times of Short ssDNA Molecules through Metallized Nanopores Fabricated by Controlled Breakdown". In: *Advanced Functional Materials* 24.48 (2014), pp. 7745–7753. DOI: 10.1002/adfm.201402468.

[259] C. Lu, Y. Liu, Y. Ying, and J. Liu. "Comparison of MoS_2, WS_2, and graphene oxide for DNA adsorption and sensing". In: *Langmuir* 33.2 (2017), pp. 630–637. DOI: 10.1021/acs.langmuir.6b04502.

[260] C. Zhu et al. "Single-Layer MoS_2 Based Nanoprobes for Homogeneous Detection of Biomolecules". In: *Journal of the American Chemical Society* 135.16 (2013), pp. 5998–6001. DOI: 10.1021/ja4019572.

[261] Y. Yoon, K. Ganapathi, and S. Salahuddin. "How Good Can Monolayer MoS_2 Transistors Be?" In: *Nano Letters* 11.9 (2011), pp. 3768–3773. DOI: 10.1021/nl2018178.

[262] T. Singh and A. Kumar. "Static Dielectric Constant of Room Temperature Ionic Liquids: Internal Pressure and Cohesive Energy Density Approach". In: *The Journal of Physical Chemistry B* 112.41 (Oct. 2008), pp. 12968–12972. DOI: 10.1021/jp8059618.

[263] M. A. Gebbie et al. "Long range electrostatic forces in ionic liquids". In: *Chem. Commun.* 53 (7 2017), pp. 1214–1224. DOI: 10.1039/C6CC08820A.

[264] M.-P. Lu, X.-Y. Dai, and M.-Y. Lu. "Probing Electron Mobility of Monolayer MoS_2 Field-Effect Transistors in Aqueous Environments". In: *Advanced Electronic Materials* 4.3 (2018), p. 1700418. DOI: 10.1002/aelm.201700418.

[265] W. Bao, X. Cai, D. Kim, K. Sridhara, and M. S. Fuhrer. "High mobility ambipolar MoS_2 field-effect transistors: Substrate and dielectric effects". In: *Applied Physics Letters* 102.4 (2013), p. 042104. DOI: 10.1063/1.4789365.

[266] A. Allain, J. Kang, K. Banerjee, and A. Kis. "Electrical contacts to two-dimensional semiconductors". In: *Nature Materials* 14.12 (2015), pp. 1195–1205. DOI: 10.1038/nmat4452.

[267] L. de Vreede et al. "Wafer scale fabrication of fused silica chips for low-noise recording of resistive pulses through nanopores". In: *Nanotechnology* (2019). DOI: 10.1088/1361-6528/ab0e2a.

[268] Y. Liu et al. "Approaching the Schottky-Mott limit in van der Waals metal-semiconductor junctions". In: *Nature* 557.7707 (2018), pp. 696–700. DOI: 10.1038/s41586-018-0129-8.

[269] M. Chhowalla, D. Jena, and H. Zhang. "Two-dimensional semiconductors for transistors". In: *Nature Reviews Materials* 1 (Aug. 2016), p. 16052. DOI: 10.1038/natrevmats.2016.52.

[270] D. Kiriya, M. Tosun, P. Zhao, J. S. Kang, and A. Javey. "Air-Stable Surface Charge Transfer Doping of MoS_2 by Benzyl Viologen". In: *Journal of the American Chemical Society* 136.22 (2014), pp. 7853–7856. DOI: 10.1021/ja5033327.

[271] H. Fang et al. "Degenerate n-Doping of Few-Layer Transition Metal Dichalcogenides by Potassium". In: *Nano Letters* 13.5 (2013), pp. 1991–1995. DOI: 10.1021/nl400044m.

[272] W. M. Parkin et al. "Raman Shifts in Electron-Irradiated Monolayer MoS_2". In: *ACS Nano* 10.4 (2016), pp. 4134–4142. DOI: 10.1021/acsnano.5b07388.

[273] M. C. Salvadori, I. G. Brown, A. R. Vaz, L. L. Melo, and M Cattani. "Measurement of the elastic modulus of nanostructured gold and platinum thin films". In: *Physical Review B - Condensed Matter and Materials Physics* 67.15 (2003). DOI: 10.1103/PhysRevB.67.153404.

[274] J. Zhou et al. "Investigation of the Hydrogen Silsesquioxane (HSQ) Electron Resist as Insulating Material in Phase Change Memory Devices". In: *Journal of Electronic Materials* 44.1 (2015), pp. 235–243. DOI: 10.1007/s11664-014-3390-0.

[275] R. H. Vervuurt, A. Sharma, Y. Jiao, W. M. Kessels, and A. A. Bol. "Area-selective atomic layer deposition of platinum using photosensitive polyimide". In: *Nanotechnology* 27.40 (2016), p. 405302. DOI: 10.1088/0957-4484/27/40/405302.

[276] T. B. H. Schroeder et al. "An electric-eel-inspired soft power source from stacked hydrogels". In: *Nature* 552.7684 (2017), pp. 214–218. DOI: 10.1038/nature24670.

[277] J. Comtet et al. "Nanoscale capillary freezing of ionic liquids confined between metallic interfaces and the role of electronic screening". In: *Nature Materials* 16 (Mar. 2017), p. 634. DOI: 10.1038/nmat4880.

Acronyms

μ-PL micro-photoluminescence. 89–91, 97

AFM atomic force microscope. 14, 17

Ag/AgCl silver/silver-chloride. 12, 13

Al_2O_3 alumina. 141

ALD atomic layer deposition. 116, 141, 143

BD brownian dynamics. 100

BN boron-nitride. 27

bp base pairs. 16, 19

BTD biased target deposition. 42

CAD computer-aided design. 116, 118

CDB controlled dielectric breakdown. 4, 5, 51

CIME interdisciplinary centre for electron microscopy. vi, 5, 32, 49

Cl^- chloride. 12, 13, 19, 20, 64, 65, 74, 79, 81, 103

CMI center for micronanotechnology. vi, 29, 150

CNC computer-numerical-control. 55

CVD chemical vapor deposition. 28, 29, 36, 38, 43, 70, 85, 90, 96, 116, 150, 151, 170, 178, 205

DAQ data acquisition. 125, 126

DFT density functional theory. 26

DI deionized. 46, 55, 56, 97, 166–169

DNA deoxyribonucleic acid. 2–8, 10–12, 14, 16–27, 32, 38–40, 42, 46, 51–53, 56, 60, 61, 113–117, 124, 129–133, 144, 178

DNAP phi29 DNA polymerase. 6

dsDNA double-stranded DNA. 4, 6, 16–19, 21–23, 26, 51, 60, 123, 126, 128, 131, 145

EBL e-beam lithography. 5, 36, 37, 42, 59, 116, 118–120, 129, 141–143, 146, 149, 150

ECR electrochemical reaction. 15, 37–39, 47, 51, 54, 55, 57, 60, 61, 64, 68, 70, 71, 84, 85, 88, 116, 117, 139, 151, 174

EDL electrical double layer. 84, 91, 93–95, 102, 103, 131, 132

EDTA ethylenediaminetetraacetic acid. 56, 178

EOF electroosmotic flow. 14, 23

FCS fluorescence correlation spectroscopy. 17

FEM finite element model. 14, 15, 86, 91, 92, 103, 104, 109, 130

FET field-effect transistor. 26–28, 30, 33, 115–118, 122, 129–131, 133, 134, 137–139, 143, 144, 149, 150, 152, 154–157

FFT fast Fourier transform. 31, 32, 48

FIB focused ion beam. 38, 70, 71, 149, 150

FRAP fluorescence recovery after photobleaching. 17

FRET Förster resonance energy transfer. 17

GHK Goldman-Hodgkin-Katz. 93, 95, 103

H_2O_2 hydrogen peroxide. 12

h-BN hexagonal boron-nitride. 5, 38, 96, 157

HfO_2 hafnium dioxide. 141, 143

HSQ hydrogen silsesquioxane. 141, 142, 145

IPA isopropyl alcohol. 46, 172

K^+ potassium. 11, 19, 20, 64–67, 74, 79, 81, 103

kbp kilobase pairs. 18, 19, 21, 22, 51, 60, 126, 128, 145, 161, 177, 178

KCl potassium chloride. 4, 11–13, 15, 21–24, 43, 44, 56, 62, 64, 66–69, 71, 73, 74, 76, 80, 85, 88, 89, 96, 97, 101, 102, 104, 107, 110, 122–125, 129–132, 141, 142, 146, 178

KOH potassium hydroxide. 36–39, 42, 70, 96, 129, 165, 166, 168, 169, 178, 180

LiCl lithium chloride. 23

LPCVD low pressure chemical vapor deposition. 166, 178

MD molecular dynamics. 9, 15, 27, 64–68, 73–75, 79, 80, 100, 123, 131

MIM metal-insulator-metal. 42, 169

MOCVD metal-organic CVD. 43, 151

MoS_2 Molybdändisulfid. iii, iv

MoS_2 molybdenum disulfide. i, ii, iv, vii, ix, 4, 5, 9–11, 13–15, 18–22, 26–33, 35–39, 41–49, 52, 53, 55, 59, 60, 62–71, 73–75, 78–87, 89–92, 96, 99, 101–104, 113, 115–119, 121–125, 128, 129, 131, 133, 134, 137–141, 143–147, 149–156, 159, 168, 170–176, 178, 180, 181, 185–187, 190–192, 194–202

MspA mycobacterium smegmatis porin A. 6

mw molecular weight. 126, 128

NPC nuclear pore complex. 8, 9

NPT constant number, pressure and temperature. 73

nt nucleotides. 18, 123, 125, 132, 178

PCB printed circuit board. 117, 118

PCR polymerase chain reaction. 177

PDF probability density function. 21, 22, 136

PDMS polydimethylsiloxane. 36–39, 46, 47, 55, 60, 138, 151, 170, 172–174

PEG polyethylene glycol. 126, 128, 131, 132, 178

PL photoluminescence. 30, 31, 90, 91

PMMA poly(methyl methacrylate). 36–39, 45, 46, 55, 71, 87, 96–98, 100, 101, 116–118, 129, 137, 140, 141, 143, 146, 149, 151, 170–172, 175, 176, 178, 180

PNP Poisson-Nernst-Planck. 67, 73, 74, 80, 99, 100

PPPM particle particle particle Mesh. 73

PRO pressure-retarded osmosis. 10

PSD power spectral density. 40, 41

PTFE polytetrafluoroethylene. 2

RED reverse electrodialysis. 10

RIE reactive ion etching. 5, 37, 59, 70, 116, 129, 141, 149, 154, 178

RTIL room temperature ionic liquid. 4, 24, 122, 132, 157

SAXS small-angle x-ray scattering. 17

SD secure digital. 118

SDS sodium dodecyl sulfate. 8

SEM scanning electron microscopy. 28, 29, 120, 142, 149, 150

SiN_x silicon nitride. 4, 5, 8, 18–21, 23, 25–27, 30, 36, 39–46, 48, 53, 59, 60, 70, 85, 87, 90, 96, 114, 116–120, 124, 125, 129, 131, 137–142, 147, 149–151, 153, 154, 166–172, 174–179

SiO_2 silicon dioxide. 4, 27, 30, 36, 39, 40, 42, 43, 90, 96, 141, 167, 169, 170, 178, 179

SMRT single-molecule real-time. 114

SNR signal-to-noise ratio. 115, 129, 134, 136, 155

ssDNA single-stranded DNA. 6, 16–18, 20, 25, 51, 123, 125, 131–133

STEM scanning transmission electron microscopy. 26

TEM transmission electron microscope. 4

TEM transmission electron microscopy. 4, 5, 15, 31, 32, 35–37, 45, 47–50, 59, 60, 64, 65, 70, 71, 84–86, 116, 117, 123, 125, 128, 139, 140, 142, 146, 147

TIRF total internal reflection fluorescence. 25

TMAH tetramethylammonium hydroxide. 39

TMD transition metal dichalcogenide. 27, 38, 46

TMDs transition metal dichalcogenides. 28, 84, 85

Tris tris(hydroxymethyl)aminomethane. 56, 178

TVD thermal vapor deposition. 28, 29

TVS thermal vapor sulfurization. 28, 29

WLC worm-like-chain model. 16

WS_2 tungsten disulfide. 5, 38

WSe_2 tungsten diselenide. 28, 29, 38

Michael Graf

PhD Candidate

Born on January 11 1989 in Olten (SO)
Nationality: Swiss

Rue Davel 3
CH-1096 Cully
+41 76 788 07 92
migra.ch@gmail.com

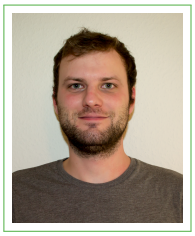

Current Research

I am currently working on nanopores and their application towards DNA sequencing and osmotic power generation. One interest is to fabricate a nanopore field-effect transistor using a 2-dimensional semiconducting material (molybdenum disulfide) to sense translocating biomolecules. The same material is also exploited to generate energy using salt concentration gradients (blue energy).

Education

Since 2014 **PhD Student in Biotechnology and Bioengineering**, *Laboratory of Nanoscale Biology, Swiss Federal Institute of Technology*, Lausanne.

2011–2013 **Master of Science MSc in Bioengineering, Minor in Biomedical Technologies**, *Swiss Federal Institute of Technology*, Lausanne.

2007–2011 **Bachelor of Science BSc in Life Sciences and Technologies**, *Swiss Federal Institute of Technology*, Lausanne.

2000–2007 **Swiss Matura**, *Kantonsschule*, Olten.

Master thesis

title *Studying the Nuclear Pore Complex using Stepwise Photobleaching*

supervisors Aleksandra Radenovic (EPFL), Jan T. Liphardt (Stanford University)

description In this work, I studied *importin* mediated transport across the nuclear pore complex. I counted their steady-state copy number by slowly bleaching the fluorescently tagged *importin* molecules. This resulted in a novel technique to count high copy numbers of protein using HiLo microscopy.

Selected Projects

2013–2014 **Civil Services**, *University Children's Hospital*, Bern.
Leading a study in electrical impedance tomography.

2012–2013 **Master Project**, *University of California*, Berkeley CA.
Studying the nuclear pore complex using stepwise photobleaching

2012–2012 **Semester Project**, *Swiss Federal Institute of Technology*, Lausanne.
OpenNanopore software package
Development of a flexible tool for data analysis of nanopore translocation experiments

2011–2011 **Civil Services**, *CHUV*, Lausanne.
Statistical analysis of brain FDG-PET scans with SPM 8
Development of a Matlab application automating the statistical analysis

Teaching

2014–2017 **Bioengineering Methods Lab**, *Master Students*, Swiss Federal Institute of Technology, Lausanne.
Practical introduction to lab work. Organizing and supervising a research project during the course of the semester.

2014–2017 **Fundamentals of Biosensors and Electronic Biochips**, *Master Students*, Swiss Federal Institute of Technology, Lausanne.
Writing exercises. Assist the students during exercise sessions. Correct exercises and exams.

Languages

German	Mother Tongue	French/English	Excellent

In Silico Skills

Programming	Python, C/C++, Java, Matlab	Imaging	ImageJ, Photoshop, Illustrator
Office	LaTeX, Word, Excel, PowerPoint, Pages, Keynote	Web	HTML, JavaScript
CAD and 3D	Autocad, Nanolithography Toolbox, Inventor, SolidWorks, Blender	Simulation	Comsol

Technical Skills

Fabrication	photo- and electron beam lithography, metal evaporation, wet and dry etching, focused ion beam, mask writing, mask alignment, ellipsometry, wafer dicing, wire bonding	Imaging	fluorescent microscopy, scanning electron microscopy, transmission electron microscopy
Electrical	low current measurements, data acquisition, current amplifiers	Wet Lab	PCR, plasmid preparation, protein expression, protein purification, gel-electrophoresis, SDS Page, Western blot

Conferences

February 4-7 2019 **Dead Sea Water Workshop**, *Poster presentation*, Ein Gedi, Israel.

June 16-23 2018 **From Solid State to Biophysics IX**, *Oral presentation and poster presentation*, Cavtat, Croatia.

February 17-21 2018 **Biophysical Society Meeting**, *Poster presentation*, San Francisco, United States.

July 16-21 2017 **Nanopore Meeting**, *Poster presentation*, Jacobs University, Bremen, Germany.

August 29-01 2017 **Flatlands**, *Oral presentation*, Swiss Federal Institute of Technology, Lausanne, Switzerland.

September 01-10 2016 **International School of Biophysics**, *Poster presentation*, Split, Croatia.

July 11-15 2016 **Workshop on Bio-inspired Nanosystems for Energy Conversion** , *Oral presentation*, Berlin, Germany.

March 22-27 2015 **Selective transport through nanopores: physics meets biology** , *Poster presentation*, Lenzerheide, Switzerland.

Honors and Awards

April 7 2019 **Honor**, *Finalist, Schmidt Science Fellows*, New York, USA.

March 25 2015 **Prize**, *Nature Nanotechnology poster prize*, Selective transport through nanopores: physics meets biology, Lenzerheide, Switzerland.

October 5 2013 **Prize**, *Prize for the best Master thesis in biomedical technologies*, EPFL, Lausanne.

October 5 2013 **Mention**, *Mention of excellence*, EPFL, Lausanne.

Publications

[1] C Raillon, P Granjon, **Michael Graf**, L J Steinbock, A Radenovic. Fast and automatic processing of multi-level events in nanopore translocation experiments. *Nanoscale* **2012**, *4*, 4916–4924.

[2] C. Raillon, P. Granjon, **Michael Graf**, A. Radenovic. Detection of RNAP-DNA complexes using solid state nanopores. *Proceedings of the Annual International Conference of the IEEE Engineering in Medicine and Biology Society, EMBS* **2013**, 4106–4109.

[3] Alan R Lowe, Jeffrey H Tang, Jaime Yassif, **Michael Graf**, William Y C Huang, Jay T Groves, Karsten Weis, Jan T Liphardt. Importin-β modulates the permeability of the nuclear pore complex in a Ran-dependent manner. *eLife* **2015**, *4*.

[4] J Feng, K Liu, **Michael Graf**, M Lihter, R D Bulushev, D Dumcenco, D T L Alexander, D Krasnozhon, T Vuletic, A Kis, A Radenovic. Electrochemical Reaction in Single Layer MoS_2: Nanopores Opened Atom by Atom. *Nano Letters* **2015**, *15*, 3431–3438.

[5] Jiandong Feng, Ke Liu, **Michael Graf**, Dumitru Dumcenco, Andras Kis, Massimiliano Di Ventra, Aleksandra Radenovic. Observation of ionic Coulomb blockade in nanopores. *Nature Materials* **2016**, *15*, 850–855.

[6] Jiandong Feng, **Michael Graf**, Ke Liu, Dmitry Ovchinnikov, Dumitru Dumcenco, Mohammad Heiranian, Vishal Nandigana, Narayana R Aluru, Andras Kis, Aleksandra Radenovic. Single-layer MoS_2 nanopores as nanopower generators. *Nature* **2016**, *536*, 197–200.

[7] **Michael Graf**, Thomas Riedel. Electrical impedance tomography: Amplitudes of cardiac related impedance changes in the lung are highly position dependent. *PLoS ONE* **2017**, *12*, e0188313.

[8] Po Ling Chang, **Michael Graf**, Chao Hsuan Hung, Aleksandra Radenovic. Orthogonal Tip-to-Tip Nanocapillary Alignment Allows for Easy Detection of Fluorescent Emitters in Femtomolar Concentrations. *Nano Letters* **2018**, *18*, 3165–3171.

[9] **Michael Graf**, Ke Liu, Aditya Sarathy, Jean-Pierre Leburton, Aleksandra Radenovic. Transverse Detection of DNA in a MoS_2 Nanopore. *Biophysical journal* **2018**, *114*, 180a.

[10] **Michael Graf**, Martina Lihter, Mukeshchand Thakur, Vasileia Georgiou, Juraj Topolancik, B. Robert Ilic, Ke Liu, Jiandong Feng, Yann Astier, Aleksandra Radenovic. Fabrication and practical applications of molybdenum disulfide nanopores. *Nature Protocols* **2019**, *14*, 1130–1168.

[11] **Michael Graf**, Martina Lihter, Dmitrii Unuchek, Aditya Sarathy, Jean-Pierre Leburton, Andras Kis, Aleksandra Radenovic. Light Enhanced Blue Energy Generation using MoS_2 Nanopores. *Joule* **2019**.

Ce document a été imprimé au Centre d'impression EPFL,
imprimerie climatiquement neutre, certifiée myClimate.